# INNOVATIONS IN HEADWATER SNOW MONITORING IN THE SOUTHERN CANADIAN ROCKIES

**CELESTE C. BARNES**
**M.Sc. University of Lethbridge, 2014**

A Thesis
Submitted to the School of Graduate Studies
of the University of Lethbridge
in Partial Fulfillment of the
Requirements for the Degree

DOCTOR OF PHILOSOPHY

in

EARTH, SPACE, AND PHYSICAL SCIENCES

Department of Geography and Environment
University of Lethbridge
LETHBRIDGE, ALBERTA, CANADA

**INNOVATIONS IN HEADWATER SNOW MONITORING IN THE SOUTHERN CANADIAN ROCKIES**

**CELESTE BARNES**

Date of Defence: July 17, 2023

| | | |
|---|---|---|
| Dr. Chris Hopkinson<br>Thesis Supervisor | Professor | Ph.D. |
| Dr. Dan Johnson<br>Thesis Examination Committee Member | Professor | Ph.D. |
| Dr. Ryan MacDonald<br>Thesis Examination Committee Member<br>MacDonald Hydrology Consultants Ltd. | Senior Hydrologist | Ph.D. |
| Dr. Stefan Kienzle<br>Internal External Examiner<br>Department of Geography and Environment | Professor | Ph.D. |
| Dr. Chris Derksen<br>External Examiner<br>Environment and Climate Change Canada | Research Scientist | Ph.D. |
| Chair, Dr. Laura Chasmer<br>Thesis Examination Committee | Associate Professor | Ph.D. |

**Abstract**

The Alberta Rocky Mountain region is a large contributor to the water supply for populations, ecosystems, wildlife, and industry. Water resource managers and governmental policy makers require estimates to ensure there is a sufficient supply to meet increasing demands while at the same time responding to potential decreases in the supply from a changing climate. This research was conducted in the Southwestern Alberta Rocky Mountains and explored precipitation patterns and quantified spatially explicit estimates of winter snowpack SWE water yields to address the need for improved headwater resource assessments. There is high spatial and temporal variability of precipitation and the winter snowpack in mountain regions. Precipitation gauges are prone to sensor- and wind-induced measurement errors. Quality Control Corrections were applied to two valley and one alpine gauge. After corrections, the alpine site had up to a 50% increase in precipitation depths while the valley sites had up to a 5% change. A seasonality component was present where the alpine site had up to 80% more precipitation in the winter months and all sites received 50% to 70% lower precipitation in the summer months. This seasonality caused valley to alpine sites to have different monthly elevational precipitation gradients. Six "single point in time" mesoscale snow water equivalent (SWE) estimates were created using a combination of a) airborne lidar derived or predicted snow depths; and b) publicly accessible snowpack monitoring datasets to constrain snow density models for each SWE estimate. The most productive elevation zone was at the mid-mountain treeline between 1900 masl to 2200 masl producing approximately half of the estimated total water yield. Precipitation corrections, elevational precipitation gradients, and SWE water yields created in this research can be used by water managers to calibrate models used to derive real-time Alberta water resource estimates.

## Contribution of Authors

### Chapter 2: Quality Control Impacts on Total Precipitation Gauge Records for Montane Valley and Ridge Sites in SW Alberta, Canada

Citation:

Barnes, C., & Hopkinson, C. (2022). Quality Control Impacts on Total Precipitation Gauge Records for Montane Valley and Ridge Sites in SW Alberta, Canada. Data, 7(6), 73. /https://doi.org/10.3390/data7060073, https://www.mdpi.com/2306-5729/7/6/73

Accompanying published dataset:

Hopkinson, C., & Barnes, C. (2022). Precipitation gauge and supplemental weather station data for three Oldman River headwater locations in SW Alberta. Federated Research Data Repository.

Author Contributions:

Conceptualization: Chris Hopkinson and Celeste Barnes
Methodology: Celeste Barnes
Software: Celeste Barnes
Validation: Chris Hopkinson
Formal analysis: Celeste Barnes
Investigation, Celeste Barnes and Chris Hopkinson
Resources: Chris Hopkinson
Data curation, Celeste Barnes
Writing - original draft preparation: Celeste Barnes
Writing - review and editing: Celeste Barnes and Chris Hopkinson
Visualization: Celeste Barnes
Supervision: Chris Hopkinson
Project administration: Chris Hopkinson
Funding acquisition: Chris Hopkinson
All of the authors have read and agreed to the published version of the manuscript.

## Chapter 3: Headwater Precipitation Gradients in the Southern Rockies of Alberta, Canada

Citation:

Barnes, C., MacDonald, R., & Hopkinson, C. (2023). Headwater Precipitation Gradients in the Southern Rockies of Alberta, Canada, Internal Review

Author Contributions:

Conceptualization: Chris Hopkinson and Celeste Barnes
Methodology: Celeste Barnes
Software: Celeste Barnes
Validation: Chris Hopkinson
Formal analysis: Celeste Barnes
Investigation, Celeste Barnes and Chris Hopkinson
Resources: Chris Hopkinson
Data curation, Celeste Barnes
Writing - original draft preparation: Celeste Barnes
Writing - review and editing: Celeste Barnes, Ryan MacDonald, and Chris Hopkinson
Visualization: Celeste Barnes
Supervision: Chris Hopkinson
Project administration: Chris Hopkinson
Funding acquisition: Chris Hopkinson
All of the authors have read and agreed to the version of the manuscript.

## Chapter 4: In-Situ LED-Based Observation of Snow Surface and Depth Transects

Citation:

Barnes, C., Hopkinson, C., Porter, T., & Xi, Z. (2020). In-Situ LED-Based Observation of Snow Surface and Depth Transects. *Sensors*, *20*(8), 2292. https://www.mdpi.com/1424-8220/20/8/2292

Author Contributions:

Conceptualization: Chris Hopkinson and Celeste Barnes
Methodology: Celeste Barnes
Software: Zhouxin Xi
Validation: Chris Hopkinson
Formal analysis: Celeste Barnes
Investigation, Celeste Barnes, Chris Hopkinson, Thomas Porter, and Zhouxin Xi
Resources: Chris Hopkinson
Data curation, Celeste Barnes, Thomas Porter, and Zhouxin Xi
Writing - original draft preparation: Celeste Barnes
Writing - review and editing: Celeste Barnes and Chris Hopkinson
Visualization: Celeste Barnes
Supervision: Chris Hopkinson
Project administration: Chris Hopkinson
Funding acquisition: Chris Hopkinson
All of the authors have read and agreed to the published version of the manuscript.

## Chapter 5: Comparing Mountain Snowpack Depth Model Results from Different Airborne Laser Scanning Flight Path Samples

Citation:

Barnes, C., & Hopkinson, C. (2022). Comparing Mountain Snowpack Depth Model Results from Different Airborne Laser Scanning Flight Path Samples. *Canadian Journal of Remote Sensing*, *48*(1), 81-92. https://doi.org/10.1080/07038992.2021.1999797

Author Contributions:

Conceptualization: Chris Hopkinson and Celeste Barnes
Methodology: Celeste Barnes
Software: Celeste Barnes
Validation: Chris Hopkinson
Formal analysis: Celeste Barnes
Investigation, Celeste Barnes and Chris Hopkinson
Resources: Chris Hopkinson
Data curation, Celeste Barnes
Writing - original draft preparation: Celeste Barnes
Writing - review and editing: Celeste Barnes and Chris Hopkinson
Visualization: Celeste Barnes
Supervision: Chris Hopkinson
Project administration: Chris Hopkinson
Funding acquisition: Chris Hopkinson
All of the authors have read and agreed to the published version of the manuscript.



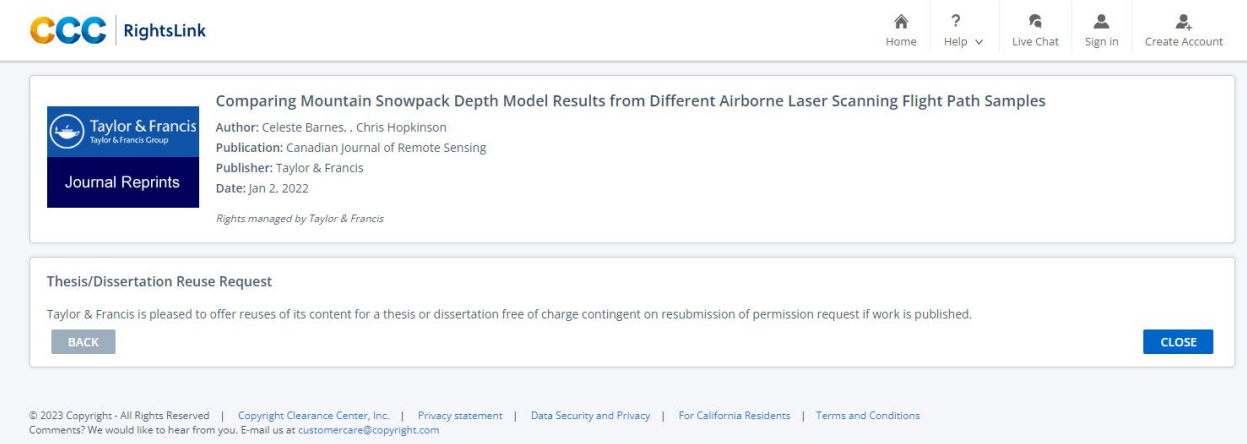

## Table of Contents

## List of Figures

## List of Tables

## List of Abbreviations

| | |
|---|---|
| ACIS | Alberta Climate Information Service |
| AEP | Alberta Environment And Protected Areas |
| ALS | Airborne Laser Scanning |
| BE | Bare-Earth |
| CFC | Canopy Fractional Coverage |
| CHM | Canopy Height Model |
| CMA | Centered Moving Average |
| CMR | Castle Mountain Ridge |
| DEM | Digital Elevation Model |
| DEM | Digital Elevation Model |
| DSM | Digital Surface Model |
| DSSM | Digital Snow Surface Model |
| DTT | Distance-To-Target |
| ELEV | Elevation |
| EPG | Elevational Precipitation Gradients |
| FBR | Forest Based Regression |
| FOV | Field Of View |
| FRDR | Federated Research Data Repository |
| GoA | Government Of Alberta |
| KM | Kilometre |
| LCP | Least Cost Path |
| LED | Light Emitting Diode |
| leddar | Led Lidar, Leddar Tech Is16 |
| LiDAR | Light Detection And Ranging |
| M | Metre |
| MA | Moving Average |
| masl | Metres Above Seal Level |
| MSP | Mesoscale Spatialized Precipitation |
| NIR | Near Infra-Red |
| QC | Quality Control |
| QCC | Quality Control Corrected |
| RF | Random Forest |
| RMSE | Root Mean Square Error |
| SAU | Snow Accumulation Unit |
| SCA | Snow Covered Area |
| SDM | Snow Depth Model |
| SPICE | Solid Precipitation Intercomparison Experiment |
| SRHC | South Racehorse Creek |
| SSM | Snow Surface Model |
| StDev | Standard Deviation |
| SWE | Snow Water Equivalent |
| T3 | ‘Expert’ Three-Transect |
| TIN | Triangular Irregular Network |
| TPI | Topographic Position Index |
| TS | Time Series |
| ULAL | University Of Lethbridge Artemis Lab |
| WCII | West Castle II |
| WCW | West Castle Watershed |
| WFS | Westcastle Field Station |
| WLNP | Waterton Lakes National Park |

# 1 Thesis Introduction

## 1.1 Introduction

Water is a life-sustaining resource. Adequate supplies are required to support healthy populations, industry, wildlife, ecosystems, and economic growth in any given region. Significant monitoring and management occurs in Alberta to control water consumption especially since there are continually increasing demands on the resource (Government of Alberta, 2017). The Government of Alberta created a "Water for Life" strategy (Alberta Environment, 2003) for the protection of water resources within the province. The intent was to ensure a sufficient healthy water supply for all sectors while promoting economic growth and maintaining existing interprovincial and international water supply agreements (Alberta Environment, 2004a, 2004b). Over time, periodical reviews have been done (Alberta Environment, 2012; AWC, 2007) and revisions were made to the strategy (Alberta Environment, 2008). A recommendation was put forward by the Alberta Water Council to work towards obtaining a better quantifiable measurement of both surface and groundwater resources (AWC, 2017).

In the mountain headwaters of Canada, the winter snowpack contributes a large proportion of the overall water resource (Natural Resources Canada, 2010; Statistics Canada, 2017). Surface water is stored in a frozen state in winter months with groundwater released as base flow (Barrows & Horton, 1907; Kienzle & Mueller, 2013; Paznekas & Hayashi, 2016). The spring melt can produce high flows leading to increased downstream flood hazard (Pomeroy et al., 2016; Wayand et al., 2015). Conversely, a lower-than-average winter snowpack can cause drought stresses and low water availability in late summer (Zhang et al., 2001). Alberta

governmental snowpack monitoring has been operational for over a century with the earliest recorded snow depth measurements taken at Beaver Hills West, AB in 1908 and Lethbridge, AB in 1921 (Environment Canada, 2023).

The snowpack attribute of prime importance is snow water equivalent (SWE) (Government of Alberta, 2018) which is obtained from two variables: snow depth and density. Alberta Environment and Protected Areas (AEP) personnel conduct monthly field sampling (Pickering, 2018) as well as maintain weather stations that include snow depth (Campbell, 2018) and SWE (Pedlar, 2018) measurements. There are significant operational and logistical costs associated with the measurement of the snowpack including the acquisition and maintenance of equipment and sensors. Therefore, sites are sparsely located in the Alberta mountain headwaters region (Nitu, 2010). Mountainous regions have high spatiotemporal snowpack variability driven by local terrain characteristics (Anderson et al., 2014; Grünewald et al., 2014) and meteorological influences (Pepin et al., 2015) such as orographic precipitation enhancement (Houze, 2012) that produces a greater amount of precipitation in the upper alpine (Mott et al., 2014).

Single-point monitoring locations are not representative of the overall land cover and terrain characteristics driving the variability of the snowpack in mountain regions (Schirmer et al., 2011). In addition, climate warming is occurring causing a shift in both temperature (Kienzle, 2018) and precipitation regimes (Luce et al., 2013) in the mountain region (Newton et al., 2021). The snow season has become shorter in duration with the onset of melt beginning weeks earlier (Shea et al., 2021) impacting the amount of water available from both annual and summer stream flows (Cohen et al., 2015; Lapp et al., 2005; MacDonald et al., 2010; Shepherd et al., 2010). Changing climate trends are contributing to gradual temperature and precipitation deviations

from past long-term normals. Models that worked reasonably well in the past will no longer be representative of future conditions (Savenije & Hrachowitz, 2017; Siirila-Woodburn et al., 2021). Changes in the timing of seasonal precipitation and snow melt impacts the available water supply. This creates a need for an improved monitoring framework based on physical sampling approaches that delivers better spatially distributed models in mountain regions.

## 1.2 Thesis Research Objectives

This thesis explores options for enhancing the Alberta Eastern Slopes snowpack monitoring framework. The research objectives explore innovations in spatial and temporal monitoring including:

- analyze and characterize mountain precipitation regimes in the southern Alberta Eastern Slopes.
- analyze and characterize mountain snow depth variability at in-situ and watershed scales.
- develop a scalable cost-effective airborne lidar snow depth sampling strategy that can be used to simulate spatially distributed snow depth over an entire watershed.
- develop a watershed snow density modelling strategy using existing publicly available monitoring data.
- develop a spatially-explicit mesoscale watershed-wide Snow Water Equivalent (SWE) modelling framework.

## 1.3 Thesis Summary

This thesis has been written using the “research paper” style with a “Thesis Introduction”, five research papers as shown in Figure 1.1 and a “Thesis Conclusion and Recommendations”.

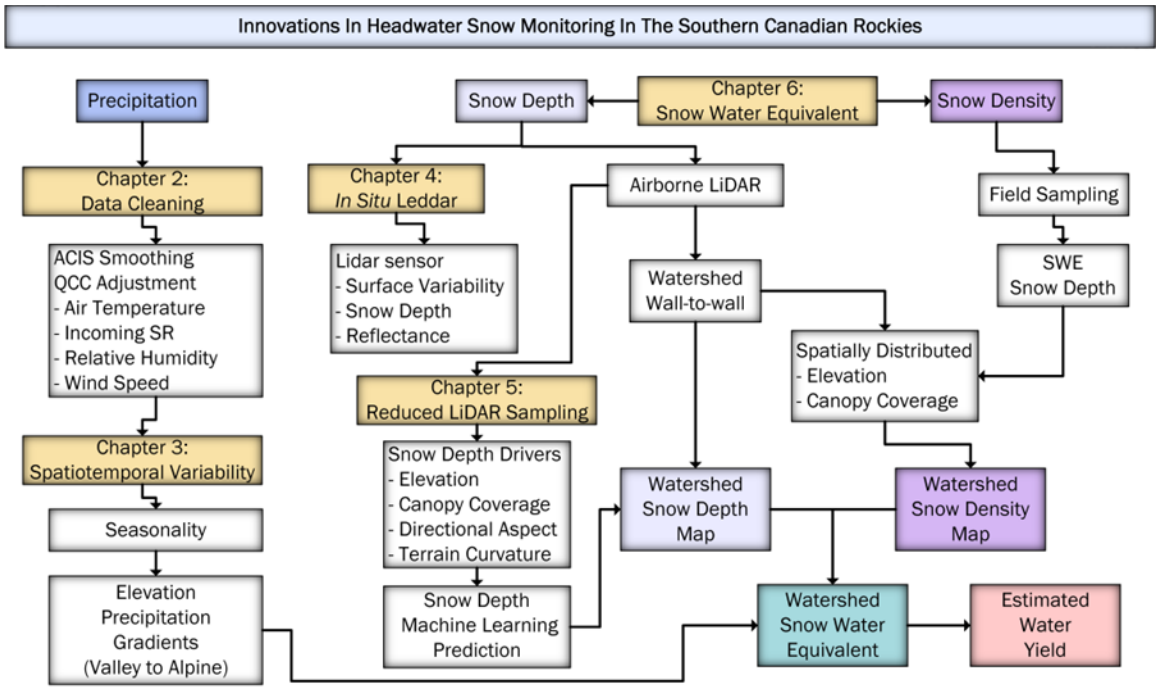

Figure 1.1. High level overview of the thesis research paper chapters (orange box). The coloured boxes show the main themes within the thesis those being precipitation (blue box), snow depth (light blue box), and snow density (purple box) that leads to Watershed Snow Water Equivalent (teal box) and Estimated Water Yield (rose box). The grey boxes between the main concepts show analysis and sections in a chapter. The arrows show the linkages between the main themes, chapter dependencies, and sections.

The organization of the research papers in this thesis begins with the exploration of spatiotemporal precipitation patterns in the Alberta southern Eastern Slopes. In chapter 2, "Quality Control Impacts on Total Precipitation Gauge Records for Montane Valley and Ridge Sites in SW Alberta, Canada" (Barnes & Hopkinson, 2022b) quality control processes for data adjustments were applied to Geonor totalizing precipitation gauge records. These gauges are sensitive to sensor noise and wind-induced measurement errors that can bias the data. In the Canadian Mountain region of southwestern Alberta, it is typical for Government managed sites to be at mountain valley and mid-mountain locations with tall forest cover sheltering the precipitation gauges. The unique component of this study is the location and setting of three Geonor precipitation gauges installed by the University of Lethbridge ARTeMiS Lab (ULAL). Two of these gauges are located at mountain valley elevations and one is on an upper mountain

alpine ridge. These sites do not have significant forest cover to shelter gauges from wind. One of these sites is also in a recently burnt forest. This study showed sensor and wind-induced measurement errors can lead to significant underestimations of recorded precipitation at the higher elevation gauge.

The "Headwater Precipitation Gradients in the Southern Rockies of Alberta, Canada" (in review) chapter (3) builds on chapter 2. Time-series analysis methods were applied to AEP and ULAL smoothed and quality control cleaned datasets to examine annual spatiotemporal precipitation patterns in the Southern Alberta Eastern Slopes. A seasonality signal was present where higher precipitation depths were observed in winter snow accumulation months and lower depths recorded in the summer months. Monthly elevational precipitation gradients did not have a constant rate of increase from valley to higher elevation sites over an annual cycle. This study demonstrated seasonality and differences in elevational precipitation gradients need to be accounted for when spatializing these data for use in hydrologic models and water resource estimates.

An experimental design for continuous measurement of snowpack depth was created examining the feasibility of using a low-cost, low-power LED LiDAR (Leddar) time-of-flight sensor in Chapter 4, "In-Situ LED-Based Observation of Snow Surface and Depth Transects" (Barnes et al., 2020) chapter. Contemporary snowpack monitoring sensors record a single averaged measurement over the field-of-view with no additional snow characteristics measured by the sensor. The Leddar sensor used in this experimental study was designed for industrial uses, such as in autonomous self-driving vehicles or traffic and production-line monitoring. It records 16 individual distance-to-target and light reflectance observations across its field-of-view. In this study, the sensor was used for environmental monitoring of a seasonal snowpack.

The Leddar sensor was selected to see if it was possible to detect changes in the snowpack over time due to snow accumulation, compaction, and melt using the continuous distance-to-target and reflectance signal. Sensor performance and accuracy were examined under varying winter temperatures and snowpack states. An additional benefit of the Leddar sensor over contemporary snowpack monitoring sensors was the recorded reflectance signature that allowed for examination of changing snowpack surface conditions over time across the 16 segments. This study demonstrated Leddar technology is a viable low-cost and low-power alternative to contemporary snow depth sensors. The most notable benefits were the two-dimensional data as well as the intensity signal showed correlation with snow surface albedo and inversely with air temperature.

One available technology to map snow depth at the watershed scale is airborne lidar. Typically, missions are designed to fly a "wall to wall" watershed which can limit single flight sampling to ~100 $km^2$ in the winter months. In chapter 5, "Comparing Mountain Snowpack Depth Model Results from Different Airborne Laser Scanning Flight Path Samples" (Barnes & Hopkinson, 2022a), an alternative method was used to sample and model snow depth at the mesoscale. Instead of flying the entire watershed, two flight line sampling configurations were created based on capturing a maximum of unique signatures of snowpack depth variability. The first was a "static goal-oriented" shortest path approach. Static goal-oriented approaches are based on using homogeneous features for path finding such as terrain and landscape features with the same slope angle, directional aspect, canopy cover, distance to water, etc. The challenge in this approach was the path finding strategy had to be implemented based on selecting and maximizing the number of unique signatures within the path and not on maximizing the same features. The second path finding strategy implemented a transect approach to fly three corridors

perpendicular to the watershed centerline. For each path, machine learning was used to predict snow depth for the balance of the watershed. This study demonstrated reduced watershed sampling could be effective for modelling mesoscale snow depth.

The final chapter (chapter 6), "Watershed Snow Water Equivalent from Lidar Snow Depth and Field-Sampled Density Models" quantified snowpack water resources in the form of spatially explicit mesoscale estimates of SWE. Watershed "wall-to-wall" lidar sampling missions were flown capturing bare-earth, early, mid, and late season snow covered surfaces. Snow density is difficult to measure at the mesoscale. Elevation and forest canopy coverage were two drivers used to develop the snow density models. Two government snow monitoring field sampling sites in close proximity to the watershed were used to constrain lower and upper limits for each snow density model that coincided with lidar surveys. In this study, only one lidar survey coincided with government field sampling. There was up to a 9-day gap between all other lidar flights and government field sampling. The snowpack state can change significantly during this period if melt or large snowfall events occur and will bias snow density estimations. Therefore, two different density models were tested, one using the closest temporal sampling and the other using the 30-year monthly mean. However, the 30-year mean may not be representative of the current snowpack state at the time of the lidar flight and may overestimate or underestimate density. Snow depth and density models were combined to create estimated water yield for each lidar snow sampling mission. By using a reduced lidar flight line snow sampling strategy combined with snow density modelling, water yield was within 80% of wall-to-wall estimates. This approach could complement government snow monitoring practices by flying a larger portion of the Alberta Eastern Slopes at a reduced cost for a single winter airborne lidar mission.

## 1.4 References


Alberta Environment. (2003). Water for Life - Alberta's Strategy for Sustainability. In. Government of Alberta. http://aep.alberta.ca/water/programs-and-services/water-for-life/strategy/downloadable-information-about-the-water-for-life-strategy.aspx

Alberta Environment. (2004a). *Alberta Environment, Water Management Operations, International Joint Commission Submission, August 2004*. http://environment.alberta.ca/documents/WMO-Submission_IJC1.pdf

Alberta Environment. (2004b). *Text, History and Geography of the 1909 Boundary Waters treaty and the 1921 Order of the International Joint Commission. A supplement to "Sharing the Waters".* http://environment.gov.ab.ca/info/library/7022.pdf

Alberta Environment. (2008). Water for Life - A Renewal. In. Edmonton, AB: Government of Alberta.

Alberta Environment. (2012). Water for Life - Progress Report December 1, 2008 - March 31, 2011. In. Edmonton, AB: Government of Alberta.

Anderson, B. T., McNamara, J. P., Marshall, H. P., & Flores, A. N. (2014). Insights into the physical processes controlling correlations between snow distribution and terrain properties. *Water Resources Research*, *50*(6), 4545-4563. https://doi.org/doi:10.1002/2013WR013714

AWC. (2007). Alberta's Water Management System POLICY ISSUES AND GAPS Final Report. In. Edmonton, AB: Alberta Water Council.

AWC. (2017). Review of Water for Life Implementation Progress: 2012–2015. In. Edmonton, AB: Alberta Water Council.

Barnes, C., & Hopkinson, C. (2022a). Comparing Mountain Snowpack Depth Model Results from Different Airborne Laser Scanning Flight Path Samples. *Canadian Journal of Remote Sensing*, *48*(1), 81-92. https://doi.org/10.1080/07038992.2021.1999797

Barnes, C., & Hopkinson, C. (2022b). Quality Control Impacts on Total Precipitation Gauge Records for Montane Valley and Ridge Sites in SW Alberta, Canada. *Data*, *7*(6), 73. https://doi.org/https://doi.org/10.3390/data7060073

Barnes, C., Hopkinson, C., Porter, T., & Xi, Z. (2020). In-Situ LED-Based Observation of Snow Surface and Depth Transects. *Sensors*, *20*(8), 2292. https://www.mdpi.com/1424-8220/20/8/2292

Barrows, H. K., & Horton, R. E. (1907). *Determination of stream flow during the frozen season*. US Government Printing Office.

Campbell, S. (2018). *Acoustic Snow Depth Sensor Operation*. Edmonton, AB: Alberta Environment and Parks Retrieved from http://environmentalmonitoring.alberta.ca/wp-content/uploads/2018/07/Acoustic-Snow-Depth-Sensor.pdf

Cohen, S., Koshida, G., & Mortsch, L. (2015). Climate and water availability indicators in Canada: Challenges and a way forward. Part III–Future scenarios. *Canadian Water Resources Journal/Revue canadienne des ressources hydriques*(ahead-of-print), 1-13. https://www.tandfonline.com/doi/full/10.1080/07011784.2015.1006021

Environment Canada. (2023). *Digital Archive of Canadian Climatological Data* Environment Canada. http://climate.weather.gc.ca/advanceSearch/searchHistoricData_e.html

Water Act, Government of Alberta (2017). www.qp.alberta.ca/documents/Acts/w03.pdf

Government of Alberta. (2018). *Snow Does Not Equal Flood: Alberta's Snowmelt and its Impact on Alberta Rivers*. Edmonton, AB: alberta.ca Retrieved from https://open.alberta.ca/publications/snow-does-not-equal-flood-alberta-s-snowmelt-and-its-impact-on-alberta-rivers

Grünewald, T., Bühler, Y., & Lehning, M. (2014). Elevation dependency of mountain snow depth. *The Cryosphere*, *8*(6), 2381-2394.

Houze, R. A. (2012). Orographic effects on precipitating clouds. *Reviews of Geophysics*, *50*(1). https://doi.org/10.1029/2011RG000365

Kienzle, S. W. (2018). Has it become warmer in Alberta? Mapping temperature changes for the period 1950–2010 across Alberta, Canada. *The Canadian Geographer / Le Géographe canadien*, *62*(2), 144-162. https://doi.org/10.1111/cag.12432

Kienzle, S. W., & Mueller, M. (2013). Mapping Alberta's surface water resources for the period 1971–2000. *Canadian Geographies / Géographies canadiennes*, *57*(4), 506-518. https://doi.org/https://doi.org/10.1111/j.1541-0064.2013.12050.x

Lapp, S., Byrne, J., Townshend, I., & Kienzle, S. (2005). Climate warming impacts on snowpack accumulation in an alpine watershed. *International Journal of Climatology*, *25*(4), 521-536. https://doi.org/10.1002/joc.1140

Luce, C. H., Abatzoglou, J. T., & Holden, Z. A. (2013). The Missing Mountain Water: Slower Westerlies Decrease Orographic Enhancement in the Pacific Northwest USA. *Science*, *342*(6164), 1360-1364. https://doi.org/10.1126/science.1242335

MacDonald, R. J., Byrne, J. M., Kienzle, S. W., & Larson, R. P. (2010). Assessing the Potential Impacts of Climate Change on Mountain Snowpack in the St. Mary River Watershed, Montana. *Journal of Hydrometeorology*, *12*(2), 262-273. https://doi.org/10.1175/2010JHM1294.1

Mott, R., Scipión, D., Schneebeli, M., Dawes, N., Berne, A., & Lehning, M. (2014). Orographic effects on snow deposition patterns in mountainous terrain. *Journal of Geophysical Research: Atmospheres*, *119*(3), 1419-1439. https://doi.org/doi:10.1002/2013JD019880

Natural Resources Canada. (2010). *Atlas of Canada, 6th Edition (archival version) Average Maximum Snow Depth*. Ottawa, ON, Government of Canada, Natural Resources Canada, Earth Sciences Sector, Atlas of Canada. https://open.canada.ca/data/en/dataset/d90ddf8f-8893-11e0-bc5e-6cf049291510

Newton, B. W., Farjad, B., & Orwin, J. F. (2021). Spatial and Temporal Shifts in Historic and Future Temperature and Precipitation Patterns Related to Snow Accumulation and Melt Regimes in Alberta, Canada. *Water*, *13*(8), 1013. https://www.mdpi.com/2073-4441/13/8/1013

Nitu, R. (2010). *CIMO Survey on National Summaries of Methods and Instruments for Solid Precipitation Measurement at Automatic Weather Stations, IOM 102, TD1544*.

Paznekas, A., & Hayashi, M. (2016). Groundwater contribution to winter streamflow in the Canadian Rockies. *Canadian Water Resources Journal / Revue canadienne des ressources hydriques*, *41*(4), 484-499. https://doi.org/10.1080/07011784.2015.1060870

Pedlar, J. (2018). *Protocols for the Measurement of Snow Water Equivalent with a Snow Pillow*. Edmonton, AB: Alberta Environment and Parks Retrieved from http://environmentalmonitoring.alberta.ca/wp-

content/uploads/2018/07/Protocols-for-the-Measurement-of-Snow-Water-Equivalent-with-Snow-Pillow.pdf

Pepin, N., Bradley, R., Diaz, H., Baraër, M., Caceres, E., Forsythe, N., Fowler, H., Greenwood, G., Hashmi, M., & Liu, X. (2015). Elevation-dependent warming in mountain regions of the world. *Nature Climate Change*, *5*(5), 424.

Pickering, R. (2018). *Snow Surveying Field Sampling Protocols*. Alberta Environment and Parks. http://environmentalmonitoring.alberta.ca/resources/standards-and-protocols/

Pomeroy, J. W., Stewart, R. E., & Whitfield, P. H. (2016). The 2013 flood event in the South Saskatchewan and Elk River basins: Causes, assessment and damages. *Canadian Water Resources Journal / Revue canadienne des ressources hydriques*, *41*(1-2), 105-117. https://doi.org/10.1080/07011784.2015.1089190

Savenije, H. H., & Hrachowitz, M. (2017). HESS Opinions Catchments as meta-organisms-a new blueprint for hydrological modelling. *Hydrology and Earth System Sciences*, *21*(2), 1107.

Schirmer, M., Wirz, V., Clifton, A., & Lehning, M. (2011). Persistence in intra-annual snow depth distribution: 1.Measurements and topographic control. *Water Resources Research*, *47*(9). https://doi.org/10.1029/2010WR009426

Shea, J. M., Whitfield, P. H., Fang, X., & Pomeroy, J. (2021). The Role of Basin Geometry in Mountain Snowpack Responses to Climate Change. *Frontiers in Water*, *3*, 4.

Shepherd, A., Gill, K. M., & Rood, S. B. (2010). Climate change and future flows of Rocky Mountain rivers: converging forecasts from empirical trend projection and down-scaled global circulation modelling. *Hydrological Processes*, *24*(26), 3864-3877. https://doi.org/10.1002/hyp.7818

Siirila-Woodburn, E. R., Rhoades, A. M., Hatchett, B. J., Huning, L. S., Szinai, J., Tague, C., Nico, P. S., Feldman, D. R., Jones, A. D., & Collins, W. D. (2021). A low-to-no snow future and its impacts on water resources in the western United States. *Nature Reviews Earth & Environment*, *2*(11), 800-819.

Statistics Canada. (2017). *Average annual runoff in Canada, 1971 to 2013*. Ottawa, ON, Statistics Canada, Environment, Energy and Transportation Statistics Division. https://www150.statcan.gc.ca/n1/pub/16-201-x/2017000/sec-2/m-c/m-c-2.1-eng.htm

Wayand, N. E., Lundquist, J. D., & Clark, M. P. (2015). Modeling the influence of hypsometry, vegetation, and storm energy on snowmelt contributions to basins during rain-on-snow floods. *Water Resources Research*, *51*(10), 8551-8569. https://doi.org/10.1002/2014WR016576

Zhang, X., Harvey, K. D., Hogg, W. D., & Yuzyk, T. R. (2001). Trends in Canadian streamflow. *Water Resources Research*, *37*(4), 987-998. https://doi.org/doi:10.1029/2000WR900357

# 2 Quality Control Impacts on Total Precipitation Gauge Records for Montane Valley and Ridge Sites in SW Alberta, Canada


## Abstract

This paper presents adjustment routines for Geonor totalizing precipitation gauge data collected from the headwaters of the Oldman River, within the southwestern Alberta Canadian Rockies. The gauges are situated at mountain valley and alpine ridge locations with varying degrees of canopy cover. These data are prone to sensor noise and environment-induced measurement errors requiring an ordered set of quality control (QC) corrections using nearby weather station data. Sensor noise at valley sites with single-vibrating wire gauges accounted for the removal of 5% to 8% (49–76 mm) of annual precipitation. This was compensated by an increase of 6% to 8% (50–76 mm) from under-catch. A three-wire ridge gauge did not experience significant sensor noise; however, the under-catch correction of snow resulted in 42% to 52% (784–1342 mm) increased precipitation. When all QC corrections were applied, the annual cumulative precipitation at the ridge demonstrated increases of 39% to 49% (731–1269 mm), while the valley gauge adjustments were −4% to 1% (−39 mm to 13 mm). Public sector totalizing precipitation gauge records often undergo minimal QC. Care must be exercised to check the corrections applied to such records when used to estimate watershed water balance or precipitation orographic enhancement. Systematic errors at open high-elevation sites may exceed nearby valley or forest sites.

**Citation:**
Barnes, C., & Hopkinson, C. (2022). Quality Control Impacts on Total Precipitation Gauge Records for Montane Valley and Ridge Sites in SW Alberta, Canada. Data, 7(6), 73. /https://doi.org/10.3390/data7060073, https://www.mdpi.com/2306-5729/7/6/73

**Accompanying published dataset:**
Hopkinson, C., & Barnes, C. (2022). Precipitation gauge and supplemental weather station data for three Oldman River headwater locations in SW Alberta. Federated Research Data Repository.

**Author Contributions:**
Conceptualization: Chris Hopkinson and Celeste Barnes
Methodology: Celeste Barnes
Software: Celeste Barnes
Validation: Chris Hopkinson
Formal analysis: Celeste Barnes
Investigation, Celeste Barnes and Chris Hopkinson
Resources: Chris Hopkinson
Data curation, Celeste Barnes
Writing - original draft preparation: Celeste Barnes
Writing - review and editing: Celeste Barnes and Chris Hopkinson
Visualization: Celeste Barnes
Supervision: Chris Hopkinson
Project administration: Chris Hopkinson
Funding acquisition: Chris Hopkinson
All of the authors have read and agreed to the published version of the manuscript.



## 2.1 Summary

The Government of Alberta (GoA) introduced the "Water for Life" strategy (Alberta Environment, 2003), partly to ensure there will be sufficient provincial water resources available for ecosystem and anthropogenic needs. Mountain headwaters provide a high proportion of the available downstream runoff (Kienzle & Mueller, 2013); however, accurate measurement of

mountain precipitation is a well-known challenge (Avanzi et al., 2021; Goodison et al., 1998; Rasmussen et al., 2012; Thiessen, 1911).

GoA Alberta Environment and Parks (AEP) and Agriculture and Forestry manage totalizing precipitation gauges throughout Alberta. On the eastern slopes of the Alberta Rocky Mountains, most gauges are sparsely located at valley and mid-mountain sites (Newton et al., 2021; Wright, 2021a). To further investigate mountain headwater precipitation regimes, the University of Lethbridge Artemis Lab (ULAL) installed three totalizing precipitation gauges at different elevations and in different landcover types, near to existing public gauges. One gauge was installed in an open alpine location, while the other two gauges were in valley sites, with one in a woodland clearing (Barnes et al., 2020) and the other in a recently burnt area (Waterton Lakes National Park, 2017) of standing dead tree stems and sparce ground cover vegetation. It was noted in the WMO Fifth Session Final Report, that the Solid Precipitation Intercomparison Experiment (SPICE) gauge management practices should follow the manufacturer's recommended installation and operational maintenance methodologies (Earle et al., 2014). However, data obtained from research sites may not be reliable as a result of improper maintenance activities (Pan et al., 2016). ULAL followed the manufacturer's recommended installation and maintenance routines for each totalizing precipitation gauge.

The data collected from the totalizing precipitation gauges are prone to noise and measurement errors (Goodison et al., 1998; Leeper et al., 2015; Peck, 1972), especially from the effects of wind-induced under-catch of snow entering the orifice (Peck, 1972; Wolff et al., 2015). Site characteristics such as the amount of natural canopy sheltering the gauge (Pan et al., 2016), as well as the installation of shielding to limit airflow around the gauge (Baghapour et al., 2017; Kochendorfer, Nitu, et al., 2017), decrease these errors. Other environmental and sensor

configuration factors can result in evaporative losses, snow covering the orifice, or false measurements of precipitation when no event is in progress (Earle et al., 2014; Kochendorfer, Nitu, et al., 2017; Kochendorfer, Rasmussen, et al., 2017). Observation quality control (QC) using data cleaning and filtering must be applied to time-series observations to remove noise and systematic measurement errors. Different techniques have been used to clean and smooth the precipitation datasets (Kochendorfer et al., 2018; Leeper et al., 2015; Pan et al., 2016). This paper explains the adjustments applied to the ULAL totalizing precipitation gauges for noise, as well as over- and under-catch, to show the relative proportions of error and potential range in accumulated precipitation in the data records. Two different procedures were used to perform QC adjustments to the precipitation observations collected in this region. The initial data filtering routine applied to the data was developed by the Alberta Climate and Information Service (ACIS) and used to ensure data consistency with publicly available precipitation datasets. Wind-induced bias corrections are not applied by ACIS; therefore, the rest of the QC routines used in this paper were developed by another research group (Pan et al., 2016). Pan et al. (2016) applied wind-induced bias adjustments to the precipitation data collected with the same sensor and shielding located in a similar Western Canadian region.

## 2.2 Data Description

The following three Geonor totalizing precipitation gauge sites were used: CMR (Castle Mountain Resort), WFS (Westcastle Field Station), and Cameron (Hopkinson & Barnes, 2022). Datasets for each site containing variables required for the QC process (shown in Table 2.1) are available from the Federated Research Data Repository (FRDR) at https://doi.org/10.20383/102.0551.

Table 2.1. Raw and processed data descriptions and units.

| Variable | Value | Units | Description |
|---|---|---|---|
| Timestamp | recorded | | Time measurement was recorded (yyyy−mm−dd hh:mm) |
| RH | recorded | % | Relative humidity |
| Wind | recorded | $ms^{-1}$ | Wind speed |
| AirTemp | recorded | °C | Air temperature |
| In_SR | recorded | $watt/m^2$ | Incoming solar radiation |
| Raw_Precip | recorded | mm | Raw precipitation record |
| ACIS_Precip | computed | mm | ACIS weighing gauge time-series data filtering |
| Noise_Precip | computed | mm | Noise removal of positive values during no precipitation |
| OC_Precip | computed | mm | Over-catch subtracted |
| UC_Precip | computed | mm | Under-catch added for snow and rain |

The CMR Geonor was installed in September 2015; however, the record was not continuous until 2017. The WFS Geonor was installed in the summer of 2017, and both the WFS and CMR records used in this analysis were continuous for four hydrological years, starting from October 2017 through to September 2021. The Cameron Geonor dataset was continuous from the date of installation in October 2018 through to September 2021.

The CMR, WFS, and Cameron precipitation records were set to zero at the beginning of each hydrologic year (1 October) to match the publicly available historical meteorological data accessible from the Alberta Climate Information Service's (ACIS) (Wright, 2021a) and Alberta Environment and Park's (AEP) "Alberta's River Forecast Centre: Awareness and Communication" system (Alberta Environment and Parks, 2019) datasets. The data collection interval for all three Geonor gauges was one measurement every 15 min. Fluid change jumps in the observed gauge level at biennial maintenance intervals were removed from each record.

## 2.3 Methods

### 2.3.1 Study Area

The study area was within the eastern slope headwaters of southwestern Alberta, Canada (Figure 2.1). ULAL installed three totalizing precipitation gauges—two in the West Castle Watershed (WCW) and one in the Waterton Lakes National Park (WLNP). The CMR gauge is located within the Castle Mountain Resort (CMR Board, 2002) along the Gravenstafel ridge on the western side of the WCW, at 2130 m above sea level (asl). The WFS gauge is situated at the University of Lethbridge Westcastle Field Station within the valley bottom of the WCW at 1400 m asl, 3 km northeast of CMR. The Cameron gauge is situated in the bottom of Cameron Valley at 1655 m asl, within Waterton Lakes National Park, 45 km southeast of WFS.

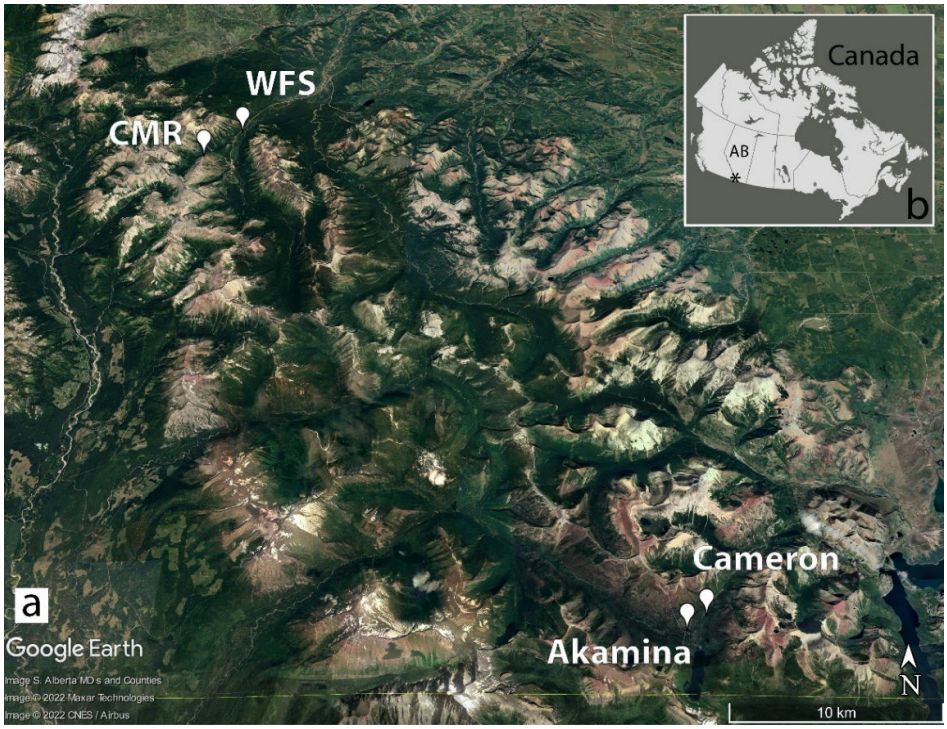


Figure 2.1. (a) Proximal locations of the CMR, WFS, and Cameron Geonor gauge sites. The AEP Akamina (mid-mountain site at an elevation of 1809 m asl) provides publicly available precipitation data. (b) Inset: study area in the Canadian Rockies of southwestern Alberta, Canada.

### 2.3.2 Sensor Specifications

Geonor T-200B (Campbell Scientific (Canada) Corp., 2011; Leeper et al., 2015) precipitation gauges with single alter wind screens and several weather sensors recording incoming shortwave radiation, air temperature, relative humidity, and wind speed were installed by the University of Lethbridge (Figure 2.2) at the CMR ridge (a), WFS valley (b), and Cameron valley (c) locations. Glycol (40%)/methanol (60%) antifreeze and a ≥ 500 mL mineral oil surface sealant were added to the Geonor gauges using standard Campbell Scientific (CS) specifications (Lang-Gorman, 2018). Standard and consistent CS CR1000 (Campbell Scientific (Canada) Corp., 2020) datalogger programming was used at all three locations.

The CMR precipitation gauge has the largest capacity 1500 mm Geonor bucket, with three vibrating wires to accommodate less frequent site visits and occasional turbulent wind conditions over the ridge. The site was selected for ease of access for maintenance activities, as well as to connect to the tele-communication and power infrastructure provided by the Castle Mountain Resort. The gauge is mounted on a tall pedestal to keep it above snow drifts and low-level blowing snow, but because it is at the upper limit of the tree line, there is minimal surrounding vegetation to shelter the gauge from strong turbulent winds. The CMR weather station is in the field of view (FOV) of a web camera located lower down the mountain side, and another web camera is located adjacent to the gauge site so that the Geonor gauge and sky conditions can be monitored.

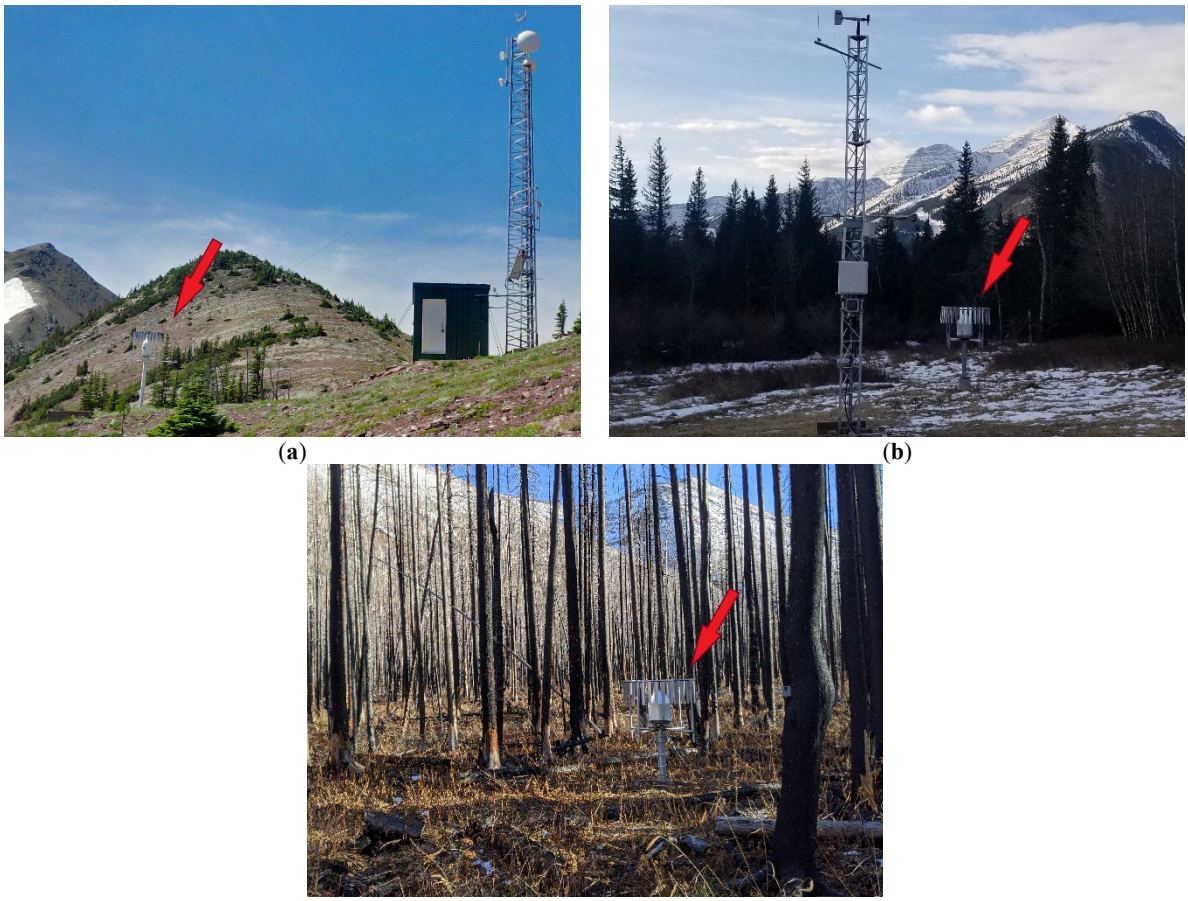

(a) (b)

(c)

Figure 2.2. Site photographs showing the totalizing precipitation gauge terrain and vegetation conditions, and adjacent weather stations: (a) CMR, (b) WFS, and (c) Cameron (the weather station is behind the observer, so it is not shown).

The CMR windspeed sensor malfunctioned from 1 November 2018 to 14 February 2019, resulting in a data gap. The missing CMR windspeed data (15 min averages) were gap filled by regression to a nearby weather station on the resort ~200 m lower down the mountain side ($r^2$ = 0.81).

A smaller 600 mm capacity Geonor gauge was installed at the WFS weather station (Table 2) (Barnes et al., 2020), as access is easy from a nearby highway, and site visits are frequent given this is a well-used university research station. This unit has a single vibrating wire, as it is located in a clearing surrounded by mixed deciduous and conifer trees, so wind conditions are more stable than the nearby CMR ridge. The gauge is in the FOV of a web camera

located on the cabin of the field station. A 600 mm capacity single-wire Geonor gauge was installed at the Cameron valley research site (Table 2.2) within an area of mature pine forest that was killed and defoliated in the Kenow wildfire of September 2017 (Waterton Lakes National Park, 2017). Publicly available precipitation data from the AEP Akamina site (Figure 2.1, located within 1.5 km of Cameron) were available for comparison.

Table 2.2. Geonor totalizing precipitation gauge and weather sensor specifications for the CMR, WFS, and Cameron sites.

| Site | CMR | WFS | Cameron |
|---|---|---|---|
| Elevation | 2130 m asl | 1400 m asl | 1655 m asl |
| Latitude | 49°19′15.18″ N | 49°20′55.17″ N | 49°2′3.52″ N |
| Longitude | 114°26′20.94″ W | 114°24′39.01″ W | 114°2′17.55″ W |
| Installation date | 17 September 2015 | 7 September 2017 | 27 October 2018 |
| Precipitation gauge | GEONOR T-200B-MD | GEONOR T-200B | GEONOR T-200B |
| Capacity | 1500 mm | 600 mm | 600 mm |
| Precision vibrating wire | 3 | 1 | 1 |
| Incoming shortwave radiation | CS CMP3 | CS CNR1 | CS CNR4 |
| Air temperature | CS T109 | CS HC2S3 | CS HMP45 |
| Relative humidity | CS HMP45 | CS HC2S3 | CS HMP45 |
| Wind speed | Met One 013A | RM Young 05103 | RM Young 05103 |

### 2.3.3 Data Cleaning and Quality Control

Systematic measurement biases are common in totalizing precipitation gauges (Goodison et al., 1998). Figure 2.3 shows the processing workflow to clean the raw data and create each adjusted precipitation variable. Evaporative losses, sensor drift (Leeper et al., 2015), and temperature- or wind-induced noise can lead to significant deviations in the data (Figure 2.4; raw measurements are displayed with a black line). Under-catch of snow (Wolff et al., 2015; Zhang et al., 2015) and rain (Pan et al., 2016) can occur as a result of wind across the gauge orifice. Over-catch of snow (Goodison et al., 1998; Kochendorfer, Nitu, et al., 2017) can occur when there is no atmospheric precipitation and wind mobilizes the snow from the ground or surrounding canopy.

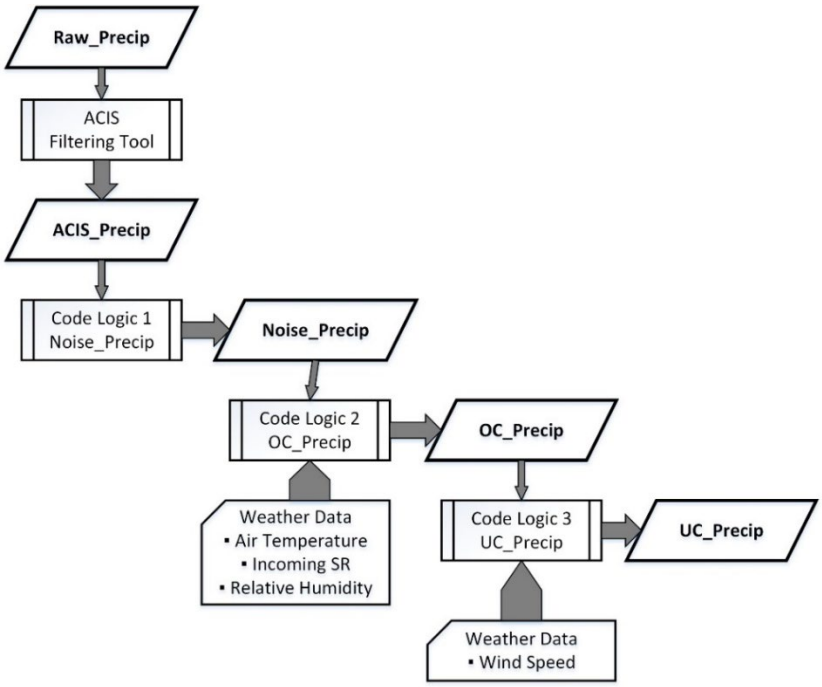


Figure 2.3. Quality control workflow diagram illustrating the sequence of steps to compute precipitation-adjusted variables, including the weather data used in each code logic block.

An ACIS "weighing gauge time-series analysis and noise filtering tool" (Wright, 2021b) was used to adjust the 15 min time-series observation values. This tool removes all negative accumulation, and the series is smoothed using a moving range window. The tool does not adjust for evaporative losses in the gauge. The ACIS filtering tool was run twice for all three Geonor time series (e.g., Figure 2.4). Once the tool completed its execution, a visual inspection was done to verify the filtered output. After several trial runs, the parameter settings listed in Table 2.3 were adopted for the ACIS_Precip variable. The second run (blue line) was used as the baseline for further adjustments.

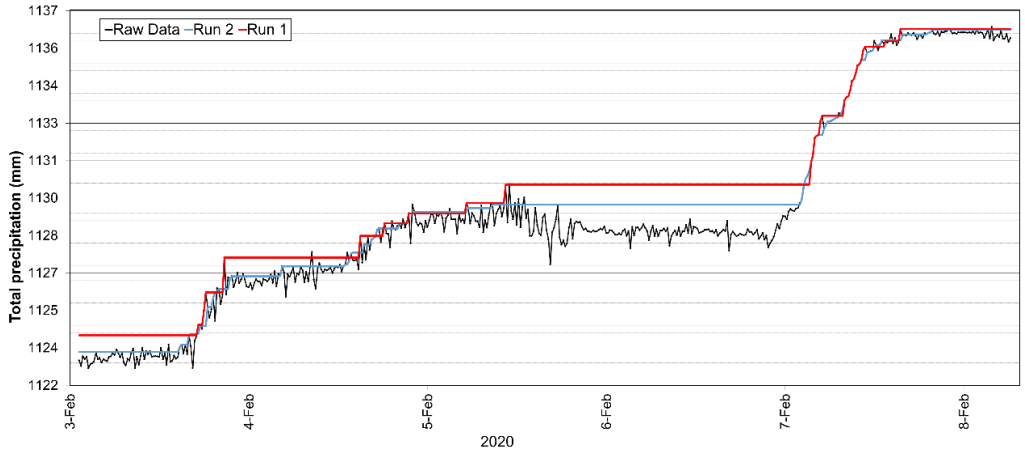


Figure 2.4. ACIS "weighing gauge time-series analysis and noise filtering tool" sample. Black line—raw data; red line—run #1; blue line—run #2.

Table 2.3. ACIS weighing gauge time-series analysis and noise filtering tool parameter settings per run.

| Run # | Range | Change Factor | Raw Count | Comments |
|---|---|---|---|---|
| 1 (red line) | 24 | 0.2 | 3 | |
| 2 (blue line) | 24 | 0.9 | 1 | Baseline used for further adjustments |

After the ACIS filtering tool execution was complete, further data cleaning was required to remove additional noise and adjust the time series for precipitation over- and under-catch (Leeper et al., 2015; Pan et al., 2016). Three additional cleaning routines were applied sequentially (as seen in Figure 3) to correct precipitation measurements. Two routines removed precipitation that did not belong in the time series, while the third added precipitation that was missed. Adjacent weather station sensor data (incoming shortwave radiation, air temperature, relative humidity, and wind speed) were used as inputs to the correction calculations. Table 2.4 lists the constants used in each code logic block (below) to compute data values for the removal of noise (Noise_Precip), over-catch (OC_Precip) from blowing snow, and under-catch (UC_Precip) of precipitation. The code logic blocks are executed sequentially for each 15 min observation (i), starting with the first observation in the data file and continuing to the end of the data file.

Table 2.4. Data cleaning threshold parameter values used for each gauge site.

| Threshold Values | CMR | WFS | Cameron | Comment |
|---|---|---|---|---|
| $Noise_{Threshold}$ | 0.11 | 0.05 | 0.05 | Threshold for small positive precipitation changes |
| $In\_SR_{Threshold}$ | 300 | 300 | 300 | Incoming SR threshold (daylight hours only) |
| $RH_{Threshold}$ | 75 | 65 | 65 | RH threshold when SR is greater than $In\_SR_{Threshold}$ |
| $AirTemp_{Threshold}$ | 0.0 | 0.0 | 0.0 | Temperature threshold to separate snow/rain |
| $WS_{Lower}$ | 1.2 | 1.2 | 1.2 | Lower wind speed bounds for under-catch |
| $WS_{Upper}$ | 6.5 | 6.5 | 6.5 | Upper wind speed bounds for under-catch |
| $H_{anemometer}$ | 14.0 | 6.5 | 3.0 | Height of anemometer (m) |
| $H_{gauge}$ | 3.0 | 2.0 | 1.75 | Height of Geonor orifice (m) |
| Roughness | 0.05 | 0.05 | 0.05 | Roughness length (m) |
| $CE_{Rain}$ | 1.05 | 1.05 | 1.05 | Catch efficiency multiplier for rain |
| $WS_{gauge}$ | | computed | | Wind speed above the Geonor orifice |
| $CE_{Snow}$ | | computed | | Catch efficiency for snow |

The noise (Noise_precip) that the ACIS tool did not filter out was subtracted from the record. This noise was defined as precipitation less than the $Noise_{Threshold}$, with no recorded measurements either before or after the observation (see Code Logic 1). The CMR noise threshold value was set to 0.11 mm, as in (Pan et al., 2016). As a result of a single vibrating wire with no averaging (Leeper et al., 2015), the WFS and Cameron gauges were more susceptible to noise than the CMR Geonor gauge, which had three vibrating wires that were averaged to a single measurement for each data record. The initial threshold setting was the same as CMR; however, it was adjusted using trial and error, until the noise signal was mitigated. The WFS and Cameron thresholds were set to 0.05 mm, which reduced the amount subtracted from the records.

**Code Logic 1.** Noise_Precip (small positive observations when no apparent precipitation event occurs)

For each observation i starting with the first observation to the end of the file:
    IF $ACIS\_Precip_{i} < Noise_{Threshold}$
    Then IF $ACIS\_Precip_{i-1} > 0$ or $ACIS\_Precip_{i+1} > 0$
        Then $Noise\_Precip_{i} = ACIS\_Precip_{i}$
        Else $Noise\_Precip_{i} = 0$
    Else $Noise\_Precip_{i} = ACIS\_Precip_{i}$
End.
□

The next step was to subtract the over-catch (OC_Precip) due to blowing snow that was unlikely to result from atmospheric precipitation (see Code Logic 2). For CMR and WFS, the

presence of over-catch during non-precipitation blowing snow conditions could be manually checked by reviewing the coincident camera imagery. While wind data have potential as a proxy for blowing snow (Pan et al., 2016) inputs, they were found to be unreliable as an automated data filtering variable because of occasional anemometer riming (Kochendorfer, Nitu, et al., 2017) at temperatures near to 0 °C, and because of the high frequency of winter blizzards where both wind and precipitation display high but uncorrelated values. Therefore, over-catch corrections were limited to precipitation recorded at temperatures below the rain/snow threshold ($AirTemp_{Threshold}$). As snow pellets can be present in the rain and snow, the $AirTemp_{Threshold}$ was set to 0 °C (Meteorological Service of Canada, 2021). A relative humidity threshold ($RH_{Threshold}$) was used to further selectively subtract the recorded precipitation. An incoming solar radiation threshold ($In\_SR_{Threshold}$) was used to remove the daytime blowing snow. To calibrate the $In\_SR_{Threshold}$, camera imagery was used to manually verify whether or not blowing snow occurred above or below a certain value. Threshold values for CMR were set to $In\_SR_{Threshold}$ (300 watt/$m^2$) and $RH_{Threshold}$ (75%) based on expert judgment, combined with blowing snow observations in web cam imagery. The $RH_{Threshold}$ was set to 65% for WFS to prevent precipitation events from being removed from the data record when there was low incoming solar radiation ($In\_SR_{Threshold}$, 300 watt/$m^2$) using camera imagery. As the Cameron site does not have a camera, the same $In\_SR_{Threshold}$ (300 watt/$m^2$) and $RH_{Threshold}$ (65%) threshold values were adopted as WFS owing to the similar gauge height and environmental characteristics.

**Code Logic 2.** OC_Precip (remove over-catch from blowing snow using air temperature, In_SR, and RH thresholds)

For each observation i:

IF $Noise\_Precip_i > 0$

Then IF $AirTemp_i > AirTemp_{Threshold}$

Then $OC\_Precip_i = Noise\_Precip_i$

Else IF $RH_i < RH_{Threshold}$

Then $OC\_Precip_i = 0$

Else IF $In\_SR_i > In\_SR_{Threshold}$

Then $OC\_Precip_i = 0$

Else $OC\_Precip_i = Noise\_Precip_i$

Else $OC\_Precip_i = 0$

End.

□

The last QC step was an under-catch (UC_Precip) correction for snow and rain (see Code Logic 3) using the formula and thresholds developed for a similar Rocky Mountain site in Western Canada (Pan et al., 2016). A lower ($WS_{Lower}$) and upper ($WS_{Upper}$) bound was used to limit the range for wind speed correction. Wind speed above the Geonor ($WS_{gauge}$) was calculated using the height of the wind speed sensor ($H_{anemometer}$), the height of the gauge orifice ($h_{gauge}$), and a roughness length parameter. The roughness length for all of the sites was set to 0.05, as each location has low-level vegetation. No further precipitation adjustment was applied for wind speeds below the lower threshold. Wind speeds above the upper threshold were set to the upper wind speed threshold value (Kochendorfer, Nitu, et al., 2017; Pan et al., 2016). The catch efficiency for snow ($CE_{Snow}$) was calculated using the wind speed above the gauge orifice. The catch efficiency for rain ($CE_{Rain}$) was set to a constant value. Setting the CMR gauge upper wind speed threshold to 9 $ms^{-1}$, as in (Pan et al., 2016), caused the under-catch to be amplified by an unreasonable amount during the snow season, so an upper limit of 6.5 $ms^{-1}$ was used, as this is typical for Arctic and northern regions (Pan et al., 2016).

**Code Logic 3.** UC_Precip (under-catch correction for snow and rain using wind speed at the top of the gauge)

For each observation i:

$WS_{gauge\ i} = Wind_{\ i} \times (ln(h_{gauge}/Roughness)/ln(H_{anenometer}/Roughness))$

IF $WS_{gauge\ i} > WS_{Upper}$
Then $WS_{gauge\ i} = WS_{Upper}$

IF $OC\_Precip_{\ i} > 0$
Then IF $WS_{gauge\ i} > WS_{Lower}$
Then IF $AirTemp_{\ i} < AirTemp_{Threshold}$
Then
$CE_{Snow} = 1.18\ e^{-0.18 \times WSgauge}$
$UC\_Precip_{\ i} = OC\_Precip_{\ i}/CE_{Snow}$
Else $UC\_Precip_{\ i} = OC\_Precip_{\ i} \times CE_{Rain}$
Else $UC\_Precip_{\ i} = OC\_Precip_{\ i}$
Else $UC\_Precip_{\ i} = OC\_Precip_{\ i}$

End.

□

The CMR, WFS, and Cameron Raw_Precip, ACIS_Precip, Noise_Precip, OC_Precip, and UC_Precip data were aggregated to daily, monthly, and annual totals. For each year in the CMR, WFS, and Cameron annual datasets, Code Logic 4 was used to calculate the amount of precipitation adjustment for each variable in the cleaning workflow.

**Code Logic 4.** Amount of precipitation adjustment for each variable in the cleaning workflow

For each year in the dataset:

ACIS-filter = ACIS_Precip − Raw_Precip
Noise-reduction = Noise_Precip − ACIS_Precip
Over-catch = OC_Precip − Noise_Precip
Under-catch = UC_Precip − OC_Precip
Total Correction = UC_Precip − Raw_Precip

End.

□

## 2.4 Aggregated Precipitation Output Results and Discussion

For comparison purposes, Figure 2.5 shows the cumulative ACIS_precip time series for CMR, WFS, and Cameron. It also includes the public AEP Akamina Pluvio totalizing precipitation gauge record, which is 1.5 km away and 154 m higher in elevation than the Cameron gauge. Although the data were collected from two different gauge types, studies have shown Geonor and Pluvio measurements are comparable (Kochendorfer, Nitu, et al., 2017). The AEP public records do not have the noise reduction or the under- or over-catch corrections applied (Nitu, 2010), so the Akamina record is most comparable to "ACIS_Precip". The Akamina record tends to show a >10% increase over Cameron because of its higher elevation and rain shadow effect on the lee side of the mountain slope (Smith, 2019), but the timing and magnitude of precipitation events are visibly synchronous.

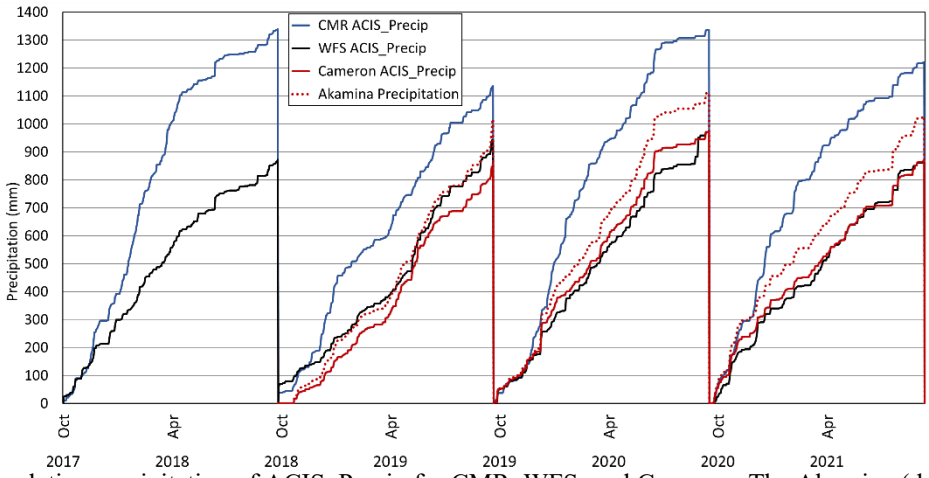


Figure 2.5. Cumulative precipitation of ACIS_Precip for CMR, WFS, and Cameron. The Akamina (dotted line) site is in close proximity to Cameron and illustrates a publicly available precipitation dataset that is comparable to ACIS_Precip.

For each site, Figure 2.6 presents the magnitude of each cumulative precipitation correction (ACIS_Precip, Noise_Precip, OC_Precip, and UC_Precip) relative to the Raw_Precip

baseline through time. The adjustments for CMR (Figure 6a), WFS (Figure 6b), and Cameron (Figure 6c) are plotted for each hydrologic year.

The Raw_precip and ACIS_precip daily total precipitation values did not deviate significantly. The WFS and Cameron valley-level gauges measured similar depths of precipitation for the years of comparable data. Similar to CMR, both gauges demonstrated minimal difference between the Raw_Precip measurements and ACIS_Precip filtered data.

There was a small amount of noise (Noise_Precip) in the CMR gauge that contributed approximately 1 to 2 mm per month. WFS and Cameron were more susceptible to noise during the colder winter months when most of the annual Noise_Precip adjustment occurred. Cameron had a higher amount of noise compared with WFS, which was possibly a function of the different canopy cover or wind turbulence surrounding the gauge sites.

Over-catch (OC_Precip) corrections on the CMR ridge were prevalent in the late winter and spring months, accounting for an additional 36 mm to 65 mm per year. The WFS and Cameron valley sites demonstrated a blowing snow over-catch correction, ranging from 5 mm to 76 mm, occurring either in October or the spring time frame, presumably due to warmer temperatures and less mobile snow.

Under-catch (UC_Precip) corrections at all sites were the greatest during snow cover months from September through to late spring. WFS under-catch corrections were frequent between October to April, while for Cameron, they occurred primarily from October to February and, to a lesser degree, during March to May. The under-catch code logic was sensitive to high wind speeds, especially during snowfall events.

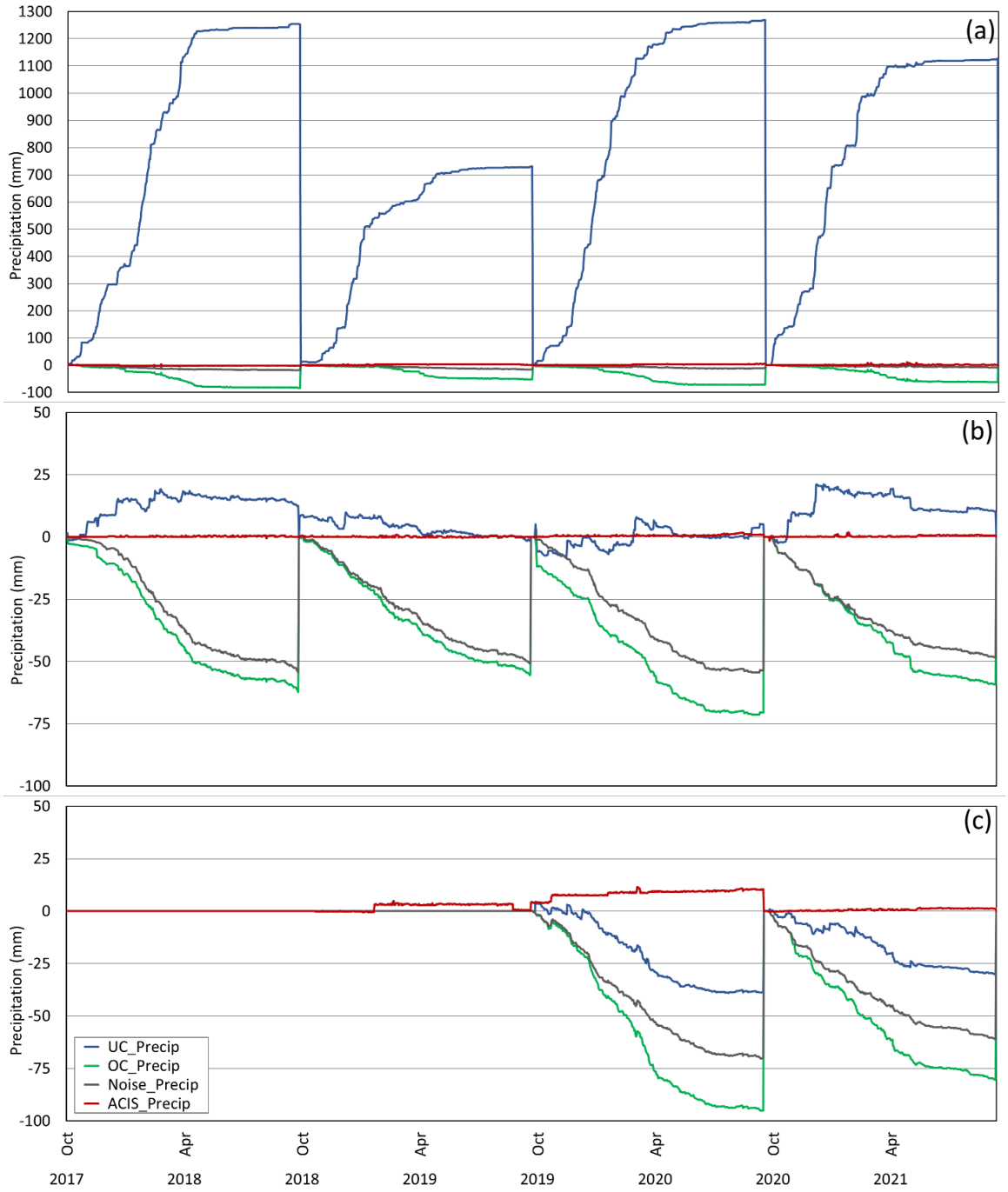


Figure 2.6. The relative ACIS_Precip, Noise_Precip, OC_Precip, and UC_Precip deviations from the Raw_Precip baseline for (a) CMR, (b) WFS, and (c) Cameron.

The high-elevation CMR ridge gauge recorded the highest annual precipitation of all of the gauges (see Figure 2.5). The annual CMR ACIS-filtered record (Table 2.5) was within a few millimeters of the raw precipitation measurements. Of the three sites, CMR displayed the largest

annual total correction, ranging between 39.2% to 48.8%, with under-catch representing the largest correction factor at up to 51.5% of the annual total for 2017–2018 and 2019–2020. This represents an approximate doubling of the raw precipitation observations for the alpine ridge location, although this is a plausible amplification of the annual precipitation, given it is known that the mean winter snow accumulations at these alpine elevations can exceed valley depths by a factor of four (Cartwright et al., 2020). WFS displayed between −0.1% to 1.4% precipitation correction, with Cameron showing a −4.2% to −3.6% annual decrease. The removal of noise and adding an under-catch correction were the most impactful adjustments for the valley gauges, resulting in an almost net zero annual change in precipitation measurement.

Table 2.5. Annual amount of precipitation adjustment for each variable in the cleaning workflow in millimeters (amount of adjustment as a percentage is listed in the brackets) computed using Code Logic 4. Weather station data were not complete for Cameron during

| Correction | 2017–2018 mm (%) | 2018–2019 mm (%) | 2019–2020 mm (%) | 2020–2021 mm (%) |
|---|---|---|---|---|
| CMR | | | | |
| ACIS filter | −2.1 (−0.2%) | 1.6 (0.1%) | 4.7 (0.4%) | 1.4 (0.1%) |
| Noise reduction | −17.5 (−1.3%) | −18.6 (−1.6%) | −15.9 (−1.2%) | −10.2 (−0.8%) |
| Over-catch | −64.6(−5.1%) | −36.0 (−3.3%) | −60.0 (−4.8%) | −54.1 (−4.7%) |
| Under-catch | 1342.0 (51.5%) | 783.7 (42.0%) | 1340.3 (51.5%) | 1189.7 (50.7%) |
| Total correction | 1258.1 (48.3%) | 730.7 (39.2%) | 1269.1 (48.8%) | 1126.9 (48.0%) |
| WFS | | | | |
| ACIS filter | 0.2 (0.0%) | 0.1 (0.0%) | 0.9 (0.1%) | 0.5 (0.1%) |
| Noise reduction | −54.7 (−6.2%) | −50.8 (−5.4%) | −54.5 (−5.6%) | −48.9 (−5.7%) |
| Over-catch | −7.8 (−1.0%) | −4.6 (−0.5%) | −16.9 (−1.9%) | −10.9 (−1.4%) |
| Under-catch | 74.9 (8.4%) | 53.9 (5.7%) | 75.6 (7.7%) | 69.5 (8.0%) |
| Total correction | 12.6 (1.4%) | −1.4 (−0.1%) | 5.1 (0.5%) | 10.2 (1.2%) |
| Cameron | | | | |
| ACIS filter | | | 6.4 (0.7%) | 1.2 (0.1%) |
| Noise reduction | | | −76.4 (−7.9%) | −62.1 (−7.2%) |
| Over-catch | | | −24.9 (−2.9%) | −19.4 (−2.5%) |
| Under-catch | | | 56.5 (6.1%) | 50.2 (6.0%) |
| Total correction | | | −38.5 (−4.2%) | −30.1 (−3.6%) |

## 2.5 Conclusions

This study applied data cleaning and QC to raw Geonor totalizing precipitation gauge records for three sites in the Canadian Rockies. The filtered ACIS_Precip and Raw_Precip data

series were tracked closely together for all three gauges at daily and longer time increments. Despite being in a more severe wind environment, the annual noise in the CMR ridge record was small (10 mm to 20 mm) compared with the WFS (49 mm to 55 mm) and Cameron (62 mm to 76 mm) valley gauges as a result of the real-time averaging of the three vibrating wires relative to the single vibrating wire of the valley sites. The annual amount of CMR blowing snow over-catch correction was 36 mm to 65 mm; for WFS, it was 5 mm to 17 mm; and for Cameron, it was 19 mm to 25 mm. This correction was applied for measurements occurring throughout the day. However, using incoming solar radiation, additional corrections were possible during daylight hours. During non-daylight hours, it was not possible to reliably separate blowing snow from blizzard conditions, which suggests the total over-catch in the records may be slightly higher than what was estimated. The CMR record was most sensitive to under-catch corrections (731 mm to 1342 mm) as a result of high wind speeds in the turbulent ridge environment. This was mostly associated with the $WS_{Upper}$ threshold value and is therefore sensitive to changes in this parameter value. The under-catch for WFS and Cameron was significantly less than that of CMR, ranging from 50 to 76 mm. This study illustrates that, with all QC adjustments applied, total precipitation records ranged between small corrections of ~−4% to 1% for valley locations up to ~49% for alpine ridge locations. Therefore, without applying such data cleaning and QC procedures, significant errors would be propagated into headwater water balance or precipitation orographic enhancement estimates derived from such records.

## 2.6 References


Alberta Environment. (2003). Water for Life - Alberta's Strategy for Sustainability. In. Government of Alberta. http://aep.alberta.ca/water/programs-and-services/water-for-life/strategy/downloadable-information-about-the-water-for-life-strategy.aspx

Alberta Environment and Parks. (2019). *Alberta's River Forecast Centre: Awareness and Communication* Alberta Environment and Parks. https://rivers.alberta.ca/#

Avanzi, F., Ercolani, G., Gabellani, S., Cremonese, E., Pogliotti, P., Filippa, G., Morra di Cella, U., Ratto, S., Stevenin, H., Cauduro, M., & Juglair, S. (2021). Learning about precipitation lapse rates from snow course data improves water balance modeling. *Hydrol. Earth Syst. Sci.*, *25*(4), 2109-2131. https://doi.org/10.5194/hess-25-2109-2021

Baghapour, B., Wei, C., & Sullivan, P. E. (2017). Numerical simulation of wind-induced turbulence over precipitation gauges. *Atmospheric Research*, *189*, 82-98. https://doi.org/https://doi.org/10.1016/j.atmosres.2017.01.016

Barnes, C., Hopkinson, C., Porter, T., & Xi, Z. (2020). In-Situ LED-Based Observation of Snow Surface and Depth Transects. *Sensors*, *20*(8), 2292. https://www.mdpi.com/1424-8220/20/8/2292

Campbell Scientific (Canada) Corp. (2011). GEONOR T-200B Series Precipitation Gauge. In (pp. 64). Campbell Scientific (Canada) Corp.

Campbell Scientific (Canada) Corp. (2020). CR1000 Datalogger Operator's Manual. In (pp. 628). Campbell Scientific (Canada) Corp. https://www.campbellsci.ca/cr1000

Cartwright, K., Hopkinson, C., Kienzle, S., & Rood, S. B. (2020). Evaluation of temporal consistency of snow depth drivers of a Rocky Mountain watershed in southern Alberta. *Hydrological Processes*, *n/a*(n/a). https://doi.org/https://doi.org/10.1002/hyp.13920

CMR Board. (2002). Castle Mountain Resort Area Structure Plan. In (pp. 61). Castle Mountain Resort, Pincher Creek, AB: Castle Mountain Resort, Pincher Creek, AB.

Earle, M., Reverdin, A., Wolff, M., Smith, C., Morin, S., & Rodica, N. (2014). Data Processing and Quality Control Methodology for the Derivation of Reference Datasets. In *Project Team and (Reduced) International Organizing Committee for the WMO Solid Precipitation Intercomparison Experiment Final Report* (Vol. Fifth Session, pp. 77). Sodankylä, Finland: World Meteorological Organization.

Goodison, B. E., Louie, P. Y., & Yang, D. (1998). *WMO solid precipitation measurement intercomparison*. World Meteorological Organization Geneva, Switzerland.

Hopkinson, C., & Barnes, C. (2022). *Precipitation gauge and supplemental weather station data for three Oldman River headwater locations in SW Alberta. Federated Research Data Repository*. https://doi.org/10.20383/102.0551

Kienzle, S. W., & Mueller, M. (2013). Mapping Alberta's surface water resources for the period 1971–2000. *Canadian Geographies / Géographies canadiennes*, *57*(4), 506-518. https://doi.org/https://doi.org/10.1111/j.1541-0064.2013.12050.x

Kochendorfer, J., Nitu, R., Wolff, M., Mekis, E., Rasmussen, R., Baker, B., Earle, M. E., Reverdin, A., Wong, K., & Smith, C. D. (2017). Analysis of single-Alter-shielded and unshielded measurements of mixed and solid precipitation from WMO-SPICE.

Kochendorfer, J., Nitu, R., Wolff, M., Mekis, E., Rasmussen, R., Baker, B., Earle, M. E., Reverdin, A., Wong, K., & Smith, C. D. (2018). Testing and development of transfer functions for weighing precipitation gauges in WMO-SPICE. *Hydrology and Earth System Sciences*, *22*(2), 1437-1452.

Kochendorfer, J., Rasmussen, R., Wolff, M., Baker, B., Hall, M. E., Meyers, T., Landolt, S., Jachcik, A., Isaksen, K., & Brækkan, R. (2017). The quantification and correction of wind-induced precipitation measurement errors. *Hydrology and Earth System Sciences*, *21*(4), 1973-1989.

Lang-Gorman, J. (2018). Protocols for Geonor Operation. In A. a. Forestry (Ed.), (pp. 10). Alberta Environment and Parks. http://environmentalmonitoring.alberta.ca/wp-content/uploads/2018/10/Geonor.pdf

Leeper, R. D., Palecki, M. A., & Davis, E. (2015). Methods to Calculate Precipitation from Weighing-Bucket Gauges with Redundant Depth Measurements. *Journal of Atmospheric and Oceanic Technology*, *32*(6), 1179-1190. https://doi.org/10.1175/jtech-d-14-00185.1

Meteorological Service of Canada. (2021). *MANOBS-Manual of Surface Weather Observation Standards* (Eighth Edition, Amendment 1 ed.). https://publications.gc.ca/collections/collection_2022/eccc/En56-238-2-2022-eng.pdf

Newton, B. W., Farjad, B., & Orwin, J. F. (2021). Spatial and Temporal Shifts in Historic and Future Temperature and Precipitation Patterns Related to Snow Accumulation and Melt Regimes in Alberta, Canada. *Water*, *13*(8), 1013. https://www.mdpi.com/2073-4441/13/8/1013

Nitu, R. (2010). *CIMO Survey on National Summaries of Methods and Instruments for Solid Precipitation Measurement at Automatic Weather Stations, IOM 102, TD1544*.

Pan, X., Yang, D., Li, Y., Barr, A., Helgason, W., Hayashi, M., Marsh, P., Pomeroy, J., & Janowicz, R. J. (2016). Bias corrections of precipitation measurements across experimental sites in different ecoclimatic regions of western Canada. *The Cryosphere*, *10*(5), 2347-2360.

Peck, E. L. (1972). Snow measurement predicament. *Water Resources Research*, *8*(1), 244-248. https://doi.org/https://doi.org/10.1029/WR008i001p00244

Rasmussen, R., Baker, B., Kochendorfer, J., Meyers, T., Landolt, S., Fischer, A. P., Black, J., Thériault, J. M., Kucera, P., Gochis, D., Smith, C., Nitu, R., Hall, M., Ikeda, K., & Gutmann, E. (2012). How Well Are We Measuring Snow: The NOAA/FAA/NCAR Winter Precipitation Test Bed. *Bulletin of the American Meteorological Society*, *93*(6), 811-829. https://doi.org/10.1175/bams-d-11-00052.1

Smith, R. B. (2019). 100 years of progress on mountain meteorology research. *Meteorological Monographs*, *59*, 20.21-20.73.

Thiessen, A. H. (1911). Precipitation Averages for Large Areas. *Monthly Weather Review*, *39*(7), 1082-1089. https://doi.org/10.1175/1520-0493(1911)39<1082b:PAFLA>2.0.CO;2

Waterton Lakes National Park. (2017). Kenow Fire: Burn severity map. In (pp. 1). Parks Canada. https://www.pc.gc.ca/en/pn-np/ab/waterton/nature/environment/feu-fire/feu-fire-kenow/brulage-burn

Wolff, M., Isaksen, K., Petersen-Øverleir, A., Ødemark, K., Reitan, T., & Brækkan, R. (2015). Derivation of a new continuous adjustment function for correcting wind-induced loss of solid precipitation: results of a Norwegian field study. *Hydrology and Earth System Sciences*, *19*(2), 951-967.

Wright, R. (2021a). *Current and Historical Alberta Weather Station Data* Alberta Climate Information Service (ACIS). http://agriculture.alberta.ca/acis/alberta-weather-data-viewer.jsp

Wright, R. (2021b). *Weighing gauge time series analysis and noise filtering tool*. In Alberta Agriculture and Forestry.

Zhang, L., Zhao, L., Xie, C., Liu, G., Gao, L., Xiao, Y., Shi, J., & Qiao, Y. (2015). Intercomparison of Solid Precipitation Derived from the Weighting Rain Gauge and Optical Instruments in the Interior Qinghai-Tibetan Plateau. *Advances in Meteorology*, *2015*, 11, Article 936724. https://doi.org/10.1155/2015/936724

# 3 Headwater Precipitation Gradients in the Southern Rockies of Alberta, Canada


## Abstract

Estimating mountainous headwater precipitation inputs can be challenging for water resource managers given sparce monitoring sites and complex physical hydroclimatic processes. Alberta Climate Information Service (ACIS) and quality control (wind-biased) corrected (QCC) precipitation datasets were used to examine Elevational Precipitation Gradients (EPGs) and the seasonality of these gradients from six (alpine, mid-mountain near treeline, and valley) southwestern Alberta headwater sites. Monthly EPG for a valley to alpine (730 m elevation difference) pair using ACIS was 19 mm/100 m in January. QCC EPG (61 mm/100 m in Jan) was greatly amplified during the winter months. An inverse precipitation gradient occurred in late spring and summer months where the valley received more precipitation than the alpine site. There was a seasonal signal present in the ACIS precipitation dataset. The alpine site received up to 80% more precipitation depths in the winter than summer months. All sites measured 50% to 70% lower precipitation in the summer months than the winter months. ACIS and QCC mesoscale spatialized precipitation (MSP) was compared to modelled snow water equivalent (SWE) yield from two mid-winter airborne laser surveys. ACIS-simulated volumes (2020: $65.08 \times 10^6 m^3$, 2021: $64.41 \times 10^6 m^3$) fell within the range of modelled SWE (2020: 12.99 to $90.21 \times 10^6 m^3$, 2021: 9.93 - $78.55 \times 10^6 m^3$). QCC-simulated volumes (2020: $122.28 \times 10^6 m^3$, 2021: $120.03 \times 10^6 m^3$) produced a higher estimate of water yield. This conforms with snowpack processes where sublimation and melt losses reduce winter snowpack yield relative to precipitation inputs.

**Citation:**

Barnes, C., MacDonald, R., & Hopkinson, C. (2023). Headwater Precipitation Gradients in the Southern Rockies of Alberta, Canada, Internal Review

**Author Contributions:**

Conceptualization: Chris Hopkinson and Celeste Barnes
Methodology: Celeste Barnes
Software: Celeste Barnes
Validation: Chris Hopkinson
Formal analysis: Celeste Barnes
Investigation, Celeste Barnes and Chris Hopkinson
Resources: Chris Hopkinson
Data curation, Celeste Barnes
Writing - original draft preparation: Celeste Barnes
Writing - review and editing: Celeste Barnes, Ryan MacDonald, and Chris Hopkinson
Visualization: Celeste Barnes
Supervision: Chris Hopkinson
Project administration: Chris Hopkinson
Funding acquisition: Chris Hopkinson
All of the authors have read and agreed to the version of the manuscript.

## 3.1 Introduction

The Canadian Rocky Mountain headwater regions are a critical source of water supply for downstream users (Alberta Environment, 2010; Schindler & Donahue, 2006). Monitoring precipitation and water yield in the Alberta headwater regions is an important element of regional water resource management and flood hazard assessment, and the need for accurate information is increasing as demands continue to increase (Grinder, 2010). Due to changing climate, there is potential for decreased water supplies originating from mountain snowpacks (Newton et al., 2021), as well as a change in the timing of snowpack melt (MacDonald et al., 2012). Precipitation in mountain regions is difficult to measure since it is influenced by complex relief and landcovers, and associated weather systems (Roe & Baker, 2006). However, hydrologists rely on accurate spatiotemporal meteorological observations as inputs to models to simulate precipitation in any given region (Craig et al., 2020).

Mountain precipitation patterns vary seasonally, with air temperature (Daly et al., 2008), and with solid or liquid precipitation type (Mekis et al., 2018). Orographic enhancement is common in mountainous areas (Houze, 2012) where ground level precipitation increases with elevation. Atmospheric circulation patterns (Smith, 1981) and mountain geometry (Rotunno & Houze, 2007) also influence air flow. Upper level winds in mountain regions can transport snow many kilometers from the originating cloud to the point where it first encounters land, whereas the transport distance of rain tends to be within a kilometer (Roe & Baker, 2006). Air parcels may split and flow around the mountain (Smith, 2019) instead of traversing upwards and over. "Feeder/seeder" cloud systems can develop above mountain ridges. Lower-level clouds feed upper-level clouds to produce enhanced precipitation at higher elevations (Haiden & Pistotnik, 2009; Mott et al., 2014). Precipitation types can vary spatially during events (Zhang et al., 2017) where rain occurs in the valleys and higher elevations receive snow. Over the course of the winter snow season, canopy interception, sublimation, redistribution of snow, and melt will alter spatial snowpack characteristics (Pomeroy et al., 1998). Furthermore, precipitation observations are complicated by sensor- and wind-induced biases (Goodison et al., 1998; Kochendorfer, Rasmussen, et al., 2017; Nitu, 2010; Rasmussen et al., 2012) that tend to result in underestimated water volumes if not corrected (Baghapour et al., 2017; Leeper et al., 2015; Pan et al., 2016; Ross et al., 2020; Smith et al., 2020; Wolff et al., 2015).

Time series (TS) analysis can be applied to climatological datasets to gain a better understanding of repeating patterns in the data. TS data can be characterized as being sequential in nature and measured in equal time intervals. Four components can be observed in a TS dataset, those being cycle (long-term increasing and decreasing patterns in the data), trend (increasing or decreasing pattern present within the time series), seasonality (repeating pattern

present at the same time interval (frequency), for example, daily, monthly, annually), and random variation (noise in the data) (Peixeiro, 2022). Given there can be strong elevational influences on precipitation in mountain regions, the goal of this study is to gain a better understanding of EPGs and to see if they are constant throughout the year or if there is a seasonal influence on precipitation in the southern Alberta Rocky Mountain Eastern Slope headwaters.

Understanding and accounting for sources of uncertainty or bias in precipitation observation data is necessary when estimating point to point gradients, especially when one location might be more prone to bias (such as wind-induced under-catch) than another. Snow water equivalent (SWE) obtained from the winter snowpack can be used for comparison to precipitation (Avanzi et al., 2021). Airborne laser scanning (ALS) technology can accurately map mountain digital elevation models (DEM) (Hopkinson et al., 2009), and a distributed snow depth model (SDM) by subtracting a snow free DEM from a digital snow surface model (DSSM) captured during snow covered conditions (Deems et al., 2013; Hopkinson et al., 2012; Hopkinson et al., 2004). The SDM is then combined with snow density (Grünewald et al., 2010) to compute SWE (López-Moreno et al., 2013). Winter precipitation observations represent snow that falls at a single point location before any physical processes occur to modify the snowpack (Kinar & Pomeroy, 2015) such as gravity- (Hancock et al., 2018) and wind- (Essery et al., 1999; Li & Pomeroy, 1997; Mott et al., 2018) induced redistribution, sublimation (Essery et al., 2003), and melt (Veatch et al., 2009) over the winter season leading up to ALS data collection. Therefore, the expectation is that accumulated precipitation measurements will produce a larger volume of areal water yield than the estimated winter snowpack SWE.

The objective of this research is to examine precipitation in the southern Alberta Eastern Slopes to determine: a) if there are similar EPGs and seasonal patterns between measurement

sites and across different elevation ranges used in this study, and b) how does mesoscale spatialized precipitation (MSP) compare with observed accumulated snowpack SWE water yield estimates at a watershed scale?

## 3.2 Methods

### 3.2.1 Study Area

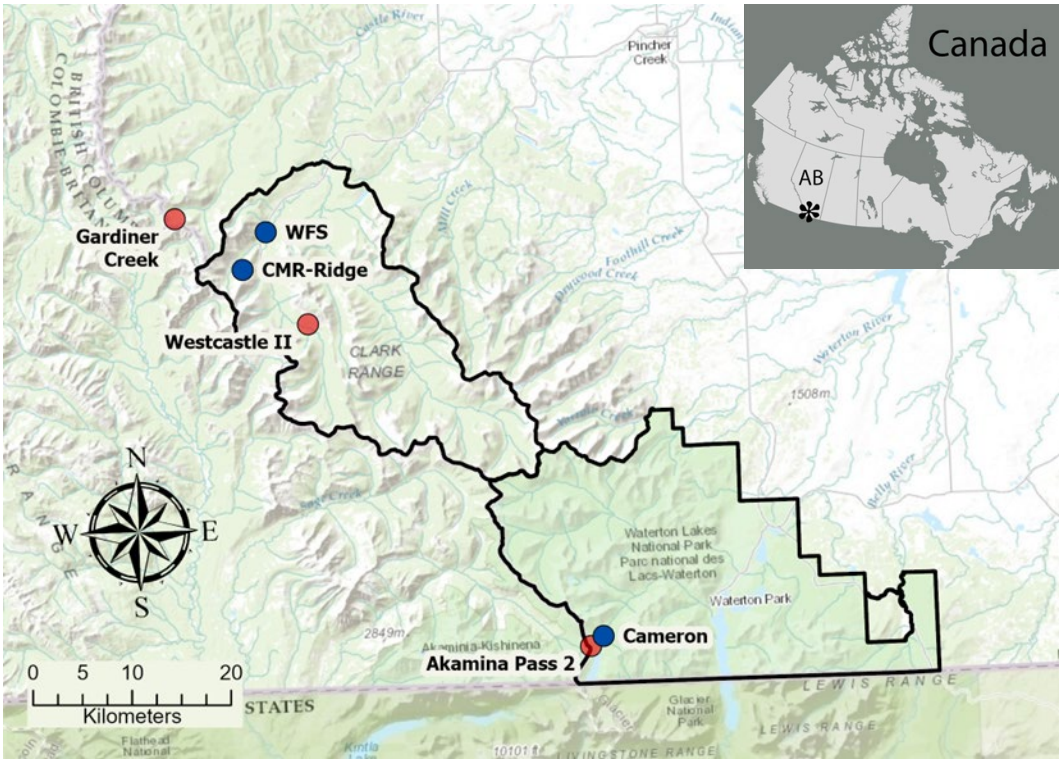


Figure 3.1: Southwestern Alberta, Rocky Mountain Eastern Slopes region. Castle watershed and WLNP boundaries (black outline). Locations showing the totalizing precipitation gauge sites: a) CMR (Castle Mountain Ridge (2130 masl)); b) WFS (Westcastle Field Station (1400 masl)); c) Akamina (1809 masl); d) Cameron (1655 masl); e) Gardiner (1940 masl); f) WC II (West Castle II (1533 masl)). Inset: Star showing the study location within Alberta, Canada.

The study area is in the Canadian Rocky Mountain eastern slope headwaters of Alberta. It is on the eastern side of the continental divide; bordering the United States and British Columbia (Figure 3.1). This region is characterized by a continental climate. Prevailing winds are out of the

southwest and Chinooks are common. The Castle Watershed (Castle) is northwest of the Waterton Lakes National Park (WLNP). University of Lethbridge ARTeMiS Lab (ULAL) installed Geonor totalizing precipitation gauges (Campbell Scientific (Canada) Corp., 2011) in Castle and WLNP (Figure 3.2 a: CMR (Castle Mountain Ridge), b: WFS (Westcastle Field Station), d: Cameron). Alberta Environment and Protected Areas (AEP) Pluvio totalizing precipitation gauges (OTT Hydromet GmbH, 2019) are shown in Figure 3.2 (c: Akamina, e: Gardiner, f: WC II (West Castle II)) are in close proximity to the ULAL installations.

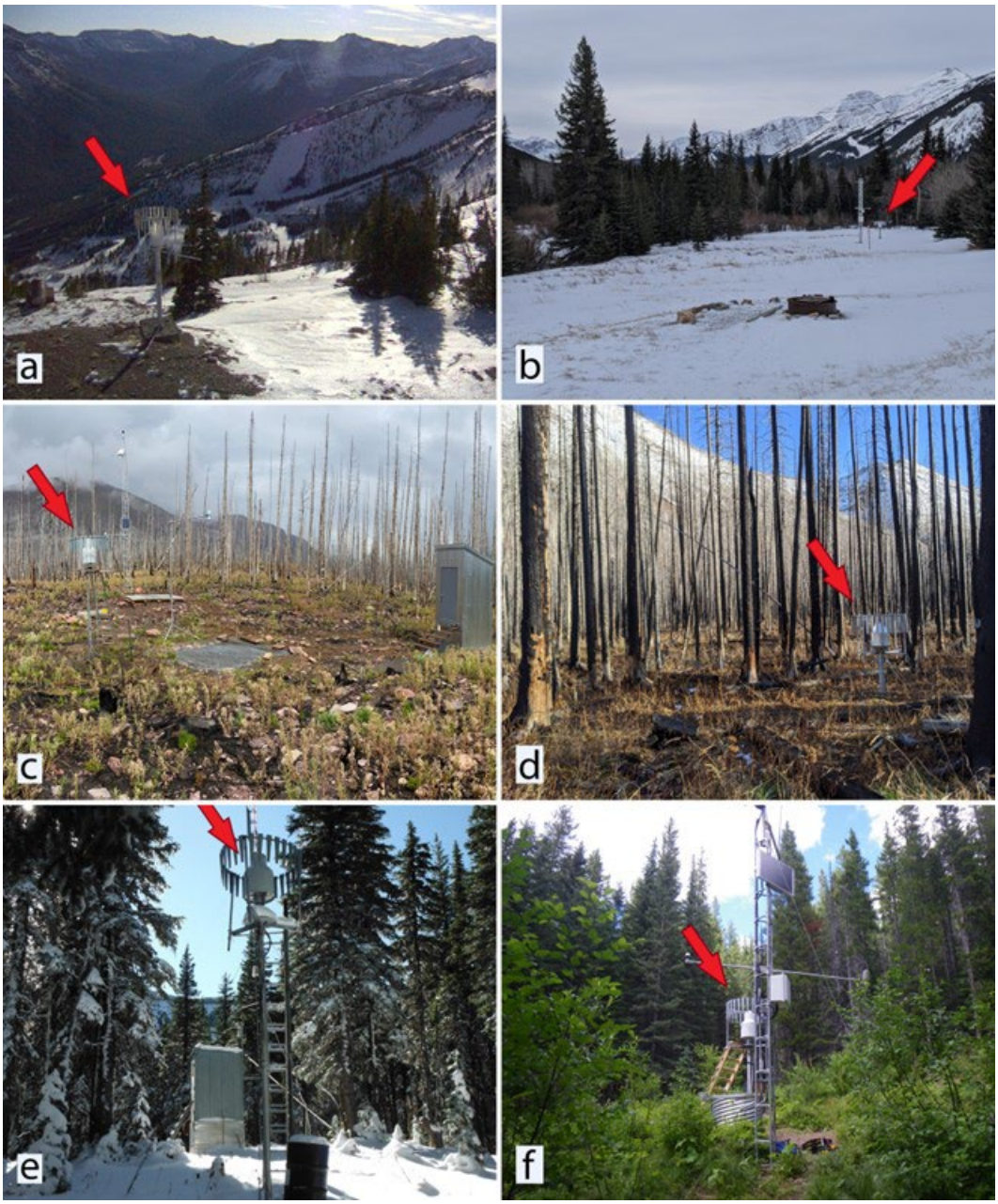

Figure 3.2: Site Characteristics. Paired sites Castle: a) CMR, b) WFS. Paired sites WLNP: c) Akamina, d) Cameron. AEP sites in close proximity to CMR and WFS: e) Gardiner, f) WC II. Photos c: courtesy of Scott Campbell (AEP), e and f: courtesy of https://acis.alberta.ca/weather-data-viewer.jsp.

The Castle Mountain Ridge (CMR) Geonor is in the northwestern portion of Castle. The Geonor was installed on the crest of Gravenstafel Ridge in Sep-2015 at an elevation of 2130 m above sea level (masl), above treeline in a primarily alpine context. The WFS Geonor was installed in Sep-2017 at 1400 m asl (Barnes et al., 2020) within a small valley floodplain clearing

at the University of Lethbridge Westcastle Field Station (WFS), 730 m lower and 3.75 km north of the CMR Ridge site and on the leeward side (see Table 3.1).

In September 2017, the Kenow wildfire (Waterton Lakes National Park, 2017) destroyed the AEP Akamina weather station and burnt most of the Cameron Valley. A third ULAL Geonor was installed in Oct-2018 within the Cameron Valley floodplain at 1655 m asl. An AEP Pluvio gauge was re-installed at the Akamina site in Sep-2018 at 1809 m asl. No significant forest canopy is present, as both WLNP sites are in the burnt area. Akamina is a mid-mountain site, 321 m lower than CMR. Cameron is 1.3 km down slope and 154 m lower on the leeward side of Akamina. Gardiner is an AEP mid-mountain site, located 7.15 km northwest of CMR and 190 m lower. West Castle II (WC II) is an AEP valley site located within Castle, 8.5 km southeast of WFS and 133 m higher.

The Gardiner (installed in January 1984) and WC II (installed in Mar 1984) Pluvio gauge sites are not in the same synoptic-scale prevailing wind field as CMR or WFS but are nearby and at two different elevations. There are other precipitation gauge stations in Southern Alberta but given the focus of this study was to examine local valley to upper elevation precipitation gradients, the analysis was limited to stations in close proximity.

Table 3.1: Values above the diagonal are distances (km) between each site. Values below the diagonal are elevation differences (m) between sites

| Site | CMR | WFS | Akamina | Cameron | Gardiner | WC II |
|---|---|---|---|---|---|---|
| | | | Distance between sites (km) | | | |
| CMR | | 3.8 | 43.0 | 43.2 | 7.2 | 7.2 |
| WFS | 730 | | 44.3 | 44.3 | 7.8 | 8.5 |
| Akamina | 321 | 409 | | 1.3 | 50.2 | 36.0 |
| Cameron | 475 | 255 | 154 | | 50.3 | 36.1 |
| Gardiner | 190 | 540 | 131 | 285 | | 14.3 |
| WC II | 597 | 133 | 276 | 122 | 407 | |
| Elevation Difference between sites (m) | | | | | | |

Precipitation gauges located in Castle and WLNP are good candidates for examining elevational precipitation gradients and seasonality because of their spatial proximity and significant elevation difference. AEP headwater precipitation weather stations are located at mid-mountain or valley sites and do not capture near proximity valley to alpine elevation measurements (Newton et al., 2021). ULAL sites compliment the AEP precipitation measurement network, as CMR is at an alpine elevation while WFS is located in a valley elevation (Barnes & Hopkinson, 2022b). The Cameron valley station is in close proximity to the AEP Akamina site but has a smaller elevation range than the sites in Castle.

### 3.2.2 Precipitation Gauge Data

Datasets used in this analysis were obtained from two different sources: i) ULAL Geonor gauges https://doi.org/10.20383/102.0551 (Barnes & Hopkinson, 2022b); and ii) publicly available AEP Pluvio gauge data. ULAL weather stations located in the southern Alberta eastern slopes have sensor- and wind-induced bias Quality Control Corrections (QCC) applied to the data (Barnes & Hopkinson, 2022b; Hopkinson & Barnes, 2022). Alberta Climate Information Service (ACIS) publicly available precipitation datasets do not have these wind-induced under-catch corrections applied (Goodison et al., 1998; Nitu, 2010) since most AEP sites do not capture required wind speed measurements. The ULAL dataset contains all Geonor precipitation observations for CMR, WFS, and Cameron and have undergone comprehensive cleaning, smoothing and correction (described in Barnes and Hopkinson (2022b)). Five individual precipitation variables represent the raw measurement (Raw_Precip), ACIS (ACIS_Precip) processed (Wright, 2021c), additional noise removal (Noise_Precip), removal of over catch

(OC_Precip), and a correction for under catch (UC_Precip), as well as the weather observations required to compute each precipitation variable.

GoA historical precipitation data for the Alberta Rocky Mountain Eastern Slopes headwater region are publicly accessible from https://acis.alberta.ca/weather-data-viewer.jsp (Alberta Climate Information Service (ACIS)) (Wright, 2021a) and https://rivers.alberta.ca/ (Alberta Environment and Protected Areas (AEP) RIVERS "Alberta's River Forecast Centre: Awareness and Communication") system (Alberta Environment and Parks, 2019). Although two different totalizing precipitation gauges (Geonor and Pluvio) were used, Kochendorfer, Nitu, et al. (2017) found measurements from these sensors to be comparable. The Pluvio gauge uses a proprietary algorithm that is intended to compensate for temperature and wind effects (OTT Hydromet GmbH, 2019). However, AEP Pluvio precipitation data do not have wind-induced bias corrections applied to recorded observations (Nitu, 2010; Wright, 2021b).

ULAL ACIS_Precip (precipitation data prior to quality control corrected (QCC), referred to as $Precip_{ACIS}$ in this chapter) was considered equivalent to the AEP public precipitation data due to comparable collection and processing. However, wind-induced bias can be significant depending on the location of the gauge (Lundquist et al., 2015). ULAL quality control corrected (referred to as $Precip_{QCC}$, equivalent to "UC_Precip" in Barnes and Hopkinson (2022b)) data were compared with $Precip_{ACIS}$ data to illustrate the potential magnitude of under-estimation due to wind biases. $Precip_{QCC}$ was not computed for Cameron prior to October 2019 due to local wind field data being unavailable. Wind data collected at the AEP Akamina site was used to apply precipitation corrections equivalent to ULAL $Precip_{QCC}$ data. Quality control corrections could not be applied to AEP Gardner and WC II precipitation since wind data were not available at these sites. ULAL CMR, WFS, Cameron, and AEP Akamina datasets were aggregated to a

daily timestep. All ULAL and AEP datasets were aggregated to cumulative monthly precipitation for comparative purposes. General statistics were computed for each site. A Spearman (non-parametric) correlation and linear regression $R^2$ matrix were calculated to examine how sites related to each other.

$Precip_{ACIS}$ data were expected to produce a lower estimate of EPG due to a systematic under-estimate of the true precipitation but have been included because others may compute EPG using publicly available records that have not been corrected or quality controlled. $Precip_{QCC}$ is expected to provide a more realistic estimate of precipitation and EPG but given under-catch bias correction is modelled it could contain more uncertainty. ULAL $Precip_{ACIS}$ equivalent datasets were used to facilitate EPG comparisons with AEP $Precip_{ACIS}$ precipitation data. Both $Precip_{ACIS}$ and $Precip_{QCC}$ datasets were used to examine the range of potential EPG estimates.

### 3.2.3 Snowpack Data

To compare $Precip_{ACIS}$ and $Precip_{QCC}$ at the watershed-level, mesoscale spatialized precipitation (MSP) with simulated SWE water yield estimation, snow depth was multiplied by snow density and area. ALS snow depth distributions are available for the West Castle Watershed (WCW). A July 2020 ALS DEM of WCW, was used to calculate area per 100 m binned elevation range. Snow depth per elevation bin was obtained from March 5, 2020 and March 4, 2021 ALS SDMs (Barnes & Hopkinson, 2022a). The snow depth range for each bin was quantified using the SDM mean depth ± one standard deviation (StDev).

Snow density was computed from AEP monthly snow depth and SWE field measurements (Pickering, 2018) in the Alberta Eastern Slopes headwater region that were

sampled within 5 days either side of the first of each month. Akamina, Gardiner, South Racehorse Creek (SRHC), and West Castle II (WC II) field sampling data from 1980 to 2021 are available from AEP https://rivers.alberta.ca/ (Alberta Environment and Parks, 2019). AEP field measurements collected at all four sites for the end of each February/beginning of March from 1980 to 2021 coincide with the dates of both March 5, 2020 and March 4, 2021 SDMs. Snow density was computed using SWE divided by snow depth for each observation in the sample set and expressed as the percentage of standard liquid water equivalent instead of kg/m$^3$. This approach was used in order to derive SWE estimates by multiplying snow depth by snow density. The intent was to use an observed range for snow density that would adequately capture watershed wide landscape and terrain variability. In this case, the range adopted was the mean ± one StDev. Both SDMs coincide with the $MSP_{ACIS}$ and $MSP_{QCC}$ collection period, snow depth and density for 2020 and 2021 fall within the mean ± one StDev range of the entire 1980 to 2021 sample set. ALS snow depth was combined with snow density observations to compute SWE. SWE estimated range for each elevation bin was calculated using equation 3.1:

$$SWE_{elev\_bin} = snow\ depth_{elev\_bin} * snow\ density_{elev\_bin} \quad (3.1)$$

### 3.2.4 Elevational Precipitation Gradients (EPG)

Elevational Precipitation Gradients (EPG) were calculated for both the $Precip_{ACIS}$ and $Precip_{QCC}$ datasets for two paired sites: 1) Castle, CMR (Figure 3.2a, upper) and WFS (Figure 3.2b, lower); and 2) WLNP, Akamina (Figure 3.2c upper) and Cameron (Figure 3.2d lower) using equation 3.2:

$$EPG = \frac{(P_{upper} - P_{lower})}{\left(\frac{Elev_{upper} - Elev_{lower}}{100}\right)} \quad (3.2)$$

where $P_{upper}$ is precipitation from the gauge at the higher elevation ($Elev_{upper}$), $P_{lower}$ is the precipitation from the gauge at the lower elevation ($Elev_{lower}$). A 7-day moving average was used to reduce noise in the EPG series.

### 3.2.5 Precipitation Time Series Components

The $Precip_{ACIS}$ monthly datasets were used to explore seasonal variations across the six sites since $Precip_{QCC}$ data were not available for Gardiner and WC II. $Precip_{ACIS}$ observations were sufficient, as accurate absolute magnitudes of precipitation or EPG are not required to explore temporal patterns, provided relative quantities do not vary systematically by site through time. Monthly means and a correlation matrix were computed for the six sites.

The time series for each gauge site was sub-divided into three of the four components of seasonality, trend, and random variance using a multiplicative model (equation 3.3). The cyclical and trend components were not used due to the time series being too short.

$$y_t = C_t * S_t * T_t * R_t \quad (3.3)$$

where $y_t$ is the observed value at timestep t (a monthly timestep was used in this study), $S_t$ is the seasonal component, $T_t$ is the Trend, $R_t$ is the random variation, and $C_t$ is the cyclical component.

An autocorrelation function (ACF) (Box et al., 2015) was used to quantify the serial correlation of the TS (time series). An ACF computes the linear relationship between two TS (time series) values. The number of timesteps separating the two TS values is referred to as the lag ($L_k$). The ACF was calculated between t and the previous TS value t - 1, where the time lag is k = 1. When a seasonal component is present in the TS, a cyclical pattern will be present in the plot. ACF was calculated for each site to determine if any seasonal patterns were present using equation 3.4:

$$ACF\ (L_k) = \frac{\sum_{t=k+1}^{tt}(y_t - \bar{y})(y_{t-k} - \bar{y})}{\sum_{t=k+1}^{tt}(y_t - \bar{y})^2} \tag{3.4}$$

where $L_k$ is the value of lag k at timestep t, tt is the total number of observations in the time series, $y_t$ is the observed value at the $t^{th}$ interval, and $\bar{y}$ is the mean of the time series.

To extract the seasonality component, the first step is to use a moving average based on the number of timesteps (t) within the repeating time interval of the TS. A 12-month moving average (MA) was computed for each site's time series using equation 3.5. The role of the MA is to smooth the TS to obtain the general upward and downward shifts in the data. Since there are an even number of time periods within the repeating time interval, each moving average value does not correspond to a month (t). A centered moving average (CMA) is created using equation 3.6 to associate a 12-month MA to the correct month (t). The CMA forms the baseline for the TS.

$$MA_t = \frac{\sum_{i=t-6}^{t+6} y_t}{12} \tag{3.5}$$

$$CMA_t = \frac{MA_t + MA_{t+1}}{2} \tag{3.6}$$

Using the CMA, the TS can be divided into each component. The seasonal index (SI) (Peixeiro, 2022) is a percentage of how far above or below the computed value is to the CMA (the baseline of the TS). Positive values indicate SI is higher than CMA and negative values mean SI is lower than CMA. SI was calculated for each month in the TS using equation 3.7.

$$SI_m = \left( \frac{\sum_{i=1}^{n} \frac{y_{m(i)}}{CMA_{m(i)}}}{n} \right) - 1 \tag{3.7}$$

where m is the month within the year, n is the number of repeating time intervals (i.e. the number of times that month is present in the TS), i is the summation iterator.

### 3.2.6 Comparing Mesoscale Spatialized Precipitation and SWE Estimated Water Yield

To evaluate winter precipitation redistribution and potential loss following gauge observation, spatialized winter precipitation was compared with ground surface snowpack accumulation at watershed scale. For the purposes of this comparison, a simplistic linear increase of precipitation with elevation was assumed since there was no data to support a more sophisticated approach. $Precip_{ACIS}$ and $Precip_{QCC}$ (total precipitation) beginning from Oct 1 of the previous year to the date of each respective ALS mission (Mar 5, 2020 and Mar 4, 2021) was used to calculated mesoscale spatialized precipitation (MSP) for comparison to WCW modelled SWE. MSP was calculated using the monthly EPG from WFS to CMR-Ridge. For the lowest

elevation bin ($Precip_{elev\_bin(m,\ j=1)}$), where j is the $j^{th}$ elevation bin, was calculated using WFS precipitation ($WFS_{precip(m)}$) where m is the month of the year, multiplied by the area of the elevation bin ($area_{elev\_bin(j=1)}$). For each subsequent elevation bin (elev_bin (j)), equation 3.8 was used to calculate precipitation ($Precip_{elev\_bin(m,j)}$) using EPG for month m.

$$Precip_{elev\_bin(m,j)} = Precip_{elev\_bin(m-1,j)} + (WFS_{precip} * (\frac{\frac{(P_{upper} - P_{lower})}{P_{lower}}}{(\frac{Elev_{upper} - Elev_{lower}}{100})})m) \quad (3.8)$$

MSP per elevation bin (j) was calculated using equation 3.9.

$$MSP_{elev\_bin(m,j)} = Precip_{elev\_bin(m,j)} * area_{elev\_bin(j)} \quad (3.9)$$

WCW mesoscale spatialized precipitation total ($MSP\_Total_{WCW}$) for days from Oct 1 to the date of the ALS mission was computed by summing both the calculated area totals for all elevation bins and all months where nm is the number of months used to calculate the total MSP and jj is the total number of elevation bins, using equation 3.10.

$$MSP\_Total_{WCW} = \sum_{\substack{t=1\ to\ nm \\ j=1\ to\ jj}} MSP(m,j) \quad (3.10)$$

SWE was calculated for each elevation bin ($SWE\_AreaYield_{elev\_bin(m,j)}$) using equation 3.11.

$$SWE\_AreaYield_{elev\_bin(j)} = SWE_{elev\_bin(j)} * area_{elev\_bin(j)} \quad (3.11)$$

WCW SWE yield ($SWE\_Yield_{WCW}$) was computed by summing the calculated area yield for all elevation bins using equation 3.12.

$$SWE\_Yield_{WCW} = \sum_{j=1}^{jj} SWE\_AreaYield(j) \quad (3.12)$$

## 3.3 Results

General statistics were calculated for each site using daily $Precip_{ACIS}$ as shown in Table 3.2. The data were non-parametric and right skewed with each site having a highly peaked distribution. The number of daily measurements for CMR, Gardiner, WC II, and WFS were 1461 (4 years). Akamina and Cameron sites had 1070 daily measurements (almost 3 years). WC II had the fewest precipitation days at 47% but the highest observed precipitation value of 87.2 mm. Cameron had the highest number of precipitation days at 71%. CMR had the lowest observed precipitation of 49.21 mm.

Table 3.2: ACIS daily precipitation statistics for CMR, Gardiner, Akamina, Cameron, WC II, and WFS. Upper: statistics for all days, Lower: statistics for only days with precipitation.

| | CMR | Gardiner | Akamina | Cameron | WC II | WFS |
|---|---|---|---|---|---|---|
| Mean (mm) | 3.5 | 3.2 | 3.0 | 2.5 | 2.9 | 2.5 |
| Median (mm) | 0.7 | 0.4 | 0.4 | 0.4 | 0.0 | 0.2 |
| StDev (mm) | 5.9 | 6.2 | 6.0 | 5.2 | 6.7 | 5.4 |
| Skewness | 2.8 | 3.5 | 4.2 | 4.6 | 5.0 | 4.4 |
| Kurtosis | 11.2 | 18.1 | 26.8 | 33.7 | 38.5 | 28.9 |
| Highest Observed (mm) | 49.2 | 70.0 | 66.7 | 63.1 | 87.2 | 61.7 |
| Precipitation Days (%) | 65% | 60% | 60% | 71% | 47% | 66% |
| Mean (mm) | 5.3 | 5.4 | 4.9 | 3.6 | 6.0 | 3.7 |
| Median (mm) | 2.7 | 2.5 | 0.8 | 0.6 | 3.0 | 1.1 |

The Spearman (non-parametric) correlation and linear regression ($R^2$) matrix using daily $Precip_{ACIS}$ for CMR, Gardiner, Akamina, Cameron, WC II, and WFS is shown in Table 3.3. The

strongest relationship was between the WLNP Akamina and Cameron sites with a correlation of 0.88 and $R^2$ of 0.78. WFS and Cameron also had a strong correlation at 0.84. The weakest correlation of 0.73 was between CMR and both WC II and Cameron. The correlation between CMR and WFS was 0.76 and $R^2$ of 0.58 even though the distance between these two sites was only 3.5 km; however, they had the largest elevation difference of 730 m.

Table 3.3: Spearman Correlation and $R^2$ for daily $Precip_{ACIS}$ between CMR, Gardiner, Akamina, Cameron, WC II, and WFS.

| | CMR | Gardiner | Akamina | Cameron | WC II | WFS |
|---|---|---|---|---|---|---|
| Linear Regression $R^2$ | | | | | | |
| CMR | | 0.62 | 0.60 | 0.55 | 0.53 | 0.58 |
| Gardiner | 0.79 | | 0.66 | 0.58 | 0.65 | 0.61 |
| Akamina | 0.77 | 0.81 | | 0.78 | 0.61 | 0.63 |
| Cameron | 0.74 | 0.76 | 0.88 | | 0.53 | 0.70 |
| WC II | 0.73 | 0.81 | 0.78 | 0.73 | | 0.55 |
| WFS | 0.76 | 0.78 | 0.79 | 0.84 | 0.74 | |
| Spearman Correlation | | | | | | |

The $Precip_{ACIS}$ monthly mean and standard deviation for each site is shown in Table 3.4. Akamina and Cameron had a three-year time series with most of the first month of the first year missing from the series whereas the other sites had four complete years. CMR had the highest monthly mean precipitation during the winter months of Nov to Mar and the lowest for May, Aug, and Sep. Gardiner's mean monthly precipitation was highest among all sites in Oct, Apr, May, and Jul. In Jun, WC II had the highest mean monthly precipitation of all the sites. All sites had lowest precipitation in Jul.

Table 3.4: $Precip_{ACIS}$ Monthly Mean and Standard Deviation (sites listed by highest to lowest elevation) for CMR, Gardiner, Akamina, Cameron, WC II, and WFS.

| $Precip_{ACIS}$ | CMR | | Gardiner | | Akamina | | Cameron | | WC II | | WFS | |
|---|---|---|---|---|---|---|---|---|---|---|---|---|
| Elev | Alpine | | Mid-Mountain | | Mid-Mountain | | Valley | | Valley | | Valley | |
| (masl) | 2130 | | 1940 | | 1809 | | 1655 | | 1533 | | 1400 | |
| | Mean | StDev | Mean | StDev | Mean | StDev | Mean | StDev | Mean | StDev | Mean | StDev |
| Month | (mm) | (mm) | (mm) | (mm) | (mm) | (mm) | (mm) | (mm) | (mm) | (mm) | (mm) | (mm) |
| Oct | 90.5 | 16.9 | 111.7 | 13.6 | 102.7 | 14.5 | 91.4 | 7.8 | 106.8 | 13.7 | 84.7 | 11.2 |
| Nov | 135.5 | 52.1 | 100.1 | 14.0 | 104.3 | 54.5 | 84.6 | 40.3 | 128.4 | 53.2 | 90.4 | 34.6 |
| Dec | 166.6 | 39.4 | 155.3 | 20.6 | 114.5 | 38.7 | 93.1 | 31.6 | 134.0 | 31.4 | 90.4 | 12.3 |
| Jan | 186.9 | 43.9 | 97.4 | 38.1 | 90.2 | 18.0 | 72.5 | 15.1 | 52.9 | 24.6 | 58.9 | 11.7 |
| Feb | 156.7 | 53.5 | 101.2 | 55.7 | 81.9 | 9.1 | 73.3 | 7.4 | 92.1 | 37.7 | 92.8 | 13.1 |
| Mar | 106.3 | 54.9 | 90.1 | 28.1 | 63.7 | 42.7 | 58.8 | 36.7 | 71.5 | 42.6 | 62.3 | 27.0 |
| Apr | 105.9 | 26.4 | 121.0 | 12.3 | 102.0 | 34.2 | 94.4 | 29.4 | 93.5 | 16.1 | 86.4 | 8.9 |
| May | 79.9 | 30.5 | 112.3 | 32.6 | 105.0 | 17.8 | 104.0 | 24.9 | 86.1 | 24.9 | 93.6 | 37.4 |
| Jun | 99.5 | 34.4 | 107.8 | 26.8 | 123.1 | 42.5 | 104.7 | 39.9 | 126.1 | 43.4 | 87.0 | 28.4 |
| Jul | 36.0 | 26.1 | 39.1 | 28.8 | 26.9 | 16.6 | 19.0 | 12.2 | 27.7 | 21.4 | 35.4 | 19.1 |
| Aug | 44.3 | 26.6 | 61.5 | 27.8 | 67.8 | 42.3 | 59.5 | 38.3 | 56.2 | 38.4 | 53.9 | 36.7 |
| Sep | 53.9 | 21.9 | 81.6 | 54.0 | 97.4 | 50.1 | 68.0 | 31.3 | 70.8 | 39.9 | 62.8 | 33.7 |
| Annual | | | | | | | | | | | | |
| Total | 1262.0 | | 1179.0 | | 1079.6 | | 923.3 | | 1046.0 | | 898.5 | |
| Min | 36.0 | | 39.1 | | 26.9 | | 19.0 | | 27.7 | | 35.4 | |
| Max | 186.9 | | 155.3 | | 123.1 | | 104.7 | | 134.0 | | 93.6 | |

$Precip_{QCC}$ monthly mean and standard deviation for CMR and WFS is shown in Table 3.5. CMR winter precipitation was amplified due to wind-induced under-catch corrections (Barnes & Hopkinson, 2022b). Monthly mean precipitation for CMR was higher during Nov to Mar and lower in Jul, Aug, and Sep. WFS had the lowest mean monthly precipitation in Jul. In Aug and Sep, WFS observed greater precipitation than CMR.

Table 3.5: $Precip_{QCC}$ Monthly Mean and Standard Deviation for CMR and WFS.

| $Precip_{QCC}$ Elev (masl) | CMR Alpine 2130 | | WFS Valley 1400 | |
|---|---|---|---|---|
| Month | Mean (mm) | StDev (mm) | Mean (mm) | StDev (mm) |
| Oct | 167.0 | 57.6 | 84.7 | 15.1 |
| Nov | 267.4 | 93.8 | 95.5 | 39.8 |
| Dec | 380.7 | 125.8 | 95.9 | 13.0 |
| Jan | 452.9 | 103.2 | 55.7 | 9.3 |
| Feb | 354.4 | 142.2 | 94.6 | 16.9 |
| Mar | 214.8 | 123.4 | 63.8 | 30.0 |
| Apr | 174.2 | 48.2 | 85.3 | 9.3 |
| May | 94.5 | 38.2 | 91.2 | 38.5 |
| Jun | 109.9 | 35.3 | 86.7 | 28.4 |
| Jul | 37.3 | 27.3 | 34.6 | 19.0 |
| Aug | 46.1 | 27.7 | 53.9 | 37.3 |
| Sep | 61.4 | 21.6 | 80.1 | 41.0 |
| Annual Total | 2360.7 | | 922.0 | |
| Min | 37.3 | | 34.6 | |
| Max | 452.9 | | 95.9 | |

### 3.3.1 Elevational Precipitation Gradients (EPG)

The $Precip_{ACIS}$ monthly means were used to calculate monthly $EPG_{ACIS}$ from WFS (the lowest elevation at 1400 masl) to each of CMR, Gardiner, Akamina, Cameron, WC II as shown in Figure 3.3a. There is a positive $EPG_{ACIS}$ between WFS and CMR during the snow-covered months of Nov to Mar. During the spring melt months of Apr to Jun and the late summer to fall months of Aug to Oct, $EPG_{ACIS}$ approaches zero or becomes negative indicating CMR has less precipitation than the lower elevation WFS site. $EPG_{ACIS}$ for the WLNP sites (Akamina and Cameron) track closely together as related to WFS with a maximum difference of 6 mm/100 m per month. All sites demonstrated $EPG_{ACIS}$ values within the range of -9 mm/100 m per month to 18 mm/100 m per month with the exception of WC II which peaked at 33 mm/100m for Dec. An inverse $EPG_{ACIS}$ (-1 to -7 mm/100 m per month) was evident between WFS and CMR in May, Aug, and Sep. Figure 3.3b shows $EPG_{QCC}$ between WFS with CMR, Akamina, and Cameron. $EPG_{QCC}$ was amplified during the snow-covered months with the highest peak in Jan at 62

mm/100 m per month between WFS and CMR. An inverse $EPG_{QCC}$ (-2 to -11 mm/100 m per month) was evident in Aug and Sep for CMR and Cameron. There was no systematic precipitation gradient suggesting other synoptic factors influence EPG at a regional scale.

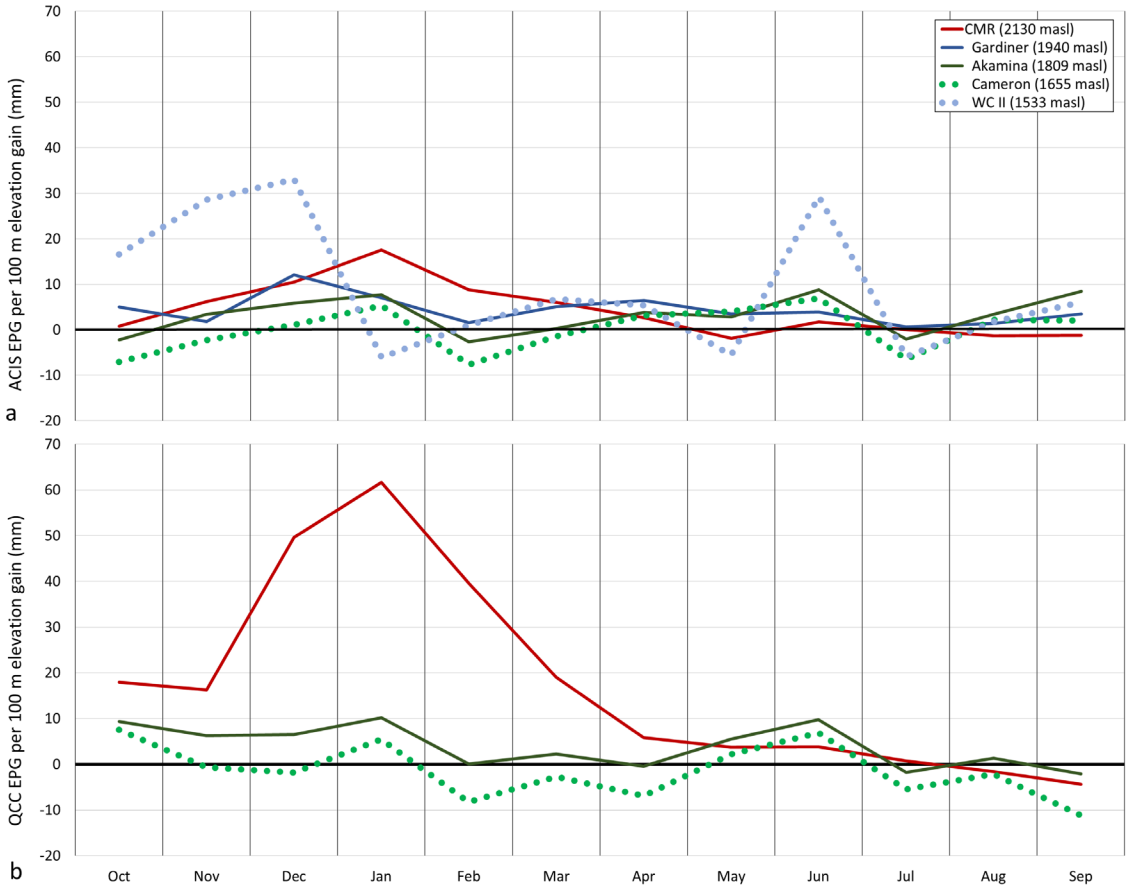


Figure 3.3: a) Monthly mean $EPG_{ACIS}$ between WFS and all sites (CMR, Gardiner, Akamina, Cameron, and WC II), b) Monthly mean $EPG_{QCC}$ between WFS and sites (Akamina, Cameron, and CMR).

Cumulative daily $Precip_{ACIS}$ (left axis) and 7-day moving average $EPG_{ACIS}$ (right axis) for the CMR/WFS Castle pair (730 m elevation difference) is shown in Figure 3.4a. The Castle $EPG_{ACIS}$ increased to a daily maximum of 1.5 mm/100 m during the winter snow accumulation months. $EPG_{ACIS}$ was not as strong during the spring melt season and the summer months with a low of -1.2 mm/100 m. An inverse $EPG_{ACIS}$ (Avanzi et al., 2015) occurred in each hydrologic year where WFS received more precipitation in the summer months than CMR. In the 2018 –

2019 hydrologic year, CMR did not receive as much precipitation in the late winter and spring as in the previous and subsequent years resulting in a lower $EPG_{ACIS}$. The Akamina/Cameron WLNP pair (154 m elevation difference) is shown in Figure 3.4b. $EPG_{ACIS}$ had a maximum of 2.7 mm/100 m. The $EPG_{ACIS}$ was higher in the fall months and lower in the early spring and summer.

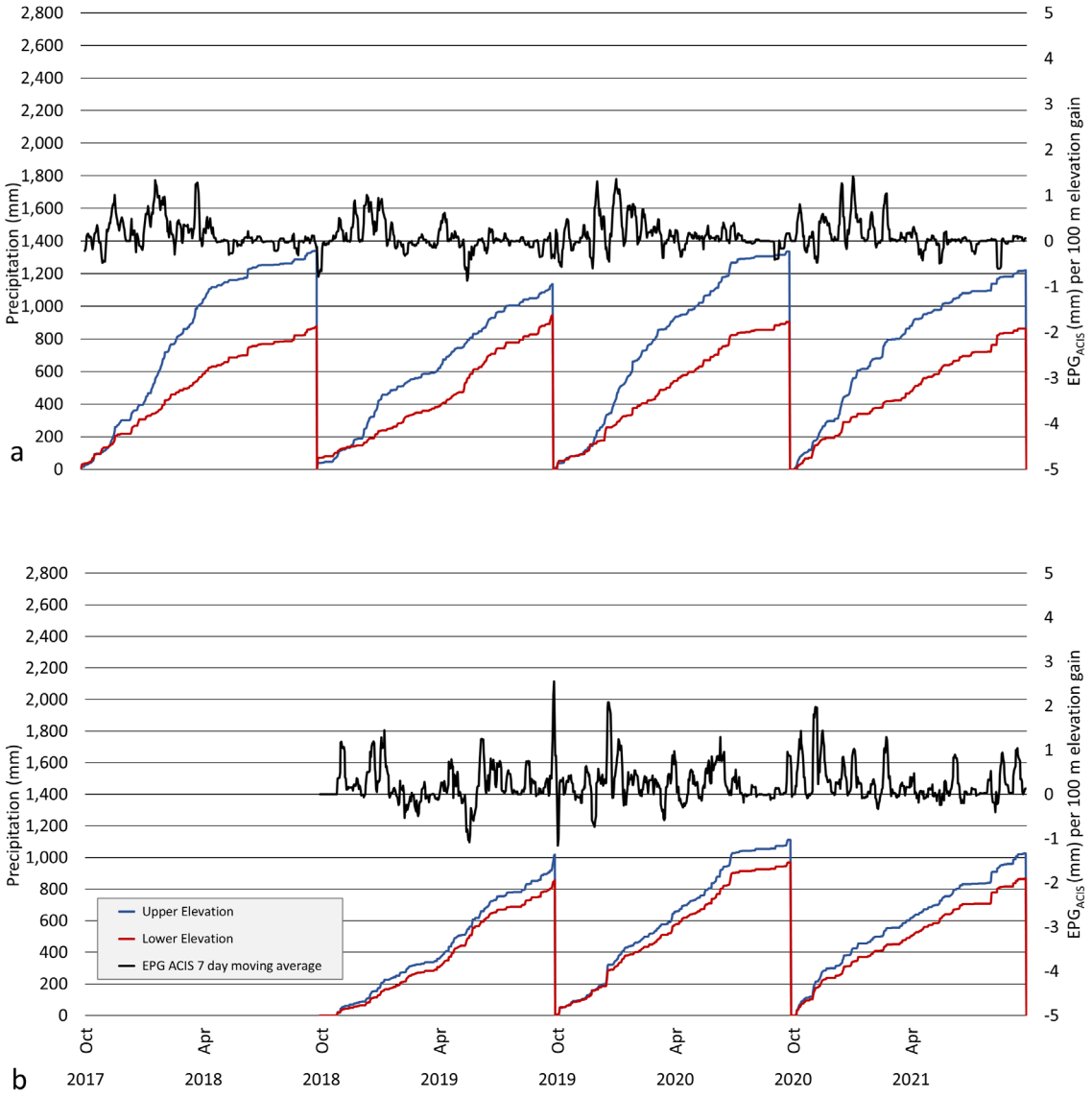


Figure 3.4: Cumulative Daily $Precip_{ACIS}$ (primary axis - left) and $EPG_{ACIS}$ (secondary axis – right using a 7-day moving average is a black line) for: a) Castle sites CMR (blue) and WFS (red) with a 730 m elevation difference. b) WLNP sites Akamina (blue) and Cameron (red) datasets with a 154 m elevation difference (the series represents the available data).

As expected, $EPG_{QCC}$ was increased relative to $EPG_{ACIS}$ in Castle (Figure 3.5a) with peak values of 4.2 mm /100 m in the winter months and decreased in the late spring and summer months. WLNP $EPG_{QCC}$ (Figure 3.5b) had a peak value of 2.1 mm/100 m. Generally, Akamina had more precipitation than Cameron throughout the entire year.

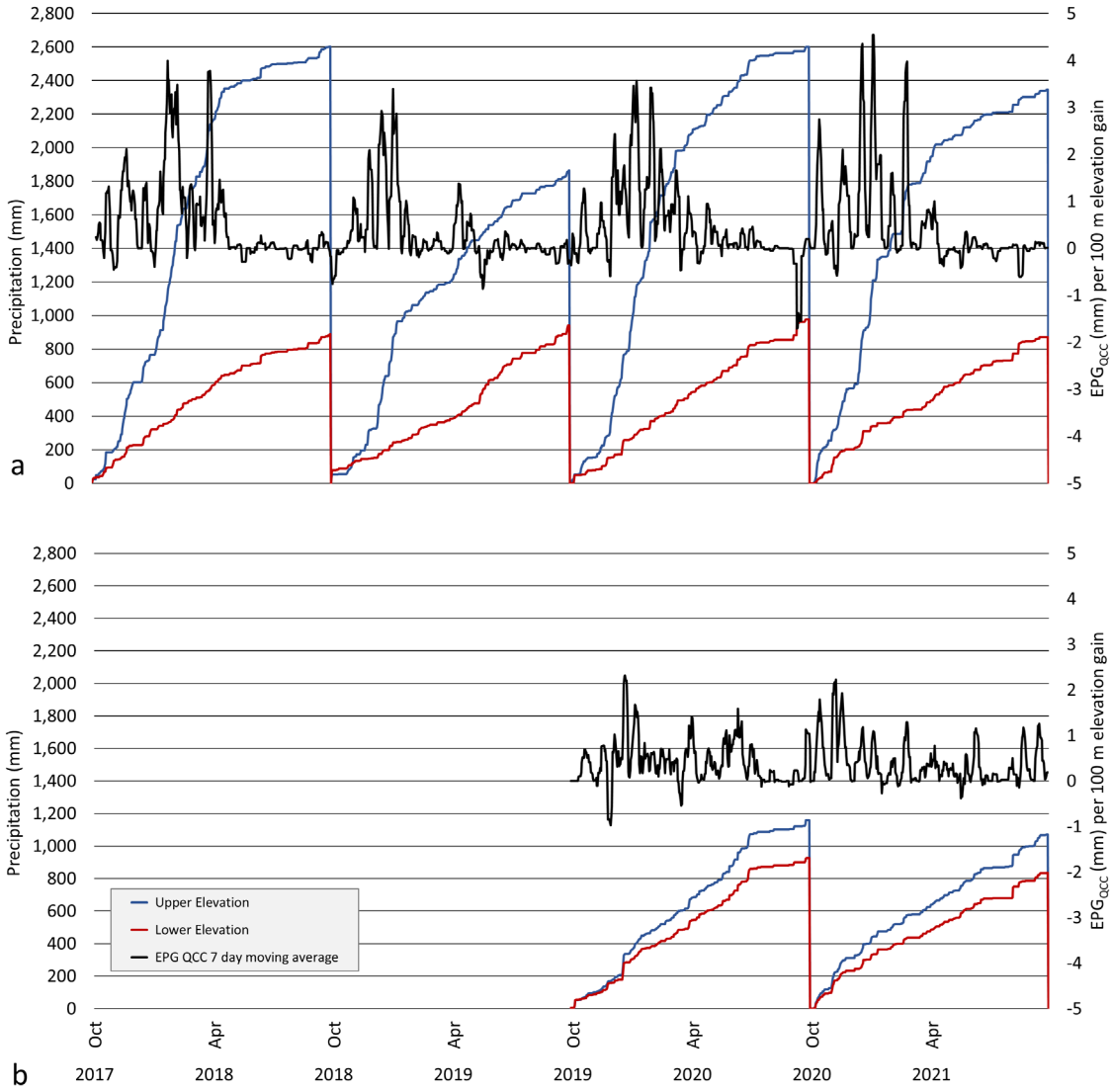


Figure 3.5: Cumulative Daily $Precip_{QCC}$ (primary axis - left) and $EPG_{QCC}$ (secondary axis – right, 7-day moving average is a black line) for: a) Castle sites CMR (blue) and WFS (red) with a 730 m elevation difference. b) WLNP sites Akamina (blue) and Cameron (red) datasets with a 154 m elevation difference (the series represents the available data).

### 3.3.2 Precipitation Time Series

Seasonal (quarterly aggregated $Precip_{ACIS}$) for all six sites is shown in Figure 3.6a. For all sites except CMR, quarterly $Precip_{ACIS}$ was higher in the fall and spring. CMR had the highest $Precip_{ACIS}$ in the winter and lowest in the summer months. Figure 3.6b shows $Precip_{QCC}$ for CMR and WFS for the same time period as the ACIS dataset. CMR $Precip_{QCC}$ was amplified and had the highest $Precip_{QCC}$ in the fall and winter. In the summer, WFS had higher $Precip_{QCC}$.

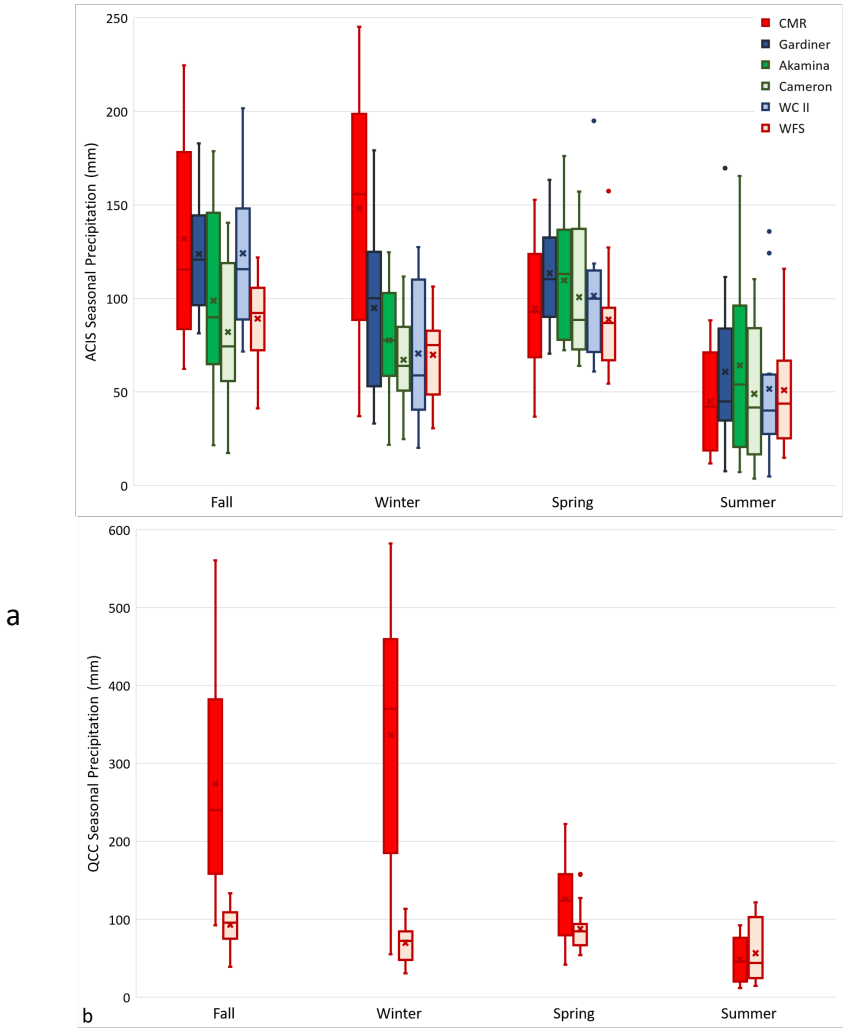


Figure 3.6: Seasonal Precipitation (mm) for a) 2017 to 2021 $Precip_{ACIS}$ for CMR, Gardiner, Akamina, Cameron, WC II, and WFS; b) 2017 to 2021 $Precip_{QCC}$ for CMR and WFS. Box and Whisker, X is mean, bar is median, top and bottom T are the range, coloured box is the interquartile range (quartile 1 to quartile 3), dots are outliers (data points that are 1.5 times above or below the interquartile range). Fall: Oct- Dec; Winter: Jan- Mar; Spring: Apr- Jun; Summer: Jul- Sep

The ACF was calculated for each site for 24 consecutive monthly lags (Figure 3.7). CMR shows a sinusoidal pattern with both positive and negative serial correlations indicating there was an annual seasonality component in the TS. This pattern was not as pronounced for the other sites. There was no consistent upward or downward trend component in the TS. As well, there was not a long enough data record to compare or determine long-term cycles that would contribute to a cyclical shift in the TS due to influences such as changing Pacific Decadal Oscillation or El Niño-Southern Oscillation global scale teleconnection patterns (Wang et al., 2006) that are unrelated to seasonality or trend.

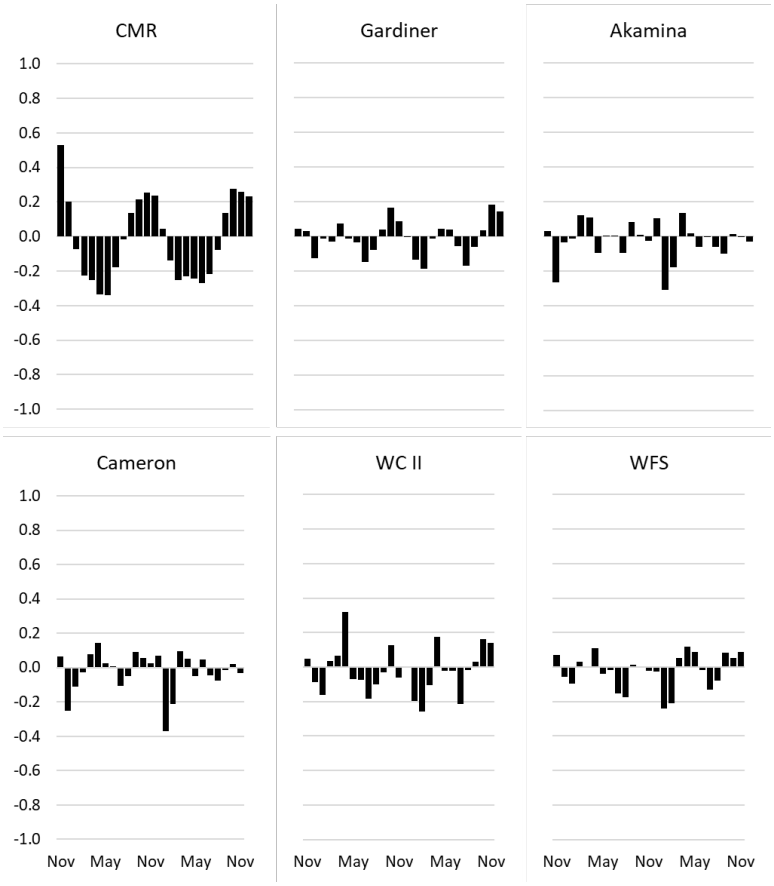


Figure 3.7: Auto Correlation Function (ACF) for CMR, Gardiner, Akamina, Cameron, WC II, and WFS. The series contains 24 consecutive months beginning with November for each site.

The Seasonality Index (Figure 3.8) was computed for each of the sites. The CMR alpine site received most of its precipitation at the beginning of the winter snow season and less during

the balance of the year, especially May through Sep. Akamina and Cameron seasonal indices are within 6 % of each other for all months except Apr, May, and Sep. All sites received the least amount of precipitation during the summer months of Jul and Aug.

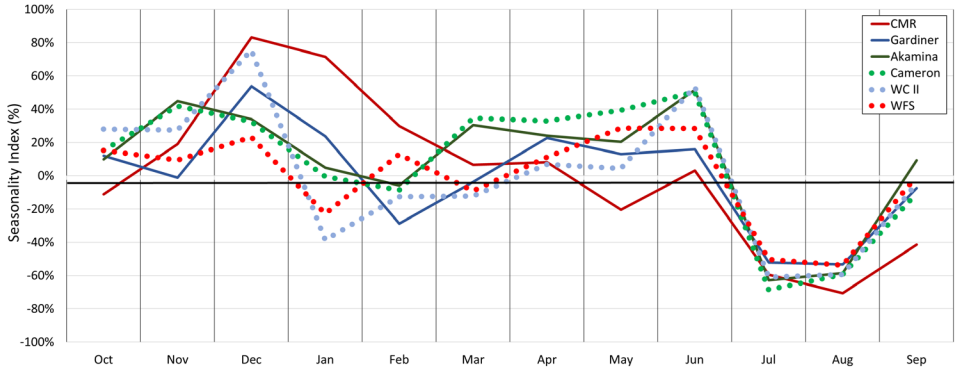


Figure 3.8: Seasonality Index for CMR, Gardiner, Akamina, Cameron, WC II, and WFS. Alpine and mid-mountain sites are a solid line. Valley sites are a dotted line.

### 3.3.3 West Castle Watershed Estimated MSP and SWE Water Yield

Estimated watershed precipitation and snow water equivalent water yields were calculated for both the annual means as well as from the beginning of the respective hydrologic year (Oct 1) to the date of each airborne lidar fight (Mar 5, 2020 and Mar 4, 2021). After accounting for EPG and elevation hypsometry, WCW annual mesoscale spatialized precipitation (MSP, Table 3.6) shows $MSP_{ACIS}$ with 133.14 x $10^6$ $m^3$ and $MSP_{QCC}$ of 175.78 x $10^6$ $m^3$ (36% higher than $MSP_{ACIS}$). The most hydrologically productive elevation range was 1900 – 2000 masl with $MSP_{ACIS}$ showing 14.98 x $10^6$ $m^3$ and $MSP_{QCC}$ 24.89 x $10^6$ $m^3$ (Figure 3.9a). The winter $MSP_{ACIS}$ and $MSP_{QCC}$ was compared to the ALS SWE (Oct 1 to the date of each ALS mission) as shown in (Figure 3.9b). The elevation range 2000 – 2100 masl was the most productive for $MSP_{QCC}$ and 1900 – 2000 masl was most productive for both $MSP_{ACIS}$ and SWE. The winter $MSP_{ACIS}$ for was ~58% of the annual $MSP_{ACIS}$ and ~70% of annual $MSP_{QCC}$.

Table 3.6: West Castle Watershed Water Yield ( x $10^6$ $m^3$) by Elevation Range. Mean annual yield for ACIS, QCC; Water yield for ACIS and QCC from Oct 1 to the date of ALS, Water yield for Mar 2020 and 2021 ALS SWE

| MSP and SWE Water Yield (x $10^6$ $m^3$) | | | | | | | | | |
|---|---|---|---|---|---|---|---|---|---|
| | | Annual | | Oct 1, 2019 to Mar 5, 2020 | | | Oct 1, 2020 to Mar 4, 2021 | | |
| Area | Elev Range | ACIS | QCC | ACIS | QCC | SWE | ACIS | QCC | SWE |
| $km^2$ | masl | (Mean) | | | | (Range) | | | (Range) |
| 11.23 | 1391 - 1500 | 10.07 | 10.33 | 4.84 | 4.80 | 0.52 - 3.35 | 4.70 | 4.90 | 0.58 - 3.23 |
| 11.86 | 1500 - 1600 | 11.23 | 13.24 | 5.70 | 7.33 | 1.17 - 5.07 | 5.58 | 7.34 | 1.27 - 4.61 |
| 11.69 | 1600 - 1700 | 11.64 | 15.35 | 6.21 | 9.45 | 1.57 - 6.86 | 6.10 | 9.38 | 1.52 - 5.96 |
| 12.15 | 1700 - 1800 | 12.70 | 18.33 | 7.06 | 12.13 | 2.10 - 9.98 | 6.96 | 11.96 | 1.74 - 8.55 |
| 12.07 | 1800 - 1900 | 13.22 | 20.58 | 7.62 | 14.35 | 2.35 - 13.23 | 7.54 | 14.09 | 1.71 - 11.20 |
| 13.08 | 1900 - 2000 | 14.98 | 24.89 | 8.91 | 18.06 | 2.21 - 15.68 | 8.85 | 17.66 | 1.53 - 13.46 |
| 11.70 | 2000 - 2100 | 13.97 | 24.54 | 8.55 | 18.37 | 2.09 - 14.29 | 8.51 | 17.93 | 1.32 - 12.37 |
| 8.94 | 2100 - 2200 | 11.13 | 20.52 | 6.99 | 15.75 | 0.85 - 10.58 | 6.97 | 15.34 | 0.26 - 9.14 |
| 6.15 | 2200 - 2300 | 7.95 | 15.32 | 5.11 | 12.00 | 0.12 - 6.63 | 5.11 | 11.67 | 0.00 - 6.13 |
| 3.35 | 2300 - 2400 | 4.50 | 9.00 | 2.95 | 7.18 | 0.00 - 3.50 | 2.95 | 6.97 | 0.00 - 3.07 |
| 0.95 | 2400 - 2500 | 1.32 | 2.74 | 0.89 | 2.22 | 0.00 - 0.81 | 0.89 | 2.15 | 0.00 - 0.66 |
| 0.26 | 2500 - 2630 | 0.38 | 0.81 | 0.26 | 0.66 | 0.00 - 0.23 | 0.26 | 0.64 | 0.00 - 0.16 |
| 103.44 | | 113.09 | 175.65 | 65.08 | 122.28 | 12.99 - 90.21 | 64.41 | 120.03 | 9.93 - 78.55 |

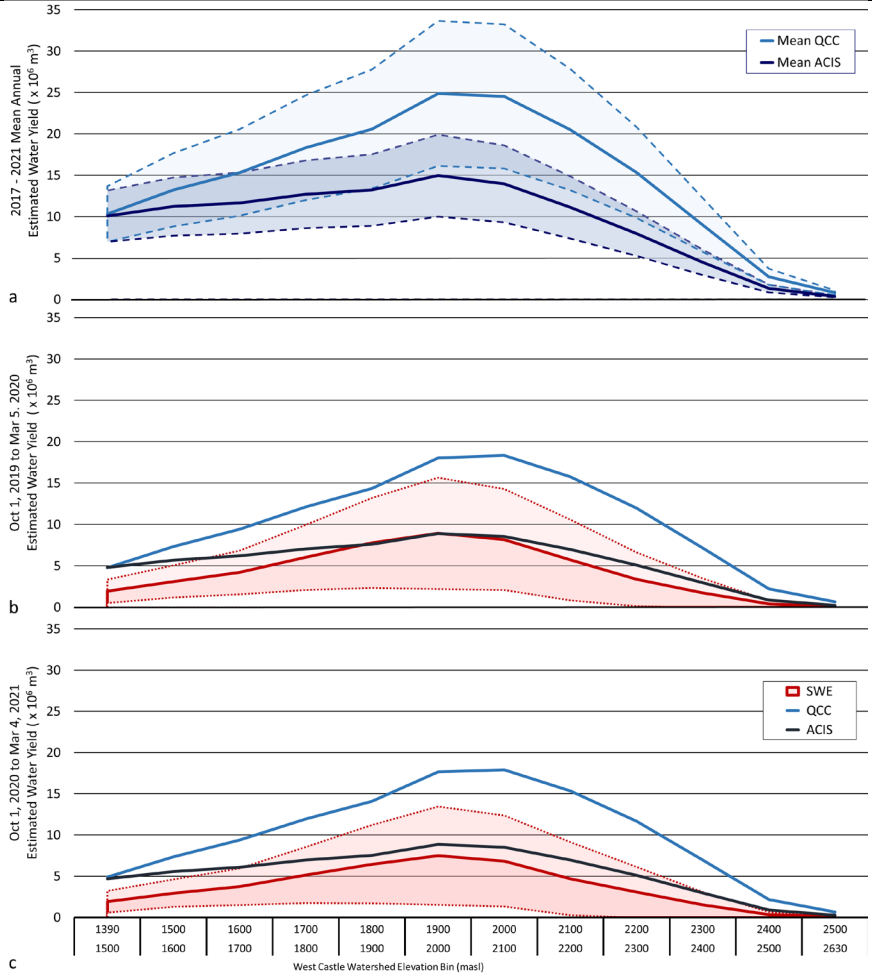


Figure 3.9: $MSP_{ACIS}$, $MSP_{QCC}$, and SWE Water yield for the West Castle Watershed. a) annual $MSP_{ACIS}$ and $MSP_{QCC}$ (mean ± 1 StDev) 2017 to 2021, b) Oct 1, 2019 to Mar 5, 2020 $MSP_{ACIS}$ and $MSP_{QCC}$, estimated SWE from Mar5, 2020 ALS SDM using mean ± 1 StDev snow depth multiplied by mean ± 1 StDev AEP derived 1980 to 2021 snow density; c) Oct 1, 2020 to Mar 4, 2021 $MSP_{ACIS}$ and $MSP_{QCC}$ and estimated SWE calculated from Mar 4, 2021 ALS SDM using mean ± 1 StDev snow depth multiplied by mean ± one StDev AEP derived 1980 to 2021 snow density.

## 3.4 Discussion

There was seasonal variation in both daily computed $EPG_{ACIS}$ and $EPG_{QCC}$ at the Castle and WLNP sites. At the local scale (valley to alpine), annual elevation precipitation gradients were generally consistent. EPG was enhanced in winter and decreased into the spring and summer. $EPG_{QCC}$ was amplified in the Castle dataset due to CMR $Precip_{QCC}$ depths that were almost double that of the $Precip_{ACIS}$ records, especially in the winter months due to high wind speeds and high rates of estimated under-catch. A similar increase occurred in WLNP $EPG_{QCC}$ although was smaller than Castle.

The monthly aggregated $Precip_{ACIS}$ demonstrated pronounced seasonality at all six AEP (Gardiner, Akamina, WC II) and ULAL (CMR, WFS, Cameron) sites. Precipitation was higher in the winter months and lower in the summer months for all sites. The seasonality index showed two peaks in the early winter as well as the spring for all sites. Akamina and Cameron had the closest seasonality patterns suggesting they encountered the same local weather patterns. There was no consistent rate of precipitation increase with elevation either seasonally or annually between all locations. Site differences can be problematic (Kochendorfer, Nitu, et al., 2017) and introduce more uncertainty in precipitation measurements. Logistically, alpine sites are difficult to access and maintain. Wind fields can be turbulent causing equipment failure and precipitation measurement errors. Local atmospheric circulation patterns (Barros & Kuligowski, 1998; Collados-Lara et al., 2018; Luce et al., 2013; Roe, 2005; Smith, 2019) and mountain geometry (Galewsky, 2009; Houze, 2012) such as slope and aspect (Daly et al., 2002; Jeong et al., 2020) can affect MSP and EPG rates. Lower level water baring clouds (similar to those seen in CMR webcam imagery (Barnes & Hopkinson, 2022b)) do not always encounter the top of mountain peaks and can precipitate only at lower elevations. Given the level of uncertainty in $EPG_{ACIS}$ and

$EPG_{QCC}$ rates, it is questionable as to how reliable modelled precipitation is in this region, especially since EPG rates vary depending on which stations are used for such calculations.

Precipitation gridded for WCW quantified modelled $MSP_{ACIS}$ and $MSP_{QCC}$ volumes. Annual $MSP_{QCC}$ was more than one third higher than $MSP_{ACIS}$. However, in the lowest elevation range, $Precip_{ACIS}$ and $Precip_{QCC}$ sensor noise and wind-induced under-catch adjustments did not differ significantly (Barnes & Hopkinson, 2022b) resulting in $MSP_{ACIS}$ and $MSP_{QCC}$ being similar for the two datasets. As elevation increased, $Precip_{ACIS}$ and $Precip_{QCC}$ diverge with differences being more than double within alpine elevation ranges. By comparing $MSP_{ACIS}$ and $MSP_{QCC}$ to ALS-derived mid-winter snowpack SWE estimations per elevation range, it was possible to visualise the potential elevational interaction of precipitation entering a mountainous watershed and the resultant snowpack following redistribution and other modifications. $MSP_{QCC}$ was above the range of modelled SWE for all elevations. $Precip_{ACIS}$ measurements appear implausibly low since the calculated $MSP_{ACIS}$ fell within the range of modelled SWE except for valley and upper alpine elevations. This is unrealistic given SWE experiences losses over the winter due to melt cycles and sublimation as well as gravity and wind-induced redistribution (Vionnet et al., 2021) from higher to lower elevations (Grünewald et al., 2014; Mott et al., 2018). SWE should be considerably lower than observed $MSP_{ACIS}$ indicating measurement errors (i.e. under-estimations) are likely large if under-catch corrections are not applied to high elevation precipitation records. However, publicly available precipitation records tend to conform to the $Precip_{ACIS}$ standard and not corrected $Precip_{QCC}$, so this needs to be considered when such data are used for water yield estimates or as inputs to hydrological models.

Aggregating the watershed elevation ranges into valley, treeline, and alpine (Table 3.7) it was possible to examine which zones generated the highest MSP and ALS derived estimated

SWE. The largest physical area in WCW is at elevations located in the lower treeline category which was the most hydrologically productive in the watershed for both MSP and ALS-modelled SWE. Although MSP was lowest within the alpine zone, it still accounted for 18% of the QCC precipitation and 14% of ACIS precipitation. The ALS-modelled winter snowpack indicated a lower 11% of watershed SWE in the upper alpine zone suggesting that gravity and wind redistribution processes (Mott et al., 2018) transportation to lower elevations, which is consistent with findings of Grünewald et al. (2014). Simulated watershed wide MSP may systematically over-estimate snow accumulation and melt in upper elevations unless snowpack redistribution is accounted for. There are no precipitation gauges located fully within the alpine elevation zone. This is a concern for spatially distributed water resources assessment, since highly productive elevations are not monitored. Therefore, alternative methods are required to better understand and quantify water resources in these higher elevations.

Table 3.7: Estimated annual and mid winter WCW $MSP_{ACIS}$, $MSP_{QCC}$, and SWE water yield ($x10^6$ $m^3$) by valley (WFS, WC II, Cameron), treeline (generally between 1700 to 2200 masl, McCaffrey and Hopkinson (2021), low treeline: Gardiner, Akamina, high treeline: CMR), and alpine.

| | Valley | | Low Treeline | | High Treeline | | Alpine | | |
|---|---|---|---|---|---|---|---|---|---|
| Elevation Range (masl) | below 1700 | | 1700 - 2000 | | 2000 - 2200 | | above 2200 | | Total |
| WCW Area ($km^2$) | 34.79 | (34%) | 37.30 | (36%) | 20.64 | (20%) | 10.71 | (10%) | 103.44 |
| Annual $MSP_{ACIS}$ | 32.94 | (29%) | 40.90 | (36%) | 25.10 | (22%) | 14.16 | (13%) | 113.09 |
| Annual $MSP_{QCC}$ | 38.92 | (22%) | 63.80 | (36%) | 45.07 | 26%) | 27.87 | (16%) | 175.65 |
| Oct 1, 2019 - Mar 5, 2020 $MSP_{ACIS}$ | 16.75 | (26%) | 23.59 | (36%) | 15.54 | (24%) | 9.21 | (14%) | 65.08 |
| Oct 1, 2019 – Mar 5, 2020 $MSP_{QCC}$ | 21.57 | (18%) | 44.54 | (36%) | 34.12 | (28%) | 22.05 | (18%) | 122.28 |
| Mar 5, 2020 ALS SWE (mean) | 9.28 | (18%) | 22.77 | (44%) | 13.91 | (27%) | 5.64 | (11%) | 51.60 |
| Oct 1, 2020 – Mar 4, 2021 $MSP_{ACIS}$ | 16.38 | (25%) | 23.35 | (36%) | 15.48 | (24%) | 9.21 | (14%) | 64.41 |
| Oct 1, 2020 – Mar 4, 2021 $MSP_{QCC}$ | 21.62 | (18%) | 43.71 | (36%) | 33.27 | (28%) | 21.43 | (18%) | 120.03 |
| Mar 4, 2021 ALS SWE (mean) | 8.59 | (19%) | 19.10 | (43%) | 11.54 | (26%) | 5.01 | (11%) | 44.24 |

## 3.5 Conclusion

This study focused on the southwestern Alberta Canadian Rocky Mountain headwaters region to examine valley to alpine elevational precipitation gradients and seasonal patterns. The goal was to determine if EPG varied with season or between sites and therefore could be applied

across the southern Alberta eastern slopes for water resources or flood forecasting. Publicly available Alberta Climate Information Service (ACIS) and quality control corrected (QCC) precipitation datasets were compared with each other as well as to observed winter snowpack distributions. Castle (WFS-valley to CMR-alpine sites with a 730 m elevation range) exhibited a more systematic elevation control at a daily timestep. However, daily computed $EPG_{ACIS}$ and $EPG_{QCC}$ showed a considerable difference for Castle with most precipitation occurring in the winter snow season between Jan to Mar. At the end of each year, $EPG_{ACIS}$ and $EPG_{QCC}$ leveled off or became slightly lower since the alpine CMR site received less precipitation than the WFS valley site. $EPG_{ACIS}$ and $EPG_{QCC}$ for WLNP (Cameron-valley to Akamina-upper slopes with a 154 m elevation range) varied throughout the year although Akamina received more annual precipitation than Cameron.

There was a strong correlation of 0.96 between the Akamina and Cameron sites due to their proximity (1.3 km) and smaller elevation difference (154 m). CMR and WFS had the biggest difference in $Precip_{ACIS}$ and $Precip_{QCC}$ as well as the largest elevation range of 730 m which resulted in the lowest correlation of 0.54. There was a weak but slightly stronger correlation of 0.59 between CMR and Gardiner, despite being almost double the distance (7.2 km) relative to WFS (3.8 km), presumably due to the smaller elevation difference (190 m vs. 730 m). Taken together, these data suggest that precipitation depth correlations in this region weaken either with spatial or elevational separations exceeding on the order of ~2 km and ~200 m, respectively.

Monthly $EPG_{ACIS}$ between the proximal WFS and CMR sites confirm the expectation of increased precipitation with elevation during the winter months. An inverse $EPG_{ACIS}$ occurred in May, Aug, and Sep. $EPG_{QCC}$ from WFS to CMR showed an amplified winter EPG pattern and

inverse EPG in Aug and Sep for all three sites. Monthly precipitation depths did not increase linearly with elevation between all sites. A pronounced seasonality was observed in the precipitation data, but the signal was more subdued at the lower elevation sites as it related to the Castle and WLNP. Since a seasonality component was observed, a single year-round linear precipitation gradient is not valid, so any model of montane precipitation across the SW Alberta headwaters requires a seasonally variable EPG.

Large differences in $Precip_{ACIS}$ and $Precip_{QCC}$ depths and an inability to directly observe gauge losses mean it is virtually impossible to validate the accuracy of precipitation depths from a water resources perspective. However, an innovative comparison of hypsometric interpolations of winter $MSP_{ACIS}$ and $MSP_{QCC}$ records to two mid-winter ALS snow-covered sampling missions over the West Castle Watershed did allow a direct comparison of atmospheric precipitation to in situ snowpack accumulation. The most hydrologically productive elevation in WCW for both mid-winter spatialized precipitation and ALS-estimated water yield was at treeline elevations between 1700 – 2200 masl.

Given melt, sublimation and redistribution processes occur throughout the winter period, accumulated snowpack is expected to be lower than total cumulative precipitation. The $MSP_{ACIS}$ watershed total was ~14% greater than ALS-estimated SWE, $MSP_{QCC}$ provided a more reasonable difference to mid-winter SWE with exceedances of 37% for the Mar 2020 and 42% Mar 2021 throughout the elevation range. This suggests that while public records require correction to provide a better absolute estimate of atmospheric precipitation, neither corrected nor uncorrected precipitation records are a reliable basis for estimating in situ snowpack water yields in such montane environments.

## 3.6 References


Alberta Environment. (2010). Facts About Water in Alberta. In (pp. 68). Edmonton, AB: Government of Alberta.

Alberta Environment and Parks. (2019). *Alberta's River Forecast Centre: Awareness and Communication* Alberta Environment and Parks. https://rivers.alberta.ca/#

Avanzi, F., De Michele, C., Gabriele, S., Ghezzi, A., & Rosso, R. (2015). Orographic Signature on Extreme Precipitation of Short Durations. *Journal of Hydrometeorology*, *16*(1), 278-294. https://doi.org/10.1175/jhm-d-14-0063.1

Avanzi, F., Ercolani, G., Gabellani, S., Cremonese, E., Pogliotti, P., Filippa, G., Morra di Cella, U., Ratto, S., Stevenin, H., Cauduro, M., & Juglair, S. (2021). Learning about precipitation lapse rates from snow course data improves water balance modeling. *Hydrol. Earth Syst. Sci.*, *25*(4), 2109-2131. https://doi.org/10.5194/hess-25-2109-2021

Baghapour, B., Wei, C., & Sullivan, P. E. (2017). Numerical simulation of wind-induced turbulence over precipitation gauges. *Atmospheric Research*, *189*, 82-98. https://doi.org/https://doi.org/10.1016/j.atmosres.2017.01.016

Barnes, C., & Hopkinson, C. (2022a). Comparing Mountain Snowpack Depth Model Results from Different Airborne Laser Scanning Flight Path Samples. *Canadian Journal of Remote Sensing*, *48*(1), 81-92. https://doi.org/10.1080/07038992.2021.1999797

Barnes, C., & Hopkinson, C. (2022b). Quality Control Impacts on Total Precipitation Gauge Records for Montane Valley and Ridge Sites in SW Alberta, Canada. *Data*, *7*(6), 73. https://doi.org/https://doi.org/10.3390/data7060073

Barnes, C., Hopkinson, C., Porter, T., & Xi, Z. (2020). In-Situ LED-Based Observation of Snow Surface and Depth Transects. *Sensors*, *20*(8), 2292. https://www.mdpi.com/1424-8220/20/8/2292

Barros, A. P., & Kuligowski, R. J. (1998). Orographic Effects during a Severe Wintertime Rainstorm in the Appalachian Mountains. *Monthly Weather Review*, *126*(10), 2648-2672. https://doi.org/10.1175/1520-0493(1998)126<2648:Oedasw>2.0.Co;2

Box, G. E., Jenkins, G. M., Reinsel, G. C., & Ljung, G. M. (2015). *Time series analysis: forecasting and control*. John Wiley & Sons.

Campbell Scientific (Canada) Corp. (2011). GEONOR T-200B Series Precipitation Gauge. In (pp. 64). Campbell Scientific (Canada) Corp.

Collados-Lara, A.-J., Pardo-Igúzquiza, E., Pulido-Velazquez, D., & Jiménez-Sánchez, J. (2018). Precipitation fields in an alpine Mediterranean catchment: Inversion of precipitation gradient with elevation or undercatch of snowfall? *International Journal of Climatology*, *38*(9), 3565-3578. https://doi.org/https://doi.org/10.1002/joc.5517

Craig, J. R., Brown, G., Chlumsky, R., Jenkinson, R. W., Jost, G., Lee, K., Mai, J., Serrer, M., Sgro, N., Shafii, M., Snowdon, A. P., & Tolson, B. A. (2020). Flexible watershed simulation with the Raven hydrological modelling framework. *Environmental Modelling & Software*, *129*, 104728. https://doi.org/https://doi.org/10.1016/j.envsoft.2020.104728

Daly, C., Gibson, W. P., Taylor, G. H., Johnson, G. L., & Pasteris, P. (2002). A knowledge-based approach to the statistical mapping of climate. *Climate Research*, *22*(2), 99-113. https://www.int-res.com/abstracts/cr/v22/n2/p99-113

Daly, C., Halbleib, M., Smith, J. I., Gibson, W. P., Doggett, M. K., Taylor, G. H., Curtis, J., & Pasteris, P. P. (2008). Physiographically sensitive mapping of climatological temperature and precipitation across the conterminous United States. *International Journal of Climatology*, *28*(15), 2031-2064. https://doi.org/10.1002/joc.1688

Deems, J. S., Painter, T. H., & Finnegan, D. C. (2013). Lidar measurement of snow depth: a review. *Journal of Glaciology*, *59*(215), 467-479.

Essery, R., Li, L., & Pomeroy, J. (1999). A distributed model of blowing snow over complex terrain. *Hydrological Processes*, *13*(1415), 2423-2438.

Essery, R., Pomeroy, J., Parviainen, J., & Storck, P. (2003). Sublimation of Snow from Coniferous Forests in a Climate Model. *Journal of Climate*, *16*(11), 1855-1864. https://doi.org/10.1175/1520-0442(2003)016<1855:sosfcf>2.0.co;2

Galewsky, J. (2009). Rain shadow development during the growth of mountain ranges: An atmospheric dynamics perspective. *Journal of Geophysical Research: Earth Surface (2003–2012)*, *114*(F1). https://doi.org/10.1029/2008JF001085

Goodison, B. E., Louie, P. Y., & Yang, D. (1998). *WMO solid precipitation measurement intercomparison*. World Meteorological Organization Geneva, Switzerland.

Grinder, B. (2010). South Saskatchewan River Basin in Alberta Water Supply Study Summary. In SSRB Water Supply Study Steering Committee (Ed.), (pp. 24). Lethbridge, AB: Alberta Agriculture and Rural Development.

Grünewald, T., Bühler, Y., & Lehning, M. (2014). Elevation dependency of mountain snow depth. *The Cryosphere*, *8*(6), 2381-2394.

Grünewald, T., Schirmer, M., Mott, R., & Lehning, M. (2010). Spatial and temporal variability of snow depth and SWE in a small mountain catchment. *The Cryosphere*, *4*(ARTICLE), 215-225.

Haiden, T., & Pistotnik, G. (2009). Intensity-dependent parameterization of elevation effects in precipitation analysis. *Advances in Geosciences*, *20*, 33-38.

Hancock, H., Prokop, A., Eckerstorfer, M., & Hendrikx, J. (2018). Combining high spatial resolution snow mapping and meteorological analyses to improve forecasting of destructive avalanches in Longyearbyen, Svalbard. *Cold Regions Science and Technology*, *154*, 120-132. https://doi.org/https://doi.org/10.1016/j.coldregions.2018.05.011

Hopkinson, C., & Barnes, C. (2022). *Precipitation gauge and supplemental weather station data for three Oldman River headwater locations in SW Alberta. Federated Research Data Repository*. https://doi.org/10.20383/102.0551

Hopkinson, C., Collins, T., Anderson, A., Pomeroy, J., & Spooner, I. (2012). Spatial Snow Depth Assessment Using LiDAR Transect Samples and Public GIS Data Layers in the Elbow River Watershed, Alberta. *Canadian Water Resources Journal / Revue canadienne des ressources hydriques*, *37*(2), 69-87. https://doi.org/10.4296/cwrj3702893

Hopkinson, C., Hayashi, M., & Peddle, D. (2009). Comparing alpine watershed attributes from LiDAR, Photogrammetric, and Contour-based Digital Elevation Models. *Hydrological Processes*, *23*(3), 451-463. https://doi.org/doi:10.1002/hyp.7155

Hopkinson, C., Sitar, M., Chasmer, L., & Treitz, P. (2004). Mapping Snowpack Depth beneath Forest Canopies Using Airborne Lidar. *Photogrammetric Engineering & Remote Sensing*, *70*(3), 323-330. https://doi.org/10.14358/PERS.70.3.323

Houze, R. A. (2012). Orographic effects on precipitating clouds. *Reviews of Geophysics*, *50*(1). https://doi.org/10.1029/2011RG000365

Jeong, H.-G., Ahn, J.-B., Lee, J., Shim, K.-M., & Jung, M.-P. (2020). Improvement of daily precipitation estimations using PRISM with inverse-distance weighting. *Theoretical and Applied Climatology*, *139*(3), 923-934. https://doi.org/10.1007/s00704-019-03012-6

Kinar, N. J., & Pomeroy, J. W. (2015). Measurement of the physical properties of the snowpack. *Reviews of Geophysics*, *53*(2), 481-544. https://doi.org/10.1002/2015RG000481

Kochendorfer, J., Nitu, R., Wolff, M., Mekis, E., Rasmussen, R., Baker, B., Earle, M. E., Reverdin, A., Wong, K., & Smith, C. D. (2017). Analysis of single-Alter-shielded and unshielded measurements of mixed and solid precipitation from WMO-SPICE.

Kochendorfer, J., Rasmussen, R., Wolff, M., Baker, B., Hall, M. E., Meyers, T., Landolt, S., Jachcik, A., Isaksen, K., & Brækkan, R. (2017). The quantification and correction of wind-induced precipitation measurement errors. *Hydrology and Earth System Sciences*, *21*(4), 1973-1989.

Leeper, R. D., Palecki, M. A., & Davis, E. (2015). Methods to Calculate Precipitation from Weighing-Bucket Gauges with Redundant Depth Measurements. *Journal of Atmospheric and Oceanic Technology*, *32*(6), 1179-1190. https://doi.org/10.1175/jtech-d-14-00185.1

Li, L., & Pomeroy, J. W. (1997). Estimates of Threshold Wind Speeds for Snow Transport Using Meteorological Data. *Journal of Applied Meteorology*, *36*(3), 205-213. https://doi.org/10.1175/1520-0450(1997)036<0205:eotwsf>2.0.co;2

López-Moreno, J. I., Fassnacht, S. R., Heath, J. T., Musselman, K. N., Revuelto, J., Latron, J., Morán-Tejeda, E., & Jonas, T. (2013). Small scale spatial variability of snow density and depth over complex alpine terrain: Implications for estimating snow water equivalent. *Advances in water resources*, *55*, 40-52. https://doi.org/https://doi.org/10.1016/j.advwatres.2012.08.010

Luce, C. H., Abatzoglou, J. T., & Holden, Z. A. (2013). The Missing Mountain Water: Slower Westerlies Decrease Orographic Enhancement in the Pacific Northwest USA. *Science*, *342*(6164), 1360-1364. https://doi.org/10.1126/science.1242335

Lundquist, J. D., Hughes, M., Henn, B., Gutmann, E. D., Livneh, B., Dozier, J., & Neiman, P. (2015). High-Elevation Precipitation Patterns: Using Snow Measurements to Assess Daily Gridded Datasets across the Sierra Nevada, California. *Journal of Hydrometeorology*, *16*(4), 1773-1792. https://doi.org/doi:10.1175/JHM-D-15-0019.1

MacDonald, R. J., Byrne, J. M., Boon, S., & Kienzle, S. W. (2012). Modelling the potential impacts of climate change on snowpack in the North Saskatchewan River Watershed, Alberta. *Water resources management*, *26*(11), 3053-3076.

McCaffrey, D., & Hopkinson, C. (2021). Modeling Watershed-Scale Historic Change in the Alpine Treeline Ecotone Using Random Forest. *Canadian Journal of Remote Sensing*. https://doi.org/10.1080/07038992.2020.1865792

Mekis, E., Donaldson, N., Reid, J., Zucconi, A., Hoover, J., Li, Q., Nitu, R., & Melo, S. (2018). An Overview of Surface-Based Precipitation Observations at Environment and Climate Change Canada. *Atmosphere-Ocean*, *56*(2), 71-95. https://doi.org/10.1080/07055900.2018.1433627

Mott, R., Scipión, D., Schneebeli, M., Dawes, N., Berne, A., & Lehning, M. (2014). Orographic effects on snow deposition patterns in mountainous terrain. *Journal of Geophysical Research: Atmospheres*, *119*(3), 1419-1439. https://doi.org/doi:10.1002/2013JD019880

Mott, R., Vionnet, V., & Grünewald, T. (2018). The Seasonal Snow Cover Dynamics: Review on Wind-Driven Coupling Processes [Review]. *Frontiers in Earth Science*, *6*(197). https://doi.org/10.3389/feart.2018.00197

Newton, B. W., Farjad, B., & Orwin, J. F. (2021). Spatial and Temporal Shifts in Historic and Future Temperature and Precipitation Patterns Related to Snow Accumulation and Melt Regimes in Alberta, Canada. *Water*, *13*(8), 1013. https://www.mdpi.com/2073-4441/13/8/1013

Nitu, R. (2010). *CIMO Survey on National Summaries of Methods and Instruments for Solid Precipitation Measurement at Automatic Weather Stations, IOM 102, TD1544*.

OTT Hydromet GmbH. (2019). Operating Instructions OTT Pluvio2 precipitation gauge. In (pp. 60). Kempten, Germany: OTT Hydromet GmbH.

Pan, X., Yang, D., Li, Y., Barr, A., Helgason, W., Hayashi, M., Marsh, P., Pomeroy, J., & Janowicz, R. J. (2016). Bias corrections of precipitation measurements across experimental sites in different ecoclimatic regions of western Canada. *The Cryosphere*, *10*(5), 2347-2360.

Peixeiro, M. (2022). *Time Series Forecasting in Python*. Manning Publications Co.

Pickering, R. (2018). *Snow Surveying Field Sampling Protocols*. Alberta Environment and Parks. http://environmentalmonitoring.alberta.ca/resources/standards-and-protocols/

Pomeroy, J. W., Gray, D. M., Shook, K. R., Toth, B., Essery, R. L. H., Pietroniro, A., & Hedstrom, N. (1998). An evaluation of snow accumulation and ablation processes for land surface modelling. *Hydrological Processes*, *12*(15), 2339-2367. https://doi.org/10.1002/(SICI)1099-1085(199812)12:15<2339::AID-HYP800>3.0.CO;2-L

Rasmussen, R., Baker, B., Kochendorfer, J., Meyers, T., Landolt, S., Fischer, A. P., Black, J., Thériault, J. M., Kucera, P., Gochis, D., Smith, C., Nitu, R., Hall, M., Ikeda, K., & Gutmann, E. (2012). How Well Are We Measuring Snow: The NOAA/FAA/NCAR Winter Precipitation Test Bed. *Bulletin of the American Meteorological Society*, *93*(6), 811-829. https://doi.org/10.1175/bams-d-11-00052.1

Roe, G. H. (2005). OROGRAPHIC PRECIPITATION. *Annual Review of Earth and Planetary Sciences*, *33*(1), 645-671. https://doi.org/10.1146/annurev.earth.33.092203.122541

Roe, G. H., & Baker, M. B. (2006). Microphysical and Geometrical Controls on the Pattern of Orographic Precipitation. *Journal of the Atmospheric Sciences*, *63*(3), 861-880. https://doi.org/10.1175/jas3619.1

Ross, A., Smith, C. D., & Barr, A. (2020). An improved post-processing technique for automatic precipitation gauge time series. *Atmos. Meas. Tech.*, *13*(6), 2979-2994. https://doi.org/10.5194/amt-13-2979-2020

Rotunno, R., & Houze, R. A. (2007). Lessons on orographic precipitation from the Mesoscale Alpine Programme. *Quarterly Journal of the Royal Meteorological Society*, *133*(625), 811-830. https://doi.org/https://doi.org/10.1002/qj.67

Schindler, D. W., & Donahue, W. F. (2006). An impending water crisis in Canada's western prairie provinces. *Proceedings of the National Academy of Sciences*, *103*(19), 7210-7216. https://doi.org/doi:10.1073/pnas.0601568103

Smith, C. D., Ross, A., Kochendorfer, J., Earle, M. E., Wolff, M., Buisán, S., Roulet, Y. A., & Laine, T. (2020). Evaluation of the WMO Solid Precipitation Intercomparison Experiment (SPICE) transfer functions for adjusting the wind bias in solid precipitation measurements. *Hydrol. Earth Syst. Sci.*, *24*(8), 4025-4043. https://doi.org/10.5194/hess-24-4025-2020

Smith, R. (1981). The influence of mountains on the atmosphere: recent advances. *Nowcasting: Mesoscale Observations and Short-Range Prediction*, *165*, 37.

Smith, R. B. (2019). 100 years of progress on mountain meteorology research. *Meteorological Monographs*, *59*, 20.21-20.73.

Veatch, W., Brooks, P. D., Gustafson, J. R., & Molotch, N. P. (2009). 'Quantifying the effects of forest canopy cover on net snow accumulation at a continental, mid-latitude site'. *Ecohydrology*, *2*(2), 115-128. https://doi.org/10.1002/eco.45

Vionnet, V., Marsh, C. B., Menounos, B., Gascoin, S., Wayand, N. E., Shea, J., Mukherjee, K., & Pomeroy, J. W. (2021). Multi-scale snowdrift-permitting modelling of mountain snowpack. *The Cryosphere*, *15*(2), 743-769.

Wang, J. Y., Whitfield, P. H., & Cannon, A. J. (2006). Influence of Pacific climate patterns on low-flows in British Columbia and Yukon, Canada. *Canadian Water Resources Journal*, *31*(1), 25-40.

Waterton Lakes National Park. (2017). Kenow Fire: Burn severity map. In (pp. 1). Parks Canada. https://www.pc.gc.ca/en/pn-np/ab/waterton/nature/environment/feu-fire/feu-fire-kenow/brulage-burn

Wolff, M., Isaksen, K., Petersen-Øverleir, A., Ødemark, K., Reitan, T., & Brækkan, R. (2015). Derivation of a new continuous adjustment function for correcting wind-induced loss of solid precipitation: results of a Norwegian field study. *Hydrology and Earth System Sciences*, *19*(2), 951-967.

Wright, R. (2021a). *Current and Historical Alberta Weather Station Data* Alberta Climate Information Service (ACIS). http://agriculture.alberta.ca/acis/alberta-weather-data-viewer.jsp

Wright, R. (2021b). Geonor Corrections. In. Edmonton, AB: Alberta Agriculture and Forestry.

Wright, R. (2021c). *Weighing gauge time series analysis and noise filtering tool*. In Alberta Agriculture and Forestry.

Zhang, Z., Glaser, S., Bales, R., Conklin, M., Rice, R., & Marks, D. (2017). Insights into mountain precipitation and snowpack from a basin-scale wireless-sensor network. *Water Resources Research*, *53*(8), 6626-6641. https://doi.org/https://doi.org/10.1002/2016WR018825

# 4 In-Situ LED-Based Observation of Snow Surface and Depth Transects


## Abstract

As part of a new snowpack monitoring framework, this study evaluated the feasibility of using an LED LIDAR (Leddar) time of flight sensor for snowpack depth measurement. The Leddar sensor has two additional features over simple sonic ranging sensors: (i) the return signal is divided into 16 segments across a 48° field of view, each recording individual distance-to-target (DTT) measurements; (ii) an index of reflectance or intensity signal is recorded for each segment. These two features provide information describing snowpack morphology and surface condition. The accuracy of Leddar sensor DTT measurements for snow depth monitoring was found to be < 20 mm, which was better than the 50 mm quoted by the manufacturer, and the precision was < 5 mm. Leddar and independent sonic ranger snow depth measurement showed strong linear agreement ($r^2$ = 0.98). There was also a strong linear relationship ($r^2$ = 0.98) between Leddar and manual field snow depth measurements. The intensity signal response was found to correlate with snow surface albedo and inversely with air temperature ($r$ = 0.77 and −0.77, respectively).



**Citation:**

Barnes, C., Hopkinson, C., Porter, T., & Xi, Z. (2020). In-Situ LED-Based Observation of Snow Surface and Depth Transects. *Sensors*, *20*(8), 2292. https://www.mdpi.com/1424-8220/20/8/2292

**Author Contributions:**

Conceptualization: Chris Hopkinson and Celeste Barnes
Methodology: Celeste Barnes
Software: Zhouxin Xi
Validation: Chris Hopkinson
Formal analysis: Celeste Barnes
Investigation, Celeste Barnes, Chris Hopkinson, Thomas Porter, and Zhouxin Xi
Resources: Chris Hopkinson
Data curation, Celeste Barnes, Thomas Porter, and Zhouxin Xi
Writing - original draft preparation: Celeste Barnes
Writing - review and editing: Celeste Barnes and Chris Hopkinson
Visualization: Celeste Barnes
Supervision: Chris Hopkinson
Project administration: Chris Hopkinson
Funding acquisition: Chris Hopkinson
All of the authors have read and agreed to the published version of the manuscript.



## 4.1 Introduction

Wintertime snow accumulation and associated snowmelt provide a significant contribution to water resources in regions with seasonal snow packs (Natural Resources Canada, 2010) as surface water is "locked up" in a frozen storage state (Barrows & Horton, 1907; Paznekas & Hayashi, 2016). Snow depth and density measurements are required to quantify the amount of snow water equivalent (SWE) that will be released from the snowpack at the time of melt. Of the two variables, snow depth is the major component of SWE (Grünewald et al., 2010). Alberta Rocky Mountain headwater snowpack monitoring (Government of Alberta, 2018) has been operational for several decades, using both destructive and non-destructive techniques (Kinar & Pomeroy, 2015). A snow probe and weighing tube are used to obtain field validation

depth and SWE (López-Moreno et al., 2013; Pickering, 2018). This provides an accurate single point measurement but disturbs the snowpack in the process, making future measurements difficult to repeat at the same location. The second operational monitoring method in the headwaters uses non-destructive sonic ranging devices (Campbell, 2018) to measure snowpack depth (Gubler, 1981; Ryan et al., 2008). Such units can be mounted on a tower pointing over the ground surface. Ultrasonic pulses are emitted and echoes are received by the sensor. The return signal is used to calculate snow depth by differencing distance-to-target (DTT) measurements when the snow surface is present from the DTT observation of the no-snow ground surface, following air temperature compensation. These sensors have a high degree of accuracy, but depth is an average obtained from the total sensor footprint (the further from the target, the larger the footprint) including undulations in the ground and snow surface. Snowpack depth is continuously recorded over the snow season. Sonic ranging sensors do not describe the snowpack morphology, structure, or density characteristics.

The intent of this study was to examine a low-cost (≈1000 Canadian dollars) and low-power (4 watt) alternative to the contemporary sonic ranging snow depth sensor. The low-cost low-power Leddar Tech IS16 (hereafter referred to as Leddar) sensor is a LIDAR (light detection and ranging) based “time of flight” device. It emits a single LED (light emitting diode)-diffused light source beam in the near infra-red (NIR) 940 nm wavelength. The return signal is divided into 16 segments. Both temperature compensated DTT and light intensity are observed and measured for each segment. The Leddar unit has added features over the sonic ranging sensor, those being a DTT and intensity response for each of the 16 segments of its footprint. There is limited light transmission into the surface of natural snowpacks (Warren, 2019), making LED technology an ideal candidate for snow depth monitoring by calculating the difference of the

DTT snow surface from the bare earth DTT. Sonic ranging sensor pulses penetrate freshly fallen snow, producing an underestimation of snowpack depth (Fischer, 2011; Ryan et al., 2008). Beyond evaluating the potential to observe snow surface height and snowpack depth, a further goal of this study is to evaluate which, if any, snowpack features can be inferred from the additional intensity signal attribute collected by LED ranging sensors.

The snowpack surface texture and reflectance change over time as the pack evolves due to increasing and decreasing depths from snow accumulation, ablation, compaction, and wind/gravity-induced redistribution (Essery et al., 1999; Pomeroy et al., 1998). As the snowpack evolves, variation in crystal grain size and structure (Deems et al., 2013; Seidel et al., 2016; Warren, 1982), density, and the amount of water within the pack occurs (Eppanapelli et al., 2018; Hannula & Pulliainen, 2019). Ice lenses form within the pack during melt and refreeze cycles (Kinar & Pomeroy, 2015). Impurities such as dust or dirt settle in the snowpack (Hannula & Pulliainen, 2019). Coalesced and/or wet snow has a lower albedo than freshly accumulated snow (Peltoniemi et al., 2005). As the snowpack ages and eventually becomes isothermal, the reflectance signature changes (Kulkarni et al., 2002; Negi et al., 2010).

The spectral response or albedo of snow is dependent on snow crystal grain size, age of the snow, and amount of water and impurities in the pack (Warren, 2019). This causes the spectral response to be different at various stages of metamorphism. “Fresh” new snow produces the highest spectral reflectance over aging snow, soils, and vegetation (Warren, 1982) in the 940 nm band, in which the Leddar unit operates. At the 940 nm band, spectral albedo ranges from approximately 0.5 to 0.9. The continuous spatiotemporal intensity signal has the potential to be used to detect changes in snowpack surface characteristics. For example, it should be possible to use the intensity signature to detect when snow is falling on the pack’s surface, since fresh snow

has a higher reflectance than older snow. These variations in the snowpack should be detectable in the Leddar's DDT and intensity signals. The expectation is to see an increase in the spectral response for new snow accumulation and a decrease as the snowpack compacts and metamorphoses over time.

This study assessed the performance and features of the Leddar sensor. The objectives were to: (1) examine the Leddar sensor performance and the controls on the Leddar intensity signal; (2) compare the continuous temporal snowpack depth measurements of the Leddar with a standard sonic ranging sensor and infrequent field depth data observations to quantify sensor precision and accuracy for this particular application.

## 4.2 Materials and Methods

### 4.2.1 Leddar and SR50A Sensor Specifications

The Leddar and SR50A sonic ranging sensors used in this study each capture DTT measurements. An approximation of the respective Leddar and SR50A DTT sampling areas is shown in Figure 4.1a. The LeddarTech IS16 sensor (Figure 4.1b) is a solid-state, pulse-based, time-of-flight LED LIDAR ranging instrument that receives return signals on a 16-channel photodetector (LeddarTech Inc., 2018). The unit's internal processing chip performs a full waveform analysis on all segments of the return signal. When the "object demerging" feature is enabled, it is possible for the sensor to detect multiple objects at varying distances and intensities within its field of view (FOV). LED technology is sensitive to ambient temperature (Kipp et al., 2014), and an inverse relationship exists between external temperature and light output (illumination) (Bullough, 2003). A temperature sensor is located on the Leddar circuit board near

the emitter optics (LeddarTech Inc., 2018; Olivier, 2016). Proprietary algorithms compensate for this temperature sensitivity and are used to calculate distance measurements within the manufacturer's specified precision and accuracy (Messiaen, 2019).

The photodetector chip on the Leddar sensor has limited distance detection (Olivier, 2016) and uses the intensity (amount of light captured by the receiver) property as part of the calculation for detecting multiple objects at varying distances within the FOV. The Leddar sensor range is zero to 50 m (Table 4.1). The sensor has a 48° × 8° sampling FOV. The ground surface footprint (seen in Figure 4.1a) is dependant on the height of the sensor above the target and defined by the beam length and depth. The length of the beam on the ground is 0.89 multiplied by the distance to the target. Each segment is 1/16 of the total beam length. The depth of the beam is 0.14 multiplied by the distance of the sensor to the target.


(**a**) (**b**)

Figure 4.1. (a) Leddar and SR50A sonic ranging device co-located on a tower. Approximation of sensor beam footprint; not to scale. Leddar segment 1 orientation is the north side of the tower. The sensor emits defuse LED light and receives return signals for 16 segments. The ground surface footprint is dependant on the height of the sensor above the target, and the beam length and depth. (b) LeddarTech IS16 pulsed based time of flight LED LIDAR sensor logging to a Raspberry Pi 3.

LeddarTech technology is used for industrial applications, such as vehicle collision detection, in which fast response times from the sensor are required (Olivier, 2016). The distance measurement accuracy reported by the manufacturer is 50 mm, the precision of the sensor (if the intensity return signal is greater than the manufacturer's specification of 15) is 6 mm, and the resolution is 10 mm. For this study, the Leddar sensor was statically mounted over the ground surface at a fixed height of 2.93 m with a calculated beam length of 2.61 m (each segment length is 0.16 m) and depth of 0.41 m. In comparison, the SR50A sensor emits ultrasonic pulses. The sensor's footprint on the ground surface is circular with an approximate radius of 0.27 multiplied by the height of the sensor above the target surface. A temperature corrected measurement for DTT is averaged over the entire footprint as a single reading. The distance range of the SR50A is 0.5 to 10 m. The SR50A DTT measurement accuracy as reported by the manufacturer is 12 mm on a 3 m high mount, and the resolution is 0.25 mm. A comparison of the technical specifications of Leddar and SR50A units is shown in Table 4.1.

Table 4.1. Leddar and SR50A sonic ranger manufacturer technical specifications (Campbell Scientific (Canada) Corp., 2016; LeddarTech Inc., 2018).

| Sensor | Leddar IS16 | SR50A Sonic Ranging Device |
|---|---|---|
| Type | Leddar LED Multichannel LIDAR sensor, built-in processing chip performing proprietary temperature adjusted Full-Waveform analysis for multi-object detection distance measurement | SR50AA Sonic Ranging Sensor with independent temperature compensation |
| Manufacturer | LeddarTech Inc. | Campbell Scientific (Canada) Corp. |
| Distance | 0 to 50 m | 0.5 to 10 m |
| Operating Temp | −40 °C to +50 °C | −45 °C to +50 °C |
| Accuracy | ±50 mm Quoted for a moving target | ±10 mm or 0.4% of DDT (greater value) |
| Precision | 6 mm (manufacturer specification if intensity > 15) | |
| Resolution | 10 mm | 0.25 mm |
| Measurement Rate | Up to 50 Hz | Less than 1.0 second |
| Emitter | Single LED diffused light source beam | Sonic Ranging ultrasonic pulses |
| Receiver | Measurement of backscatter on a 16-Channel photodetector array | Listening for return echoes |
| Beam Length | 48° (Distance from sensor * 0.8905) | 30° (Radius = 0.268 * Height) |
| Segment Length | 1/16 of the Beam Length (Beam Length / 16) | N/A |
| Beam Depth | 8° (Distance from sensor * 0.1402) | N/A |
| Wavelength | 940 nm (infrared) | 50 kHz (Ultrasonic) electrostatic transducer |

### 4.2.2 Field Deployment Setup, Configuration, and Data

Leddar and SR50A instrument testing and snowpack validation were completed at the University of Lethbridge West Castle Field Station (WFS), located in the headwaters of the Oldman River Basin, Alberta, Canada from 2017 (December 14) to 2018 (April 27). The Leddar unit was mounted on the weather station tower coincident with a SR50A such that the beams of the two sensors partially overlapped, as shown in Figure 4.1a. The ground surface beneath the Leddar and SR50A sensors had a downward slope of 0.07 m over a distance of 3.0 m. Meteorological data was collected at the tower site for wind speed, wind direction, temperature (temp), barometric pressure (BP), relative humidity (RH), and incoming and reflected shortwave (SW) and longwave (LW) radiation (Figure 4.2). A temperature sensor under the Leddar unit at the ground surface collected ground temperature. A totalizing precipitation gauge located nine meters south of the tower provided cumulative precipitation data.

To validate Leddar and SR50A sensor snow depth measurements, eleven site visits took place from December 21 to April 27. Biweekly to monthly field measurements occurred during the months of December to March. At the onset of snowmelt, sampling was done at a weekly to daily time interval. Snow depth field measurements using a graduated avalanche probe were taken by standing behind the tower out of the sensor field of view and sampled directly under the Leddar unit. Field depth measurements collocated and coincident in time with the Leddar deployment were collected to support and validate both the Leddar and SR50A measurements. Leddar, SR50A, and meteorological data were extracted from the 15-minute timestep dataset for a four-hour time period when field measurements occurred. The mean, minimum, and maximum were calculated for the SR50A. The mean for the Leddar was derived from the mean value of all

segments. Minimum and maximum were extracted based on the range of values from all segments of the Leddar sensor.

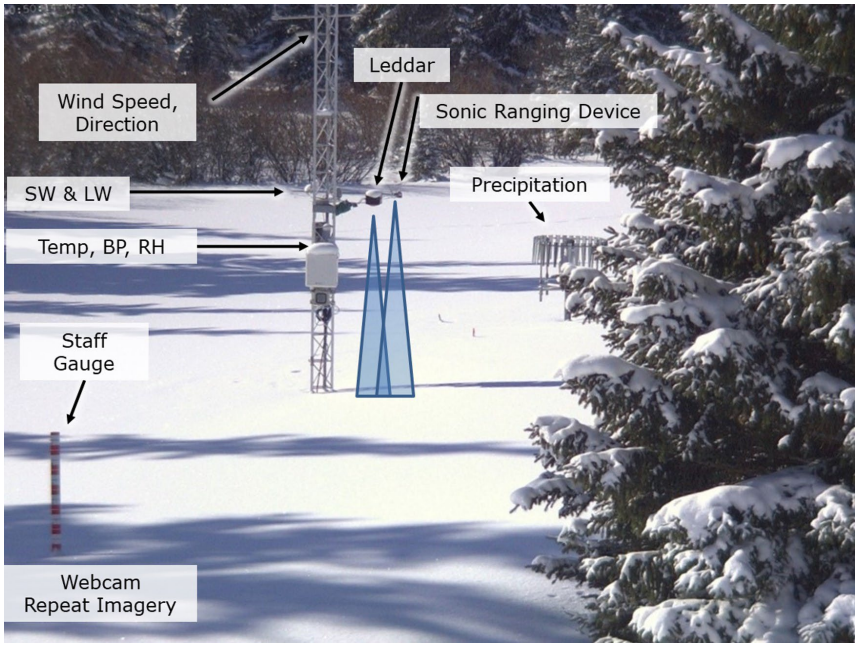


Figure 4.2. The West Castle Field Station tower and snow depth monitoring sensors (Leddar and SR50A), the totalizing precipitation gauge located south of the tower, and the meteorological sensors for the 2017–2018 snow season collecting wind speed, wind direction, air temperature (temp), barometric pressure (BP), relative humidity (RH), and incoming and reflected shortwave (SW) and longwave (LW) radiation. A temperature sensor was located at the ground surface to collect ground temperature.

#### 4.2.2.1 LeddarTech IS16 (Leddar) Configuration and Laboratory Calibration

The Leddar configuration settings determine the accuracy, precision, and resolution of the emitted and return signals for DTT and intensity measurements (Figure 4.2). The Leddar's LED pulse rate is 102.4 kHz. The parameter configuration selected maximized the accuracy and precision of object detections that resulted in a maximum range of 21.3 m (LeddarTech Inc., 2018). "Crosstalk removal" and "object demerging" were both enabled to reduce return signal degradation from objects detected in other segments.

The control and logger system for the Leddar sensor had a similar design to that of (Xi et al., 2019), wherein the Leddar unit was used for 3D digital canopy foliage sampling. The Leddar

unit (Figure 4.1b) was connected to a Raspberry Pi 3 (RP) running the Raspbian OS through a 2.0, 12 Mbits/s USB cable (Figure 4.3). A computer program (Xi, 2017) executed Leddar SDK (software development kit) commands to obtain DTT, intensity, and status flag for a 15-minute time step. At the start of the collection interval, the Leddar unit was "turned on" to acquire continuous pulse measurements for a period of one minute. For each measurement, the 16-channel photodetector divided the return signal into separate segments where a full waveform analysis was performed by the Leddar onboard processing chip. The resulting measurement was returned to the RP. The program then went into a "wait" state for the next 14 minutes.

The RP program converted Leddar range measurements (R) into vertical distance ($V_T$) (Baltsavias, 1999) values using Equation (4.1).

$$V_T = (R_i + R_c)\cos(\varphi)\cos(\alpha + \beta(i-8.5) + \gamma(i-8.5)^2) \quad (4.1)$$

$R_i$ is the range measurement of the $i^{th}$ segment, $R_c$ is the fixed shift of the range measurement from the true range, $\varphi$ is the fixed zenith boresight shift, $\alpha$ is the azimuth boresight shift, $\beta$ is the $i^{th}$ segment's angle deviation from the boresight on Leddar beam plane, and $\gamma$ is the $2^{nd}$ order non-linear angle deviation (8.5 is the offset to the center of segments 1 to 16). Leddar calibration parameters were determined in the laboratory. The Leddar unit was mounted facing a flat level reference surface with no zenith deviation ($\varphi = 0$). Measurements were taken at varying boresight angles ($\alpha$) and vertical distances ($V_T$) from Leddar optical emitter center to the reference surface. $R_c$, $\alpha$, $\beta$, and $\gamma$ are the calibration parameters. $V_T$, $R_i$, and $\varphi$ are known values. This made it possible to infer $R_c$, $\beta$, and $\gamma$ from Equation (4.1) based on the Gauss–Newton

algorithm with Huber robust function (Binder & Kostina, 2013) to get the best parameter fit in order to evaluate the accuracy of the Leddar measurement.

Table 4.2. Leddar measurement configuration settings used for the 2017–2018 snow season.

| Parameter | Configuration | Description |
|---|---|---|
| Distance Units | cm | Unit of measurement for distance to target |
| Accumulations | 1024 | Range: 0 to 1024. Higher values enhance the range for DTT below 10 m, reduce the measurement rate and noise |
| Measurement Rate | 1.5625 Hz | Range: 1.5625 to 50 Hz. Rate of signal measurement. Lower values give highest accuracy and precision (also known as Refresh Rate) |
| Oversampling | 8 | Range: 1–8. High values reduce measurement rate and increase accuracy |
| Point Count | 12 | The number of base sample points |
| Threshold Offset | 0.00 | Range: −5% to 100%. Modifies intensity threshold. At 100%, no detections. Negative values increase likelihood of false measurements. |
| LED Control | Automatic | LED power level setting |
| Change Delay | 1 (640 ms) | Number of measurements before sensor changes LED power level |
| Object Demerging | Enabled | Indicates detection of multiple objects in return signal |
| Crosstalk Removal | Enabled | Degradation compensation from object detections in other segments |
| Useful Range | 21.3 m | Leddar sensor computed value based on configuration settings |

Two data files were created: the first containing the raw measurements per pulse for each of the 16 segments stored on the RP (see Figure 4.3 *raw.txt Data File at the top right of the diagram); the second created from the downloaded raw RP data file through a post-processing step. The raw RP data file contained a record for each segment number, timestamp, $V_T$, intensity, and status flag of the return signal. For each of the 16 segments, two possible status flags could be received, those being “Flag = 1” and “Flag = 35.” Depending on the status flag received for the measurement cycle, the program captured between 20 to 60 observations for the 15-minute time interval. The post processing step creates a single record in the second data file for each 15-minute collection interval using the raw RP data as the input file. The record contains the timestamp; and for each segment the record is appended to include segment number, the mean distance to target and intensity for each flag, the count of the number of measurements for each

flag, the total number of measurements, and a percentage of the number of "Flag = 1" returns for the given 15-minute measurement interval (see Figure 4.3 *Final.csv Data File at the bottom left of the diagram).

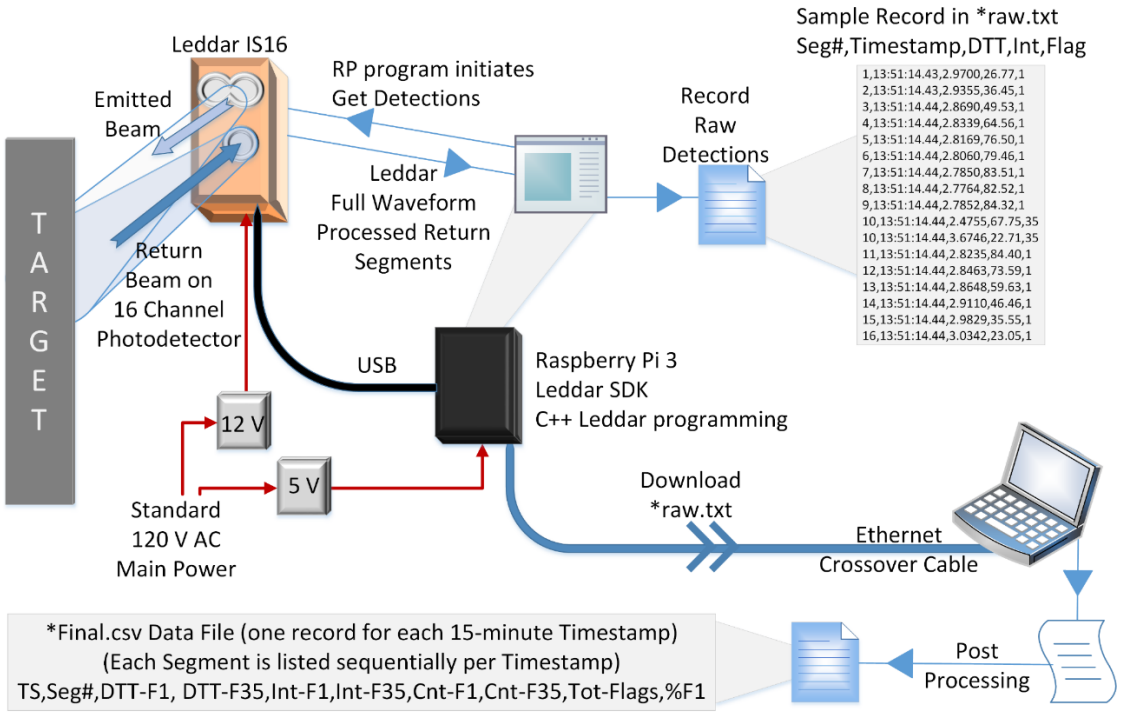


Figure 4.3. Data flow diagram of the Leddar-Raspberry Pi for the 2017−2018 Snow Season. TS refers to timestamp, Seg# refers to segment number, DTT-F# is the distance to target for flag number, Int-F# is the intensity for flag number, Cnt-F# is the number of returns received for the status flag number, Tot-Flags is the total count of both flag numbers, and %F1 is the percentage of Flag = 1 returns for the segment.

The Leddar's on-board processing chip computes status "Flag = 1" as a valid return signal of a single object detected in the emitted beam. "Flag = 35" is a valid return but is interpreted by the sensor as more than one object detected within the same segment as a result of the enabled "object demerging" configuration setting. "Flag = 35" is considered noise in the data due to an implicit assumption that no objects should exist between the statically mounted Leddar sensor and the ground or snowpack surface. These measurements are retained in the final post processed data file, but they are not used for the snowpack depth calculation. The presence of

"Flag = 35" does not mean all data for a given segment are invalid. If the timestamp contains data with the "Flag = 1" status, a valid return signal has been received for the specific segment. As part of the quality control process, the "noisy" (Flag = 35) $V_T$ and intensity values are discarded from the specific segment. The count of noisy returns is retained and used in the analysis.

#### 4.2.2.2 SR50A Sonic Ranging Device

The SR50A was configured using a Campbell Scientific CR1000 data logger (Campbell Scientific (Canada) Corp., 2016) with standardized temperature-adjusted programming for a 15-minute data collection interval for the distance to target measurement. Real-time temperature compensation is performed using the temperature sensor located adjacent to the Leddar and SR50A on the instrument tower (Figure 4.2).

#### 4.2.2.3 Meteorological Sensors

Quality assurance corrections were applied to the complete meteorological dataset. The totalizing precipitation weighing gauge accumulates rain and snow in a catchment bucket. It is susceptible to diurnal and long-term drift, evaporation, the under-catch of snow caused by wind during a precipitation event, and the over-catch from blowing snow (Earle et al., 2014; Kochendorfer et al., 2018). Totalizing precipitation weighing gauge data adjustments followed the methodology described by (Leeper et al., 2015; Pan et al., 2016). Initial manual cleaning was completed to correct gauge measurements resulting from sensor maintenance tasks such as

emptying liquid when the catchment bucket was full. To correct for diurnal, long term drift, and evaporation, negative and small positive changes were removed using a threshold of 0.11 mm unless a precipitation event was in progress in prior and subsequent measurements. To reduce overestimation of under catch above the sensor, the correction of the wind field was limited to speeds greater than 1.2 $ms^{-1}$ and less than 6.5 $ms^{-1}$. Precipitation measurements were calculated using the change in the catchment bucket volume from the previous measurement.

Incoming shortwave radiation (SWI) and reflected shortwave radiation (SWR) were collected from a Campbell Scientific CNR1 (Campbell Scientific (Canada) Corp., 2015) net radiometer mounted on the same tower as the Leddar and SR50A units. CNR1 SWI and SWR data were used to calculate albedo (ratio of SWR over SWI) for both a one-hour and daily averaged interval. Measurements greater than one were discarded as SWI must always be greater than SWR. Undulations in the snow surface or other highly reflective objects in close proximity to the CNR1 can produce additional backscatter that is recorded by the sensor (Mannstein, 1985). There were five days when the albedo calculation was greater than one. For those days, daily albedo was computed using the mean from the previous and subsequent day.

### 4.2.3 Aggregated Datasets for Analysis

The final post-processed 15-minute dataset contained 12,844 records. Snow depth ($D_{snow}$) was calculated for each of the Leddar segments and SR50A sensors by subtracting the baseline "no-snow" ($V_o$ = 2.93 m) ground measurements from subsequent "snow" surface ($V_T$) measurements (Equation (4.2)). The mean Leddar $D_{snow}$, $V_T$, and intensity were calculated across the 16 segments, where $V_T$ is estimated from Equation (4.1). Several of the Leddar segments possessed "noisy" (Flag = 35) data records, which were removed prior to calculating the means.

$$D_{snow} = V_o - V_T \quad (4.2)$$

Aggregated datasets were created using quality-controlled data for all sensors to reduce the dataset to a manageable size. A daily timestep was created using the 24-hour mean for all variables. To maintain a higher temporal resolution while retaining diurnal variability, a second data file contained records for the mean of the 15-minute data at a one-hour timestep. The dataset contained 3159 one-hour observations. The "proportion of clean returns" is the total number of one-hour observations containing "Flag = 1" (clean) data relative to the "total number of observations" for the timestep. The calculated percentage is the "total observations" divided by the total number of "clean" observations. The "proportion of noisy returns" is the total number of one-hour observations divided by the total number of "Flag = 35" (noise) one-hour observations.

### 4.2.4 Controls on the Leddar Intensity Signal

To investigate the drivers of the Leddar intensity signal through time, a Pearson's correlation matrix was computed for the hourly dataset to examine relationships and potential collinearity between variables. Variables selected were wind speed (WS), daily albedo, air temperature, relative humidity (RH), ground temperature, SR50A snow depth, hourly precipitation, the Leddar $V_T$, intensity, and proportion of clean returns per timestep. Univariate statistical analysis was completed for the Leddar intensity and proportion of clean return signals for air temperature, daily albedo, $V_T$, and relative humidity after being identified as "variables of interest" in the correlation matrix. The correlation analysis was limited to only sample periods when complete snow cover was present beneath the Leddar unit (21 December 2017 to 27 April 2018).

### 4.2.5 In-Situ Evaluation of LeddarTech IS16 Sensor's Precision, Accuracy, and Performance

An initial test of the Leddar sensor precision was completed in the field on 14 December 2017 before the start of the 2017–2018 data collection. A 1.22 m × 2.44 m painted plywood reflective target used by (Okhrimenko et al., 2019) for LIDAR radiometric calibration was placed level on the ground to compensate for the sloped surface under the Leddar sensor to increase the intensity of the return signal. Leddar DTT and intensity data as well as SR50A DTT measurements were captured in 15-minute increments for a four-hour time period. The SR50A and the Leddar segment 16 beams did not fall fully within the target surface due to the sensor field of view being larger than the target dimension. The Leddar beam length was 2.61 m, which exceeded the painted target's length of 2.44 m. Leddar status "Flag = 1" observations were used to calculate the mean distance to target and intensity for each of the 16 segments.

A second analysis was completed to evaluate the precision of the Leddar unit when operating over a snowpack surface under completely stable conditions; i.e., during a period when the snowpack was in a stable state such that settling, compaction, and crystallization had no significant impact on sensor observations. Several criteria were used to select a time period to test for consistent measurement in snow depth once snowpack settling had taken place. Influences from solar radiation were removed by selecting a sampling interval between 20:00 to 06:00. The air temperature was less than –5.0 °C prior to and throughout the sampling interval to avoid the melting and refreezing metamorphoses of crystalline structures (Pomeroy et al., 1998; Warren, 1982). No precipitation event occurred for several days prior to observation to remove accumulation, compaction, and settling influences (Peltoniemi et al., 2005). Wind speeds approaching zero were desired to remove redistribution of the snowpack surface (Essery et al.,

1999). Due to an unusually warm winter with few days between precipitation events, there was only one time period from 26 December 2017 to 27 December 2017 meeting these criteria.

## 4.3 Results and Discussion

The Leddar daily data were used to plot both snowpack depth and intensity for the winter 2017–2018 snow season. Figure 4.4 shows snowpack depth variability across the 16 segments of the sensor footprint, while increases in depth through time represent the snow fall accumulation events. Settling, compaction, or a mid winter melt are seen as decreases in depth over time. Snowpack surface morphology and texture within the sensor field of view are illustrated orthogonal to the time axis. The rapid reduction in snow depth at the end of the time series was due to spring melting as air temperatures and day length increased in mid to late April.

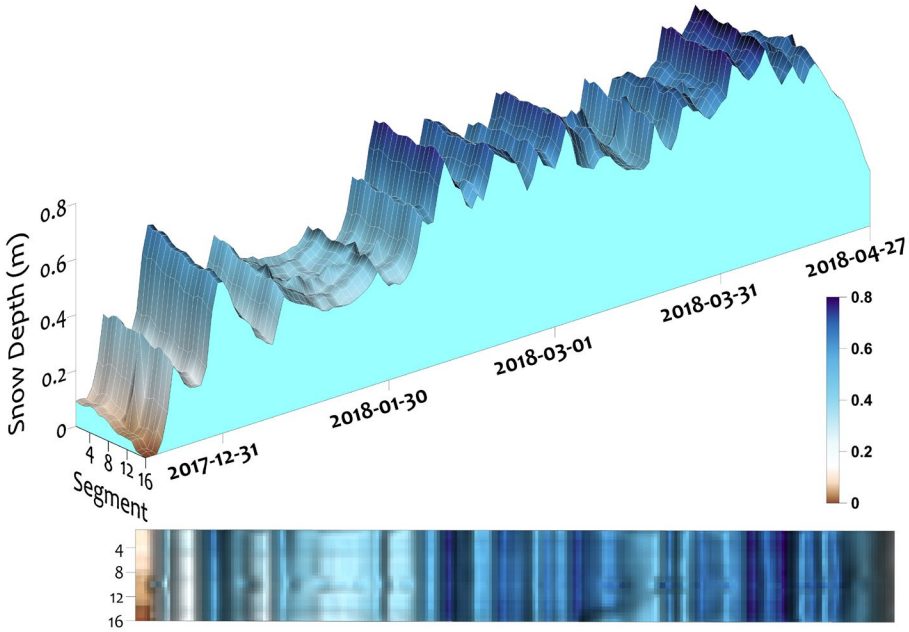

Figure 4.4. Leddar snow depth 15 December 2017 to 27 April 2018.

The Leddar intensity for the 16 segments is shown in Figure 4.5. At the beginning and end of the series, low intensities are associated with patchy snow combined with bare soil and

vegetation at the ground surface level. Higher intensity values occur when snow cover completely fills the sensor field of view. During the period of 100% snow covered area (SCA), intensity increases immediately following snow accumulation events and then gradually decreases as the snowpack settles and metamorphoses. These patterns of increasing and decreasing intensity are synchronous with increases and decreases in depth, but the magnitudes of depth and intensity change are not visually correlated. Intensity responses are strongest at nadir segments with decreasing values toward the outer edge of the field of view. The laser radar equation shows there is an inverse relationship with DDT and the intensity response (Baltsavias, 1999; Grams et al., 1972). Segments at nadir are closest to the ground surface and have the highest intensity. For each segment starting at nadir going to the edge segments of the sensor, distance to the ground increases and there is a corresponding decrease in intensity.

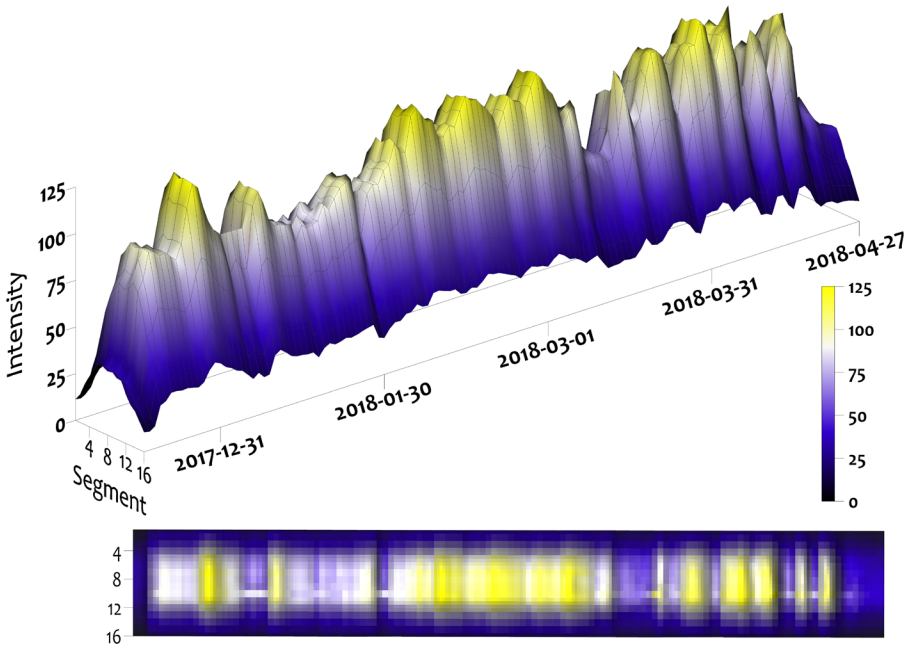


Figure 4.5. Leddar intensity return signal from 15 December 2017 to 27 April 2018. Before the implementation of all of the quality control steps.

### 4.3.1 LeddarTech IS16 Sensor Performance

#### 4.3.1.1 Signal data noise

The Leddar DTT measurement is dependent on the "clean" ("Status Flag = 1") return signals and intensity amplitude. Due to the Leddar demerging configuration setting being "enabled," the sensor occasionally recorded signals with a "Flag = 35" status (noisy returns). Analysis was completed for the entire hourly time series (14 December 2017 to 27 April 2018) dataset to evaluate the amounts of "clean" (proportion of clean returns) and "noisy" (proportion of noisy returns) return signals for all segments (Table 4.3a). The proportion of timestep observations with no clean returns (Table 4.3b) is the amount of missing clean data for the individual 15-minute data sampling measurements. Intensity (Table 4.3c) for segments near nadir received the highest values, while edge segments received the lowest intensity measurements. Of note, the two edge segments on both sides of nadir had minimum intensity values below the manufacturer's specifications for DTT accuracy threshold which occurred during the time period of no-snow. Segment 10 had an abnormally high noise fraction throughout most of the observation period. This segment does not appear to be representative of the sensor. The noise was potentially caused by internal damage or contamination within the optical receiver.

Table 4.3. From 14 December 2017 to 27 April 2018, n = 3211 (1-hour timestep) per segment (SEG) for the entire data collection period. (a) Leddar data series proportion of clean and noise returns. (b) The proportion of timestep observations with no clean returns refers to the amount of data for all 15-minute measurement cycles where the sensor did not detect any clean readings. (c) Leddar intensity signal minimum, maximum, mean, and range.

| SEG | Proportion of Clean returns | Proportion of Noisy returns | Proportion of timestep observations with no Clean returns | Intensity | | | |
|---|---|---|---|---|---|---|---|
| | | | | Min | Max | Mean | Range |
| 1 | 99.2% | 0.8% | 0.0% | 10.0 | 45.2 | 29.3 | 35.2 |
| 2 | 99.7% | 0.3% | 0.0% | 13.7 | 61.6 | 40.8 | 47.9 |
| 3 | 97.5% | 2.5% | 0.0% | 18.6 | 82.0 | 55.0 | 63.4 |
| 4 | 96.4% | 3.6% | 0.1% | 24.8 | 105.1 | 70.9 | 80.3 |
| 5 | 94.6% | 5.4% | 0.1% | 26.0 | 123.2 | 83.4 | 97.2 |
| 6 | 91.1% | 8.9% | 2.1% | 30.3 | 128.0 | 87.8 | 97.6 |
| 7 | 88.9% | 11.1% | 2.2% | 32.1 | 134.0 | 92.6 | 101.9 |
| 8 | 84.9% | 15.1% | 5.6% | 31.6 | 131.7 | 92.7 | 100.1 |
| 9 | 81.7% | 18.3% | 5.5% | 31.3 | 134.5 | 94.8 | 103.1 |
| 10 | 33.4% | 66.6% | 38.5% | 29.2 | 135.3 | 105.1 | 106.1 |
| 11 | 87.5% | 12.5% | 1.2% | 29.3 | 136.1 | 94.3 | 106.8 |
| 12 | 84.8% | 15.2% | 5.9% | 24.6 | 118.8 | 83.9 | 94.2 |
| 13 | 88.4% | 11.6% | 0.3% | 20.4 | 96.1 | 66.3 | 75.7 |
| 14 | 97.0% | 3.0% | 0.0% | 17.6 | 75.6 | 51.9 | 58.0 |
| 15 | 98.5% | 1.5% | 0.4% | 12.9 | 57.8 | 39.7 | 44.8 |
| 16 | 96.9% | 3.1% | 1.4% | 7.7 | 38.3 | 26.0 | 30.6 |
| | (**a**) | | (**b**) | | | (**c**) | |

The noise was plotted over time to find potential relationships with snowpack conditions and meteorological influences. Figure 4.6 shows the proportion of the data per time step that received noisy returns in relation to the total number of returns. The least amount of noise was observed in the middle of the series once the SCA was fully present at the end of December and before melt conditions initially occurred in mid-March. Segments near nadir experienced more noise during episodic snowmelt periods late in the winter season, when there was higher water content in the snowpack. Some noise may have been caused by solar contamination, precipitation, wind redistribution of snowpack surface grains, or higher moisture content when the pack entered a freeze/thaw stage or became isothermal and melted out.

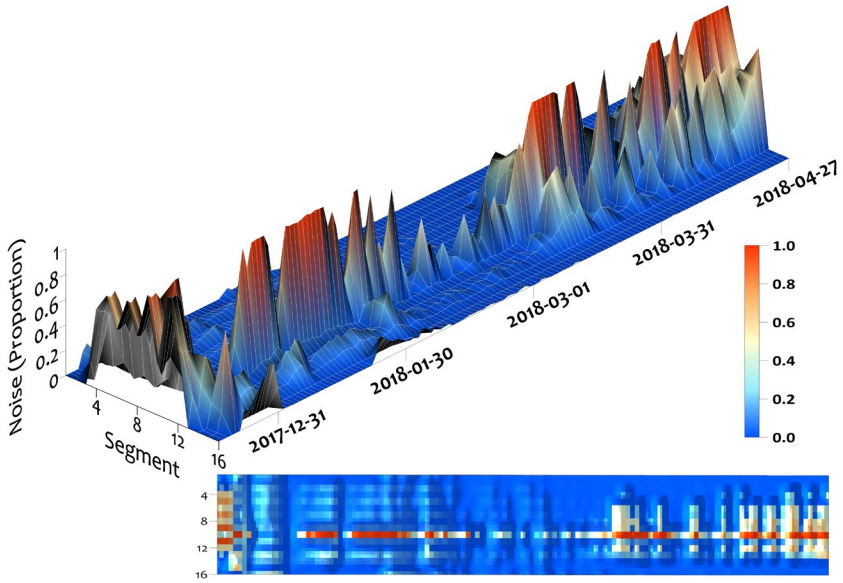


Figure 4.6. Leddar "noise" in the data from 14 December 2017 to 27 April 2018. The noise is the proportion of the data per time step that received noisy returns in relation to the total number of returns. Time series of readings culminated in Table 4.3a—proportion of noisy returns.

#### 4.3.1.2 Temperature Sensitivity

The high-resolution time series data demonstrated the intensity amplitude shifted by 10 or more units immediately before some snowfall events (Figure 4.7). This indicated at least some of the shift in signal intensity associated with snowpack accumulation events was not a function of the snowpack surface condition but instead was impacted by the inverse relationship between LED light output power and ambient temperature (Huang et al., 2009). Figure 4.7 show five events (precipitation: blue bars; air temperature: black; intensity: red) with increases and decreases in the intensity response prior to and during the events. These data show that signal intensity tends to vary inversely with air temperature leading into the precipitation event, and is likely a hardware response demonstrating some thermal sensitivity within the Leddar unit. Consultation with the manufacturer confirmed both internal hardware components and environmental conditions influence the sensitivity of the Leddar intensity signal (Messiaen, 2019). Further analysis is required to separate out the ambient temperature influence on the

hardware vs. the surface reflectance response; however, this preliminary illustration of an inverse relationship with temperature suggests that temperature-based correction of the intensity response, while not implemented here, could be achievable.

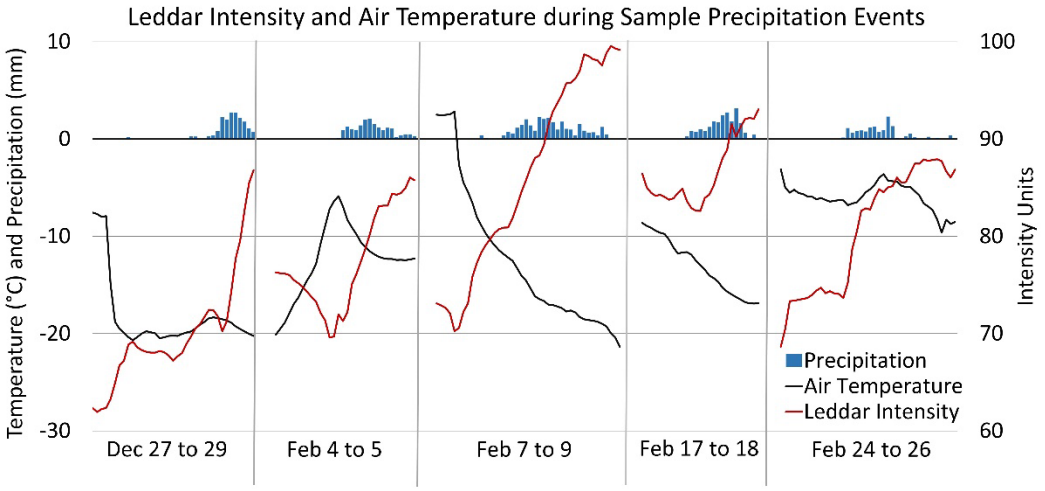


Figure 4.7.Leddar intensity (mean all segments), air temperature, sample precipitation events. Initial examination of the Leddar intensity signal suggests an LED light output sensitivity to air temperature.

#### 4.3.1.3 Controls on the Leddar Intensity Signal

The full winter season 1-hour dataset with Leddar intensity signal, proportion of clean returns, air temperature, daily albedo, and Leddar $V_T$ data show moderate to strong correlations (Table 4.4).

Table 4.4. Pearson's Correlation coefficient (r) for the Leddar (mean of all segments) sensor and other meteorological variables for the given timestep. "% Clean" is the proportion of clean returns.

| | **Daily Albedo** *r* | **Air Temperature** *r* | **Leddar $V_T$** *r* | **Leddar Intensity** *r* |
|---|---|---|---|---|
| **Leddar Intensity** | 0.77 | -0.77 | -0.43 | - |
| **Leddar % Clean** | 0.59 | -0.57 | -0.13 | 0.74 |

The daily albedo and Leddar intensity return signal show a correlation of 0.77. There should be a relationship between these two variables as they are both a measure of reflectance. Higher reflectance values are received from fresh dry snow when smaller snow grain sizes are

present (Dozier et al., 2009). Lower reflectance values occur as the snowpack metamorphoses as a result of changes in crystal structure and increased snow grain size (Dozier & Painter, 2004; Negi et al., 2010). Reflectance of aged, wet, and melting snow is lower than that of fresh, dry snow (Dozier et al., 1988; Peltoniemi et al., 2005). Ice layers formed from melt/freeze cycles have similar reflectance properties to that of wet snow (Hannula & Pulliainen, 2019; Warren, 2019). Albedo and the proportion of clean Leddar returns showed a moderate correlation of 0.59, which indicates that noise tends to diminish as snowpack reflectance increases.

There is a correlation of −0.77 between the air temperature and the Leddar intensity signal (Table 4.4). In addition to potential hardware influences (discussed above), air temperature also influences the snowpack properties of grain size and structure (Warren, 1982). As air temperatures increase and approach 0 °C, the snowpack begins to ripen (higher water content) and surface reflectance reduces (Kaasalainen et al., 2006).

There is negative correlation between air temperature and the proportion of clean Leddar returns at −0.57 (Table 4.4). The proportion of clean returns was elevated during cooler temperatures. As air temperature approached 0 °C and warmer, more noise was present in the data. This could be influenced by another driver that auto-correlates with seasonal variations in temperature, such as freeze/thaw conditions at the surface of the pack during the melt phase, suggesting noise levels increase as the snow surface melts.

No relationship exists for $V_T$ and the clean return signal ($r = -0.13$), but $V_T$ and intensity demonstrate a correlation of −0.43. The further the target is from the sensor, the less backscatter received (Kashani et al., 2015). Since the Leddar unit was statically mounted on a tower facing the ground surface, the largest DDT values occur before the snowpack is present. At this point, the sensor is observing the vegetation and soils which have a lower spectral reflectance than

snow in the NIR 940 nm band. As the snowpack builds, DDT is reduced, and Leddar intensity increases due to the higher albedo of snow, as well as the shorter range. As the pack starts to melt out, spectral reflectance values decrease from the higher water content in the snowpack as well as the increased distance to the ground surface.

Intensity and proportion of clean returns are positively correlated ($r$ = 0.74, Table 4.4). The intensity signal and proportion of clean returns were plotted through time once the snowpack emerged. Box plots in Figure 8 are broken down by hour-of-the-day and further by month. Both the proportion of clean returns (Figure 4.8a) and the intensity signal (Figure 4.8b) show diurnal patterns. Signal "noise" and intensity ranges are elevated during daylight hours from midday onwards, which appear to correspond with temperature and daylight variations. Maximum noise and lowest intensity are associated with warmer afternoon temperatures, while minimal noise and slightly elevated Leddar reflectance occur in the morning after sunrise but during local diffuse sky radiation. The pattern was more dominant in March and April, when most daytime air temperatures were above 0 °C. The least amount of noise occurred in February when air temperatures were between −20 to −35 °C with only a few days approaching or above 0 °C. There are two potential contributing factors: (i) occasional melt, ripening processes, and higher water content at the surface of the snowpack; and/or (ii) solar contamination of the signal during the afternoon. With the diurnal variation in sensible heat flux and net surface radiation balance over the snowpack, it is possible the Leddar signal is sensitive to the changing snowpack surface structure and increasing snow grain size. There is a corresponding increase in noise levels in March and April when diurnal energy inputs to the pack can be most extreme. Any sensitivity to changes in surface structure, would be expected to be observed during the onset of melt conditions late in the season.

Solar contamination cannot be ruled out, however, as the skyview surrounding the instrument tower is most open to the west with mountain ridges dominating the south and north skyline. Consequently, if solar contamination occurs, it would be expected in the afternoon, with the level of contamination increasing as the solar zenith and range in azimuth increase later in the season. It is believed that both surface freeze/thaw processes and solar contamination play a role in influencing diurnal intensity and noise patterns, but further investigation is required to quantify the relative influence and identify which is dominant.

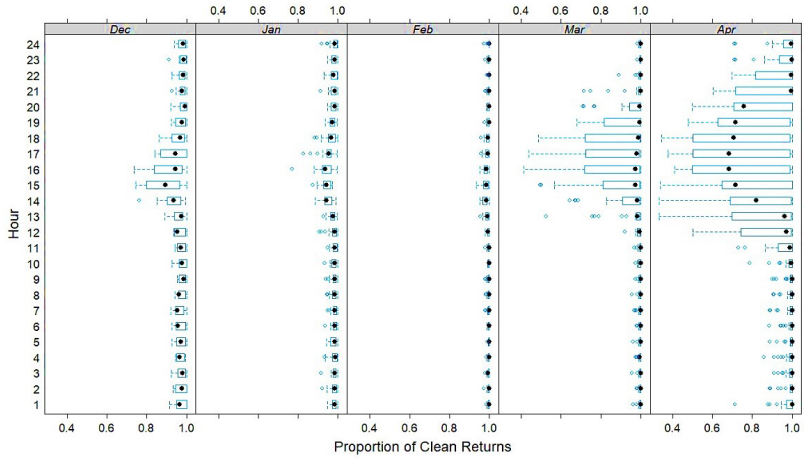


(**a**)

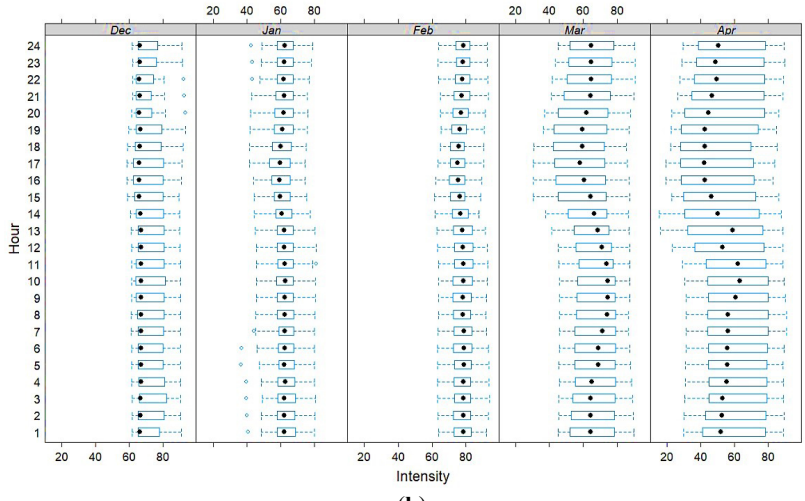


(**b**)

Figure 4.8. Proportion of clean signals (a) and mean hourly Leddar signal intensity (b) by month from December to April. The box delineates the lower 25th and upper 75th percentiles. The dashed T-lines are the minimum and maximum values and open circles to the left and right of the dashed T-line are outliers. The black dot inside the box is the mean.

### 4.3.2 Range and Depth Observations

#### 4.3.2.1 Leddar Calibration

The root-mean-square-error (RMSE) of range-to-$V_T$ calibration conducted in the laboratory using Equation (4.1) was 13.0 mm. The parameter values (and standard error): β, 3.134° (0.010°); γ was −0.044° (0.003°); and $R_c$ was −0.307 m (< 0.001 m). The calibrated β was just over the LeddarTech product specification of 3.0° (LeddarTech Inc., 2018).

Results of the Leddar and SR50A reflective target testing from December 14, 2017 (as described in 4.2.5), are shown in Figure 4.9. The Leddar DTT follows a systematic arc from the optical receiver to the target surface (LeddarTech Inc., 2018). Segment DTT is shortest at nadir and increases toward the edge segments. The range of DTT values show consistent measurements for all segments within 20 mm and a maximum standard deviation for all segments of 5 mm (Figure 4.9a) over a four-hour duration. The SR50A measurement varied to a higher degree with a DTT range of 210 mm and a standard deviation of 70 mm. Under controlled conditions, variation in the Leddar measurements was very low and more precise than the SR50A. The intensity signal (Figure 4.9b) follows an expected systematic inverse pattern with highest values at nadir and decreasing towards the outer segments. The footprint for segment 16 was at the edge of the target and was contaminated with bare soil and grass returns, resulting in the lowest intensity relative to other segments. The intensity measurement over the four-hour period for segment 16 was 11.1 which was below the Leddar manufacturer's threshold of 15. However, the DTT standard deviation for segment 16 was 3 mm. The temporal stability of measurements from this Leddar sensor testing are consistent with the findings of (Parsons & Hopkinson, 2016) in their preliminary investigation of the Leddar technology.

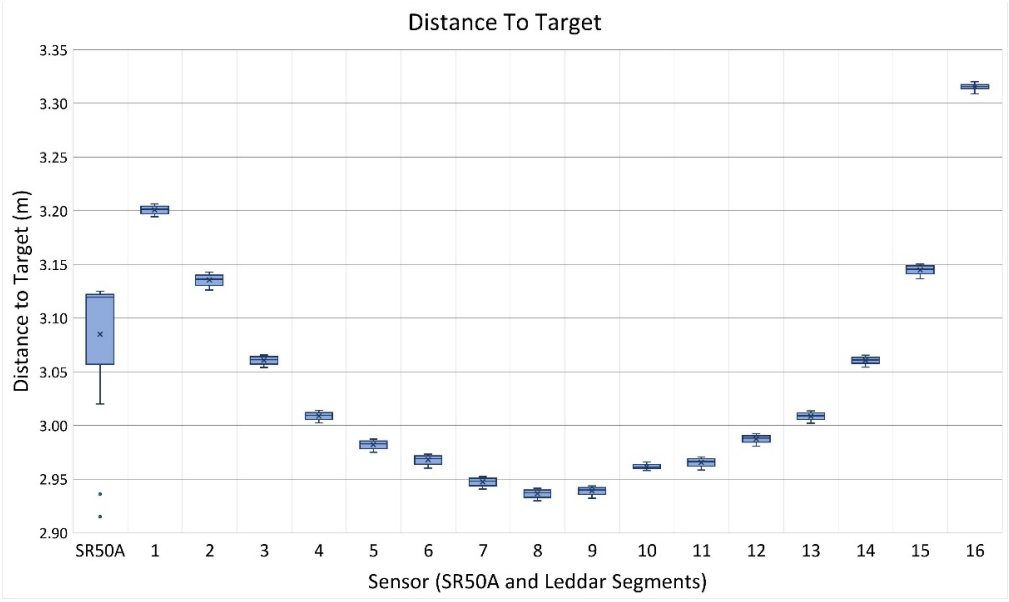


**(a)**

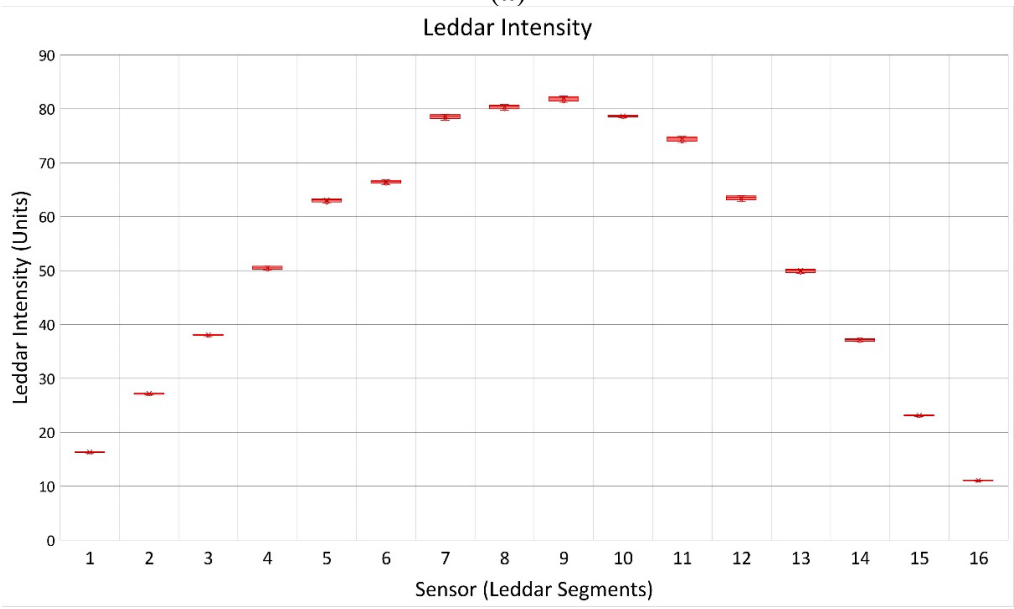


**(b)**

Figure 4.9. Reflective target placed on the ground under the Leddar unit. SR50A footprint and Leddar Segment 16 were not contained within the target surface. (a) Boxplot of Leddar and SR50A DTT, (b) boxplot of Leddar Intensity. (Note: SR50A does not return intensity signal measurements).

#### 4.3.2.2 Snow Depth Validation

The full winter season 1-hour Leddar and SR50A depth dataset contained 3211 records. Table 4.5 shows snowpack depth for the SR50A and each Leddar segment when the snowpack reached maximum depth on 8 April 2018 at 10:00. Snow depth varies across the Leddar field of

view with lowest measurements of 0.75 m in segments 5 through 7 and largest observations of 0.85 m for segments 14–16. This difference is easily within the expected variance associated with the slightly sloping ground surface and undulations in the snowpack surface. The snow depth recorded for the SR50A was 0.83 m. The SR50A measurement falls within the range of the Leddar snow depth for segments 13 and 14. SR50A observations are not necessary expected to be the same as any individual Leddar segment due to the size and shape of the different sampling footprints (Figure 4.1).

Table 4.5.Maximum snowpack depth occurred on 8 April 2018 10:00. Leddar segments and SR50A snow depth. From 14 December 2017 to 27 April 2018 winter season 1-hour dataset, n = 3211.

| SR50A | Leddar Segment (m) | | | | | | | | | | | | | | | |
|---|---|---|---|---|---|---|---|---|---|---|---|---|---|---|---|---|
| (m) | 1 | 2 | 3 | 4 | 5 | 6 | 7 | 8 | 9 | 10 | 11 | 12 | 13 | 14 | 15 | 16 |
| 0.83 | 0.81 | 0.79 | 0.80 | 0.77 | 0.75 | 0.75 | 0.75 | 0.76 | 0.77 | 0.75 | 0.78 | 0.78 | 0.81 | 0.85 | 0.85 | 0.85 |

Comparable Leddar, SR50A, and field validation data are presented in Table 4.6. The Leddar "Proportion clean returns" reduces as air temperatures increase during melt conditions. The Leddar footprint shows a range in snow depth from a low of 0.08 m to a high of 0.17 m across all segments. The SR50A snow depth measurement was between zero to 0.04 m for all site visits except the last when significant melt occurred in a short period of time.

Table 4.6. Manual field measurement, SR50A, Leddar (all 16 segments), mean air temperature, and daily albedo. Manual snow depth measurements taken from behind the tower out of the sensor footprints under the Leddar unit, but exact location varied with each visit.

| Site Visit Date | 21-Dec | 05-Jan | 20-Jan | 21-Feb | 04-Mar | 09-Apr | 15-Apr | 19-Apr | 26-Apr | 27-Apr | 27-Apr |
|---|---|---|---|---|---|---|---|---|---|---|---|
| Start Time | 18:30 | 11:00 | 15:00 | 10:45 | 14:45 | 14:00 | 14:00 | 18:15 | 06:00 | 07:00 | 11:15 |
| End Time | 22:30 | 15:00 | 19:00 | 14:45 | 18:45 | 18:00 | 18:00 | 21:45 | 10:00 | 11:00 | 12:30 |
| Snow Depth (m) | | | | | | | | | | | |
| Manual Field Sample | 0.35 | 0.40 | 0.36 | 0.70 | 0.74 | 0.77 | 0.53 | 0.58 | 0.28 | 0.20 | 0.17 |
| SR50A Mean | 0.31 | 0.44 | 0.36 | 0.66 | 0.72 | 0.71 | 0.59 | 0.57 | 0.29 | 0.21 | 0.17 |
| SR50A Min | 0.29 | 0.42 | 0.35 | 0.65 | 0.72 | 0.70 | 0.59 | 0.56 | 0.28 | 0.20 | 0.06 |
| SR50A Max | 0.31 | 0.45 | 0.36 | 0.69 | 0.72 | 0.73 | 0.60 | 0.58 | 0.29 | 0.22 | 0.20 |
| Leddar Mean | 0.28 | 0.36 | 0.31 | 0.61 | 0.66 | 0.65 | 0.54 | 0.53 | 0.23 | 0.14 | 0.12 |
| Leddar Min | 0.24 | 0.32 | 0.27 | 0.54 | 0.61 | 0.59 | 0.48 | 0.46 | 0.16 | 0.08 | 0.06 |
| Leddar Max | 0.38 | 0.40 | 0.37 | 0.70 | 0.74 | 0.75 | 0.62 | 0.61 | 0.32 | 0.24 | 0.21 |
| Proportion clean returns | 92% | 83% | 81% | 93% | 93% | 59% | 47% | 49% | 79% | 63% | 28% |
| Air Temperature (°C) | -6.2 | 3.2 | -0.3 | -13.4 | -7.4 | 7.4 | 7.5 | 5.0 | 4.8 | 5.1 | 16.8 |
| Daily Albedo | 0.84 | 0.83 | 0.80 | 0.81 | 0.85 | 0.77 | 0.69 | 0.73 | 0.59 | 0.58 | 0.58 |

A regression plot of Leddar and SR50A snow depth (Figure 4.10a) shows strong agreement between the two sensors ($r^2$ = 0.98). Figure 4.10b shows the mean for the Leddar snowpack depth values across all segments plotted against the single field snow depth measurement below the Leddar unit. There is low confidence that the manually collected field data represent the whole Leddar or SR50A sampling footprint. Single manual sampling depth observations were obtained from the back of the tower outside the sensor footprints reaching approximately 1 m to the location under the Leddar unit attempting to minimize snow surface disturbance. The manual measurements fall within the Leddar segment array distribution range as seen in Table 4.6 but were not co-located to any individual segment. The Leddar segment means tend to fall below the field measurement resulting in a bias on the order of ~0.05 m due to variability in snow depth among all segments or manual field measurement errors such as the probe not penetrating to the ground surface from ice layers at the base of the pack. However, despite this small bias Leddar and field depth data show a strong regression ($r^2$ = 0.98).

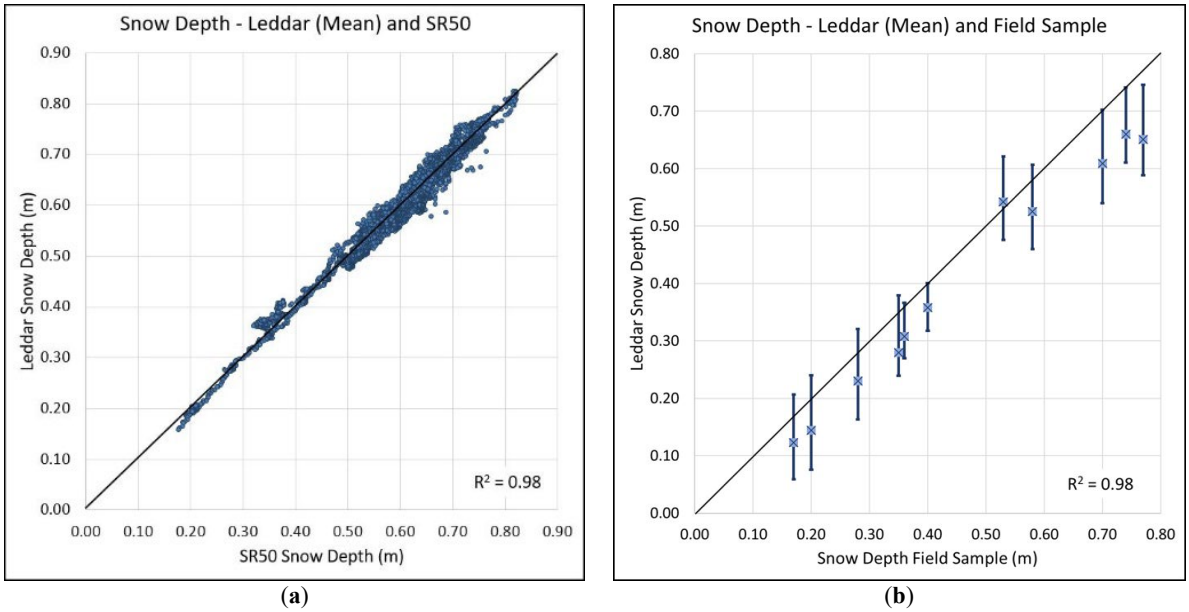


(**a**) (**b**)

Figure 4.10. (a) Plot of Leddar segment mean against SR50A mean snowpack depth. (b) Plot of Leddar segment depth range (bars) and mean (blue square) against manual field measurements.

#### 4.3.2.3 Leddar Snow Depth Stability

The night-time sampling interval that met the stable sampling constraints of air temperatures consistently below −5 °C with no precipitation or wind, was a 10-hour period between 20:00 on 26 December 2017 to 06:00 27 December 2017. Table 4.7 shows snow depth for the Leddar segments and SR50A. The range in snow depth measurement of each individual Leddar segments was <5 mm, while the range in SR50A snow depth over the single footprint was >20 mm. The precision observed for the Leddar sensor exceeds the manufacturer quoted 6 mm when intensity is greater than 15 (LeddarTech Inc., 2018).

Table 4.7. Leddar and SR50A sensor snow depth data from 20:00 26 December 2017 to 06:00 27 December 2017 nighttime sampling period meeting the minimum specifications.

| Leddar | Snow Depth (m) | | | | |
|---|---|---|---|---|---|
| Segment | Mean | STDev | Min | Max | Range |
| 1 | 0.191 | 0.001 | 0.190 | 0.194 | 0.004 |
| 2 | 0.181 | 0.001 | 0.180 | 0.183 | 0.003 |
| 3 | 0.189 | 0.001 | 0.188 | 0.190 | 0.002 |
| 4 | 0.179 | 0.001 | 0.178 | 0.181 | 0.003 |
| 5 | 0.157 | 0.001 | 0.156 | 0.158 | 0.002 |
| 6 | 0.162 | 0.001 | 0.161 | 0.164 | 0.003 |
| 7 | 0.161 | 0.001 | 0.160 | 0.163 | 0.003 |
| 8 | 0.174 | 0.001 | 0.173 | 0.176 | 0.003 |
| 9 | 0.179 | 0.001 | 0.178 | 0.182 | 0.003 |
| 10 | 0.169 | 0.001 | 0.168 | 0.172 | 0.003 |
| 11 | 0.173 | 0.001 | 0.172 | 0.175 | 0.003 |
| 12 | 0.176 | 0.001 | 0.175 | 0.178 | 0.003 |
| 13 | 0.191 | 0.001 | 0.189 | 0.193 | 0.003 |
| 14 | 0.212 | 0.001 | 0.211 | 0.215 | 0.004 |
| 15 | 0.197 | 0.002 | 0.195 | 0.200 | 0.005 |
| 16 | 0.211 | 0.001 | 0.210 | 0.214 | 0.004 |
| SR50A (m) | 0.174 | 0.008 | 0.164 | 0.185 | 0.021 |

## 4.4 Conclusions

This proof of concept study examined the feasibility of using a LeddarTech IS16 LED LIDAR-based sensor for snowpack surface morphology, depth, and reflectance measurements.

The sensor was co-located and tested against a Campbell Scientific SR50A sonic ranging snow depth sensor during the 2017–2018 winter season. Controls on the intensity signal, comparison to SR50A snow depths, Leddar distance-to-target (DTT) precision, and accuracy were evaluated.

The Leddar sensor data showed variability in magnitude of the intensity signal during the formation, settling, ripening, and ablation of the snowpack as well as when precipitation events took place. Prior to snowpack formation, vegetation and soils produced more noise in the dataset as well as lower intensity responses. Lower intensity and increased noise also occurred during surface melt conditions. More noise was present in segments closer to nadir than at the edges of the Leddar footprint. Diurnal variations in the intensity and noise levels increased later in the season, suggesting that solar contamination of the Leddar signal could be present and that mitigation measures need to be explored. There was a high correlation between albedo and the intensity signal (0.77) as well as noise (0.59). Air temperature demonstrated a negative correlation (−0.77) with intensity, which was likely at least partly a function of hardware sensitivity, though it could also be influenced by surface melt lowering the intensity response. Further analysis is required to quantify and better understand the impact of air temperature on the intensity signal.

The Leddar sensor data showed variability in snow depth measurements across the 16-segment footprint during snowpack accumulation, compaction, and ablation events. Examining sensor performance when the snowpack was in a stable state showed Leddar snow depth observations varied <5 mm in comparison to >20 mm for the SR50A measurements. These Leddar observations exceed the manufacturer's specification for accuracy at 50 mm and precision of 6 mm for intensity values greater than 15. Despite the environmental sensitivities experienced by the Leddar unit, the sensor demonstrated accurate and precise depth

measurements throughout the winter season. The Leddar and SR50A snow depth measurements displayed a strong linear relationship ($r^2$ = 0.98), with virtually no bias and a slope of 0.99. Leddar and manual field measurements also showed strong agreement ($r^2$ = 0.98). Leddar measurements during initial testing using a reflective target were within 20 mm for DTT, compared to 210 mm for the SR50A sensor.

LED LIDAR has great potential for low-cost monitoring of a range of snowpack conditions, including depth measurements for 16 independent beam segments, surface morphology, and possibly surface reflectance if temperature influences on the internal optics can be mitigated. The base components used in this study were obtained for a combined approximate cost of <CA$1000, which is similar to a new sonic ranging sensor. Meanwhile, *in-situ* Leddar snow depth observations can be made at higher precision and accuracy, over multiple segments along a transect, while the intensity signal and noise response show promise for either characterising snow surface properties and/or perhaps precipitation. Compared to traditional laser-based ranging sensors, LED LIDAR has a low intermittent operational power requirement, making it a suitable candidate for remote deployment where power options are limited.

## 4.5 References


Baltsavias, E. P. (1999). Airborne laser scanning: basic relations and formulas. *ISPRS Journal of Photogrammetry and Remote Sensing*, *54*(2), 199-214. https://doi.org/https://doi.org/10.1016/S0924-2716(99)00015-5

Barrows, H. K., & Horton, R. E. (1907). *Determination of stream flow during the frozen season*. US Government Printing Office.

Binder, T., & Kostina, E. (2013). Gauss–Newton Methods for Robust Parameter Estimation. In *Model Based Parameter Estimation* (pp. 55-87). Springer.

Bullough, J. (2003). *LED Lighting Systems*. Lighting Research Center. http://www.lrc.rpi.edu/programs/NLPIP/lightinganswers/pdf/PRINT/LED.pdf

Campbell, S. (2018). *Acoustic Snow Depth Sensor Operation*. Edmonton, AB: Alberta Environment and Parks Retrieved from http://environmentalmonitoring.alberta.ca/wp-content/uploads/2018/07/Acoustic-Snow-Depth-Sensor.pdf

Campbell Scientific (Canada) Corp. (2015). CNR1 Net Radiometer. In (pp. 32). Edmonton, AB: Campbell Scientific (Canada) Corp.

Campbell Scientific (Canada) Corp. (2016). SR50A and SR50AT Sonic Ranging Sensors. In (pp. 64). Edmonton, AB: Campbell Scientific (Canada) Corp.

Deems, J. S., Painter, T. H., & Finnegan, D. C. (2013). Lidar measurement of snow depth: a review. *Journal of Glaciology*, *59*(215), 467-479.

Dozier, J., Davis, R., Chang, A., & Brown, K. (1988). The spectral bidirectional reflectance of snow. Spectral Signatures of Objects in Remote Sensing,

Dozier, J., Green, R. O., Nolin, A. W., & Painter, T. H. (2009). Interpretation of snow properties from imaging spectrometry. *Remote Sensing of Environment*, *113*, S25-S37. https://doi.org/https://doi.org/10.1016/j.rse.2007.07.029

Dozier, J., & Painter, T. H. (2004). MULTISPECTRAL AND HYPERSPECTRAL REMOTE SENSING OF ALPINE SNOW PROPERTIES. *Annual Review of Earth and Planetary Sciences*, *32*(1), 465-494. https://doi.org/10.1146/annurev.earth.32.101802.120404

Earle, M., Reverdin, A., Wolff, M., Smith, C., Morin, S., & Rodica, N. (2014). Data Processing and Quality Control Methodology for the Derivation of Reference Datasets. In *Project Team and (Reduced) International Organizing Committee for the WMO Solid Precipitation Intercomparison Experiment Final Report* (Vol. Fifth Session, pp. 77). Sodankylä, Finland: World Meteorological Organization.

Eppanapelli, L. K., Lintzén, N., Casselgren, J., & Wåhlin, J. (2018). Estimation of liquid water content of snow surface by spectral reflectance. *Journal of cold regions engineering*, *32*(1), 05018001.

Essery, R., Li, L., & Pomeroy, J. (1999). A distributed model of blowing snow over complex terrain. *Hydrological Processes*, *13*(1415), 2423-2438.

Fischer, A. P. (2011). The Measurement Factors in Estimating Snowfall Derived from Snow Cover Surfaces Using Acoustic Snow Depth Sensors. *Journal of Applied Meteorology and Climatology*, *50*(3), 681-699. https://doi.org/10.1175/2010jamc2408.1

Government of Alberta. (2018). *Snow Does Not Equal Flood: Alberta's Snowmelt and its Impact on Alberta Rivers*. Edmonton, AB: alberta.ca Retrieved from https://open.alberta.ca/publications/snow-does-not-equal-flood-alberta-s-snowmelt-and-its-impact-on-alberta-rivers

Grams, G. W., Jr., I. H. B., Schuster, B. G., & DeLuisi, J. S. (1972). Complex Index of Refraction of Airborne Fly Ash Determined by Laser Radar and Collection of Particles at 13 km. *Journal of the Atmospheric Sciences*, *29*(5), 900-905. https://doi.org/10.1175/1520-0469(1972)029<0900:Cioroa>2.0.Co;2

Grünewald, T., Schirmer, M., Mott, R., & Lehning, M. (2010). Spatial and temporal variability of snow depth and SWE in a small mountain catchment. *The Cryosphere*, *4*(ARTICLE), 215-225.

Gubler, H. (1981). An Inexpensive Remote Snow-Depth Gauge based on Ultrasonic Wave Reflection from the Snow Surface. *Journal of Glaciology*, *27*(95), 157-163. https://doi.org/10.3189/S002214300001131X

Hannula, H.-R., & Pulliainen, J. (2019). Spectral reflectance behavior of different boreal snow types. *Journal of Glaciology*, *65*(254), 926-939. https://doi.org/10.1017/jog.2019.68

Huang, B.-J., Tang, C.-W., & Wu, M.-S. (2009). System dynamics model of high-power LED luminaire. *Applied Thermal Engineering*, *29*(4), 609-616. https://doi.org/https://doi.org/10.1016/j.applthermaleng.2008.03.038

Kaasalainen, S., Kaasalainen, M., Mielonen, T., Suomalainen, J., Peltoniemi, J. I., & Näränen, J. (2006). Optical properties of snow in backscatter. *Journal of Glaciology*, *52*(179), 574-584. https://doi.org/10.3189/172756506781828421

Kashani, A., Olsen, M., Parrish, C., & Wilson, N. (2015). A Review of LIDAR Radiometric Processing: From Ad Hoc Intensity Correction to Rigorous Radiometric Calibration. *Sensors*, *15*(11), 28099. http://www.mdpi.com/1424-8220/15/11/28099

Kinar, N. J., & Pomeroy, J. W. (2015). Measurement of the physical properties of the snowpack. *Reviews of Geophysics*, *53*(2), 481-544. https://doi.org/10.1002/2015RG000481

Kipp, S., Mistele, B., & Schmidhalter, U. (2014). The performance of active spectral reflectance sensors as influenced by measuring distance, device temperature and light intensity. *Computers and Electronics in Agriculture*, *100*, 24-33. https://doi.org/https://doi.org/10.1016/j.compag.2013.10.007

Kochendorfer, J., Nitu, R., Wolff, M., Mekis, E., Rasmussen, R., Baker, B., Earle, M. E., Reverdin, A., Wong, K., & Smith, C. D. (2018). Testing and development of transfer functions for weighing precipitation gauges in WMO-SPICE. *Hydrology and Earth System Sciences*, *22*(2), 1437-1452.

Kulkarni, A. V., Srinivasulu, J., Manjul, S. S., & P, M. (2002). Field based spectral reflectance studies to develop NDSI method for snow cover monitoring [journal article]. *Journal of the Indian Society of Remote Sensing*, *30*(1), 73-80. https://doi.org/10.1007/bf02989978

LeddarTech Inc. (2018). *Leddar™ Sensor Module User Guide*. LeddarTech Inc.

Leeper, R. D., Palecki, M. A., & Davis, E. (2015). Methods to Calculate Precipitation from Weighing-Bucket Gauges with Redundant Depth Measurements. *Journal of Atmospheric and Oceanic Technology*, *32*(6), 1179-1190. https://doi.org/10.1175/jtech-d-14-00185.1

López-Moreno, J. I., Fassnacht, S. R., Heath, J. T., Musselman, K. N., Revuelto, J., Latron, J., Morán-Tejeda, E., & Jonas, T. (2013). Small scale spatial variability of snow density and depth over complex alpine terrain: Implications for estimating snow water equivalent. *Advances in water resources*, *55*, 40-52. https://doi.org/https://doi.org/10.1016/j.advwatres.2012.08.010

Mannstein, H. (1985). The interpretation of albedo measurements on a snowcovered slope. *Archives for meteorology, geophysics, and bioclimatology, Series B*, *36*(1), 73-81.

Messiaen, P. (2019). LeddarTech IS16 [case #1499]. In C. Barnes (Ed.), (Leddar IS16 LED temperature sensitivity ed.). Quebec, Quebec: LeddarTech Inc.

Natural Resources Canada. (2010). *Atlas of Canada, 6th Edition (archival version) Average Maximum Snow Depth*. Ottawa, ON, Government of Canada, Natural Resources Canada, Earth Sciences Sector, Atlas of Canada. https://open.canada.ca/data/en/dataset/d90ddf8f-8893-11e0-bc5e-6cf049291510

Negi, H. S., Singh, S. K., Kulkarni, A. V., & Semwal, B. S. (2010). Field-based spectral reflectance measurements of seasonal snow cover in the Indian Himalaya. *International Journal of Remote Sensing*, *31*(9), 2393-2417. https://doi.org/10.1080/01431160903002417

Okhrimenko, M., Coburn, C., & Hopkinson, C. (2019). Multi-Spectral Lidar: Radiometric Calibration, Canopy Spectral Reflectance, and Vegetation Vertical SVI Profiles. *Remote Sensing*, *11*(13), 1556. https://www.mdpi.com/2072-4292/11/13/1556

Olivier, P. (2016). *Leddar Optical Time-of-Flight Sensing Technology: A New Approach to Detection and Ranging*. LeddarTech Inc. https://leddartech.com/download/leddar-optical-time-flight-sensing-technology-new-approach-detection-ranging

Pan, X., Yang, D., Li, Y., Barr, A., Helgason, W., Hayashi, M., Marsh, P., Pomeroy, J., & Janowicz, R. J. (2016). Bias corrections of precipitation measurements across experimental sites in different ecoclimatic regions of western Canada. *The Cryosphere*, *10*(5), 2347-2360.

Parsons, N. R., & Hopkinson, C. (2016). *The Development of an In-situ Light Emitting Diode Detection And Ranging Technology for Monitoring Snow Depth and Snow Surface Topography*.

Paznekas, A., & Hayashi, M. (2016). Groundwater contribution to winter streamflow in the Canadian Rockies. *Canadian Water Resources Journal / Revue canadienne des ressources hydriques*, *41*(4), 484-499. https://doi.org/10.1080/07011784.2015.1060870

Peltoniemi, J. I., Kaasalainen, S., Naranen, J., Matikainen, L., & Piironen, J. (2005). Measurement of directional and spectral signatures of light reflectance by snow. *IEEE Transactions on Geoscience and Remote Sensing*, *43*(10), 2294-2304. https://doi.org/10.1109/TGRS.2005.855131

Pickering, R. (2018). *Snow Surveying Field Sampling Protocols*. Alberta Environment and Parks. http://environmentalmonitoring.alberta.ca/resources/standards-and-protocols/

Pomeroy, J. W., Gray, D. M., Shook, K. R., Toth, B., Essery, R. L. H., Pietroniro, A., & Hedstrom, N. (1998). An evaluation of snow accumulation and ablation processes for land surface modelling. *Hydrological Processes*, *12*(15), 2339-2367. https://doi.org/10.1002/(SICI)1099-1085(199812)12:15<2339::AID-HYP800>3.0.CO;2-L

Ryan, W. A., Doesken, N. J., & Fassnacht, S. R. (2008). Evaluation of Ultrasonic Snow Depth Sensors for U.S. Snow Measurements. *Journal of Atmospheric and Oceanic Technology*, *25*(5), 667-684. https://doi.org/10.1175/2007jtecha947.1

Seidel, F. C., Rittger, K., Skiles, S. M., Molotch, N. P., & Painter, T. H. (2016). Case study of spatial and temporal variability of snow cover, grain size, albedo and radiative forcing in the Sierra Nevada and Rocky Mountain snowpack derived from imaging spectroscopy. *The Cryosphere*, *10*(3).

Warren, S. G. (1982). Optical properties of snow. *Reviews of Geophysics*, *20*(1), 67-89. https://doi.org/doi:10.1029/RG020i001p00067

Warren, S. G. (2019). Optical properties of ice and snow. *Philosophical Transactions of the Royal Society A*, *377*(2146), 20180161.

Xi, Z. (2017). *Rasbian Leddar Detection Sampling Computer Program*. In University of Lethbridge.

Xi, Z., Hopkinson, C., Rood, S. B., Barnes, C., Xu, F., Pearce, D., & Jones, E. (2019). A Lightweight Leddar Optical Fusion Scanning System (FSS) for Canopy Foliage Monitoring. *Sensors*, *19*(18), 3943.

# 5 Comparing Mountain Snowpack Depth Model Results from Different Airborne Laser Scanning Flight Path Samples


## Abstract

The objective of this study is to evaluate the performance of an Airborne Laser Scanning (ALS) snow sampling strategy using two distinct flight paths within a mountainous watershed. Drivers of snow depth variability (canopy, elevation, topographic position index, aspect) were used to generate a classified snow accumulation unit (SAU) raster for the Westcastle watershed, Alberta (103 $km^2$). A "Least Cost Path" (LCP) analysis and an 'expert' three-transect selection (T3) were used to create two flight path scenarios that each sampled <18% of the watershed area and maximized the number of represented SAUs. Watershed "wall-to-wall" snow depth was predicted from the T3, LCP, and combined T3+LCP sampling data using ESRI's Forest Based Regression. The variance was ~ 83% for each of the three FBR scenarios. However, validation of the watershed-wide observed versus FBR predicted snow depth at watershed-scale produced $R^2$ = 0.72 and RMSE = 0.38m for the combined T3+LCP flight line and $R^2$ = 0.66 (RMSE = 0.43m) for T3 alone. The LCP sampling did not perform as well ($R^2$ = 0.34, RMSE = 0.61m), indicating grid cell-level SAU attributes need to be supplemented by latitudinal and longitudinal sampling that captures beyond grid cell-level hydro-climatological trends across the watershed. By flying sampling corridors that capture land surface attributes representative of the spatial variability of snow depth, watershed-scale snow volumes can be predicted.



**Citation:**

Barnes, C., & Hopkinson, C. (2022). Comparing Mountain Snowpack Depth Model Results from Different Airborne Laser Scanning Flight Path Samples. *Canadian Journal of Remote Sensing*, *48*(1), 81-92. https://doi.org/10.1080/07038992.2021.1999797

**Author Contributions:**

Conceptualization: Chris Hopkinson and Celeste Barnes
Methodology: Celeste Barnes
Software: Celeste Barnes
Validation: Chris Hopkinson
Formal analysis: Celeste Barnes
Investigation, Celeste Barnes and Chris Hopkinson
Resources: Chris Hopkinson
Data curation, Celeste Barnes
Writing - original draft preparation: Celeste Barnes
Writing - review and editing: Celeste Barnes and Chris Hopkinson
Visualization: Celeste Barnes
Supervision: Chris Hopkinson
Project administration: Chris Hopkinson
Funding acquisition: Chris Hopkinson
All of the authors have read and agreed to the published version of the manuscript.



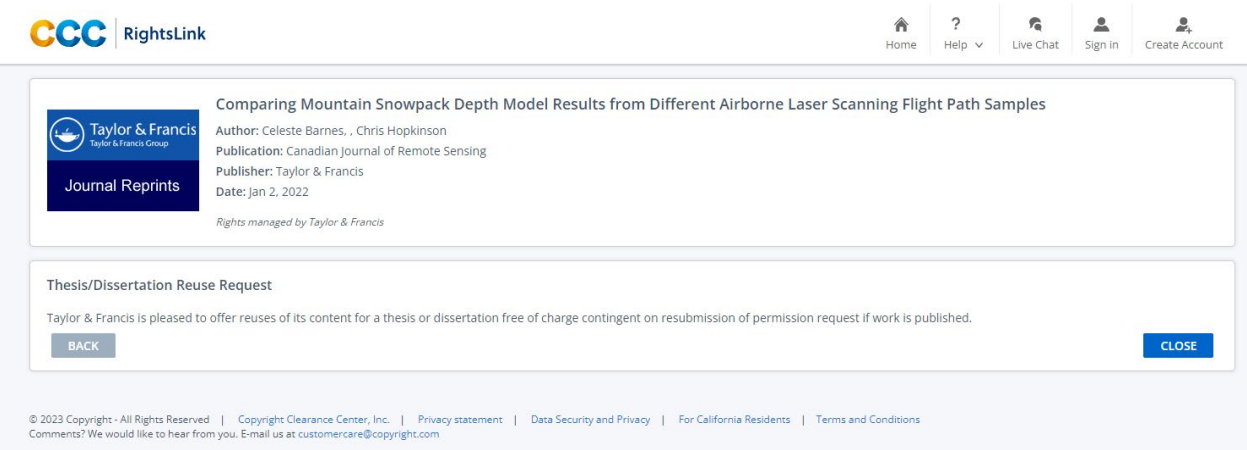

## 5.1 Introduction

Winter snow accumulation and subsequent snowmelt can be a dominant contributor to a region's water resources, as is the case in Western Canada (Natural Resources Canada, 2010). This has been recognised in the Government of Alberta's "Water for Life" initiatives that promoted better understanding and sustainable management of water resources draining the Eastern Slopes of the Canadian Rockies (Alberta Environment, 2003). Mountain snowpack monitoring (Government of Alberta, 2018) is an important part of Alberta's water supply (Alberta Environment, 2003) and flood risk forecasting (Alberta Environment, 2009). The Government of Alberta collects field snowpack data across the Eastern Slopes every month during winter (Pickering, 2018).

There is high spatial variability of snow depth in mountain environments (Botteron et al., 2013) so manual sampling alone cannot characterize snowpack depths and volumes at a watershed-scale. Quantifying the Snow Water Equivalent (SWE) stored in the snowpack is a key factor in estimating available mountain headwater resources, and it is obtained by multiplying snowpack depth and density. Depth is the more important variable to capture due to site level averages ranging from no snow to centimetres to metres, while late winter density tends to fall within a limited range of 30-50% (Cartwright et al., 2020). An overarching objective of the research presented is to devise an efficient remote sensing snow depth sampling and prediction framework that complements existing field monitoring to deliver a spatially explicit operational data product at the watershed-scale.

Airborne laser scanning (ALS) can map mesoscale watersheds at sub-metre spatial resolution. A high-resolution snow depth model (SDM) is created from ALS by subtracting a snow-free digital elevation model (DEM) from an ALS snow surface model (SSM) (Deems et

al., 2013; Hopkinson, Collins, et al., 2012; Hopkinson et al., 2004). ALS coverage for a single flight mission over the mountains in winter is limited to a few hundred square kilometres. Due to limited daylight and favourable flying conditions in winter, ALS snow depth mapping across entire Canadian Rockies' headwater watersheds is not viable as an operational public sector monitoring tool. Therefore, there is a need for suitable flight line sampling strategies that do not rely on "wall-to-wall" coverage (e.g. (Cartwright et al., 2021). Due to the physical constraints of fixed wing aircraft operations, the only practical flight configurations for airborne sampling are either grid or corridor-based missions. Therefore, it is not possible to design a perfect random sampling approach, as to do so would, for practical purposes, require we cover most of the watershed area, and thus defeat the purpose of sampling, which is to save time and cost. The intent of the aerial sampling design is to include as much randomness in the sample as is practically feasible by following a path that contains as much sample variance as possible (Kothari, 2004; Teddlie & Yu, 2007).

To reduce ALS mission sampling time, a single corridor-based flight line through the watershed can be created using a "Path Finding" strategy (Madkour et al., 2017). Static goal-oriented shortest-path algorithms attempt to find routes from predetermined source to destination points of interest (Zhiguang & Doren, 2011) based on the shortest distance and "cost" accumulated from cells between the two points. Path finding techniques are used in a variety of areas, a few of those being transportation systems, computer games (Zhiguang & Doren, 2011), sightseeing tours (Wörndl et al., 2017), migration patterns (Gustas & Supernant, 2017), and wildlife monitoring (Alexander et al., 2016). Landscape features are used to develop cost surfaces, which are used to find the easiest traversable routes between points of interest (also known as the "static goals").

The objective of this technical note is to build on preliminary lidar sampling and imputation work by Cartwright et al. (2021) and evaluate two systematic ALS flight line sampling strategies for predicting watershed-wide snow depth. The proposed sampling strategy involves finding flight paths through the watershed that adequately represent snow depth variation across terrain and landcover classes, such that a watershed-wide map of spatially explicit snow depth can be predicted.

## 5.2 Experimental Design

Phase one of this snowpack monitoring framework was demonstrated by (Cartwright et al., 2020; Cartwright et al., 2021). Watershed-wide snow depth was predicted using the R-Studio (R Core Team, 2020; RStudio Team, 2020) Random Forest tool. Two ALS sample lines flown along either edge of the Westcastle watershed demonstrated that while snow depth could be modeled across the watershed, this form of flight path sampling produced large errors due to under-represented SAUs. The present study is the next phase in the development of an operational snow depth monitoring framework, where two different sampling strategies are systematically tested and compared. The innovation here is not that ALS or Random Forest can be used to reconstruct snow depth beyond the area sampled, rather it is that the flight line sampling path matters and that reasonable watershed-wide estimates can be obtained with < 20% sampling if configured to capture the main sources of snow depth variation in the watershed. The ALS sampling scenarios were tested with the same 24-Feb-2014 ALS SDM dataset used by Cartwright et al. (2021), where watershed-wide snow depth mapped at 1m grid cell resolution was observed to vary from 0 to >10 m, with a mean of 1.5 m. The ESRI 64-bit ArcPro (ESRI, 2020a) version 2.5 software routines were used for spatial prediction purposes, as these tools are

simple to implement and are accessible to public sector practitioners. The random forest algorithm based on Breiman (2001) was introduced into ArcPro. The tool simplifies the selection of most of the training and prediction configuration parameters and adds the potential for future automation. The purpose of this phase of the study is to evaluate two sampling strategies that attempt to represent the natural variability in snowpack at watershed-scale in a time- and cost-effective manner, and then to predict snow depth across the full watershed.

While dominant snow depth controls vary across mountain regions (Grünewald et al., 2013), elevation, aspect, terrain relief, and forest cover are known to be important drivers of late winter snowpack distributions in Alberta's Eastern Slopes (Cartwright et al., 2020). Snow depth tends to increase with elevation above the valley floor and is greatest in the treeline ecotone (Hopkinson, Pomeroy, et al., 2012). More snow is present below rocky outcrops (Grünewald et al., 2014) and across shallower slopes with features such as gullies and bowls. In alpine areas, there is no significant vegetation to trap snow, and high winds cause scouring resulting in snow-free or shallow snow depths on exposed high elevation slopes. Snow depth increases on leeward sides of slopes from blowing snow (Anderson et al., 2014; Mott et al., 2014). Snow is more persistent over north-facing aspects and melts out more quickly over south-facing aspects (Dornes et al., 2008). Mature and denser vegetative canopies intercept snow resulting in less snow at the ground surface (Veatch et al., 2009).

Landscape and terrain drivers of snow depth were combined into a Snow Accumulation Unit (SAU) raster for the watershed, such that equivalent SAU signatures can exist in multiple locations within the watershed. The flight paths over these SAUs need to be constrained to a small number of "straight-line" segments with minor heading changes, so an airplane can fly through the watershed with minimal attitude variation. Using airborne corridor flight paths

means strict random sampling is not possible from a practical standpoint. ALS flight lines were created by traversing the watershed capturing as many unique SAU signatures as possible. Random Forest (RF) machine learning was then used to train and predict the spatial variation in watershed-wide snow depth from the sampled flight path data. RF machine learning is a statistical tool (Breiman, 2001) that fits both categorical or continuous data with probability or regression decision trees. The seeding function in RF algorithms is used to randomly sample data within the flown corridor to build decision trees for model training and subsequent prediction.

## 5.3 Data and Methods

The study area is the Westcastle watershed (103 $km^2$) in the Canadian Rocky Mountain Eastern Slope headwaters of the Oldman River Basin, Alberta (McCaffrey & Hopkinson, 2020).

To create the base snow depth model (SDM), two ALS "wall-to-wall" surveys were flown over the Westcastle watershed by Airborne Imaging (Calgary, Alberta). The "snow-off" survey took place on 20-Sep-2014 using a Leica ALS 70 sensor at an altitude of 11,000 ft and ground speed of 140 kts. The pulse repetition rate was 130 kHz, scan frequency of 27 Hz, and Field Of View (FOV) was 42°. The "snow-on" survey was collected on 24-Feb-2014 using an ALTM 3100EA sensor at a flying altitude of 11,000 ft and ground speed of 130 kts. The pulse repetition rate was 50 kHz, scan frequency of 28.5 Hz, and scan angle was ± 20. The datasets were processed in the horizontal NAD83(CSRS) / UTM zone 11N and vertical CGVD28 reference frames.

ALS data collected from both survey missions were processed using Bentley (Bentley Systems Inc., 2016) MicroStation version 8i/TerraScan (Terrasolid Limited, 2020), Golden (Golden Software LLC, 2020) Surfer version 11, and Golden Scripter. The Bentley/TerraScan

software application was used to process the raw point clouds for both missions. The "wall-to-wall" point dataset was divided into tiles for QA and classification. Air and isolated points were deleted from the datasets. Ground was classified from single and last returns. The TerraScan ground classification algorithm uses a "minimal" point selection criterion where only points on a plane that vary in elevation or slope by a set threshold are added to the ground class. The ground class was output from Bentley/TerraScan and used to create a gridded digital elevation model (DEM). Golden Scripter was configured with a triangular irregular network (TIN) interpolation method at a one-metre grid cell size to create a DEM (one for each of the snow-off and snow-on datasets). The SDM was created by subtracting the snow-off DEM ($DEM_{snow\text{-}off}$) from the snow-on DEM ($DEM_{snow\text{-}on}$).

$$SDM = DEM_{snow\text{-}on} - DEM_{snow\text{-}off} \tag{5.1}$$

A canopy height model (CHM) requires both a digital surface model (DSM) and a DEM from the same point cloud dataset. The DSM is generated from all points in all classes. Bentley/TerraScan was used to output an "all" point dataset. There is potential for multiple points to be located within the same grid cell when gridding the data, therefore Golden Scripter was configured using a localized maximum interpolation method with "all" data to create the DSM. The CHM was generated by subtracting the DEM from the DSM.

$$CHM = DSM - DEM \tag{5.2}$$

The DEM, SDM, and CHM models were aggregated to 100 m grid cell size for fast model execution, to minimise the influence of 1m grid cell level noise or errors and in preparation for future implementations at regional scales, which is the ultimate goal of this operational research.

A watershed SAU raster was created using four dominant snow depth drivers, those being canopy height, elevation, topographic position index (TPI) (Weiss, 2001), and aspect (Cartwright et al., 2020) to stratify the watershed into feature class signatures. For the purpose of identifying unique snow depth driver signatures, feature classes were binned into a minimal number of categories to reduce the complexity and number of unique SAUs required for pathfinding. Three of the four characteristics (Figure 5.1), elevation, TPI, and aspect, were computed from the 100 m aggregated DEM. The elevation driver was binned into 200 m intervals up to the upper edge of the treeline ecotone. The highest elevation class greater than 2,200 m represents exclusively alpine terrain (Downing & Pettapiece, 2006). TPI was classified into "Depression" for grid cell values < -0.1 and "Upland" > 0.1. The TPI algorithm outputs values near zero for landforms with a flat or constant slope plane. The category "Flat" represents values between -0.1 and 0.1. Aspect was classified into cardinal directions of "North", "East", "South", and "West". The fourth driver, canopy height (Figure 5.1), was extracted from the aggregated 100 m mean CHM. The Short or "Open" class represented mean canopy height < 0.5 m, the "Intermediate" class 0.5 < 4 m, and the "Tall" class > 4 m. These four data types were combined to develop a spatially distributed SAU model for the snow depth drivers across the watershed. Some signature combinations do not exist in the Westcastle watershed. For example, there are no SAUs representing "tall-canopy" at alpine elevations, as the alpine zone is, by definition, above treeline.

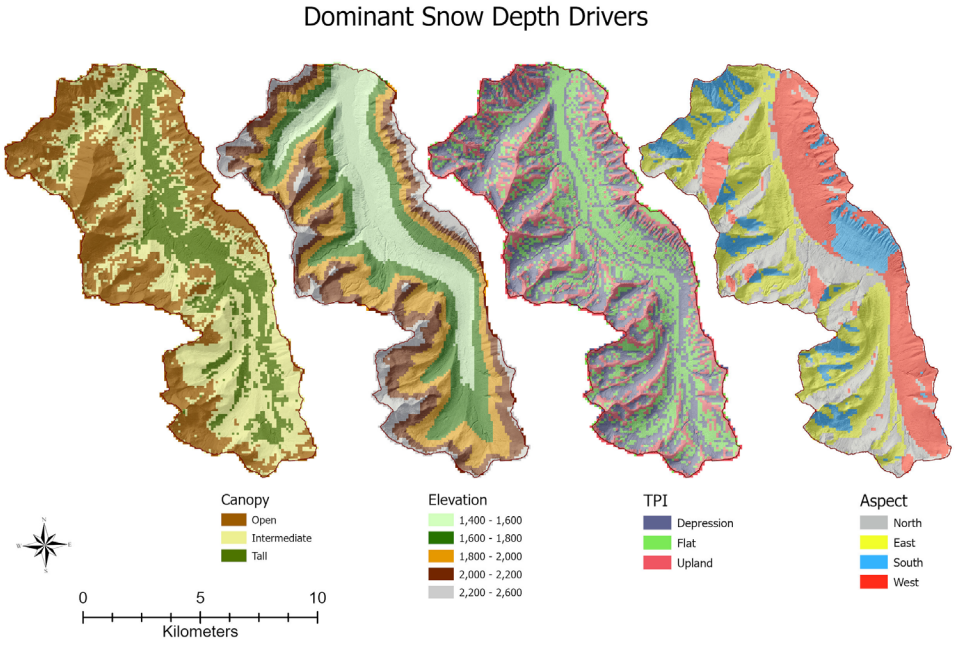


Figure 5.1. Westcastle Snow Depth drivers – left: Canopy; left-centre: Elevation; right-centre: TPI (topographic position index); right: Aspect.

Two corridor-based path finding strategies were used to create ALS sampling flight lines that covered as large a range as possible of snowpack driver conditions experienced in the watershed (shown in Figure 5.2). As the watershed has a dominant north to south linear orientation, one of the flight lines was set up to approximately follow this latitudinal gradient while attempting to sample the natural variability in SAUs along this length in an efficient manner. This flight path was created using an ESRI (2020b) ArcPro "Least Cost Path" (LCP) "static goal-oriented" analysis. The LCP algorithm finds a continuous path from a start point to end point with the least accumulated cost. The "cost" surface for the LCP flight line was generated from the SAU raster. The "cost" assigned to each grid cell was derived from the percentage of the grid cell's SAU category that was represented in the entire watershed. SAUs of small contiguous areas were favoured to maximize the number of SAUs. The LCP path start point was located at the outlet of the watershed adjacent to the University of Lethbridge

Westcastle field station (WFS) where several hydro-meteorological variables are monitored, including snow depth (Barnes et al., 2020). Several LCP endpoints were identified and tested furthest from the start point to ensure the full watershed would be traversed to define a sampling line that passed through as many SAUs as possible. The LCP algorithm created an irregular path through the watershed, which could not be flown as presented due to the number and steepness of sharp turns. The path was smoothened by constraining heading changes to less than 30°, to ensure the turns could be implemented in a survey aircraft, producing an operationally viable flight path where the entire LCP derived path was covered within the extent of the sensor swath.

Another sampling flight configuration that emphasized east to west variations was generated using an 'expert' selection criterion to sample the length, width, and elevation range of the watershed. The watershed was divided into three zones (north, centre, and south). Corridors at 500 m spacing intervals were created perpendicular to the watershed centreline. One corridor was selected from each of the north, centre, and south zones such that the total number of combined SAUs was maximized.

Snow depth was extracted from the 24-Feb-2014 ALS SDM for the LCP, T3, and "combined T3 + LCP" flight line swaths and used to train a "Forest Based Regression" (FBR) model (ESRI's ArcPro "Random Forest" tool, (ESRI, 2020c)) for the entire watershed. The SAU raster was not used as an input to the FBR models since the snow depth drivers were divided into categorical classes to get a good cross section representation of land covers and terrain types for sampling purposes only. For the FBR training and prediction models, only continuous variables were used to mitigate potential bias in subsequent variable importance results (Strobl et al., 2007), and all variables were weighted equally. ESRI's FBR tool allows for multiple raster and vector data for explanatory training variable inputs. Latitude, longitude and slope were added

along with the CHM, DEM, TPI, and aspect rasters; as these geographic variables are proxies for synoptic weather patterns and in situ environmental controls. FBR training and validation strategies focus on leaving out a portion of the sampled dataset during model training (Gasch et al., 2015). These data are then used in the validation phase (Juel et al., 2015; Li, 2016). All three FBR model configuration settings were 500 trees, 100 independent runs with 20% of the total dataset randomly excluded (set aside) from the training run and subsequently used for the model validation run. After several iterations of model training for each of the models, performance improved when the configuration setting for the number of trees increased from 100 to 500 but no improvement occurred beyond values > 500. Validation results for model training are based on the median R-Squared, p-value, and standard error of all 100 runs. These trained models were then used to predict watershed-wide "wall-to-wall" snow depth. Each of the flight line-sampled then predicted "wall-to-wall" snow depth models were then compared with the observed (i.e. fully surveyed) watershed-wide SDM.

## 5.4 Results and Discussion

The final SAU raster (Figure 5.2) contained 163 of a possible 180 spatially distributed SDM signatures for the Westcastle watershed. The LCP flight line traversed north-south through the watershed. The "LCP Result" (brown) is the path computed by the ESRI LCP toolset. The black line shows the "LCP Flight Line". The "LCP Flight Swath" sampled 138 unique SAUs. The "Transect Lines" (blue) used three transects (T3) in an east-west orientation from a north, centre, and south watershed zone. The "Transect Flight Swath" contained the same number of grid cells as the LCP flight swath and sampled 143 SAUs (5 more than the LCP configuration).

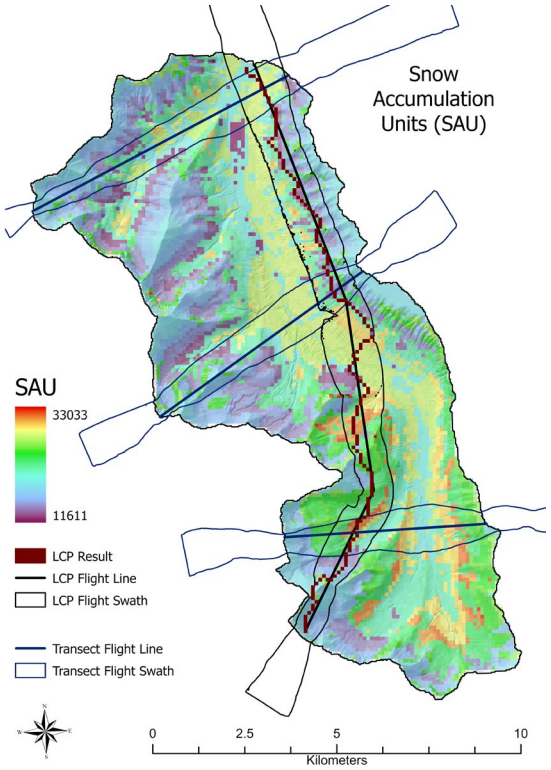


Figure 5.2. SAU map for the Westcastle watershed illustrating the ALS sample flight paths and swaths for the LCP and T3 configurations. SAU values are derived by snow depth driver categories added together where Canopy is the x0,000 variable; Elevation is xx00; TPI is x0, and Aspect is the x (one's variable).

Table 5.1 presents the breakdown of SAUs for the "wall-to-wall" watershed, LCP and T3 flight lines. The SAU section lists each of the snow depth driver category breakpoints. The "Watershed" section shows the number of grid cells and percentage each class occupies in the "wall-to-wall" extent. The columns under "Watershed" for LCP and T3 show the number of sampled grid cells and percentage within the watershed. The "Flight Line" column contains the sampling percentage of the category within the flight line. Of note, there is an elevation sampling bias for the T3 flight line. The largest number of watershed grid cells (2509) was in the "1800 – 2000 m" category (24.4% of the watershed). T3 had the highest sampling in the lowest (1400 - 1600) elevation category at 708 grid cells (30.8%) which was 39.0% of flight line samples. For the LCP flight line, there is a sampling bias in aspect. The "East" directional "Aspect" followed by "West" contains the highest number of grid cells within the watershed at 3618 (35.2%) and

2792 (27.1%), respectively. LCP sampled the largest number of grid cells in the "West" aspect at 757 (27.1% of the watershed) which was 41.7% of flight line samples. Sampling for "East" was next highest at 384 grid cells (LCP flight line of 21.1%) but represented the lowest percentage in the watershed at 10.6%.

Table 5.1. SAU (Snow Accumulation Unit) snow depth drivers; GC – the number of grid cells in the category; % - percentage of the category within the watershed; FL% - percentage of the category sampled within the flight line.

| | **Watershed Wall-to-Wall** | | **LCP Flight Line Sampled** | | | **T3 Flight Line Sampled** | | |
|---|---|---|---|---|---|---|---|---|
| ***Snow Accumulation Unit (SAU)*** | | | | | Flight | | | Flight |
| | | | Watershed | | Line | Watershed | | Line |
| *Driver* | GC | % | GC | % | FL% | GC | % | FL% |
| *Canopy* | | | | | | | | |
| Open | 3956 | 38.4% | 609 | 15.4% | 33.5% | 483 | 12.2% | 26.6% |
| Intermediate | 4028 | 39.1% | 645 | 16.0% | 35.5% | 763 | 18.9% | 42.0% |
| Tall | 2308 | 22.4% | 563 | 24.4% | 31.0% | 571 | 24.7% | 31.4% |
| *Elevation* | | | | | | | | |
| 1400 - 1600 | 2300 | 22.3% | 438 | 19.0% | 24.1% | 708 | 30.8% | 39.0% |
| 1600 - 1800 | 2388 | 23.2% | 468 | 19.6% | 25.8% | 440 | 18.4% | 24.2% |
| 1800 - 2000 | 2509 | 24.4% | 534 | 21.3% | 29.4% | 280 | 11.2% | 15.4% |
| 2000 - 2200 | 2061 | 20.0% | 269 | 13.1% | 14.8% | 273 | 13.2% | 15.0% |
| 2200 - 2600 | 1034 | 10.0% | 108 | 10.4% | 5.9% | 116 | 11.2% | 6.4% |
| *TPI* | | | | | | | | |
| Depression | 4105 | 39.9% | 688 | 16.8% | 37.9% | 748 | 18.2% | 41.2% |
| Flat | 3491 | 33.9% | 732 | 21.0% | 40.3% | 681 | 19.5% | 37.5% |
| Upland | 2696 | 26.2% | 397 | 14.7% | 21.8% | 388 | 14.4% | 21.4% |
| *Aspect* | | | | | | | | |
| North | 2305 | 22.4% | 347 | 15.1% | 19.1% | 438 | 19.0% | 24.1% |
| East | 3618 | 35.2% | 384 | 10.6% | 21.1% | 618 | 17.1% | 34.0% |
| South | 1577 | 15.3% | 329 | 20.9% | 18.1% | 240 | 15.2% | 13.2% |
| West | 2792 | 27.1% | 757 | 27.1% | 41.7% | 521 | 18.7% | 28.7% |
| *Watershed Totals* | 10,292 | 100% | 1817 | 17.7% | 100% | 1817 | 17.7% | 100% |

The FBR-Training run "Prediction Interval" charts in Figure 5.3 show the training and validation prediction, P05 and P95 confidence intervals for T3, LCP and "Combined T3 + LCP". The confidence intervals for the LCP flight line are slightly larger than those of the T3 flight line. The upper end snow depth prediction for LCP is lower than both the T3 and combined T3 + LCP models. The "Variable Importance" (the most important "Explanatory Training" variables) for the LCP flight line (Figure 5.3, "Importance") was latitude (31%) followed by longitude (18%), elevation (14%), canopy (12%), and aspect (11%). Both the TPI and slope were the least

important in this model. In comparison, the T3 flight line (Figure 5.3, “Importance”) shows the most important was elevation (24%) followed by canopy (18%), TPI (16%), latitude (15%) and aspect (11%). Longitude and slope were the least important in this trained model. In the combined T3 + LCP training model (Figure 5.3, “Importance”), the most important variable was latitude (22%) then elevation (20%) followed by canopy (15%), aspect (14%), TPI (12%) and longitude (11%). Slope was the least important variable. The “Training” R-Squared values for all models are high at 0.97. Similarly, the p-value and Standard Error values are close to zero. FBR models can over-fit the training data to the model (Altman & Krzywinski, 2017; Tang et al., 2018). A more accurate measure of model fit uses the “Validation” R-Squared, p-value and Standard Error statistics, which are calculated using the data set aside during training as shown in Figure 5.3, “Validation” section. The validation R-Squared value for the T3 flight line ($R^2$ = 0.84) is only marginally better than both the LCP flight line ($R^2$ = 0.83) and combined T3 + LCP ($R^2$ = 0.83). These FBR validation results from the T3 + LCP run are not significantly different to T3 and LCP, despite containing more sample data.

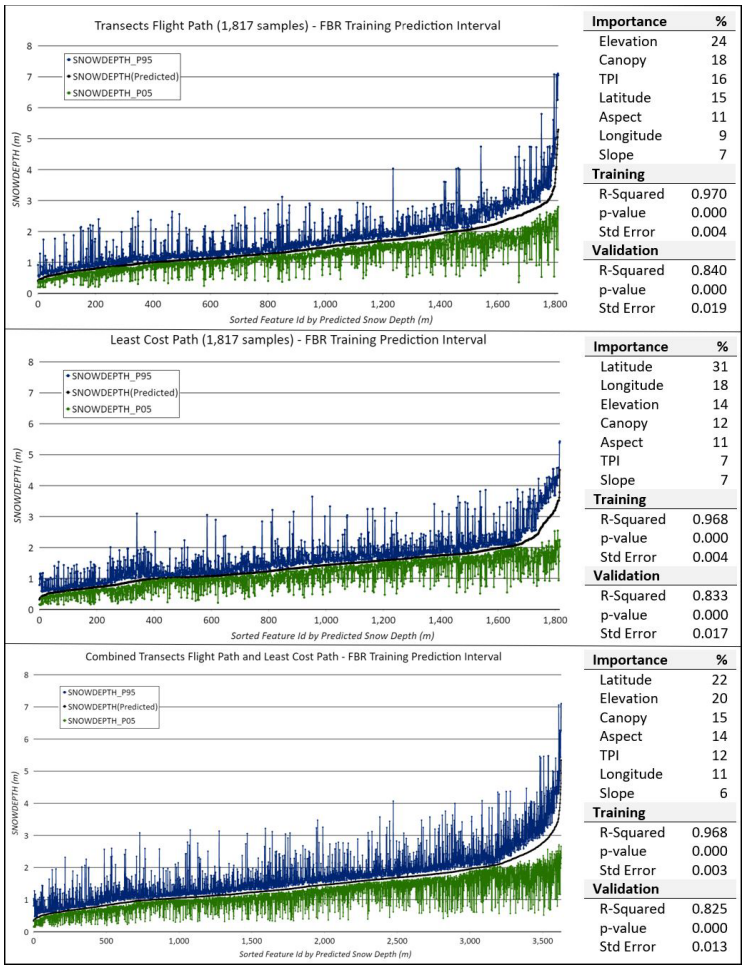


Figure 5.3. Forest Based Regression Snow Depth Prediction: Top: T3 (n = 1,817). Center: LCP (n = 1,817). Bottom: Combined T3 + LCP (n=3,634), where n is the number of grid cell samples.

The FBR-Prediction runs for the "wall-to-wall" watershed produced validation "Out of Bag Errors" (explained variance) for all three models of 83%. The Root Mean Squared Error (RMSE) for the T3 flight line was RMSE = 0.29, the LCP flight line had a RMSE = 0.26, and the combined T3 + LCP was RMSE = 0.28. However, a more comprehensive independent evaluation of the FBR-Prediction model results is shown in Figure 5.4 where watershed-wide FBR predicted snow depth was compared to the full watershed-wide ALS SDM. Areas in blue indicate an overestimation of snow depth and red an underestimation. All FBR models show snow depth underestimations near ridges and steeper slopes. The T3 flight line model (Figure

5.4a) predicts snow depth better in the lower elevations with some underestimation at alpine elevations. The elevation sampling bias (Table 5.1) associated with the T3 flight line suggests more attention is needed to set up flight lines to uniformly sample the elevation distribution given the high rank importance of this driver variable. The LCP model (Figure 5.4b) shows overestimation on the eastern side of the watershed and underestimation in the northern west side, suggesting that the dominant north-south trend of the line was insufficient to capture meso-scale east-west variations in snow depth. The aspect with the largest representation in the watershed (Table 5.1) is East (35% of the grid cells). The LCP flight line has a sampling bias in aspect with 42% of the flight line samples having a West aspect (27% of the watershed grid cells). Only 11% of the watershed sampling for the LCP flight line is in the East aspect category. The combined T3 + LCP also underestimates depth in alpine areas.


Figure 5.4. Watershed "Wall-to-Wall" Difference for FBR Predicted snow depth minus Actual snow depth for the 24-Feb-2014 ALS SDM. Positive values (blue) are an over estimation of snow depth. Negative values (red) are an under estimation of snow depth. (a) T3, (b) LCP, and (c) Combined T3 + LCP

A scatter plot of the watershed "wall-to-wall" ALS SDM observed versus FBR predicted snow depth (Figure 5.5) shows the combined T3 + LCP has the highest agreement with $R^2$ = 0.72, and T3 with $R^2$ = 0.66. The LCP flight line does not perform as well with $R^2$ = 0.34, most likely due to insufficient representation of the east-west trends (i.e. longitudinal variation) in snow depth across the mountain range. The calculated (Predicted – Observed) means for the combined T3 + LCP model of -0.04 m (RMSE = 0.38 m) is small but suggests beyond grid-cell

level environmental controls, such as gravity- or wind-induced snowpack redistribution may need to be further considered as part of the prediction routine to mitigate such bias. The ESRI FBR toolset interpolates predicted values within the sample range of the explanatory training data variables. Prediction for data point values outside the range of the training data are not extrapolated by the algorithm. The T3 and LCP sampled flight lines do not contain the entire range of FBR explanatory variable data.

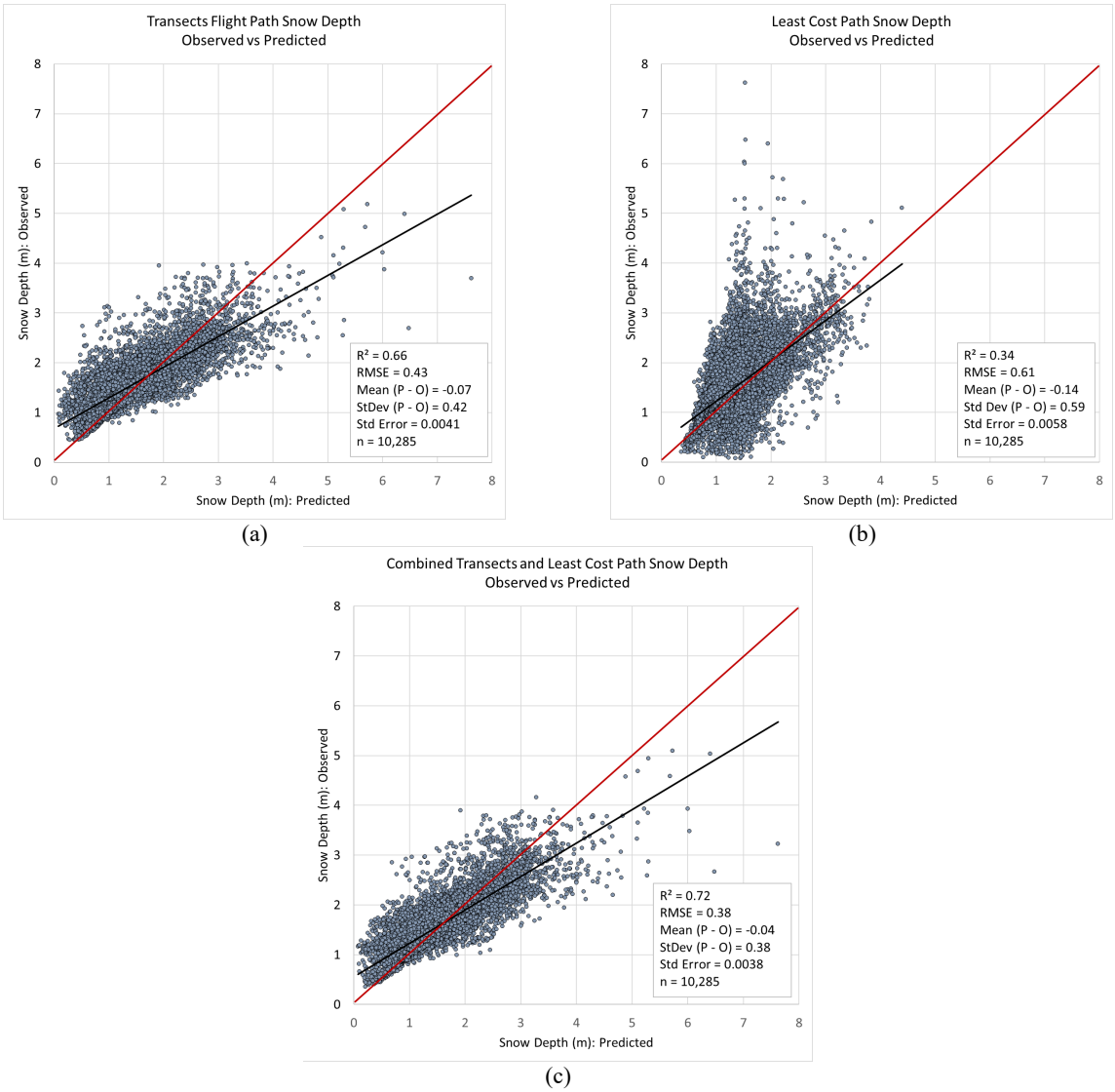


Figure 5.5. ALS SDM observed snow depth versus FBR predicted snow depth. (a) T3, (b) LCP, (c) Combined T3 + LCP

## 5.5 Conclusion

A Snow Accumulation Unit (SAU) model was created for the Westcastle watershed using canopy, elevation, TPI and aspect. The watershed was categorized into 163 SAUs, and two ALS flight sampling configurations were created from the SAU layer, each sampling ~18% of the watershed area. An ArcPro "Least Cost Path" (LCP) analysis was used as a seed to generate a simplified flight path containing 138 SAUs. An east-west flight configuration was created using an 'expert' selection of three transects (T3) perpendicular to the watershed centre line representing 143 SAUs. The Forest Based Regression (FBR) prediction models explained ~83% of the variance with latitude being the most important variable for the LCP model, while elevation was most important for the T3 model. Comparing predicted and observed snow depth for the LCP, T3 and combined LCP + T3 FBR models, there was underestimation in the upper alpine regions and overestimation in lower elevations. Watershed "wall-to-wall" ALS observed versus FRB predicted snow depth produced the highest $R^2$ of 0.72 (RMSE = 0.38 m) for the combined T3 + LCP model, $R^2$ of 0.66 (RMSE = 0.43 m) for T3, and the lowest $R^2$ of 0.34 (RMSE = 0.67 m) for the LCP flight line. The predicted minus observed snow depth means range from -0.04 m for T3 + LCP to -0.14 m for LCP only. While the explanation of variance within sampled flight lines was > 80%, when comparing the FBR sample-predicted SDM to the observed watershed SDM, the explanation of variance dropped by 10 to 15%. By adopting a flight line sampling approach relative to "wall-to-wall", the overall average depth prediction is still within ~0.1 m (or <7%) of observed. From an operational time and cost savings perspective, the reduction in explained variance and potential for a small amount of bias is acceptable. These results indicate that flight line sampling and machine learning prediction can be effective at reconstructing snow depth at the watershed-scale but the orientation and SAU sampling

configuration are key aspects of sampling that must be optimised to represent the dominant snow depth driver attributes across the watershed. Utilizing an optimal sampling of representative SAUs versus “wall-to-wall” mapping approach reduces flight time over the watershed by ~ 80%, which: a) greatly reduces the logistical costs for a watershed-scale snow depth data collection; and/or b) allows for snow depth sampling and modelling over an area of > 500 $km^2$ for the time it would normally take to survey ~100 $km^2$.

## 5.6 References


Alberta Environment. (2003). Water for Life - Alberta's Strategy for Sustainability. In. Government of Alberta. http://aep.alberta.ca/water/programs-and-services/water-for-life/strategy/downloadable-information-about-the-water-for-life-strategy.aspx

Alberta Environment. (2009). Water for Life - Action Plan. In. Edmonton, AB: Government of Alberta.

Alexander, J. L., Olimb, S. K., Bly, K. L. S., & Restani, M. (2016). Use of least-cost path analysis to identify potential movement corridors of swift foxes in Montana. *Journal of Mammalogy*, *97*(3), 891-898. https://doi.org/10.1093/jmammal/gyw032

Altman, N., & Krzywinski, M. (2017). Ensemble methods: bagging and random forests [Article]. *Nature Methods*, *14*, 933+. https://link.gale.com/apps/doc/A625179388/HRCA?u=leth89164&sid=googleScholar&xid=7d23e5a1

Anderson, B. T., McNamara, J. P., Marshall, H. P., & Flores, A. N. (2014). Insights into the physical processes controlling correlations between snow distribution and terrain properties. *Water Resources Research*, *50*(6), 4545-4563. https://doi.org/doi:10.1002/2013WR013714

Barnes, C., Hopkinson, C., Porter, T., & Xi, Z. (2020). In-Situ LED-Based Observation of Snow Surface and Depth Transects. *Sensors*, *20*(8), 2292. https://www.mdpi.com/1424-8220/20/8/2292

Bentley Systems Inc. (2016). *MicroStation*. In (Version 8i) Bentley Systems Inc.,.

Botteron, C., Dawes, N., Leclère, J., Skaloud, J., Weijs, S. V., & Farine, P.-A. (2013). Soil Moisture & Snow Properties Determination with GNSS in Alpine Environments: Challenges, Status, and Perspectives. *Remote Sensing*, *5*(7), 3516-3543. http://www.mdpi.com/2072-4292/5/7/3516

Breiman, L. (2001). Random Forests. *Machine Learning*, *45*(1), 5-32. https://doi.org/10.1023/A:1010933404324

Cartwright, K., Hopkinson, C., Kienzle, S., & Rood, S. B. (2020). Evaluation of temporal consistency of snow depth drivers of a Rocky Mountain watershed in southern Alberta. *Hydrological Processes*, *n/a*(n/a). https://doi.org/https://doi.org/10.1002/hyp.13920

Cartwright, K., Mahoney, C., & Hopkinson, C. (2021). Machine Learning Based Imputation of Mountain Snowpack Depth within an Operational Lidar Sampling Framework in Southwest Alberta. *Canadian Journal of Remote Sensing*(In Review).

Deems, J. S., Painter, T. H., & Finnegan, D. C. (2013). Lidar measurement of snow depth: a review. *Journal of Glaciology*, *59*(215), 467-479.

Dornes, P. F., Pomeroy, J. W., Pietroniro, A., Carey, S. K., & Quinton, W. L. (2008). Influence of landscape aggregation in modelling snow-cover ablation and snowmelt runoff in a sub-arctic mountainous environment. *Hydrological Sciences Journal*, *53*(4), 725-740. https://doi.org/10.1623/hysj.53.4.725

Downing, D. J., & Pettapiece, W. W. (2006). Natural Regions Committee 2006. Natural Regions and Subregions of Alberta In. Edmonton, AB: Government of Alberta. Pub. No. T/852. .

ESRI. (2020a). *ArcGIS Pro*. In Copyright © 1995-2020 Esri.

ESRI. (2020b). *ArcGIS Pro Cost Path (Spatial Analyst)*. In Copyright © 1995-2020 Esri. https://pro.arcgis.com/en/pro-app/latest/tool-reference/spatial-analyst/creating-the-least-cost-path.htm

ESRI. (2020c). *ArcGIS Pro Forest-based Classification and Regression (Spatial Statistics)*. In Copyright © 1995-2020 Esri. https://pro.arcgis.com/en/pro-app/latest/tool-reference/spatial-statistics/forestbasedclassificationregression.htm

Gasch, C. K., Hengl, T., Gräler, B., Meyer, H., Magney, T. S., & Brown, D. J. (2015). Spatio-temporal interpolation of soil water, temperature, and electrical conductivity in 3D + T: The Cook Agronomy Farm data set. *Spatial Statistics*, *14, Part A*, 70-90. https://doi.org/https://doi.org/10.1016/j.spasta.2015.04.001

Golden Software LLC. (2020). *Surfer*. In Copyright © 1993-2021, Golden Software, LLC.

Government of Alberta. (2018). *Snow Does Not Equal Flood: Alberta's Snowmelt and its Impact on Alberta Rivers*. Edmonton, AB: alberta.ca Retrieved from https://open.alberta.ca/publications/snow-does-not-equal-flood-alberta-s-snowmelt-and-its-impact-on-alberta-rivers

Grünewald, T., Bühler, Y., & Lehning, M. (2014). Elevation dependency of mountain snow depth. *The Cryosphere*, *8*(6), 2381-2394.

Grünewald, T., Stötter, J., Pomeroy, J. W., Dadic, R., Moreno Baños, I., Marturià, J., Spross, M., Hopkinson, C., Burlando, P., & Lehning, M. (2013). Statistical modelling of the snow depth distribution in open alpine terrain. *Hydrol. Earth Syst. Sci.*, *17*(8), 3005-3021. https://doi.org/10.5194/hess-17-3005-2013

Gustas, R., & Supernant, K. (2017). Least cost path analysis of early maritime movement on the Pacific Northwest Coast. *Journal of Archaeological Science*, *78*, 40-56. https://doi.org/https://doi.org/10.1016/j.jas.2016.11.006

Hopkinson, C., Collins, T., Anderson, A., Pomeroy, J., & Spooner, I. (2012). Spatial Snow Depth Assessment Using LiDAR Transect Samples and Public GIS Data Layers in the Elbow River Watershed, Alberta. *Canadian Water Resources Journal / Revue canadienne des ressources hydriques*, *37*(2), 69-87. https://doi.org/10.4296/cwrj3702893

Hopkinson, C., Pomeroy, J., Debeer, C., Ellis, C., & Anderson, A. (2012). Relationships between snowpack depth and primary LiDAR point cloud derivatives in a mountainous environment. *IAHS-AISH publication*, 354-358.

Hopkinson, C., Sitar, M., Chasmer, L., & Treitz, P. (2004). Mapping Snowpack Depth beneath Forest Canopies Using Airborne Lidar. *Photogrammetric Engineering & Remote Sensing*, *70*(3), 323-330. https://doi.org/10.14358/PERS.70.3.323

Juel, A., Groom, G. B., Svenning, J.-C., & Ejrnæs, R. (2015). Spatial application of Random Forest models for fine-scale coastal vegetation classification using object based analysis of aerial orthophoto and DEM data. *International Journal of Applied Earth Observation and Geoinformation*, *42*(Supplement C), 106-114. https://doi.org/https://doi.org/10.1016/j.jag.2015.05.008

Kothari, C. R. (2004). *Research methodology: Methods and techniques*. New Age International.

Li, J. (2016). Assessing spatial predictive models in the environmental sciences: Accuracy measures, data variation and variance explained. *Environmental Modelling & Software*, *80*, 1-8. https://doi.org/https://doi.org/10.1016/j.envsoft.2016.02.004

Madkour, A., Aref, W. G., Rehman, F. U., Rahman, M. A., & Basalamah, S. (2017). A survey of shortest-path algorithms. *arXiv preprint arXiv:1705.02044*. https://arxiv.org/abs/1705.02044

McCaffrey, D., & Hopkinson, C. (2020). Repeat Oblique Photography Shows Terrain and Fire-Exposure Controls on Century-Scale Canopy Cover Change in the Alpine Treeline Ecotone. *Remote Sensing*, *12*(10), 1569. https://www.mdpi.com/2072-4292/12/10/1569

Mott, R., Scipión, D., Schneebeli, M., Dawes, N., Berne, A., & Lehning, M. (2014). Orographic effects on snow deposition patterns in mountainous terrain. *Journal of Geophysical Research: Atmospheres*, *119*(3), 1419-1439. https://doi.org/doi:10.1002/2013JD019880

Natural Resources Canada. (2010). *Atlas of Canada, 6th Edition (archival version) Average Maximum Snow Depth*. Ottawa, ON, Government of Canada, Natural Resources Canada, Earth Sciences Sector, Atlas of Canada. https://open.canada.ca/data/en/dataset/d90ddf8f-8893-11e0-bc5e-6cf049291510

Pickering, R. (2018). *Snow Surveying Field Sampling Protocols*. Alberta Environment and Parks. http://environmentalmonitoring.alberta.ca/resources/standards-and-protocols/

R Core Team. (2020). *R: A language and environment for statistical computing. R Foundation for Statistical Computing*. In © The R Foundation. http://www.R-project.org/

RStudio Team. (2020). *RStudio: Integrated Development for R*. In RStudio, PBC. http://www.rstudio.com/

Strobl, C., Boulesteix, A.-L., Zeileis, A., & Hothorn, T. (2007). Bias in random forest variable importance measures: Illustrations, sources and a solution. *BMC Bioinformatics*, *8*(1), 25. https://doi.org/10.1186/1471-2105-8-25

Tang, C., Garreau, D., & von Luxburg, U. (2018). When do random forests fail? NeurIPS, Montreal, Canada.

Teddlie, C., & Yu, F. (2007). Mixed methods sampling: A typology with examples. *Journal of mixed methods research*, *1*(1), 77-100.

Terrasolid Limited. (2020). *Terrasolid*. In Copyright © 2008-2013 Arttu Soininen, Terrasolid. All rights reserved.

Veatch, W., Brooks, P. D., Gustafson, J. R., & Molotch, N. P. (2009). 'Quantifying the effects of forest canopy cover on net snow accumulation at a continental, mid-latitude site'. *Ecohydrology*, *2*(2), 115-128. https://doi.org/10.1002/eco.45

Weiss, A. (2001). Topographic position and landforms analysis. Poster presentation, ESRI user conference, San Diego, CA,

Wörndl, W., Hefele, A., & Herzog, D. (2017). Recommending a sequence of interesting places for tourist trips [journal article]. *Information Technology & Tourism*, *17*(1), 31-54. https://doi.org/10.1007/s40558-017-0076-5

Zhiguang, X., & Doren, M. V. (2011, 10-12 June 2011). A Museum Visitors Guide with the A* pathfinding algorithm. 2011 IEEE International Conference on Computer Science and Automation Engineering,

# 6 Mapping Watershed Snow Water Equivalent from Lidar Snow Depth and Field-Sampled Density Models

## Abstract

This study presented a snowpack monitoring framework for estimating mesoscale water yield for the West Castle watershed (WCW) located in the Alberta Rocky Mountain Eastern Slopes. Snow water equivalent (SWE) was derived from watershed snow depth and density models. Airborne lidar "bare-earth" (2014 and 2020 summer flights) were used to create digital elevation and canopy fractional coverage models (CFC). "Snow-covered" sampling (Feb 2014, Apr 2018, Mar 2020, Jan 2021. Mar 2021, Apr 2021 winter flights) were used to create snow depth models (SDM). Snow density models were stratified by elevation and the CFC modifier was used to reduced density by a maximum of 10%. Governmental AEP snow water field sampling data were used to test two snow density modelling strategies (scenario A: closest temporal sampling date, B: 30-year monthly mean sampling). A valley and a mid-mountain AEP site were used to constrain lower and upper spatially distributed density model limits for WCW. The CFC modifier reduce WCW water yield by 8% to 11%. Only the Feb 2014 lidar flight occurred on the same day as AEP snow sampling, however the 44.42 x $10^6$ $m^3$ computed water yield for scenario A was 7% lower than for scenario B (47.45 x $10^6$ $m^3$). For all other lidar snow sampling flights, there was an AEP field sampling gap of 3 days to a maximum of 9 days. WCW computed water yield differed for each of the snow density modelling scenarios. The largest deviation was for the Mar 2021 lidar flight where computed water yield was 14% higher for scenario A (43.60 x $10^6$ $m^3$) than B (37.37 x $10^6$ $m^3$). However, with limited field sample data, results of this study show promise as a new remote sensing snowpack water resources monitoring and mapping framework for Alberta's Eastern Slopes.

## 6.1 Introduction

Rocky Mountain snowpacks draining the Eastern Slopes of Alberta are the primary water resource for downstream Prairie regions (Oldman Watershed Council, 2014). Alberta's water supply is highly regulated (Alberta Environment, 2003) to ensure there is sufficient water to support a growing population and economy while maintaining healthy ecosystems. Headwater snow water equivalent (SWE) estimates are derived from snow depth and density measurements (Campbell, 2018; Pedlar, 2018; Pickering, 2018) and are observed as part of Alberta's long term water resource monitoring program. To estimate snow density and SWE, various techniques exist at in-situ (Kang & Barros, 2011; Naderpour et al., 2017; Proksch et al., 2015; Vivian et al., 2007) and larger regional sampling scales (Cornwell et al., 2016; Mizukami & Perica, 2008; Painter et al., 2016). However, there is a need to quantify the amount of water present in the Alberta Rocky Mountain Eastern Slopes snowpack in a cost-effective manner using existing government monitoring infrastructure and innovative watershed snow sampling.

The seasonal snowpack is in constant evolution (Grünewald et al., 2010) beginning with the first snowfall to complete melt out (Mott et al., 2018). Both snow depth and density vary over time during the snow accumulation and ablation period from Fall to Spring. At the beginning of the snow season, snowpack depth and density increase. Snow density is lowest for freshly fallen snow (Judson & Doesken, 2000). As the snowpack ages, crystals change shape and increase in grain size (Deems et al., 2013; Warren, 1982) resulting in a corresponding increase in density from metamorphosis, compaction, and freeze/melt cycles (Kinar & Pomeroy, 2015). Snow density has a linear relationship with time (Sturm & Holmgren, 1998; Winkler et al., 2021). Once the snowpack reaches the ablation stage, continued metamorphoses and melt causes depth to decrease and density to continue increasing (Bartlett et al., 2006; Hedstrom & Pomeroy, 1998;

Hill et al., 2019; Riboust et al., 2019; Verseghy, 2009). There is a hysteresis effect over time (Hill et al., 2019; Riboust et al., 2019) between snow depth and density primarily due to compaction, grain crystal metamorphose, and changes in liquid water content in the snowpack between the accumulation and ablation melt out phases.

In mountainous regions, there is high spatial variability in snowpack structure (Sturm et al., 1995), deposition (Kinar & Pomeroy, 2015), accumulation, ablation (Avanzi et al., 2021; Broberg, 2021), and timing of melt (DeBeer & Pomeroy, 2009; DeWalle et al., 2002; Newton et al., 2021). Snow is persistent in higher elevations with the exception of wind scoured locations (Löffler, 2005). Ablation occurs faster on south facing aspects (Anderson et al., 2014; Dornes et al., 2008) which in turn impacts snow depth and density (Grünewald et al., 2010) based on increased solar radiation. Spatial variability of snow density (Onuchin & Burenina, 1996) is influenced by landform (Anderson et al., 2014), terrain/ elevation (Mizukami & Perica, 2008; Seidel et al., 2016), wind loading (Mott et al., 2018; Sturm & Holmgren, 1998), gravity induced redistribution (Essery et al., 1999; Pomeroy et al., 1998), meteorological conditions, and snowpack age (Judson & Doesken, 2000; López-Moreno et al., 2013). Within a forest stand, density varies based on canopy cover (Bonner et al., 2022; Parajuli et al., 2020; Sun et al., 2022; Veatch et al., 2009) as forest canopies are more sheltered than open areas and reduced solar radiation penetrates the canopy (Garvelmann et al., 2014; Kostadinov et al., 2019).

The objective of this paper is continued development of an operational snow water equivalent modelling framework with a focus on snow density modelling using drivers that are deterministically distributed across a mountainous watershed. To estimate snow depth, established airborne lidar methodologies have been developed that allow for the creation of snow depth models (SDM) at a watershed scale (Barnes & Hopkinson, 2022; Deems et al., 2013;

Hopkinson et al., 2012). Snow density variability is small (Mizukami & Perica, 2008) in comparison to snow depth. However, there is a need to model variability in density across mountain watersheds to gain a better understanding of spatial snowpack controls and their variation through time. Sparce meteorological monitoring sites are insufficient to adequately estimate regional spatially distributed precipitation estimates (Bergeron, 1960; Daly et al., 2002; Thiessen, 1911) and therefore regional SWE estimates. There is a need to utilize practical methods that can scale up single point measurements to mesoscale estimates. In this study, AEP monthly snow depth and SWE field measurements were used to constrain watershed wide snow density lower and upper limits. However, it was not always the case these field measurements were taken on the same day as lidar snow sampling missions. Given the linearity in snow density over time, is it reasonable to: a) model watershed snow density based on the closest temporal AEP field sampling point (here after referred to as model A); or b) conversely, should snow density models use 30-year monthly mean AEP field samples (here after referred to as model B)? lidar derived snow depth was combined with each of these two snow density modelling approaches to generate spatially distributed maps of SWE which were subsequently used to calculate watershed water yield.

## 6.2 Methods

### 6.2.1 Study Area

The study area is located in southwestern Alberta as seen in Figure 6.1; adjacent and north of the Canada-United States border on the eastern side of the continental divide. The West Castle Watershed (WCW) shown by the polygon in Figure 6.1, is in the headwaters of the

Oldman River Basin (McCaffrey & Hopkinson, 2020). WCW is approximately 103 $km^2$ with an elevation range of 1240 m. A mature forest re-established itself after a 1936 wildfire burnt a significant portion of the West Castle region (Government of Alberta, 2015). Cattle range land (Government of Alberta, 2015), random camping, and Off Highway Vehicle (OHV) usage situated in valley elevations had negative impacts on native vegetation (Timoney, 1998). The Castle Mountain Resort is located in the northern part of WCW.

There are a limited number of Canadian mountain (Nitu, 2010) meteorological and snow monitoring sites in close proximity to WCW. Long term Government of Alberta, Environment and Protected Areas (AEP) snowpack monitoring stations, specifically South Racehorse Creek (SRHC), Gardiner Creek (Gardiner), and Akamina Pass (Akamina) are located at mid-mountain elevations near treeline (1809 masl (metres above sea level) to 1940 masl) in the Southern Alberta Eastern Slopes. The West Castle II (WCII) snow course is at a valley elevation (1533 masl) within WCW.

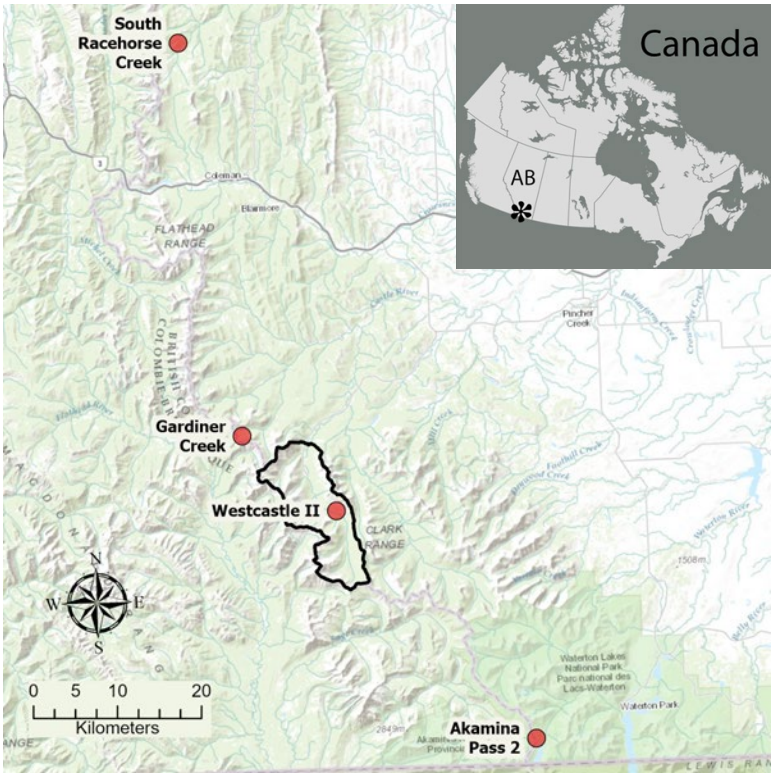


Figure 6.1: Southern Alberta Eastern Slopes located in Alberta, Canada. GoA snow monitoring and snow course sampling sites: (a) Akamina Pass (mid-mountain elevation: 1809 masl), (b) West Castle II (valley elevation: 1533 masl), (c) Gardiner Creek (mid-mountain elevation: 1940 masl), and (d) South Racehorse Creek (mid-mountain elevation: 1920 masl). West Castle Watershed is highlighted with the polygon. Inset: Star showing the study location within Alberta, Canada.

WCW is a long narrow watershed with approximately a 19 km north-south extent and ~8 km east-west extent. The watershed outlet is located at the stream (1390 masl) close to the University of Lethbridge West Castle Field Station (WFS) as seen in Figure 6.2a and the highest elevation is 2630 masl. Figure 6.2b shows WCW divided into three equal area elevation boundaries containing open and forest canopy. The lower elevation ranges from 1,390 masl to 1,695 masl. This zone consists mostly of grassland, shrubs, and mixed deciduous/coniferous forests (Timoney, 1998). Soils are present in the grassland and forested areas. Sedimentary rocks underlay most of the region although there is bedrock exposure. The mid-elevation range between 1695 masl to 1970 masl contains shallow soil profiles as well as exposed bedrock (Downing & Pettapiece, 2006; Timoney, 1998). Conifers, shrub, and herb vegetation are found

in this zone. The upper elevation from 1970 masl to 2630 masl generally has its lower boundary at treeline (Downing & Pettapiece, 2006). This region is mostly bedrock, sparse vegetation of lichens, and herbs (Downing & Pettapiece, 2006; Timoney, 1998). Fire suppression practices were introduced after the 1936 wildfire (Government of Alberta, 2015) and changed the fire cycle. As a result, Douglas fir, alder, and willow have encroached into lodge pole pine stands and huckleberry dominated locations (Kershaw, 2008).

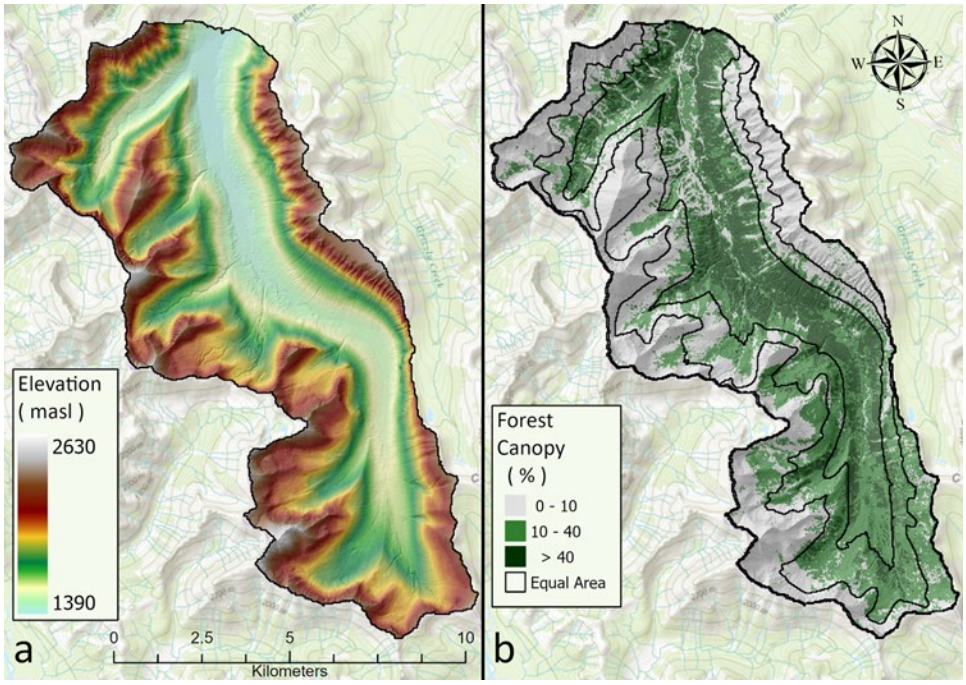


Figure 6.2: WCW. a: Elevation range of 1390 masl to 2630 masl. b: Forest Canopy: open (0%), wooded/shrub (0% to 10%), and forest (10% to 40%) as defined by Zhu and Waller (2003), WCW "Equal Area" elevation ranges: lower elevation range is 1390 masl to 1695 masl, mid elevation range is 1695 masl to 1970 masl, and upper WCW range is from 1970 to 2630 masl.

### 6.2.2 Data

#### 6.2.2.1 Lidar

Model inputs use spatially distributed landform and canopy variables derived from airborne lidar bare-earth and SDMs. Airborne lidar missions were flown over WCW by Airborne

Imaging (Calgary, Alberta) from 2014 to 2021 as shown in Table 6.1. Beginning in 2020, ALTM Titan MW surveys operated with a "terrain following" technique which altered the flying height from a fixed to a variable altitude based on the area of interest DEM. The addition of the 532 nm wavelength aided in detecting snow which is highly reflective in this wavelength whereas soils features are more dominant in the 1550 nm wavelength. "Bare-earth" (BE) surveys were completed during summertime months and snow-covered surveys during mid to late winter months. The Riegl Q1560 lidar sensor had the highest sampled point density of 12.4 points/$m^2$ for the 2021-Jan-22 flight. The lowest point density was captured by the ALTM 3100EA sensor for the 2014-Feb-24 mission at 1.55 points/$m^2$.

Table 6.1: WCW airborne lidar sampling missions. PRF (pulse repetition frequency). Field of View (FOV).

| Lidar Mission Date | Point Density ( $m^2$ ) | Sensor | Flying Height (ft MSL) | Ground Speed (kts) | PRF (kHz) | FOV (deg) | Scan Freq (Hz) | Laser Wavelength (nm) |
|---|---|---|---|---|---|---|---|---|
| Bare Earth | | | | | | | | |
| 20-Sep2014 | 3.97 | Leica ALS 70 | 11,000 | 140 | 130 | 42 | 27 | 1064 |
| 2020-Jul-28 | 4.63 | ALTM Titan MW | 8825 – 10,646 | 130 - 175 | 75 | 50 | 32 | 532, 1064, 1550 |
| Snow | | | | | | | | |
| 2014-Feb-24 | 1.55 | ALTM 3100EA | 11,000 | 130 | 50 | 40 | 28.5 | 1064 |
| 2018-Apr-20 | 9.05 | Riegl Q1560 | 11,000 – 11,800 | 140 | 133.3 | 42 | 113 | 1064 |
| 2020-Mar-5 | 4.29 | ALTM Titan MW | 8825 – 10,646 | 117 -202 | 75 | 50 | 32 | 532, 1064, 1550 |
| 2021-Jan-22 | 12.4 | Riegl Q1560 | 11,300 – 11,800 | 140 | 355.6 | 60 | 178 | 1064 |
| 2021-Mar-4 | 4.67 | ALTM Titan MW | 8825 – 10,646 | 138 - 163 | 75 | 50 | 32 | 532, 1064, 1550 |
| 2021-Apr-6 | 4.75 | ALTM Titan MW | 8825 – 10,646 | 140 - 163 | 75 | 50 | 32 | 532, 1064, 1550 |

The datasets were processed in the horizontal NAD83(CSRS)/UTM zone 11N and vertical CGVD28 reference frames. Datasets acquired in the WGS84 reference frame were transformed using Blue Marble Global Mapper and Geographic Calculator (Blue Marble Geographics, 2022) using the Canadian HT-2v coordinate transformation model before data cleaning and quality control. The airborne lidar data cleaning and gridding process is described in Barnes and Hopkinson (2022). All lidar datasets were gridded to a 1 m spatial resolution. As part of the new snowpack monitoring framework, future studies will incorporate land cover datasets to characterize terrain features at the provincial scale. Therefore, the lidar data was

further aggregated to a 30 m grid cell size to be comparable with other publicly available DEM and satellite land cover data products such as ASTER DEM or Landsat. All lidar datasets were normalized to the same spatial extent.

Previous work by Barnes and Hopkinson (2022) evaluated a new a machine learning approach to predict watershed wide snow depth from two different reduced airborne lidar sampling flight paths. These datasets as described in section 6.2.3.1 were included in this study.

#### 6.2.2.2 In situ Snow depth and SWE Field data

Long term continuous AEP observational snow depth and SWE field data were collected at Akamina, Gardiner, WCII, and SRHC from November 1991 to May 2021. Each reported sampling measurement at the given location represents the mean value collected from several individual measurements. No index of quality or variance is included in this data. For this study, snow density was expressed as a percentage of water equivalent (standard water density is 1000 $kg/m^3$) therefore, as an example, a density of 30% would be 300 $kg/m^3$. This convention was used in order to derive SWE estimates by multiplying snow depth by snow density. General statistics and regression analysis were done to examine seasonal patterns and to establish WCW lower and upper snow density limits. Gardiner and WCII sites were used for snowpack density model stratification and SWE calibration. AEP field measurements are generally sampled within five days on either side of the end of each month (Pickering, 2018). Therefore, AEP data may not temporally align with lidar snow sampling flights.

AEP Gardiner snow pillow data were used to create snow depletion curves for each hydrologic year coinciding with all lidar snow sampling missions. There was a data gap in the Gardiner 2017 – 2018 hydrologic year. To impute this missing data, the Gardiner time series was

regressed against the South Racehorse Creek snow pillow data which was the closest site (in distance and elevation) for the months of Feb to Apr from 1992 to 2021.

University of Lethbridge Artemis Lab (ULAL) snow depth and SWE field data were collected at varying accessible locations in WCW from 2018-2021. In 2018, a more intensive field sampling campaign took place to support snow depth validation for a new Leddar snow depth sensor (Barnes et al., 2020) where some sampling occurred twice during the same day (early morning and early evening). Ski lifts at Castle Mountain Ski Resort, located in WCW, allowed access to higher elevations. Figure 6.3 shows typical snowpack conditions on the CMR ridge. Snow sampling was completed within forest canopy at elevations ranging from 1400 masl to 1760 masl as well as in open areas with an elevation range of 1400 masl to 2140 masl. Attempts were made to sample "same day field measurements" at varying locations in the watershed as well as at the University of Lethbridge Westcastle Field Station (WFS). ULAL field sampling was completed either on the day of or day after the lidar snow sampling. All ULAL field sampling that was coincident with airborne lidar flights were used for snow density model validation.


Figure 6.3: ULAL Field Sampling location on the CMR-Ridge showing scoured to deep snowpacks within a 100 m distance. Photo courtesy of Jason Crawford – Director of Mountain Operations, Castle Mountain Resort

### 6.2.3 West Castle Watershed Snow Water Equivalent Model (SWE) and Water Yield

The workflow diagram to create watershed SWE and water yield is seen in Figure 6.4 and described in this section. Airborne lidar derived digital elevation and surface models (DEM and DSM respectively) were created for bare-earth (BE) and snow depth extraction. A forest canopy fractional coverage surface was derived from the BE DEM for snow density modelling. WCW SWE models were created by multiplying snow depth with snow density models. Statistics were calculated to derive water yield for WCW.

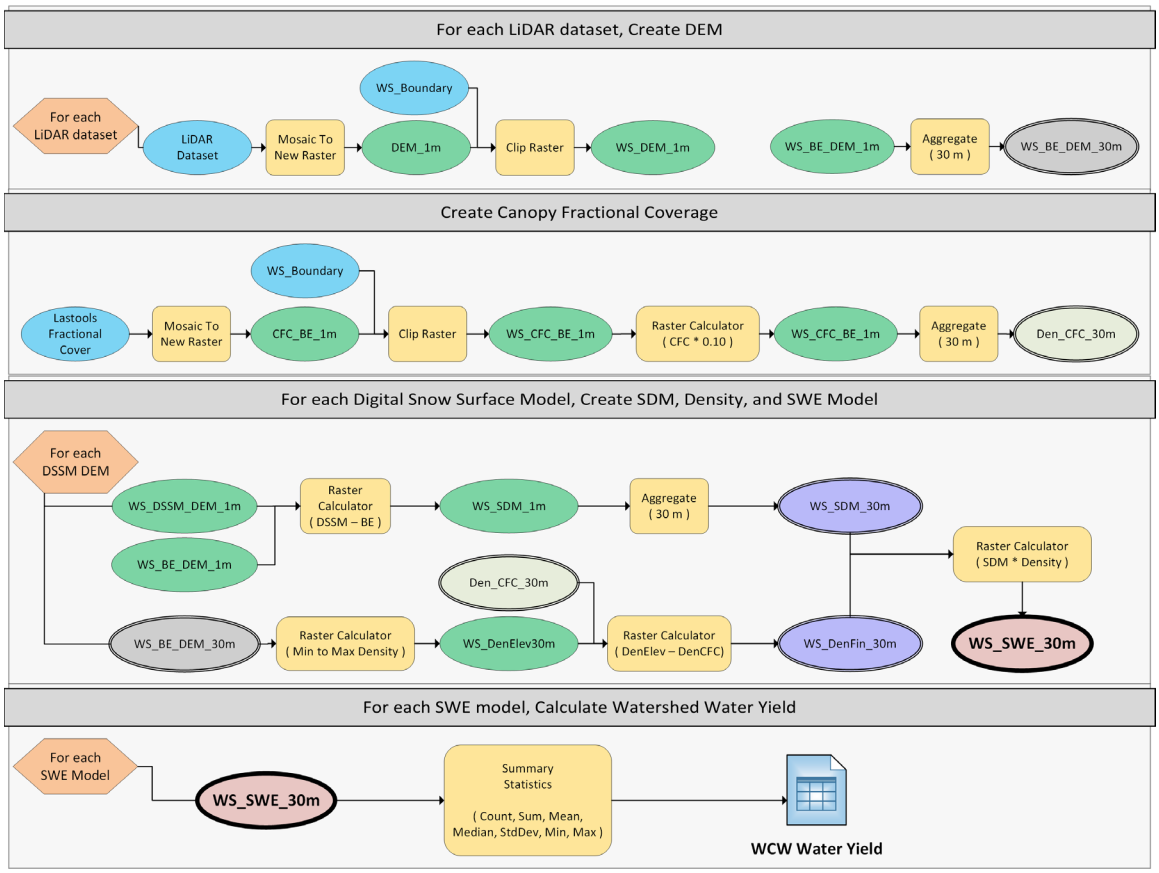

Figure 6.4: Water Yield and SWE model workflow. WCW density model Min and Max values are found in Table 6.7.

Snow water depletion curves were created from the Gardiner weather station snow water (SW) sensor to understand the continuous annual snow water equivalent for each year when lidar snow sampling was completed. Gardiner only represents the snowpack at the higher elevations near treeline. The valley bottom and lower elevations are not represented by SW depletion curves since the WCII site does not have a SW sensor. In 2018, Gardiner's snow water sensor malfunctioned and stopped recording in mid Feb, well before the April lidar flight. To fill the data gap for Gardiner, a regression analysis was done using the SHRC snow water sensor beginning on the date the Gardiner sensor stopped functioning to the end of Apr 2018. The regression for May was not included since it was not strong due to the reduced covariance between the sites caused by different rates of melt.

#### 6.2.3.1 Snow Depth Model

Watershed "wall-to-wall" SDMs were created by differencing the digital snow surface model (DSSM) datasets from the BE (bare-earth) DEM as described in Barnes and Hopkinson (2022). ESRI's (ESRI, 2020) forest based regression (FBR) was used to predict watershed "wall-to-wall" snow depth for the 2014-Feb-24 lidar dataset for two different flight path configurations that sampled ~18% of watershed. The FBR command was configured with terrain feature variables that characterized elevation, terrain curvature (TPI), aspect, slope, canopy height, latitude, and longitude. FBR is computationally prohibitive to run at a 1 m grid cell size therefore predicted surfaces were computed for a 30 m grid cell size. Two separate analyses were completed, the first included the Feb 2014 wall-to-wall dataset in the temporal comparisons where the dataset was normalized to the same spatial extent as the balance of the lidar datasets. The second was an independent analysis using the two lidar sampling strategies for the Feb 2014 observed wall-to-wall and FBR predicted snow depths as described in (Barnes & Hopkinson, 2022).

#### 6.2.3.2 Snow Density Model

Two deterministic drivers were used that described the spatiotemporal density variations for the West Castle watershed. Elevation was one of the drivers of snow density (Mizukami & Perica, 2008). The other driver was forest canopy fractional coverage (CFC). The 2020-Jul-28 BE lidar derived DEM and DSM were used to create the elevation-based and CFC snow density models for each lidar DSSM dataset (see Figure 6.4) as described in sections 6.2.3.2.1 and 6.2.3.2.2 respectively.

Code Block 6-1: Snow Density calculation for each grid cell. The snow density model in this study used: Upper_Elev (1940 (masl) for Gardiner), Lower_Elev (1533 for WCII), WS_Elev_Lowest (1390 for WCW), WS_Elev_Const (2000 masl elevation for maximum density), Upper_Density (Gardiner), Lower_Density (WCII)

```
Upper_Elev = Upper_Site_ElevationLower_Elev  = Lower_Site_Elevation
WS_Elev_Lowest = WS_Lowest_Elevation
WS_Elev_Const = WS_Elevation_For_Maximum_Density

Upper_Density = Upper_Site_Density
Lower_Density = Lower_Site_Density

DensityPer100m
        = (Upper_Density - Lower_Density) / (Upper_Elev -  Lower_Elev) /100)

Density_WS_Elev_Lowest
        = Lower_Density – (((Lower_Elev - WS_Elev_Lowest) / 100) * DensityPer100m

Density_WS_Elev_Above_Constant
        = Upper_Density + (((WS_Elev_Const - Upper_Elev) / 100) * DensityPer100m

If BareEarth_DEM  < WS_Elev_Const
        Then Density_Elevation
                = (BareEarth_DEM - WS_Elev_Lowest)/100) * DensityPer100m) + Density_WS_Elev_Lowest)
        Else Density_Elevation = Density_WS_Elev_Above_Constant

Density_Value = Density_Elevation – (CanopyFractionalCoverage * 0.10)
```

#### 6.2.3.2.1 Elevation

The snow density model (see Code Block 6-1) used the long-term AEP Gardiner and WCII manual snow depth and SWE field sampling sites located within and in close proximity to WCW. An elevation density gradient range was computed from valley bottom to treeline (2000 masl). Although density increases with elevation (Mizukami & Perica, 2008), there are no AEP sampling locations in the upper mountain alpine areas.  Therefore, elevations above 2000 masl were assigned the maximum calculated density value. Once each DSSM density modelling scenario elevation range was calculated, values were applied spatially to each grid cell of the DEM.

For the model (A) elevation gridding scenario, WCW density limits based on the closest AEP field sampling point in time, Gardiner and WCII field density observations collected near

the time of each lidar snow sampling mission were used to calculate the range of density in the watershed. For the 2020-Mar-5 lidar snow sampling, AEP did not complete field sampling for Gardiner. In this case, the mean value from Gardiner's "end of February" samples that corresponded to WCII's observed value was used as the upper limit. A manual examination of modelled snow density model grid cells where ULAL samples coincided with each lidar mission was completed to validate the model.

The model (B) elevation gridding scenario, 30-year monthly mean AEP field samples, the mean value was calculated for Gardiner and WCII field density observations that were collected at the end of each month as seen in Table 6.2. Lidar snow sampling flights are listed for each corresponding "End of month sampling" period.

Table 6.2: AEP sampling month corresponding to lidar flights used in the elevation density model B: "30-year monthly means".

| AEP End of month sampling | Jan | Feb | Mar | Apr |
|---|---|---|---|---|
| Lidar DSSM snow sampling flight | 2021-Jan-22 | 2014-Feb-24<br>2020-Mar-5<br>2021-Mar-4 | 2021-Apr-6 | 2018-Apr-20 |

#### 6.2.3.2.2 Forest Canopy

The CFC produces an index (0% to 100%) of forest canopy "openness" where open areas have a CFC value equal to zero. Shrubs and low vegetation have values closer to zero and denser forest canopy where there is more snow interception and reduced fall-through have higher CFC values that can approach 100%. Bonner et al. (2022) found snow density within the Marmot Creek, AB (~ 180 km north of WCW) forest canopy to be 10% lower than in open areas. This was consistent with WCW field sampling conducted within forested and open areas. The Lastool set (Isenburg, 2022) was used to create the CFC. The first step was to normalize the DEM with the lasheight tool, where the DEM ground elevation was set to zero. The lascanopy tool was subsequently used to compute an index of canopy coverage for a 30 m resolution by dividing the

total number of lidar points above the height cutoff (1.37 m which is a standard height for forest attribute measurements that also approximates the height at which ground cover can be separated from forest canopy cover) by the total number of points. The CFC index for each grid cell was used to adjust snow density where no modification was applied to open areas (CFC = 0). For lower vegetated to forested areas (CFC index > 0), CFC values were multiplied by 0.01 to limit the decrease in snow density to a maximum of 10% (as seen in Code Block 6-1).

## 6.3 Results

### 6.3.1 WCW Lidar Derived Snow Depth

WCW modelled snow depth is shown in Figure 6.5 and Table 6.3 for each WCW lidar flight. Appendix A shows the distribution of 20 cm snow depth categories broken into 100 m elevation bins. Deepest snow depths were generally seen in the track and runout zone of avalanche paths. Depths less than 20 cm for the earlier Jan and Feb flights were 0% to 1.8%. The two Mar SDMs showed more snow in the valley for the 2020 flight than the 2021 flight and 7.2% of the snowpack was less than 20 cm for the Mar 2021 fight. The 2018-Apr-20 snowpack was still present in valley locations with a deeper snowpack throughout most of the watershed in comparison to all other lidar snow sampling datasets. The snowpack was ablating by the 2021-Apr-6 lidar snow sampling flights and had 12.6% of the WCW snow depth less than 20 cm.

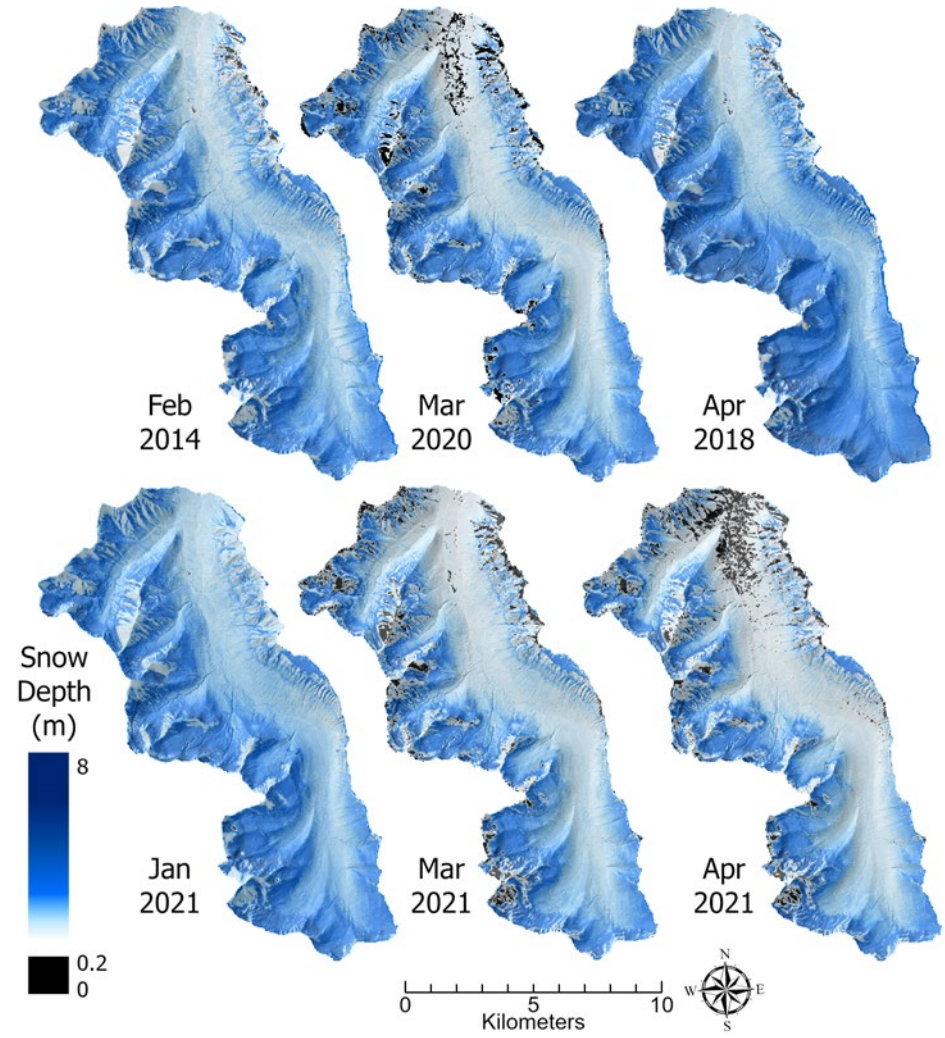

Figure 6.5: West Castle Snow Depth for 30 m watershed model. Black represents modelled snow depth < 20 cm.

Table 6.3: Computed Snow Depth by 20 cm categories for each lidar flight

| Snow Depth ( m ) | Feb-2014 | Apr-2018 | Mar-2020 | Jan-2021 | Mar-2021 | Apr-2021 |
|---|---|---|---|---|---|---|
| 0.0 - 0.2 | 1.8% | 1.3% | 3.9% | 0.0% | 7.2% | 12.6% |
| 0.2 - 0.4 | 3.2% | 1.8% | 6.6% | 0.1% | 7.7% | 11.1% |
| 0.4 - 0.6 | 4.9% | 2.4% | 9.1% | 2.5% | 9.6% | 11.4% |
| 0.6 - 0.8 | 7.1% | 5.0% | 10.7% | 4.9% | 12.1% | 10.7% |
| 0.8 - 1.0 | 9.8% | 6.8% | 9.5% | 9.9% | 11.0% | 8.5% |
| 1.0 - 1.2 | 10.7% | 7.6% | 8.1% | 12.9% | 9.7% | 7.5% |
| 1.2 - 1.4 | 10.2% | 8.8% | 7.3% | 12.7% | 8.6% | 7.2% |
| 1.4 - 1.6 | 9.4% | 8.1% | 7.5% | 10.7% | 7.2% | 6.2% |
| 1.6 - 1.8 | 9.0% | 7.2% | 6.7% | 9.4% | 6.0% | 5.2% |
| 1.8 - 2.0 | 7.7% | 6.8% | 6.1% | 7.9% | 4.9% | 3.9% |
| 2.0 - 2.2 | 6.2% | 7.1% | 5.2% | 6.7% | 3.7% | 3.2% |
| 2.2 - 2.4 | 4.9% | 6.2% | 4.1% | 5.4% | 2.8% | 2.6% |
| 2.4 - 2.6 | 3.6% | 5.7% | 3.2% | 4.2% | 2.3% | 2.2% |
| 2.6 - 2.8 | 2.8% | 4.7% | 2.5% | 3.2% | 1.6% | 1.7% |
| 2.8 - 3.0 | 2.2% | 3.8% | 2.1% | 2.5% | 1.2% | 1.3% |
| 3.0 - 3.2 | 1.6% | 3.0% | 1.6% | 1.8% | 0.9% | 1.0% |
| 3.2 - 3.4 | 1.1% | 2.5% | 1.1% | 1.3% | 0.7% | 0.7% |
| 3.4 - 3.6 | 0.8% | 2.1% | 0.9% | 0.9% | 0.5% | 0.6% |
| 3.6 - 3.8 | 0.6% | 1.7% | 0.7% | 0.7% | 0.4% | 0.4% |
| 3.8 - 4.0 | 0.4% | 1.3% | 0.6% | 0.5% | 0.3% | 0.4% |
| 4.0 - 4.2 | 0.3% | 1.0% | 0.4% | 0.4% | 0.3% | 0.3% |
| 4.2 - 4.4 | 0.2% | 0.9% | 0.3% | 0.3% | 0.2% | 0.2% |
| 4.4 - 4.6 | 0.2% | 0.6% | 0.3% | 0.2% | 0.2% | 0.2% |
| 4.6 - 4.8 | 0.2% | 0.6% | 0.2% | 0.2% | 0.1% | 0.2% |
| 4.8 - 5.0 | 0.1% | 0.4% | 0.2% | 0.1% | 0.1% | 0.1% |
| 5.0 - 5.2 | 0.1% | 0.3% | 0.2% | 0.1% | 0.1% | 0.1% |
| 5.2 - 5.4 | 0.1% | 0.3% | 0.2% | 0.1% | 0.1% | 0.1% |
| 5.4 - 5.6 | 0.1% | 0.2% | 0.1% | 0.1% | 0.1% | 0.1% |
| 5.6 - 5.8 | 0.1% | 0.2% | 0.1% | 0.1% | 0.1% | 0.1% |
| > 5.8 | 0.4% | 1.5% | 0.6% | 0.2% | 0.3% | 0.4% |

### 6.3.2 Snow Density

AEP monthly snow density derived field sampling for the months of interest from Jan 1992 to Apr 2021 as seen in Figure 6.6 and Table 6.4, shows a seasonal variation between the four sites. All sites had an increase in snow density from Jan to Apr. Gardiner has the highest elevation and had the highest mean snow density from Jan (34%) to Mar (42%). SRHC is 20 m lower in elevation than Gardiner however consistently had the lowest snow density for each month of all the mid-mountain sites. Of all the mid-mountain sites, Akamina has the lowest elevation however, had the same Apr monthly mean snow density (42%) as Gardiner. The

monthly mean snow density for the valley WCII site was highest in Apr at 37% although the snowpack was completely depleted in two of the sampling years.

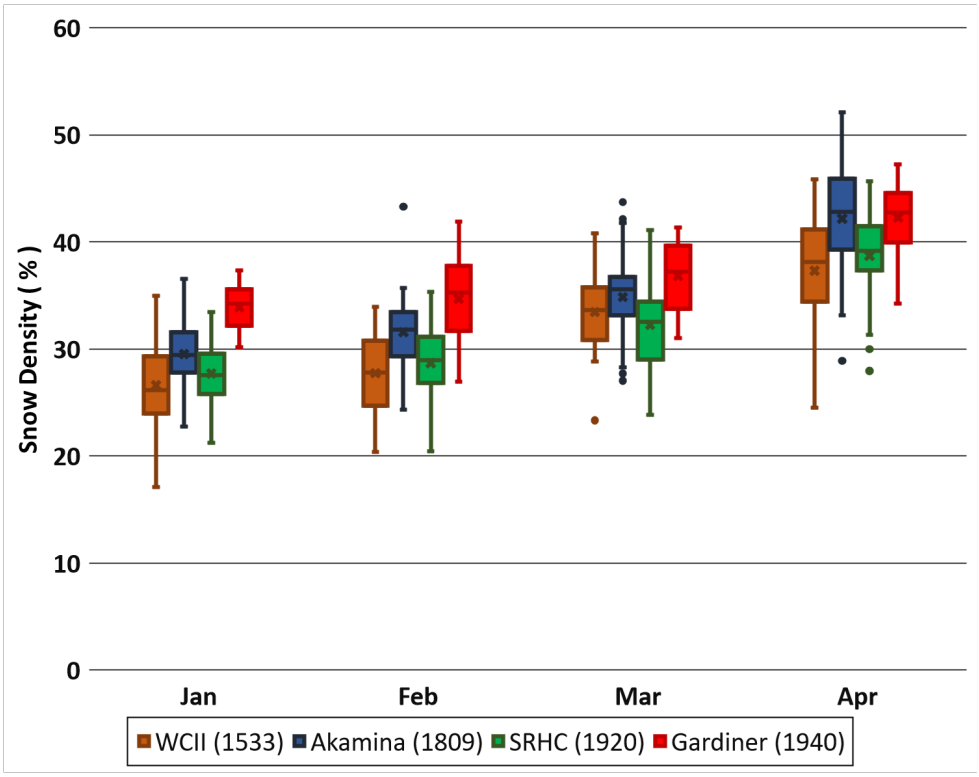


Figure 6.6: The Box plot shows the snow density of each site by month. The "X" is the mean, the bar within the box is median value. The "T"s show the upper and lower range of the data. The coloured box is the interquartile range (quartile 1 to quartile 3), dots are outliers (data points that are 1.5 times above or below the interquartile range).

Table 6.4: Statistics for AEP Snow Density Sampling from 1992 to 2021. Snow density was expressed as a percentage of water equivalent (standard water density is 1000 kg/m3) in order to derive SWE estimates by multiplying snow depth by snow density.

| Month | | WCII (1533 masl) | Akamina (1809 masl) | SRHC (1920 masl) | Gardiner (1940 masl) |
|---|---|---|---|---|---|
| Jan | Max | 35 | 37 | 34 | 37 |
| | Min | 17 | 23 | 21 | 30 |
| | Mean | 27 | 30 | 28 | 34 |
| | Median | 26 | 30 | 28 | 34 |
| | StDev | 4 | 3 | 3 | 2 |
| | n | 29 | 30 | 26 | 22 |
| Feb | Max | 34 | 43 | 35 | 42 |
| | Min | 20 | 24 | 20 | 27 |
| | Mean | 28 | 32 | 29 | 35 |
| | Median | 28 | 32 | 29 | 35 |
| | StDev | 4 | 4 | 3 | 4 |
| | n | 29 | 30 | 26 | 25 |
| Mar | Max | 41 | 44 | 41 | 41 |
| | Min | 23 | 27 | 24 | 31 |
| | Mean | 34 | 35 | 32 | 37 |
| | Median | 34 | 36 | 33 | 37 |
| | StDev | 4 | 4 | 4 | 3 |
| | n | 30 | 30 | 26 | 25 |
| Apr | Max | 46 | 52 | 46 | 47 |
| | Min | 25 | 29 | 28 | 34 |
| | Mean | 37 | 42 | 39 | 42 |
| | Median | 38 | 43 | 39. | 43 |
| | StDev | 6 | 6 | 4 | 3. |
| | n | 27 | 28 | 27 | 25 |
| Total | 120 | 115 | 118 | 105 | 97 |

Statistical regressions between the AEP WCII and mid-mountain sites (as seen in Table 6.5) showed a strong linear agreement ($r^2$ = 0.98 and 0.99) for Jan to Mar. The linear relationship ($r^2$ = 0.89 and 0.91) was not as strong in Apr when WCII was in the ablation stage in some years. There was an elevational influence observed in AEP field sampling measurements. SRHC had lower snow density than Gardiner and Akamina from Jan to Apr.

Table 6.5: Snow Density Regressions: y = mx + b, where m is the Slope of the line and b = 0. WCII vs Akamina, WCII vs Gardiner, WCII vs SRHC. Coefficient of determination is denoted as $R^2$.

| | Akamina | | Gardiner | | SRHC | |
|---|---|---|---|---|---|---|
| Month | Slope | $R^2$ | Slope | $R^2$ | Slope | $R^2$ |
| Jan | 1.10 | 0.99 | 1.28 | 0.98 | 1.03 | 0.98 |
| Feb | 1.12 | 0.98 | 1.25 | 0.99 | 1.02 | 0.99 |
| Mar | 1.04 | 0.99 | 1.10 | 0.99 | 0.95 | 0.99 |
| Apr | 1.11 | 0.91 | 1.10 | 0.89 | 1.01 | 0.91 |

ULAL snow density derived field measurements (see in Table 6.6) are listed by sampling date. Relationships of interest were elevation and forest canopy. Repeat sampling at all upper elevations in WCW was not possible due to accessibility and snow sampling field resources. Data regressions for ULAL snow density sampling showed strong agreement between the open areas and canopy as well as with elevation. During 2018, more frequent snow sampling occurred at the WFS site. Density increased during the accumulation phase from Jan to mid Apr. At the end of Apr, snow density was 36% to 39% when the snowpack was isothermal and melted out.

Table 6.6: Statistics for ULAL Snow Density Field Sampling (Max, Min, Mean, Median, StDev are shown in percentage values, n is the count of the number of samples)

| Date | Elev | Location | | Max | Min | Mean | Median | StDev | n |
|---|---|---|---|---|---|---|---|---|---|
| 2014-02-24 | 1413 | CMR-Valley snow-pit | open | | | 27 | | | 1 |
| 2014-02-24 | 1406 | WFS | canopy | 28 | 16 | 24 | 24 | 3 | 20 |
| | | | | | | | | | |
| 2018-01-05 | 1403 | WFS | open | 27 | 8 | 14 | 13 | 4 | 30 |
| 2018-01-20 | 1403 | WFS | open | 50 | 13 | 22 | 21 | 6 | 40 |
| 2018-02-21 | 1403 | WFS | open | 44 | 24 | 27 | 26 | 6 | 10 |
| 2018-03-04 | 1403 | WFS | open | 26 | 9 | 20 | 21 | 4 | 35 |
| 2018-04-09 | 1403 | WFS | open | 46 | 21 | 35 | 35 | 4 | 30 |
| 2018-04-15 | 1403 | WFS | open | 63 | 27 | 41 | 41 | 8 | 20 |
| 2018-04-19 | 1403 | WFS | open | 40 | 17 | 29 | 30 | 7 | 15 |
| 2018-04-26 | 1403 | WFS | open | 49 | 29 | 38 | 37 | 5 | 22 |
| 2018-04-26 | 1403 | WFS | open | 42 | 33 | 39 | 40 | 3 | 6 |
| 2018-04-27 | 1403 | WFS | open | 57 | 16 | 36 | 37 | 7 | 34 |
| 2018-04-27 | 1403 | WFS | open | 44 | 27 | 37 | 40 | 6 | 6 |
| | | | | | | | | | |
| 2019-03-14 | 1403 | WFS | open | 23 | 18 | 21 | 21 | 2 | 9 |
| 2019-03-14 | 1403 | WFS | canopy | 18 | 12 | 15 | 15 | 3 | 2 |
| 2019-03-16 | 2136 | Ridge | open | 35 | 20 | 28 | 31 | 6 | 5 |
| 2019-04-05 | 1403 | WFS | open | 41 | 13 | 32 | 32 | 8 | 12 |
| 2019-04-05 | 1403 | WFS | canopy | 34 | 10 | 22 | 21 | 9 | 5 |
| | | | | | | | | | |
| 2020-01-30 | 1403 | WFS | canopy | 23 | 19 | 21 | 21 | 2 | 4 |
| 2020-03-05 | 1403 | WFS | open | 32 | 23 | 28 | 29 | 4 | 5 |
| 2020-03-05 | 2136 | Ridge | open | 49 | 32 | 39 | 35 | 10 | 3 |
| | | | | | | | | | |
| 2021-01-23 | 1403 | WFS | open | 48 | 21 | 29 | 26 | 9 | 7 |
| 2021-01-23 | 1403 | WFS | canopy | 16 | 10 | 13 | 13 | 4 | 2 |
| 2021-01-23 | 1754 | Huckleberry | open | 34 | 27 | 32 | 33 | 3 | 5 |
| 2021-01-23 | 2136 | Ridge | open | 44 | 25 | 36 | 37 | 7 | 5 |
| 2021-03-05 | 1403 | WFS | open | 35 | 20 | 29 | 28 | 5 | 12 |
| 2021-03-05 | 1403 | WFS | canopy | 32 | 15 | 24 | 25 | 5 | 10 |
| 2021-03-05 | 1754 | Huckleberry | open | 33 | 30 | 32 | 31 | 1 | 5 |
| 2021-03-05 | 1752 | Huckleberry | canopy | 28 | 19 | 23 | 24 | 4 | 5 |
| 2021-03-05 | 1754 | North Run - Slope | canopy | 34 | 21 | 29 | 30 | 5 | 5 |
| 2021-03-05 | 1759 | North Run - Flat | canopy | 31 | 21 | 27 | 28 | 4 | 5 |

#### 6.3.2.1 WCW Snow Density

The two snow density modelling scenarios, model A (Closest Sampling Date) and model B (30-year Mean Sampling) are shown in Table 6.7. The 2014-Feb-24 AEP Field sampling occurred on the same day as the lidar snow sampling flight. The lower limit was the same for both model sampling scenarios. The upper limit for model B was 36% as opposed to 33% for model A. AEP field sampling did not occur on the same day for all other lidar snow sampling flights. AEP sampling for the 2021-Apr-6 lidar flight was 9 days earlier (occurring on 2021-Mar-28). The lower and upper snow density limits were 4% higher for the model B scenario. AEP sampling for the 2021-Jan-22 was 6 days after the flight. The WCW snow density lower and upper limits were reduced by 1% for the model B scenario. Snow density during the 2021 snow season showed an increasing progression through the year for model B at both WCII and Gardiner whereas model A had the highest snow density range for the Mar lidar snow sampling flight.

Table 6.7: ALS Mission Snow Density limits using WCII and Gardiner field samples. WCW lower limit (1390 masl). Upper limit for Treeline ( > 2000 masl) to WCW highest elevation. Model B shows the standard deviation for WCII and Gardiner field measurements in brackets.

| | | Model A: Closest Sampling Date ( % ) | | | | Model B: 30-year Mean Sampling ( % ) | | | |
|---|---|---|---|---|---|---|---|---|---|
| Lidar Snow Sampling | AEP Field Sampling | WCII Density | Gardiner Density | WCW Lower Limit | WCW Upper Limit | WCII Density | Gardiner Density | WCW Lower Limit | WCW Upper Limit |
| 2014-Feb-24 | 2014-Feb-24 | 27 | 32 | 25 | 33 | 28 (3) | 35 (4) | 25 | 36 |
| 2018-Apr-20 | 2018-Apr-26 | 38 | 44 | 36 | 44 | 37 (6) | 42 (3) | 36 | 42 |
| 2020-Mar-5 | 2020-Mar-2 | 30 | 35 | 28 | 36 | 28 (3) | 35 (4) | 25 | 36 |
| 2021-Jan-22 | 2021-Jan-28 | 28 | 35 | 25 | 36 | 26 (4) | 34 (2) | 24 | 35 |
| 2021-Mar-4 | 2021-Feb-24 | 24 | 42 | 18 | 44 | 28 (3) | 35 (4) | 25 | 36 |
| 2021-Apr-6 | 2021-Mar-28 | 29 | 33 | 28 | 33 | 34 (3) | 37 (3) | 32 | 37 |

For visualization purposes, WCW snow density maps for model A are shown in Figure 6.7 (model B maps are not visually different from model A maps). Lower snow densities were present near the beginning of the snow season in Jan and Feb. Higher densities occurred near the

end of the snow season in Apr. The Mar 2021 lidar snow sampling flight had a higher range of snow density than the Mar 2020 flight.

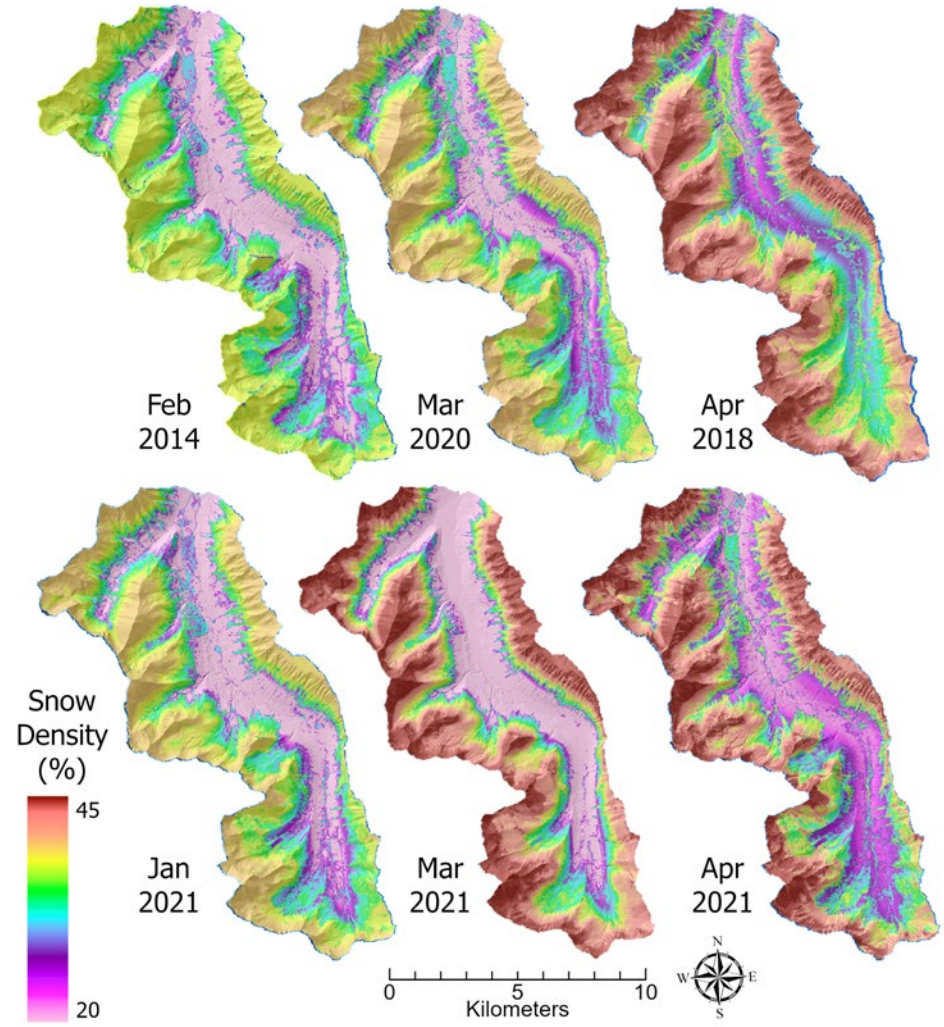


Figure 6.7: West Castle Snow Density for 30 m watershed model computed for model A: closest AEP field sampling point in time.

### 6.3.3 WCW Snow Water Equivalent

WCW modelled snow water equivalent computed using snow density model A is shown in Figure 6.8. There were lower SWE values in valley elevations for the 2021-Apr-6 flight as the snowpack was in the process of ablating. In comparison, the 2018-Apr-20 snowpack was still

present in most of the valley and watershed. Higher SWE estimates were produced in the valley, upper elevations, and throughout the watershed.

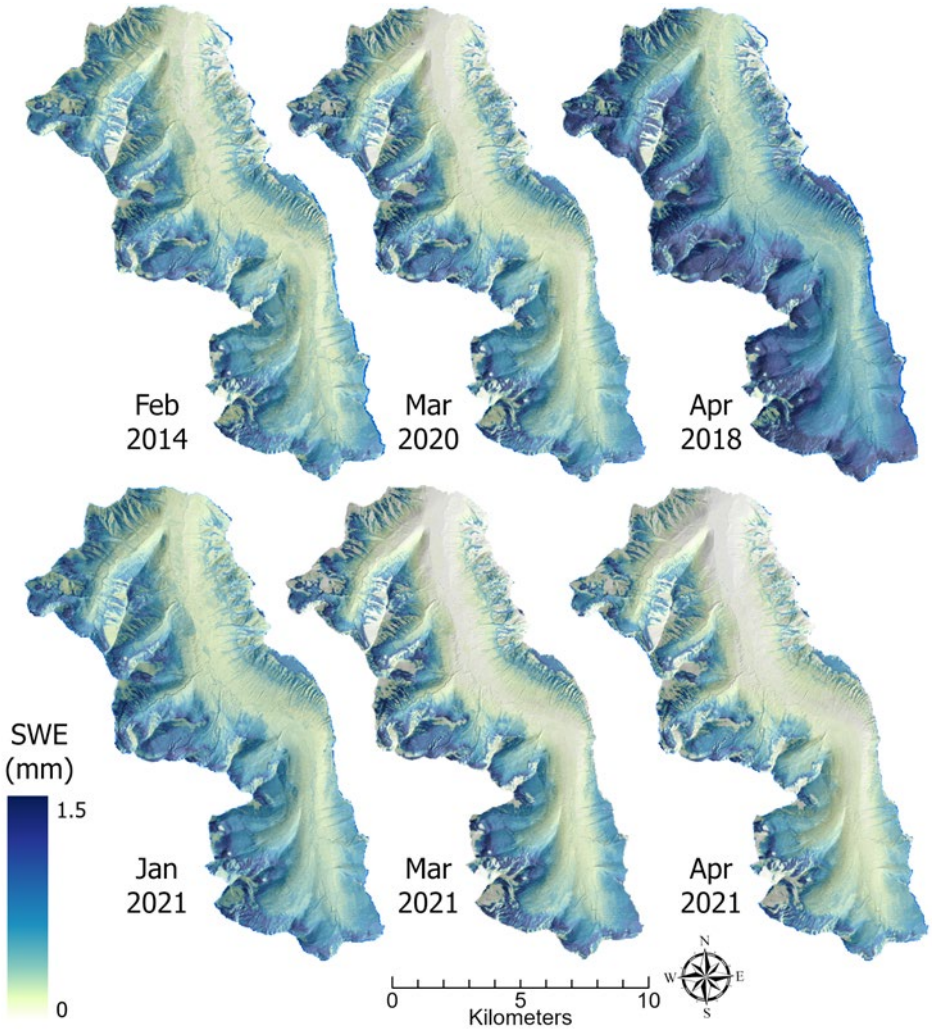


Figure 6.8: West Castle Snow Water Equivalent for 30 m watershed model computed for model A: closest AEP field sampling point in time. For visual comparison purposes of all flights, maximum SWE was set to 1500 mm, however, values can exceed this upper limit.

The 2014-Feb-24 lidar snow sampling flights with ESRI Forest based regression "observed" and "predicted" snow depth SWE estimates are shown in Figure 6.9. Lower SWE estimates were produced in the northwestern mid-mountain to alpine locations using the LCP

flight line. For the T3 flight line, higher SWE estimates occurred in the upper reaches of the watershed in comparison to the observed wall-to-wall SWE estimates.

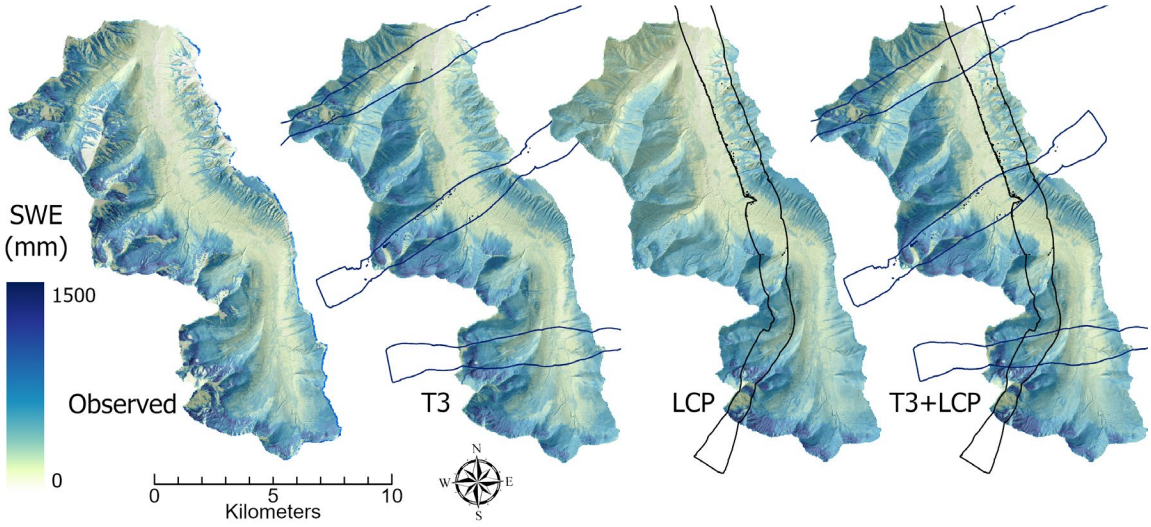


Figure 6.9: West Castle Snow Water Equivalent model for the 30 m observed and FBR predicted snow depth computed for model A: closest AEP field sampling point in time. The "observed" SWE was the "wall-to-wall" lidar snow sampling. T3 and LCP show where each snow depth flight line sampling was located in the watershed. For interest, T3&LCP was created using both flightlines for snow depth model prediction. For visual comparison purposes, maximum SWE was set to 1500 mm, however, values can exceed this upper limit.

### 6.3.4 WCW Water Yield

Gardiner snow water depletion curves with corresponding lidar snow sampling flights are shown in Figure 6.10. The lowest snow water year was 2020 – 2021. In this year, the Gardiner snow water sensor recorded 287 mm on the day of the 2021-Jan-22 snow sampling flight, 2021-Mar-4 had 325 mm and 2021-Apr-6 measured 386 mm. In comparison, the 2017 - 2018 Gardiner snow water showed the highest amount at 725 mm for the 2018-Apr-22 lidar snow sampling flight. Two lidar snow sampling flights occurred one year apart, however, the 2020-Mar-5 recorded 665 mm whereas the 2021-Mar-4 was less than half the snow water at 325 mm. The 2014-Feb-24 Gardiner snow water was 509 mm.

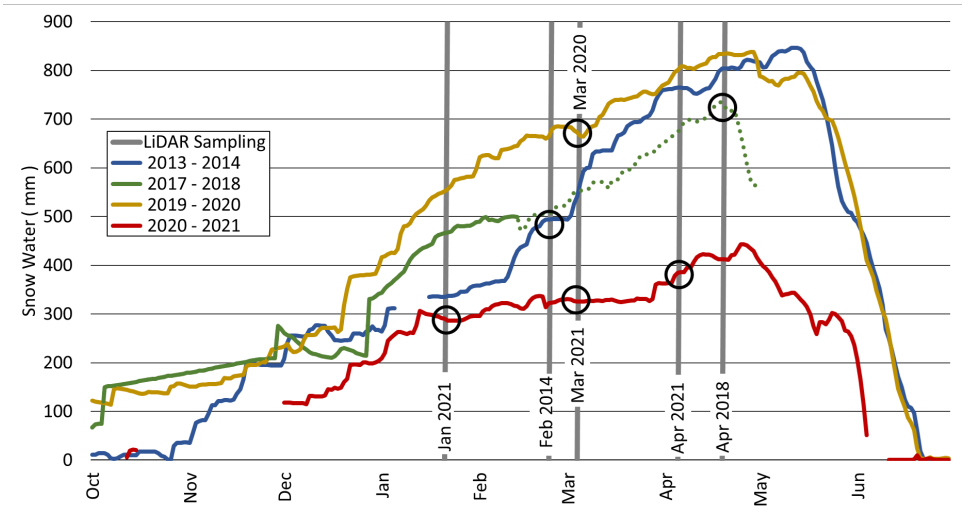


Figure 6.10: AEP Gardiner Snow Water for each lidar mission date (highlighted by the black circle). Missing data for the Gardiner 2017 - 2018 SW year (green dotted line, see Figure 6.11 for regression results) was regressed from Feb to the end of Apr 2018 using SRHC SW ($R^2 = 0.91$).

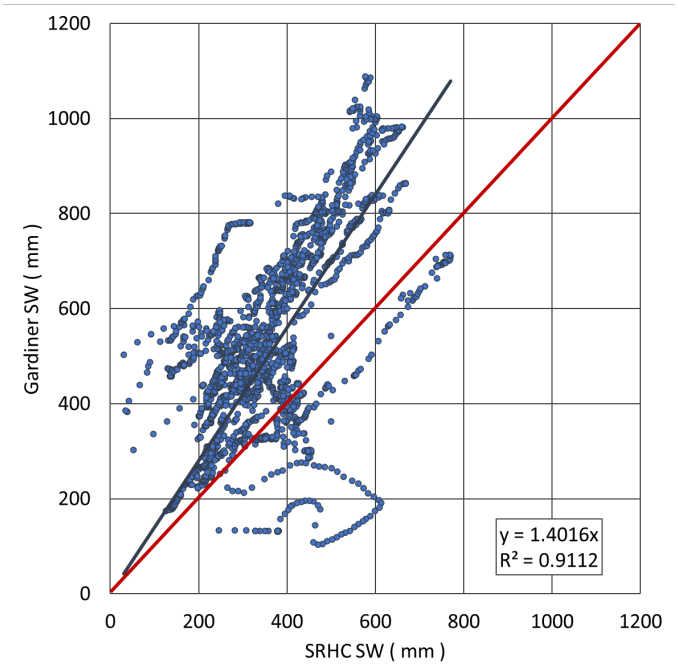


Figure 6.11: AEP Gardiner vs SRHC Snow Water Regression for Feb, Mar, and Apr 1992 to 2021 field

West Castle water yield was calculated for each temporal lidar snow sampling flight shown in Table 6.8. The model (A) scenario with both the elevation and CFC snow density resulted in the lowest yield for 2021-Apr-6 at 33.89 x $10^6$ $m^3$. The 2018-Apr-20 lidar flight

occurred two weeks later in the hydrologic year however had the highest calculated water yield of 80.76 x $10^6$ $m^3$. The forest canopy CFC adjustment reduced computed watershed water yield from 8% to 11% for all flights compared to using only the elevation snow density computation. Comparing model A and B snow density "Elev & CFC" scenarios, the largest difference in water yield was for the 2021-Apr-6 flight. The 2021-Mar-4 flight had a lower water yield for model B (37.37 x $10^6$ $m^3$) compared to using model A for snow density (43.60 x $10^6$ $m^3$).

Table 6.8: Water Yield for the Lidar sampling of the WCW (Area: 101.95 $km^2$). All "Scenario Comparison" water yield percentages are in relation to the density from model A: Closest Sampling Date divided by model B: 30-year monthly mean ( A / B ). Values > 100 are model B had higher water yield estimations than model A, whereas values < 100 are lower model B estimations than model A. (Elev refers to elevation)

| Model | A: Closest Sampling Date x $10^6$ $m^3$ | | | B: 30-year Monthly Mean x $10^6$ $m^3$ | | | Scenario Comparison | |
|---|---|---|---|---|---|---|---|---|
| Lidar Mission | Elev & CFC | Elev Only | CFC Influence ( % ) | Elev & CFC | Elev Only | CFC Influence ( % ) | Elev & CFC ( % ) | Elev Only ( % ) |
| 2014-Feb-24 | 44.42 | 49.35 | 10.1 | 47.45 | 53.15 | 10.7 | 106.8 | 107.7 |
| 2018-Apr-20 | 80.76 | 87.89 | 8.1 | 77.61 | 84.74 | 8.4 | 96.1 | 96.4 |
| 2020-Mar-5 | 46.25 | 51.06 | 9.4 | 44.88 | 49.68 | 9.7 | 97.0 | 97.3 |
| 2021-Jan-22 | 50.28 | 56.59 | 11.1 | 49.03 | 55.33 | 11.4 | 97.5 | 97.8 |
| 2021-Mar-4 | 43.60 | 47.93 | 9.0 | 37.37 | 41.69 | 10.4 | 85.7 | 87.0 |
| 2021-Apr-6 | 33.89 | 37.49 | 9.6 | 38.33 | 41.93 | 8.6 | 113.1 | 111.8 |

WCW water yield is shown for both snow density modelling scenarios grouped into 100 m elevation ranges (see Table 6.9). For both scenarios, the most productive elevation range was 1900 – 2000 masl with between 17.3% to 19.4% estimated water yield for all lidar snow sampling flights. Valley elevations below 1600 masl contributed 5.5% of the total water yield for the Mar-2021 model A in comparison to 7.7% for model B. In contrast, the Jan-2021 valley elevations had a 10.3% and 10.0% (for model A and B respectively) contribution to total watershed water yield while elevations above 2200 masl produced 11.4% and 11.6% for snow density model A and B scenarios.

Table 6.9: Water Yield (x $10^6$ $m^3$) categorized by 100 m elevation ranges for model A: "Closest Sampling Date" and model B: "30-year Monthly Mean" using "Elevation & CFC" snow density models. WCW Area: 101.95 $km^2$. The percentages refer to how much of the water yield each range contributed to the total for each lidar flight.

| Elev Range (masl) | Area ($km^2$) | Feb-2014 | Apr-2018 | Mar-2020 | Jan-2021 | Mar-2021 | Apr-2021 |
|---|---|---|---|---|---|---|---|
| Model A: Closest Sampling Date | | | | | | | |
| 1390 - 1500 | 11.20 | 1.70 (3.8%) | 3.07 (3.8%) | 1.20 (2.6%) | 2.21 (4.4%) | 0.75 (1.7%) | 0.67 (2.0%) |
| 1500 - 1600 | 11.84 | 2.64 (6.0%) | 4.76 (5.9%) | 2.13 (4.6%) | 3.00 (6.0%) | 1.58 (3.6%) | 1.39 (4.1%) |
| 1600 - 1700 | 11.69 | 3.63 (8.2%) | 6.31 (7.8%) | 3.22 (7.0%) | 3.82 (7.6%) | 2.63 (6.0%) | 2.16 (6.4%) |
| 1700 - 1800 | 12.16 | 5.26 (11.8%) | 9.03 (11.2%) | 5.19 (11.2%) | 5.49 (10.9%) | 4.55 (10.4%) | 3.71 (10.9%) |
| 1800 - 1900 | 12.04 | 6.54 (14.7%) | 11.77 (14.6%) | 7.26 (15.7%) | 7.19 (14.3%) | 6.71 (15.4%) | 5.34 (15.8%) |
| 1900 - 2000 | 13.05 | 7.76 (17.5%) | 14.17 (17.5%) | 8.71 (18.8%) | 8.70 (17.3%) | 8.74 (20.0%) | 6.58 (19.4%) |
| 2000 - 2100 | 11.60 | 7.26 (16.3%) | 13.45 (16.7%) | 8.16 (17.6%) | 8.27 (16.4%) | 8.45 (19.4%) | 6.23 (18.4%) |
| 2100 - 2200 | 8.73 | 5.12 (11.5%) | 9.64 (11.9%) | 5.56 (12.0%) | 5.87 (11.7%) | 5.61 (12.9%) | 4.22 (12.5%) |
| 2200 - 2300 | 5.78 | 2.93 (6.6%) | 5.54 (6.9%) | 3.14 (6.8%) | 3.60 (7.2%) | 3.05 (7.0%) | 2.36 (7.0%) |
| 2300 - 2400 | 2.88 | 1.22 (2.7%) | 2.32 (2.9%) | 1.32 (2.9%) | 1.64 (3.3%) | 1.24 (2.8%) | 0.99 (2.9%) |
| 2400 - 2500 | 0.76 | 0.29 (0.6%) | 0.56 (0.7%) | 0.29 (0.6%) | 0.41 (0.8%) | 0.25 (0.6%) | 0.20 (0.6%) |
| 2500 - 2630 | 0.21 | 0.07 (0.2%) | 0.15 (0.2%) | 0.08 (0.2%) | 0.10 (0.2%) | 0.05 (0.1%) | 0.04 (0.1%) |
| Total | | 44.42 | 80.76 | 46.25 | 50.28 | 43.60 | 33.89 |
| Model B: 30 Year Monthly Mean | | | | | | | |
| 1390 - 1500 | 11.20 | 1.77 (3.7%) | 3.02 (3.9%) | 1.07 (2.4%) | 2.07 (4.2%) | 1.06 (2.8%) | 0.80 (2.1%) |
| 1500 - 1600 | 11.84 | 2.73 (5.7%) | 4.65 (6.0%) | 1.94 (4.3%) | 2.84 (5.8%) | 1.83 (4.9%) | 1.64 (4.3%) |
| 1600 - 1700 | 11.69 | 3.72 (7.8%) | 6.13 (7.9%) | 3.00 (6.7%) | 3.67 (7.5%) | 2.65 (7.1%) | 2.51 (6.6%) |
| 1700 - 1800 | 12.16 | 5.46 (11.5%) | 8.75 (11.3%) | 4.93 (11.0%) | 5.32 (10.9%) | 4.17 (11.2%) | 4.23 (11.0%) |
| 1800 - 1900 | 12.04 | 6.96 (14.7%) | 11.37 (14.7%) | 7.00 (15.6%) | 7.01 (14.3%) | 5.75 (15.4%) | 6.02 (15.7%) |
| 1900 - 2000 | 13.05 | 8.36 (17.6%) | 13.65 (17.6%) | 8.50 (18.9%) | 8.52 (17.4%) | 7.08 (18.9%) | 7.36 (19.2%) |
| 2000 - 2100 | 11.60 | 7.91 (16.7%) | 12.76 (16.4%) | 8.11 (18.1%) | 8.15 (16.6%) | 6.70 (17.9%) | 7.00 (18.3%) |
| 2100 - 2200 | 8.73 | 5.60 (11.8%) | 9.14 (11.8%) | 5.53 (12.3%) | 5.78 (11.8%) | 4.46 (11.9%) | 4.74 (12.4%) |
| 2200 - 2300 | 5.78 | 3.21 (6.8%) | 5.26 (6.8%) | 3.12 (7.0%) | 3.54 (7.2%) | 2.44 (6.5%) | 2.65 (6.9%) |
| 2300 - 2400 | 2.88 | 1.33 (2.8%) | 2.20 (2.8%) | 1.31 (2.9%) | 1.62 (3.3%) | 0.99 (2.7%) | 1.11 (2.9%) |
| 2400 - 2500 | 0.76 | 0.32 (0.7%) | 0.53 (0.7%) | 0.29 (0.6%) | 0.40 (0.8%) | 0.20 (0.5%) | 0.22 (0.6%) |
| 2500 - 2630 | 0.21 | 0.08 (0.2%) | 0.14 (0.2%) | 0.08 (0.2%) | 0.10 (0.2%) | 0.04 (0.1%) | 0.05 (0.1%) |
| Total | | 47.45 | 77.61 | 44.88 | 49.03 | 37.37 | 38.33 |

WCW water yield for the 2014-Feb-24 Forest Based Regression predicted snow depth flight paths are shown in Table 6.10. The observed WCW wall-to-wall snow depth combined with snow density model (A) was used as the baseline estimate for all predicted snow depth flight path water yields. T3 and T3+LCP estimated a higher water yield than the observed wall-to-wall whereas LCP estimated a lower water yield. Comparing snow density model (A) and model (B), LCP was lower than the observed wall-to-wall water yield. Both the T3 and T3+LCP estimated a higher water yield than the observed wall-to-wall.

Table 6.10: Water Yield (X $10^6$ $m^3$) for the 2014-Feb-24 lidar sampling of the WCW Wall-to-Wall observed and T3, LCP, T3+LCP 30 m FBR predicted snow depth and Elevation & CFC snow density. All "Scenario Comparison" water yield percentages are in relation to the WCW snow density model A: Closest Sampling Date multiplied by the Observed Wall-to-Wall sampled snow depth. Predicted values > 100 are higher water yield estimations, values < 100 are lower estimations.

| Model | A: Closest Sampling Date | | B: 30-year Monthly Mean | |
|---|---|---|---|---|
| (Area: 104.41 $km^2$) | Elevation and CFC | Scenario Comparison (%) | Elevation and CFC | Scenario Comparison (%) |
| Observed Wall-to-Wall | 45.70 | | 49.65 | 109 |
| T3+LCP (Predicted Depth) | 47.12 | 103 | 51.20 | 112 |
| T3 (Predicted Depth) | 47.55 | 104 | 51.66 | 113 |
| LCP (Predicted Depth) | 40.77 | 89 | 44.33 | 97 |

## 6.4 Discussion

The underlying goal of this research and snowpack monitoring framework was to quantify water yield for the West Castle watershed. This study focused on single point in time SWE estimates. West Castle water yield was calculated using airborne lidar derived snow depth and density models based on AEP snowpack field sampling.

### 6.4.1 Airborne Lidar Sampling

Airborne lidar sampling was used to obtain the bare-earth (BE) and digital snow surface model (DSSM). Ground surface classification can be problematic for summer lidar sampling (the bare earth DEM). Lidar points may not penetrate to the ground surface in locations of denser ground vegetation consisting of small shrubs and grasses located mostly in non-forested areas below alpine elevations. This has the effect of raising the BE DEM surface above the true ground surface. When differencing the DSSM from BE, an underestimation of snow depth will occur where these vegetation features are located. In winter, an overestimation of snow depth can occur in the SDM where grasses and shrubs are covered by snow. When submergent shrubs and dead fallen vegetation caused by wildfire are beneath the snow, the surface appears to be very stable.

However, air pockets between the feature and ground surface will produce an over-estimation of snow depth. Ski hill operations decrease snow depth from grooming compaction and increase depth after artificial snow making. Locations with features such as wind-blown cornices that overhang the lee side of hills produce a gap between the snowpack and ground surface. SDM uncertainty is generally within 10 cm (Hopkinson et al., 2012; Raleigh & Small, 2017). However, with deeper snowpacks, proportional depth uncertainty reduces and density becomes the larger source of uncertainty (Raleigh & Small, 2017). Snow depth progression of lidar flights through 2020-2021 (the lowest accumulated snow season) with less than 20 cm (Table 6.3 and Appendix A) was 0% in Jan and increased to 7.2% in Mar. Apr and had 12.6% of the WCW snow depth less than 20 cm with 4.5% of that area in valley elevations of the watershed. However, the valley elevations (Table 6.9) only contributed 2% of the total water yield for the Apr 2021 lidar flight. These sources of error have an influence on modelled snowpack depth from true depth. This will impact the overall wall-to-wall estimate of SWE and water yield for the watershed.

### 6.4.2 Snow Density

The AEP Pickering (2018) “Snow Surveying Field Sampling Protocols” document was created in 2018 to ensure snow sampling conducted by all personnel would be comparable throughout Alberta in order to obtain consistent (past and future) data measurements. The only requirement in this protocol is for manual field snow sampling to be completed within 5 days either side of the first of the month. Generally, several samples are taken at each location in an open area or small clearing with minimal canopy to obtain the final snow depth and SWE

measurement for that point in time. However, the public dataset does not contain information regarding the level of uncertainty or error, number of samples, or precise physical sampling location. In examining AEP snowpack field sampling sites in the southern eastern slopes of Alberta, SHRC had lower mean and median snow density difference from Gardiner ranging from 6% in Feb to 3% in Apr. Based on the density model calculation, Gardiner and SRHC should have a density within 1% of each other over the snow season since SRHC is only 20 m lower in elevation than Gardiner. Akamina (131 m lower in elevation than Gardiner) had a lower difference in mean snow density than Gardiner in Jan (4%). By the end of Apr, mean density was the same for both Gardiner and Akamina. The computed snow density for Apr models would have a difference of less than 1%. The WCII valley site (387 m lower than SHRC) had a mean density difference within 1% of SRHC for Jan and Feb. However, WCII had a snow density mean of 1% higher than SRHC for Mar. This suggests other influencing factors contributed to snow density differences between these four sites. For example, SHRC is south facing, and Gardiner is north facing. There was insufficient data as well as no clear empirical method to adjust snow density based on aspect, therefore it was not included as a model parameter.

Temporal modelled snow density had to align with the associated lidar snow depth sampling mission. Two different model scenarios were created, the first being the closest sample based utilizing the nearest neighbour field sampling (model A) versus long term 30-year monthly mean sampled density (model B) to constrain the analysis. The snow density model assumed a homogeneous snowpack throughout WCW for elevation and canopy calculated density. Specifically, the model had a linear increase in density with elevation to treeline followed by constant density from treeline to the upper reaches of the watershed. Density was then reduced based on forest canopy fractional coverage. The forest canopy influence (see Table 6.8 and

Figure 6.2) on snow density accounted for an 8% to 11% reduction in computed WCW water yield for both modelling scenarios. Locations with denser forest canopy combined with deep snowpacks caused the CFC modifier to have a large influence on the SWE calculation at the watershed scale. However, it is important to note model B estimated 14% less yield for 2021-Mar-4 and was 13% higher for the 2021-Apr-6 flight for both canopy options (CFC included and removed) of the WCW calculation. There were no further adjustments applied to the models to account for density variability in this version of the snowpack monitoring framework. However, snow density models cannot assume to be representative of the entire WCW spatial area with limited AEP calibration and ULAL validation snow depth and SWE field sampling data points.

ULAL field sampling collections that were coincident with lidar flights were used to verify point locations of modelled snow density had similar values. Only one crew was available to conduct field sampling so this limited the number of point measurements that could be obtained for each lidar flight within WCW. The heterogeneity of the snowpack with wind-scoured locations and deep packs existed within short distances on the alpine ridge as seen in Figure 6.3. Sampling on the ridge was difficult due to thick ice lenses within the pack that were difficult to cut through. It was not possible to reach the base of the snowpack for all measurement points to ensure an entire snow column was sampled. Forest canopy sampling began in the 2019 winter season therefore canopy validation was only possible for the 2020 – 2021 lidar flights. This limited the number of ULAL field sampled points that could be compared to snow density model grid cells.

There were three lidar snow sampling flights in the 2020-2021 snow season that captured the seasonal progression of the snowpack. This year had the lowest measured snow water in the Gardiner snow water depletion curve as well as the least SW differentiation of 99 mm between

the three lidar mission dates. Gardiner snow water peaked at 443 mm by the end of Apr 2021 which was still lower than the measured SW of all other lidar snow sampling flights. For Mar and Apr 2021 flights, there was patchy snow in the valley, so the snowpack was beyond the end of the depletion curve at the lower elevations whereas the rest of the watershed was still somewhere on the depletion curve. This is problematic since melt occurs at different rates and times from site to site throughout the watershed (Shea et al., 2021). From Jan to Mar, snow is generally still accumulating at all elevations. By the end of Mar, WCW may still be accumulating snow at upper elevations while lower elevations are isothermal and melting out. The Apr 2018 lidar snow sampling flight had the highest calculated water yield. The pack did not start to melt out until the end of Apr 2018 after the lidar flight occurred due to colder air temperatures (below 0° C) that prevented the snowpack from melting in valley elevations (Barnes et al., 2020).

### 6.4.3 Snow Water Equivalent and WCW Water Estimates

Water yield estimates (see Table 6.11) for the WCW lower, mid, and upper elevations as seen in Figure 6.2, show the lowest elevation range had the least water yield for both snow density modelling (A and B) scenarios. In contrast, the upper elevation category (above 1970 masl) was the most productive with 43% to 49% of estimated water yield for the watershed. However, there are no AEP sampling sites in these upper elevations (within southwestern Alberta) to calibrate snow density models. Since AEP field sampling was used to constrain the lower and upper density ranges for WCW, which model is more appropriate to use? AEP sampling had a gap of six to nine days for four of the lidar snow covered area acquisitions. There could be significant changes in the snowpack state between AEP sampling and lidar missions.

The long-term 30-year monthly mean (model B) may be a better modelling choice since it is not possible to know if the closest sampling date (model A) is truly representative of snow density for the watershed. However, when shorter time intervals occur between AEP and lidar sampling dates, model A might be a more appropriate option to account for differences in water year (higher or lower) precipitation volumes. If AEP manual field sampling estimates of snow depth and SWE are highly reliable, model A may be more representative of WCW snow density. Unfortunately, there is no indication of data variance or standard deviation for individual temporal measurements. One option is to run both snow density models since each scenario produced a different watershed water yield. The Feb 2014 was the only date when AEP sampling occurred on the same day as the lidar snow sampling flight. Comparing both snow density modelling scenarios with the WCW FRB predicted snow depth (see Table 6.10), water yields were within 3% to 13%. This may be an acceptable range of mesoscale water yield estimates from the perspective of developing a time sensitive, "cost effective", and reduced snowpack sampling monitoring framework.

Table 6.11: Water Yield ( x $10^6$ $m^3$) with percentage of total yield broken into three equal area elevation ranges as seen in Figure 6.2 for the model A: "Closest Sampling Date" and model B: "30-year Monthly Mean" Elevation & CFC snow density modelling scenarios. WCW Area: 101.95 $km^2$. "Days between Flight and AEP Sampling": negative values represent the number of days AEP sampling occurred before the lidar snow sampling flight, positive values indicate the number of days after the lidar flight.

| Days between Flight and AEP Sampling | | A: Closest Sampling Date | | | | B: 30-year Monthly Mean | | | |
|---|---|---|---|---|---|---|---|---|---|
| | | | Lower | Mid | Upper | | Lower | Mid | Upper |
| | | Total | 1390 – 1695 masl | 1695 – 1970 masl | 1970 – 2630 masl | Total | 1390 – 1695 masl | 1695 – 1970 masl | 1970 – 2630 masl |
| Feb-2014 | 0 | 44.42 | 7.75 (17.4%) | 17.39 (39.1%) | 19.28 (43.4%) | 47.45 | 7.98 (16.8%) | 18.43 (38.8%) | 21.04 (44.3%) |
| Apr-2018 | + 6 | 80.76 | 13.75 (17.0%) | 30.98 (38.4%) | 36.03 (44.6%) | 77.61 | 13.42 (17.3%) | 29.94 (38.6%) | 34.24 (44.1%) |
| Mar-2020 | - 3 | 46.25 | 6.34 (13.7%) | 18.68 (40.4%) | 21.24 (45.9%) | 44.88 | 5.81 (13.0%) | 17.99 (40.1%) | 21.07 (47.0%) |
| Jan-2021 | + 6 | 50.28 | 8.80 (17.5%) | 18.93 (37.6%) | 22.56 (44.9%) | 49.03 | 8.36 (17.0%) | 18.45 (37.6%) | 22.22 (45.3%) |
| Mar-2021 | - 8 | 43.60 | 4.78 (11.0%) | 17.42 (39.9%) | 21.41 (49.1%) | 37.37 | 5.37 (14.4%) | 14.98 (40.1%) | 17.02 (45.5%) |
| Apr-2021 | - 9 | 33.89 | 4.07 (12.0%) | 13.74 (40.5%) | 16.09 (47.5%) | 38.33 | 4.78 (12.5%) | 15.51 (40.5%) | 18.04 (47.1%) |

## 6.5 Conclusion

This study investigated a cost-effective framework to estimate mesoscale snow water equivalent yields. West Castle SWE and water yield was computed using airborne lidar snow depth sampling. AEP SWE field observations (collected within 5 days on either side of the first of the month) were used to create and constrain snow density models for each lidar-derived snow depth model. AEP field data collections do not always coincide with lidar flights; therefore two different snow density modeling scenarios were tested: A) sampling that was in near temporal proximity to lidar flights; and B) from calculated 30-year density monthly means. There was a 4% to 14% difference in WCW water yield between the two snow density modeling scenarios (A and B). Three of the lidar snow sampling flights were conducted in 2021. AEP sampling occurred 6 days after the January flight, however, the water yield was within 3% for both scenario A (50.28 x $10^6$ $m^3$) and B (49.03 x $10^6$ $m^3$). AEP sampling was completed prior to each of the March (eight days) and April (nine days) flights. There was an estimated 14% higher water yield for the proximal sampling in March (A = 43.60 x $10^6$ $m^3$ and B = 37.37 x $10^6$ $m^3$) and 13% lower water yield for April (A = 33.89 x $10^6$ $m^3$ and B = 38.33 x $10^6$ $m^3$). Since the snowpack state can change significantly between the time of the lidar flight and the snow density sampling, scenario B is a reasonable alternative modelling scenario. Snow density models could potentially be improved with additional terrain attributes such as directional aspect and slope. The inclusion of wind field data might allow for snowpack compaction corrections on wind loaded slopes.

WCW water yield was computed for two selective snow depth sampling and prediction configurations (described in (Barnes & Hopkinson, 2022)) and compared to the fully sampled wall-to-wall observed snow depth for the February 2014 lidar data set. AEP field sampling

occurred on the same day as the flight. The wall-to-wall observed water yield for scenario A was 45.70 x $10^6$ $m^3$. The three transect flight sampling configuration produced a water yield of 47.55 x $10^6$ $m^3$, 4% higher than the observed snow depth. The least cost path sampling configuration produced a water yield of 40.77 x $10^6$ $m^3$, 11% lower than the observed snow depth. Sample-based estimates of total watershed SWE that are within 11% of observed suggest this a viable alternative to full wall-to-wall lidar snow sampling, given this opens up the possibility for spatially-explicit yield estimates over much greater areas.

A breakdown of water yield by elevation zones showed valley elevations from 1390 masl to 1500 masl produced between 2% to 4% of the overall water yield for all flights. The most productive elevations ranged from 1970 masl to 2630 masl and contributed 43% to 49% of the water yield for all lidar snow surveys. The alpine (between 2300 masl to 2630 masl) zone contributed 4% to 5% of watershed SWE. However, no AEP snow monitoring is performed at these higher elevations in southern Alberta so there is the possibility for a small over- or under-estimation of SWE given snow density was set to a constant value at elevations above 2000 masl.

This snowpack monitoring framework only requires derived or predicted snow depths from airborne lidar samples, bare-earth DEM, DSM, and AEP snow density measurements. Once model estimates have been demonstrated to work reasonably well, this methodology can be applied to other watersheds. The next step in this innovative water resource monitoring workflow is to scale up from the watershed to larger mountain drainage basins using lidar sampling, publicly available geospatial data layers, field sampling and distributed meteorological data inputs.

## 6.6 References


Alberta Environment. (2003). Water for Life - Alberta's Strategy for Sustainability. In. Government of Alberta. http://aep.alberta.ca/water/programs-and-services/water-for-life/strategy/downloadable-information-about-the-water-for-life-strategy.aspx

Anderson, B. T., McNamara, J. P., Marshall, H. P., & Flores, A. N. (2014). Insights into the physical processes controlling correlations between snow distribution and terrain properties. *Water Resources Research*, *50*(6), 4545-4563. https://doi.org/doi:10.1002/2013WR013714

Avanzi, F., Ercolani, G., Gabellani, S., Cremonese, E., Pogliotti, P., Filippa, G., Morra di Cella, U., Ratto, S., Stevenin, H., Cauduro, M., & Juglair, S. (2021). Learning about precipitation lapse rates from snow course data improves water balance modeling. *Hydrol. Earth Syst. Sci.*, *25*(4), 2109-2131. https://doi.org/10.5194/hess-25-2109-2021

Barnes, C., & Hopkinson, C. (2022). Comparing Mountain Snowpack Depth Model Results from Different Airborne Laser Scanning Flight Path Samples. *Canadian Journal of Remote Sensing*, *48*(1), 81-92. https://doi.org/10.1080/07038992.2021.1999797

Barnes, C., Hopkinson, C., Porter, T., & Xi, Z. (2020). In-Situ LED-Based Observation of Snow Surface and Depth Transects. *Sensors*, *20*(8), 2292. https://www.mdpi.com/1424-8220/20/8/2292

Bartlett, P. A., MacKay, M. D., & Verseghy, D. L. (2006). Modified snow algorithms in the Canadian land surface scheme: Model runs and sensitivity analysis at three boreal forest stands. *Atmosphere-Ocean*, *44*(3), 207-222. https://doi.org/10.3137/ao.440301

Bergeron, T. (1960). Operation and results of "Project Pluvius.". *Physics of Precipitation, Geophys. Monogr*, *5*, 152-157.

Blue Marble Geographics. (2022). *Global Mapper Suite, Geographic Calculator*. In Copyright © 2023 Blue Marble Geographics.

Bonner, H. M., Raleigh, M. S., & Small, E. E. (2022). Isolating forest process effects on modelled snowpack density and snow water equivalent. *Hydrological Processes*, *36*(1), e14475. https://doi.org/https://doi.org/10.1002/hyp.14475

Broberg, L. (2021). Relative snowpack response to elevation, temperature and precipitation in the Crown of the Continent region of North America 1980-2013. *PLoS ONE*, *16*(4), e0248736. https://doi.org/10.1371/journal.pone.0248736

Campbell, S. (2018). *Acoustic Snow Depth Sensor Operation*. Edmonton, AB: Alberta Environment and Parks Retrieved from http://environmentalmonitoring.alberta.ca/wp-content/uploads/2018/07/Acoustic-Snow-Depth-Sensor.pdf

Cornwell, E., Molotch, N., & McPhee, J. (2016). Spatio-temporal variability of snow water equivalent in the extra-tropical Andes Cordillera from distributed energy balance modeling and remotely sensed snow cover. *Hydrology and Earth System Sciences*, *20*(1), 411.

Daly, C., Gibson, W. P., Taylor, G. H., Johnson, G. L., & Pasteris, P. (2002). A knowledge-based approach to the statistical mapping of climate. *Climate Research*, *22*(2), 99-113. https://www.int-res.com/abstracts/cr/v22/n2/p99-113

DeBeer, C. M., & Pomeroy, J. W. (2009). Modelling snow melt and snowcover depletion in a small alpine cirque, Canadian Rocky Mountains. *Hydrological Processes*, *23*(18), 2584-2599. https://doi.org/10.1002/hyp.7346

Deems, J. S., Painter, T. H., & Finnegan, D. C. (2013). Lidar measurement of snow depth: a review. *Journal of Glaciology*, *59*(215), 467-479.

DeWalle, D. R., Henderson, Z., & Rango, A. (2002). Spatial and temporal variations in snowmelt degree-day factors computed from SNOTEL data in the Upper Rio Grande basin. Proceedings of the Western Snow Conference,

Dornes, P. F., Pomeroy, J. W., Pietroniro, A., Carey, S. K., & Quinton, W. L. (2008). Influence of landscape aggregation in modelling snow-cover ablation and snowmelt runoff in a sub-arctic mountainous environment. *Hydrological Sciences Journal*, *53*(4), 725-740. https://doi.org/10.1623/hysj.53.4.725

Downing, D. J., & Pettapiece, W. W. (2006). Natural Regions Committee 2006. Natural Regions and Subregions of Alberta In. Edmonton, AB: Government of Alberta. Pub. No. T/852. .

ESRI. (2020). *ArcGIS Pro Forest-based Classification and Regression (Spatial Statistics)*. In Copyright © 1995-2020 Esri. https://pro.arcgis.com/en/pro-app/latest/tool-reference/spatial-statistics/forestbasedclassificationregression.htm

Essery, R., Li, L., & Pomeroy, J. (1999). A distributed model of blowing snow over complex terrain. *Hydrological Processes*, *13*(1415), 2423-2438.

Garvelmann, J., Pohl, S., & Weiler, M. (2014). Variability of Observed Energy Fluxes during Rain-on-Snow and Clear Sky Snowmelt in a Midlatitude Mountain Environment. *Journal of Hydrometeorology*, *15*(3), 1220-1237. https://doi.org/10.1175/jhm-d-13-0187.1

Government of Alberta. (2015). History and Description of the Castle River Range Reference Area. In (pp. 44). Edmonton, AB: Government of Alberta.

Grünewald, T., Schirmer, M., Mott, R., & Lehning, M. (2010). Spatial and temporal variability of snow depth and SWE in a small mountain catchment. *The Cryosphere*, *4*(ARTICLE), 215-225.

Hedstrom, N. R., & Pomeroy, J. W. (1998). Measurements and modelling of snow interception in the boreal forest. *Hydrological Processes*, *12*(10-11), 1611-1625. http://www.usask.ca/hydrology/papers/Hedstrom_Pomeroy_1998.pdf

Hill, D. F., Burakowski, E. A., Crumley, R. L., Keon, J., Hu, J. M., Arendt, A. A., Wikstrom Jones, K., & Wolken, G. J. (2019). Converting snow depth to snow water equivalent using climatological variables. *The Cryosphere*, *13*(7), 1767-1784. https://doi.org/10.5194/tc-13-1767-2019

Hopkinson, C., Collins, T., Anderson, A., Pomeroy, J., & Spooner, I. (2012). Spatial Snow Depth Assessment Using LiDAR Transect Samples and Public GIS Data Layers in the Elbow River Watershed, Alberta. *Canadian Water Resources Journal / Revue canadienne des ressources hydriques*, *37*(2), 69-87. https://doi.org/10.4296/cwrj3702893

Isenburg, M. (2022). *Efficient LiDAR Processing Software (Corporate License)*. In rapidlasso, (c) 2007-2022 info@rapidlasso.de - https://rapidlasso.de.

Judson, A., & Doesken, N. (2000). Density of Freshly Fallen Snow in the Central Rocky Mountains. *Bulletin of the American Meteorological Society*, *81*(7), 1577-1588. https://doi.org/10.1175/1520-0477(2000)081<1577:Doffsi>2.3.Co;2

Kang, D. H., & Barros, A. P. (2011). Full-System Testing in Laboratory Conditions of an L-Band Snow Sensor System for In Situ Monitoring of Snow-Water Content. *IEEE Transactions on Geoscience and Remote Sensing*, *49*(3), 908-919. https://doi.org/10.1109/TGRS.2010.2072786

Kershaw, R. (2008). *Exploring the Castle: discovering the backbone of the world in southern Alberta*. Rocky Mountain Books. http://uleth.summon.serialssolutions.com/2.0.0/link/0/eLvHCXMwdV25DsIwDLUQLEgMQLkPZWKjSkPbtHOh8AFdOqHQpIKFBRj4e-y2nBJjFMmKpch-vp4BVsLmyx-bILiX-aFxuHYwKPLCPCA_LbmrhDJ-OfC9FXEapDu5fvfLYih9ul3sG6pw_KJM8hClk-VtoHnlRJmf2EkxIB5KBBQIUyo2p-dZEGs1SflwHnEb6jRQ0IGaOXehV_Jy3NmCEemrKhbr3i2wXs1wDCEZixSVX3swjzdJtFsWQvdVqmX_fFgg-tBS1KJ-vhajbHoIzD9QzUtnuXQyV9PiRmM8Y5w8cF2p5WoEgz_Sxn9vJtAsGxgoJzCFRo5_1swqXR8OEWen

Kinar, N. J., & Pomeroy, J. W. (2015). Measurement of the physical properties of the snowpack. *Reviews of Geophysics*, *53*(2), 481-544. https://doi.org/10.1002/2015RG000481

Kostadinov, T. S., Schumer, R., Hausner, M., Bormann, K. J., Gaffney, R., McGwire, K., Painter, T. H., Tyler, S., & Harpold, A. A. (2019). Watershed-scale mapping of fractional snow cover under conifer forest canopy using lidar. *Remote Sensing of Environment*, *222*, 34-49. https://doi.org/10.1016/j.rse.2018.11.037

Löffler, J. (2005). Snow cover dynamics, soil moisture variability and vegetation ecology in high mountain catchments of central Norway. *Hydrological Processes*, *19*(12), 2385-2405. https://doi.org/10.1002/hyp.5891

López-Moreno, J. I., Fassnacht, S. R., Heath, J. T., Musselman, K. N., Revuelto, J., Latron, J., Morán-Tejeda, E., & Jonas, T. (2013). Small scale spatial variability of snow density and depth over complex alpine terrain: Implications for estimating snow water equivalent. *Advances in water resources*, *55*, 40-52. https://doi.org/https://doi.org/10.1016/j.advwatres.2012.08.010

McCaffrey, D., & Hopkinson, C. (2020). Repeat Oblique Photography Shows Terrain and Fire-Exposure Controls on Century-Scale Canopy Cover Change in the Alpine Treeline Ecotone. *Remote Sensing*, *12*(10), 1569. https://www.mdpi.com/2072-4292/12/10/1569

Mizukami, N., & Perica, S. (2008). Spatiotemporal Characteristics of Snowpack Density in the Mountainous Regions of the Western United States. *Journal of Hydrometeorology*, *9*(6), 1416-1426. https://doi.org/10.1175/2008jhm981.1

Mott, R., Vionnet, V., & Grünewald, T. (2018). The Seasonal Snow Cover Dynamics: Review on Wind-Driven Coupling Processes [Review]. *Frontiers in Earth Science*, *6*(197). https://doi.org/10.3389/feart.2018.00197

Naderpour, R., Schwank, M., & Mätzler, C. (2017). Davos-Laret Remote Sensing Field Laboratory: 2016/2017 Winter Season L-Band Measurements Data-Processing and Analysis. *Remote Sensing*, *9*(11), 1185. http://www.mdpi.com/2072-4292/9/11/1185

Newton, B. W., Farjad, B., & Orwin, J. F. (2021). Spatial and Temporal Shifts in Historic and Future Temperature and Precipitation Patterns Related to Snow Accumulation and Melt Regimes in Alberta, Canada. *Water*, *13*(8), 1013. https://www.mdpi.com/2073-4441/13/8/1013

Nitu, R. (2010). *CIMO Survey on National Summaries of Methods and Instruments for Solid Precipitation Measurement at Automatic Weather Stations, IOM 102, TD1544*.

Oldman Watershed Council. (2014). Oldman Integrated Watershed Management Plan Headwaters Action Plan 2013-13 Final. In (pp. 64). Lethbridge, AB: Oldman Watershed Council.

Onuchin, A. A., & Burenina, T. A. (1996). Climatic and Geographic Patterns in Snow Density Dynamics, Northern Eurasia. *Arctic and Alpine Research*, *28*(1), 99-103. https://doi.org/10.1080/00040851.1996.12003153

Painter, T. H., Berisford, D. F., Boardman, J. W., Bormann, K. J., Deems, J. S., Gehrke, F., Hedrick, A., Joyce, M., Laidlaw, R., Marks, D., Mattmann, C., McGurk, B., Ramirez, P., Richardson, M., Skiles, S. M., Seidel, F. C., & Winstral, A. (2016). The Airborne Snow Observatory: Fusion of scanning lidar, imaging spectrometer, and physically-based modeling for mapping snow water equivalent and snow albedo. *Remote Sensing of Environment*, *184*, 139-152. https://doi.org/https://doi.org/10.1016/j.rse.2016.06.018

Parajuli, A., Nadeau, D. F., Anctil, F., Parent, A.-C., Bouchard, B., Girard, M., & Jutras, S. (2020). Exploring the spatiotemporal variability of the snow water equivalent in a small boreal forest catchment through observation and modelling. *Hydrological Processes*, *34*(11), 2628-2644. https://doi.org/https://doi.org/10.1002/hyp.13756

Pedlar, J. (2018). *Protocols for the Measurement of Snow Water Equivalent with a Snow Pillow*. Edmonton, AB: Alberta Environment and Parks Retrieved from http://environmentalmonitoring.alberta.ca/wp-content/uploads/2018/07/Protocols-for-the-Measurement-of-Snow-Water-Equivalent-with-Snow-Pillow.pdf

Pickering, R. (2018). *Snow Surveying Field Sampling Protocols*. Alberta Environment and Parks. http://environmentalmonitoring.alberta.ca/resources/standards-and-protocols/

Pomeroy, J. W., Gray, D. M., Shook, K. R., Toth, B., Essery, R. L. H., Pietroniro, A., & Hedstrom, N. (1998). An evaluation of snow accumulation and ablation processes for land surface modelling. *Hydrological Processes*, *12*(15), 2339-2367. https://doi.org/10.1002/(SICI)1099-1085(199812)12:15<2339::AID-HYP800>3.0.CO;2-L

Proksch, M., Löwe, H., & Schneebeli, M. (2015). Density, specific surface area, and correlation length of snow measured by high-resolution penetrometry. *Journal of Geophysical Research: Earth Surface*, *120*(2), 346-362. https://doi.org/10.1002/2014jf003266

Raleigh, M. S., & Small, E. E. (2017). Snowpack density modeling is the primary source of uncertainty when mapping basin-wide SWE with lidar. *Geophysical Research Letters*, *44*(8), 3700-3709. https://doi.org/doi:10.1002/2016GL071999

Riboust, P., Thirel, G., Le Moine, N., & Ribstein, P. (2019). Revisiting a simple degree-day model for integrating satellite data: implementation of SWE-SCA hystereses. *J. Hydrol. Hydromech*, *67*(1), 70-81.

Seidel, F. C., Rittger, K., Skiles, S. M., Molotch, N. P., & Painter, T. H. (2016). Case study of spatial and temporal variability of snow cover, grain size, albedo and radiative forcing in the Sierra Nevada and Rocky Mountain snowpack derived from imaging spectroscopy. *The Cryosphere*, *10*(3).

Shea, J. M., Whitfield, P. H., Fang, X., & Pomeroy, J. (2021). The Role of Basin Geometry in Mountain Snowpack Responses to Climate Change. *Frontiers in Water*, *3*, 4.

Sturm, M., & Holmgren, J. (1998). Differences in compaction behavior of three climate classes of snow. *Annals of Glaciology*, *26*, 125-130. https://doi.org/10.3189/1998AoG26-1-125-130

Sturm, M., Holmgren, J., & Liston, G. E. (1995). A seasonal snow cover classification system for local to global applications. *Journal of Climate*, *8*(5), 1261-1283.

Sun, N., Yan, H., Wigmosta, M. S., Lundquist, J., Dickerson-Lange, S., & Zhou, T. (2022). Forest Canopy Density Effects on Snowpack Across the Climate Gradients of the Western United States Mountain Ranges. *Water Resources Research*, *58*(1), e2020WR029194. https://doi.org/https://doi.org/10.1029/2020WR029194

Thiessen, A. H. (1911). Precipitation Averages for Large Areas. *Monthly Weather Review*, *39*(7), 1082-1089. https://doi.org/10.1175/1520-0493(1911)39<1082b:PAFLA>2.0.CO;2

Timoney, K. (1998). Environmentally significant areas inventory of the Rocky Mountain natural region of Alberta. *Prepared for: Corporate Management Service, Alberta Environmental Protection, Edmonton, Alberta*, 106.

Veatch, W., Brooks, P. D., Gustafson, J. R., & Molotch, N. P. (2009). 'Quantifying the effects of forest canopy cover on net snow accumulation at a continental, mid-latitude site'. *Ecohydrology*, *2*(2), 115-128. https://doi.org/10.1002/eco.45

Verseghy, D. (2009). CLASS–the Canadian Land Surface Scheme (Version 3.4). *Environment Canada, Toronto, Ont*.

Vivian, M., Bernt, L., V., H. K., & Robert, L. K. (2007). Predicting snow density using meteorological data. *Meteorological Applications*, *14*(4), 413-423. https://doi.org/doi:10.1002/met.40

Warren, S. G. (1982). Optical properties of snow. *Reviews of Geophysics*, *20*(1), 67-89. https://doi.org/doi:10.1029/RG020i001p00067

Winkler, M., Schellander, H., & Gruber, S. (2021). Snow water equivalents exclusively from snow depths and their temporal changes: the Δsnow model. *Hydrol. Earth Syst. Sci.*, *25*(3), 1165-1187. https://doi.org/10.5194/hess-25-1165-2021

Zhu, Z., & Waller, E. (2003). Global forest cover mapping for the United Nations Food and Agriculture Organization forest resources assessment 2000 program. *Forest science*, *49*(3), 369-380.

# 7 Conclusion and Recommendations

Headwater SWE estimates are important to aid in water resource and flood hazard forecasting. Such forecasting relies heavily on in situ observations and models. In this research, innovations in integrated remote and in situ sensing were evaluated to address the need for improved headwater snowpack resource assessment. Two over-arching montane water resources research themes were explored in this thesis: 1) spatial, temporal and elevational precipitation patterns; and 2) single point in time assessments of spatially-explicit watershed snowpack conditions.

## 7.1 Summary

This thesis explored spatiotemporal precipitation patterns in the Alberta southern Eastern Slopes, and estimated snow water in the West Castle Watershed (WCW). The second chapter (Barnes & Hopkinson, 2022b) involved the smoothing and quality control process of totalizing precipitation data collected at one valley and one alpine site located in West Castle and a valley site in Waterton Lakes National Park. Using the quality controlled cleaned precipitation data, the third chapter (In Review) explored elevational precipitation gradients and seasonal relationships between the sites. By understanding the spatiotemporal distribution of precipitation in the southern Eastern Slopes, this set up the thesis to focus on the winter snowpack monitoring framework. The balance of the research was conducted in the smaller WCW mesoscale mountainous region. Chapter 4 (Barnes et al., 2020) tested a non-traditional LED Lidar sensor during the snow season from initial accumulation to final melt to measure and quantify snow depth variability at the in-situ spatial scale. The fifth chapter (Barnes & Hopkinson, 2022a)

developed and assessed two airborne lidar sampling configurations using spatially distributed drivers of snow depth over WCW. A forest-based regression model was used to predict snow depth for the balance of the "wall-to-wall" watershed. The sixth chapter tested the development of spatially distributed snow density models combined with "wall-to-wall" lidar sampled snow depth models to generate snow water estimates for the West Castle Watershed.

## 7.2 Implications and outcomes

Standard lidar post-processing techniques for ground classification can be challenging in mountain regions due to terrain features that have abrupt changes in elevation such as rocky outcrops, cliff faces, naturally occurring overhangs, and cornices. Currently, automated ground classification and data cleaning processes must be supplemented by manual point cloud classification to capture the ground surface on these types of features. Snow is highly reflective in the 1064 nm band and soils are highly reflective in 1550 nm band making points sampled in these channels easier to identify and move into the ground class. However, when winter snow covered flights occur with high winds, blowing snow can result in additional noise points to be classified as vegetation. This is not a big problem since only the ground class is used to create snow depth models. This manual point cloud classification process can take tens to hundreds of hours to complete for a single airborne lidar mission. Lidar manufacturers have been working towards addressing this issue. For example, Teledyne Geospatial (Galaxy Onboard | Teledyne Geospatial (teledyneoptech.com)) has developed a system that completes "real-time" classification and lidar point cloud processing while performing survey operations and data collection. However, this technology is not necessarily accessible by all sectors who use airborne

lidar systems. There is a need to examine efficiencies to improve the amount of time required to perform lidar point cloud classification and data quality assurance.

Airborne lidar is an effective method to survey and sample snow depth at the mesoscale. In chapter 5, airborne lidar snow depth sampling configuration tests suggested that systematic transect sampling (T3) performed better than a Least Cost Path (LCP) optimised sampling path for wall-to-wall watershed snow depth imputation. The T3 path configuration followed a largely expert selection process with constraints on line spacing and orientation. The resulting top two snow depth prediction variables were the physically-based drivers of elevation then forest canopy cover. The LCP configuration was a semi-automated technique where start and end were user-defined and the optimal path smoothened following aircraft trajectory constraints. The best two LCP snow depth predictors were latitude and longitude, or systematic spatial variations, as opposed to grid-cell based physical attributes. A combination of both configurations appears to maximize snow depth variability sampling and model output accuracy. A completely automated selection technique is required to create these flight paths.

When hydrological models use data from a single or small number of measurement sites for precipitation distribution, the true variability across a watershed may not be represented or simulated. There is high spatiotemporal variability of precipitation, especially in mountainous regions (Thiessen, 1911). Single point locations are insufficient to characterize the spatial and temporal distributions of precipitation depths over valley to alpine elevation ranges. In chapter 3, mean annual precipitation for the alpine site was 1262 mm whereas the valley site located 3.5 km north recorded mean annual precipitation of 899 mm. A seasonality component was identified where 80% higher precipitation depths were recorded in the alpine during the winter months and 70% lower depths in the summer months. This seasonality changes the elevational precipitation

gradients through the year. Depending on the timing within a hydrologic model, single elevational precipitation gradients will underestimate precipitation depths in the alpine during winter months and overestimate precipitation in the summer months. Hydrologic models may not perform well especially for watersheds containing a higher proportion of alpine areas (Shea et al., 2021), as seasonal discrepancies in precipitation will likely propagate into seasonal discrepancies in simulated runoff or model calibration errors.

This thesis focused on quantifying snow water yield estimates for the West Castle watershed that is approximately 100 $km^2$. In WCW, the most productive elevations of snow water equivalent were found at near treeline elevations between 1900 masl to 2200 masl. However, AEP field snow sampling sites (used to constrain snow density models) are generally at valley to mid-mountain elevations and not in the upper treeline to alpine zone due to logistical access challenges, cost of installation and maintenance, and equipment failure caused by strong winds.

## 7.3 Recommendations and Next Steps

There is an opportunity to use this snow monitoring framework to complement mountain headwater supply and flood forecast monitoring. In chapter 6, there are six “single point in time” data modelling estimates that can be used to compare to past governmental monitoring and hydrological modelling scenarios. To calibrate hydrological models, a recommendation is to implement seasonal and spatially variable elevational precipitation gradients for water resource estimation. There is also a need for additional observation data to explore the underlying physics associated with the enhancement (or otherwise) and seasonality patterns of precipitation depths in the alpine.

Opportunities to improve and better quantify precipitation and snowpack across the AEP network could be explored. For example, one suggestion is to compare watershed SWE totals using the lidar-based SWE modeling framework to nearby in situ AEP site measurements for the same timeframes to see if the spatial and in situ SWE estimates co-vary. If the data do not co-vary, then single point AEP monitoring sites may be weak proxies of regional water yields. New or shifted monitoring sites might better represent regional yields but with hydro-climatological trends deviating from long-term historical norms, it is believed the existing monitoring frameworks need to be supplemented with new spatially-explicit sampling and prediction modelling workflows, as has been demonstrated in this thesis.

The next step in this research is to scale the framework up to the Alberta Eastern Slopes (an area greater than 50,000 $km^2$). In chapter 5, the data required to predict wall-to-wall snow depth using the selective lidar flight line snow depth sampling was extracted from a digital elevation model and digital surface model. In chapter 6, the snow density model was created using the long-term Government of Alberta Environment and Protected Areas monthly snow sampling field data that were in close proximity to WCW and were near valley and treeline elevations. All spatial data was aggregated to a 30 m resolution to align with publicly available DEM and satellite land cover data products such as ASTER DEM or Landsat. To upscale and adapt this framework for the Eastern Slopes, data sources need to be identified to replace the DSM (required to extract the landcover that is used for snow depth prediction).

With finite resources, funding, expertise, and time, wall-to-wall lidar snow depth mapping is impractical over very large areas where missions can take days to complete while snow conditions continue to vary. Cost reduction and the desire to sample larger spatial extents such as the entire Alberta Eastern Slopes drives the need to improve optimal flight path selection.

WCW has a long, narrow, North/South orientation with most of the area below alpine elevations. Wall-to-wall prediction using reduced lidar snow depth sampling did not adequately represent shallow and scoured snowpacks in the alpine. An analysis needs be completed to examine the sensitivity and attributes of watersheds with different landcovers, orientations, and mountain geometry to identify where model improvements can be made. A recommendation for the next steps in flight path sample design is to use a deep learning approach to test 1000s of flight path iterations over the greatest number of snow depth drivers while also observing flight configuration safety and flying constraints such as: a) the plane needs to fly a line that minimizes turns and deviations; and b) terrain-following paths must avoid abrupt changes in terrain elevation. Ground classification improvements are also needed to speed up data processing and improve accuracy given the current process of manual terrain and snow surface cleaning could constitute a bottleneck within a public sector water resource monitoring and forecasting program.

## 7.4 References


Barnes, C., & Hopkinson, C. (2022a). Comparing Mountain Snowpack Depth Model Results from Different Airborne Laser Scanning Flight Path Samples. *Canadian Journal of Remote Sensing*, *48*(1), 81-92. https://doi.org/10.1080/07038992.2021.1999797

Barnes, C., & Hopkinson, C. (2022b). Quality Control Impacts on Total Precipitation Gauge Records for Montane Valley and Ridge Sites in SW Alberta, Canada. *Data*, *7*(6), 73. https://doi.org/https://doi.org/10.3390/data7060073

Barnes, C., Hopkinson, C., Porter, T., & Xi, Z. (2020). In-Situ LED-Based Observation of Snow Surface and Depth Transects. *Sensors*, *20*(8), 2292. https://www.mdpi.com/1424-8220/20/8/2292

Shea, J. M., Whitfield, P. H., Fang, X., & Pomeroy, J. (2021). The Role of Basin Geometry in Mountain Snowpack Responses to Climate Change. *Frontiers in Water*, *3*, 4.

Thiessen, A. H. (1911). Precipitation Averages for Large Areas. *Monthly Weather Review*, *39*(7), 1082-1089. https://doi.org/10.1175/1520-0493(1911)39<1082b:PAFLA>2.0.CO;2

# 8 Appendix A: WCW Snow Depth Distribution

as a percentage of the watershed total for 100 m elevation bins for each lidar flight.

Feb 2014 Lidar flight snow depth per elevation bin (masl)

| Snow Depth (m) | 1390 – 1500 | 1500 – 1600 | 1600 – 1700 | 1700 – 1800 | 1800 – 1900 | 1900 – 2000 | 2000 – 2100 | 2100 – 2200 | 2200 – 2300 | 2300 – 2400 | 2400 – 2500 | 2500 – 2630 | Total ( % ) |
|---|---|---|---|---|---|---|---|---|---|---|---|---|---|
| 0.0 - 0.2 | 0.05% | 0.02% | 0.06% | 0.10% | 0.13% | 0.19% | 0.25% | 0.28% | 0.26% | 0.30% | 0.06% | 0.01% | 1.72% |
| 0.2 - 0.4 | 0.38% | 0.03% | 0.05% | 0.09% | 0.14% | 0.35% | 0.41% | 0.42% | 0.53% | 0.51% | 0.19% | 0.07% | 3.16% |
| 0.4 - 0.6 | 1.63% | 0.26% | 0.16% | 0.15% | 0.23% | 0.39% | 0.45% | 0.54% | 0.56% | 0.36% | 0.15% | 0.03% | 4.90% |
| 0.6 - 0.8 | 2.78% | 1.21% | 0.55% | 0.33% | 0.26% | 0.39% | 0.38% | 0.48% | 0.42% | 0.24% | 0.08% | 0.02% | 7.13% |
| 0.8 - 1.0 | 2.99% | 2.93% | 1.12% | 0.63% | 0.39% | 0.39% | 0.40% | 0.41% | 0.32% | 0.19% | 0.04% | 0.01% | 9.83% |
| 1.0 - 1.2 | 2.01% | 3.23% | 2.14% | 0.90% | 0.70% | 0.45% | 0.39% | 0.40% | 0.35% | 0.17% | 0.04% | 0.01% | 10.79% |
| 1.2 - 1.4 | 0.75% | 1.99% | 2.76% | 1.50% | 0.98% | 0.85% | 0.46% | 0.44% | 0.31% | 0.15% | 0.03% | 0.01% | 10.24% |
| 1.4 - 1.6 | 0.24% | 0.87% | 1.90% | 2.05% | 1.43% | 1.28% | 0.72% | 0.46% | 0.30% | 0.14% | 0.03% | 0.01% | 9.44% |
| 1.6 - 1.8 | 0.06% | 0.47% | 1.00% | 2.00% | 1.62% | 1.53% | 1.11% | 0.67% | 0.35% | 0.15% | 0.04% | 0.01% | 9.01% |
| 1.8 - 2.0 | 0.01% | 0.27% | 0.66% | 1.31% | 1.28% | 1.41% | 1.24% | 0.86% | 0.47% | 0.14% | 0.03% | 0.00% | 7.69% |
| 2.0 - 2.2 | 0.01% | 0.11% | 0.44% | 0.94% | 1.03% | 1.32% | 1.01% | 0.74% | 0.42% | 0.18% | 0.02% | 0.00% | 6.22% |
| 2.2 - 2.4 | 0.00% | 0.05% | 0.24% | 0.62% | 0.88% | 0.87% | 1.00% | 0.65% | 0.41% | 0.14% | 0.02% | 0.01% | 4.88% |
| 2.4 - 2.6 | 0.00% | 0.02% | 0.12% | 0.36% | 0.67% | 0.72% | 0.80% | 0.49% | 0.30% | 0.11% | 0.01% | 0.00% | 3.60% |
| 2.6 - 2.8 | 0.00% | 0.02% | 0.06% | 0.27% | 0.50% | 0.55% | 0.69% | 0.41% | 0.24% | 0.06% | 0.02% | 0.00% | 2.80% |
| 2.8 - 3.0 | 0.00% | 0.01% | 0.03% | 0.19% | 0.36% | 0.50% | 0.50% | 0.38% | 0.18% | 0.06% | 0.02% | 0.00% | 2.21% |
| 3.0 - 3.2 | 0.00% | 0.01% | 0.02% | 0.12% | 0.28% | 0.34% | 0.43% | 0.23% | 0.12% | 0.03% | 0.01% | 0.00% | 1.59% |
| 3.2 - 3.4 | 0.00% | 0.00% | 0.01% | 0.08% | 0.22% | 0.24% | 0.27% | 0.18% | 0.07% | 0.04% | 0.01% | 0.00% | 1.12% |
| 3.4 - 3.6 | 0.00% | 0.00% | 0.00% | 0.05% | 0.15% | 0.20% | 0.20% | 0.13% | 0.07% | 0.03% | 0.01% | 0.00% | 0.83% |
| 3.6 - 3.8 | 0.00% | 0.00% | 0.00% | 0.04% | 0.13% | 0.13% | 0.14% | 0.07% | 0.04% | 0.03% | 0.01% | 0.00% | 0.59% |
| 3.8 - 4.0 | 0.00% | 0.00% | 0.00% | 0.03% | 0.08% | 0.10% | 0.10% | 0.06% | 0.03% | 0.02% | 0.01% | 0.00% | 0.43% |
| 4.0 - 4.2 | 0.00% | 0.00% | 0.00% | 0.02% | 0.08% | 0.08% | 0.08% | 0.04% | 0.03% | 0.01% | 0.00% | 0.00% | 0.34% |
| 4.2 - 4.4 | 0.00% | 0.00% | 0.00% | 0.01% | 0.04% | 0.06% | 0.05% | 0.04% | 0.02% | 0.02% | 0.01% | 0.00% | 0.25% |
| 4.4 - 4.6 | 0.00% | 0.00% | 0.00% | 0.01% | 0.04% | 0.04% | 0.05% | 0.03% | 0.02% | 0.02% | 0.00% | 0.00% | 0.21% |
| 4.6 - 4.8 | 0.00% | 0.00% | 0.00% | 0.00% | 0.02% | 0.05% | 0.03% | 0.03% | 0.02% | 0.02% | 0.00% | 0.00% | 0.17% |
| 4.8 - 5.0 | 0.00% | 0.00% | 0.00% | 0.00% | 0.01% | 0.03% | 0.03% | 0.03% | 0.02% | 0.01% | 0.00% | 0.00% | 0.13% |
| 5.0 - 5.2 | 0.00% | 0.00% | 0.00% | 0.00% | 0.01% | 0.03% | 0.03% | 0.02% | 0.00% | 0.01% | 0.00% | 0.00% | 0.11% |
| 5.2 - 5.4 | 0.00% | 0.00% | 0.00% | 0.00% | 0.02% | 0.02% | 0.02% | 0.02% | 0.01% | 0.00% | 0.00% | 0.00% | 0.09% |
| 5.4 - 5.6 | 0.00% | 0.00% | 0.00% | 0.00% | 0.01% | 0.02% | 0.02% | 0.02% | 0.00% | 0.00% | 0.00% | 0.00% | 0.08% |
| 5.6 - 5.8 | 0.00% | 0.00% | 0.00% | 0.00% | 0.01% | 0.02% | 0.01% | 0.01% | 0.00% | 0.00% | 0.00% | 0.00% | 0.06% |
| > 5.8 | 0.00% | 0.00% | 0.00% | 0.00% | 0.05% | 0.12% | 0.08% | 0.09% | 0.03% | 0.01% | 0.00% | 0.00% | 0.38% |
| Total ( % ) | 10.91% | 11.48% | 11.34% | 11.79% | 11.74% | 12.67% | 11.34% | 8.62% | 5.88% | 3.14% | 0.85% | 0.23% | 100.00% |

Apr 2018 Lidar flight snow depth per elevation bin (masl)

| Snow Depth (m) | 1390 – 1500 | 1500 – 1600 | 1600 – 1700 | 1700 – 1800 | 1800 – 1900 | 1900 – 2000 | 2000 – 2100 | 2100 – 2200 | 2200 – 2300 | 2300 – 2400 | 2400 – 2500 | 2500 – 2630 | Total ( % ) |
|---|---|---|---|---|---|---|---|---|---|---|---|---|---|
| 0.0 - 0.2 | 0.08% | 0.02% | 0.05% | 0.09% | 0.09% | 0.13% | 0.17% | 0.19% | 0.18% | 0.26% | 0.04% | 0.00% | 1.31% |
| 0.2 - 0.4 | 0.20% | 0.02% | 0.04% | 0.07% | 0.10% | 0.15% | 0.16% | 0.21% | 0.27% | 0.33% | 0.13% | 0.03% | 1.71% |
| 0.4 - 0.6 | 0.67% | 0.05% | 0.05% | 0.08% | 0.13% | 0.22% | 0.23% | 0.24% | 0.26% | 0.25% | 0.10% | 0.04% | 2.34% |
| 0.6 - 0.8 | 2.70% | 0.50% | 0.16% | 0.11% | 0.15% | 0.23% | 0.26% | 0.26% | 0.34% | 0.19% | 0.08% | 0.02% | 5.02% |
| 0.8 - 1.0 | 3.04% | 1.39% | 0.56% | 0.20% | 0.19% | 0.28% | 0.27% | 0.34% | 0.30% | 0.16% | 0.05% | 0.02% | 6.80% |
| 1.0 - 1.2 | 2.09% | 2.37% | 1.12% | 0.45% | 0.21% | 0.27% | 0.28% | 0.32% | 0.27% | 0.17% | 0.04% | 0.01% | 7.61% |
| 1.2 - 1.4 | 1.35% | 3.29% | 1.60% | 0.84% | 0.37% | 0.31% | 0.30% | 0.31% | 0.24% | 0.14% | 0.04% | 0.01% | 8.81% |
| 1.4 - 1.6 | 0.57% | 2.00% | 2.16% | 1.33% | 0.71% | 0.38% | 0.32% | 0.31% | 0.27% | 0.13% | 0.03% | 0.01% | 8.20% |
| 1.6 - 1.8 | 0.13% | 0.95% | 2.01% | 1.51% | 0.90% | 0.64% | 0.40% | 0.33% | 0.27% | 0.10% | 0.03% | 0.01% | 7.27% |
| 1.8 - 2.0 | 0.04% | 0.46% | 1.48% | 1.45% | 1.05% | 1.06% | 0.52% | 0.37% | 0.28% | 0.11% | 0.03% | 0.01% | 6.85% |
| 2.0 - 2.2 | 0.01% | 0.26% | 0.92% | 1.64% | 1.35% | 1.26% | 0.83% | 0.47% | 0.26% | 0.12% | 0.04% | 0.01% | 7.17% |
| 2.2 - 2.4 | 0.01% | 0.12% | 0.52% | 1.24% | 1.26% | 1.17% | 0.85% | 0.59% | 0.33% | 0.11% | 0.03% | 0.01% | 6.24% |
| 2.4 - 2.6 | 0.00% | 0.05% | 0.32% | 0.85% | 0.95% | 1.21% | 0.96% | 0.74% | 0.41% | 0.13% | 0.02% | 0.00% | 5.65% |
| 2.6 - 2.8 | 0.00% | 0.02% | 0.18% | 0.55% | 0.77% | 1.04% | 0.95% | 0.68% | 0.39% | 0.12% | 0.02% | 0.00% | 4.72% |
| 2.8 - 3.0 | 0.00% | 0.01% | 0.07% | 0.41% | 0.64% | 0.78% | 0.78% | 0.52% | 0.33% | 0.15% | 0.02% | 0.01% | 3.72% |
| 3.0 - 3.2 | 0.00% | 0.00% | 0.05% | 0.28% | 0.53% | 0.58% | 0.67% | 0.42% | 0.30% | 0.14% | 0.01% | 0.01% | 2.98% |
| 3.2 - 3.4 | 0.00% | 0.00% | 0.02% | 0.18% | 0.43% | 0.51% | 0.60% | 0.39% | 0.26% | 0.08% | 0.02% | 0.00% | 2.50% |
| 3.4 - 3.6 | 0.00% | 0.00% | 0.02% | 0.14% | 0.39% | 0.43% | 0.52% | 0.35% | 0.19% | 0.05% | 0.02% | 0.00% | 2.12% |
| 3.6 - 3.8 | 0.00% | 0.00% | 0.01% | 0.10% | 0.29% | 0.36% | 0.45% | 0.28% | 0.13% | 0.04% | 0.01% | 0.00% | 1.68% |
| 3.8 - 4.0 | 0.00% | 0.00% | 0.01% | 0.08% | 0.23% | 0.31% | 0.34% | 0.21% | 0.12% | 0.03% | 0.01% | 0.00% | 1.34% |
| 4.0 - 4.2 | 0.00% | 0.00% | 0.01% | 0.06% | 0.17% | 0.23% | 0.26% | 0.16% | 0.08% | 0.03% | 0.01% | 0.00% | 1.00% |
| 4.2 - 4.4 | 0.00% | 0.00% | 0.01% | 0.04% | 0.16% | 0.17% | 0.25% | 0.14% | 0.06% | 0.03% | 0.01% | 0.00% | 0.86% |
| 4.4 - 4.6 | 0.00% | 0.00% | 0.00% | 0.03% | 0.11% | 0.14% | 0.16% | 0.10% | 0.05% | 0.02% | 0.00% | 0.00% | 0.62% |
| 4.6 - 4.8 | 0.00% | 0.00% | 0.00% | 0.03% | 0.09% | 0.11% | 0.15% | 0.08% | 0.05% | 0.04% | 0.01% | 0.00% | 0.55% |
| 4.8 - 5.0 | 0.00% | 0.00% | 0.00% | 0.01% | 0.07% | 0.09% | 0.10% | 0.06% | 0.03% | 0.01% | 0.01% | 0.00% | 0.37% |
| 5.0 - 5.2 | 0.00% | 0.00% | 0.00% | 0.01% | 0.06% | 0.07% | 0.07% | 0.06% | 0.03% | 0.02% | 0.00% | 0.00% | 0.33% |
| 5.2 - 5.4 | 0.00% | 0.00% | 0.00% | 0.01% | 0.06% | 0.07% | 0.07% | 0.04% | 0.03% | 0.02% | 0.01% | 0.00% | 0.29% |
| 5.4 - 5.6 | 0.00% | 0.00% | 0.00% | 0.01% | 0.04% | 0.06% | 0.05% | 0.03% | 0.02% | 0.02% | 0.00% | 0.00% | 0.24% |
| 5.6 - 5.8 | 0.00% | 0.00% | 0.00% | 0.00% | 0.04% | 0.05% | 0.05% | 0.03% | 0.01% | 0.01% | 0.00% | 0.00% | 0.21% |
| > 5.8 | 0.00% | 0.00% | 0.00% | 0.02% | 0.18% | 0.40% | 0.34% | 0.33% | 0.12% | 0.08% | 0.03% | 0.01% | 1.51% |
| Total ( % ) | 10.90% | 11.51% | 11.36% | 11.80% | 11.69% | 12.72% | 11.35% | 8.58% | 5.88% | 3.11% | 0.86% | 0.23% | 100.00% |

Mar 2020 Lidar flight snow depth per elevation bin (masl)

| Snow Depth (m) | 1390 – 1500 | 1500 – 1600 | 1600 – 1700 | 1700 – 1800 | 1800 – 1900 | 1900 – 2000 | 2000 – 2100 | 2100 – 2200 | 2200 – 2300 | 2300 – 2400 | 2400 – 2500 | 2500 – 2630 | Total ( % ) |
|---|---|---|---|---|---|---|---|---|---|---|---|---|---|
| 0.0 - 0.2 | 0.86% | 0.05% | 0.08% | 0.12% | 0.23% | 0.43% | 0.51% | 0.46% | 0.39% | 0.49% | 0.14% | 0.02% | 3.78% |
| 0.2 - 0.4 | 3.05% | 0.56% | 0.17% | 0.14% | 0.18% | 0.35% | 0.42% | 0.57% | 0.53% | 0.40% | 0.15% | 0.05% | 6.58% |
| 0.4 - 0.6 | 3.25% | 2.27% | 0.78% | 0.22% | 0.25% | 0.33% | 0.41% | 0.55% | 0.50% | 0.36% | 0.13% | 0.04% | 9.10% |
| 0.6 - 0.8 | 2.44% | 3.72% | 1.70% | 0.64% | 0.26% | 0.36% | 0.33% | 0.42% | 0.45% | 0.26% | 0.09% | 0.04% | 10.71% |
| 0.8 - 1.0 | 0.99% | 2.59% | 2.70% | 1.09% | 0.38% | 0.36% | 0.35% | 0.40% | 0.37% | 0.22% | 0.06% | 0.02% | 9.52% |
| 1.0 - 1.2 | 0.22% | 1.30% | 2.44% | 1.82% | 0.63% | 0.37% | 0.35% | 0.42% | 0.35% | 0.19% | 0.04% | 0.02% | 8.13% |
| 1.2 - 1.4 | 0.03% | 0.62% | 1.36% | 2.14% | 1.24% | 0.61% | 0.39% | 0.39% | 0.33% | 0.14% | 0.04% | 0.01% | 7.29% |
| 1.4 - 1.6 | 0.01% | 0.22% | 0.84% | 1.72% | 1.78% | 1.41% | 0.55% | 0.43% | 0.32% | 0.15% | 0.05% | 0.01% | 7.49% |
| 1.6 - 1.8 | 0.00% | 0.08% | 0.51% | 1.01% | 1.46% | 1.83% | 0.96% | 0.44% | 0.32% | 0.11% | 0.04% | 0.00% | 6.76% |
| 1.8 - 2.0 | 0.00% | 0.03% | 0.31% | 0.85% | 0.97% | 1.47% | 1.28% | 0.72% | 0.36% | 0.12% | 0.04% | 0.01% | 6.14% |
| 2.0 - 2.2 | 0.00% | 0.01% | 0.17% | 0.67% | 0.82% | 1.02% | 1.11% | 0.84% | 0.46% | 0.10% | 0.03% | 0.00% | 5.23% |
| 2.2 - 2.4 | 0.00% | 0.01% | 0.09% | 0.43% | 0.67% | 0.84% | 0.92% | 0.65% | 0.36% | 0.13% | 0.02% | 0.01% | 4.13% |
| 2.4 - 2.6 | 0.00% | 0.00% | 0.07% | 0.24% | 0.62% | 0.64% | 0.70% | 0.46% | 0.28% | 0.13% | 0.02% | 0.00% | 3.17% |
| 2.6 - 2.8 | 0.00% | 0.01% | 0.03% | 0.17% | 0.47% | 0.54% | 0.63% | 0.37% | 0.20% | 0.09% | 0.02% | 0.00% | 2.53% |
| 2.8 - 3.0 | 0.00% | 0.00% | 0.02% | 0.15% | 0.37% | 0.43% | 0.55% | 0.32% | 0.18% | 0.06% | 0.01% | 0.00% | 2.09% |
| 3.0 - 3.2 | 0.00% | 0.00% | 0.01% | 0.10% | 0.29% | 0.33% | 0.42% | 0.23% | 0.12% | 0.05% | 0.01% | 0.00% | 1.56% |
| 3.2 - 3.4 | 0.00% | 0.00% | 0.01% | 0.07% | 0.20% | 0.24% | 0.29% | 0.16% | 0.08% | 0.03% | 0.01% | 0.00% | 1.09% |
| 3.4 - 3.6 | 0.00% | 0.00% | 0.01% | 0.06% | 0.15% | 0.18% | 0.25% | 0.12% | 0.05% | 0.03% | 0.01% | 0.00% | 0.85% |
| 3.6 - 3.8 | 0.00% | 0.00% | 0.01% | 0.03% | 0.12% | 0.16% | 0.17% | 0.10% | 0.05% | 0.03% | 0.01% | 0.00% | 0.68% |
| 3.8 - 4.0 | 0.00% | 0.00% | 0.00% | 0.02% | 0.11% | 0.13% | 0.15% | 0.09% | 0.05% | 0.01% | 0.01% | 0.00% | 0.57% |
| 4.0 - 4.2 | 0.00% | 0.00% | 0.00% | 0.02% | 0.06% | 0.10% | 0.10% | 0.05% | 0.03% | 0.02% | 0.00% | 0.00% | 0.40% |
| 4.2 - 4.4 | 0.00% | 0.00% | 0.00% | 0.01% | 0.06% | 0.07% | 0.07% | 0.05% | 0.03% | 0.03% | 0.01% | 0.00% | 0.32% |
| 4.4 - 4.6 | 0.00% | 0.00% | 0.00% | 0.02% | 0.04% | 0.06% | 0.07% | 0.05% | 0.03% | 0.02% | 0.00% | 0.00% | 0.29% |
| 4.6 - 4.8 | 0.00% | 0.00% | 0.00% | 0.01% | 0.04% | 0.06% | 0.05% | 0.04% | 0.02% | 0.01% | 0.00% | 0.00% | 0.23% |
| 4.8 - 5.0 | 0.00% | 0.00% | 0.00% | 0.01% | 0.04% | 0.05% | 0.04% | 0.03% | 0.01% | 0.01% | 0.00% | 0.00% | 0.20% |
| 5.0 - 5.2 | 0.00% | 0.00% | 0.00% | 0.01% | 0.03% | 0.04% | 0.04% | 0.03% | 0.01% | 0.01% | 0.00% | 0.00% | 0.18% |
| 5.2 - 5.4 | 0.00% | 0.00% | 0.00% | 0.01% | 0.04% | 0.03% | 0.04% | 0.03% | 0.02% | 0.01% | 0.00% | 0.00% | 0.18% |
| 5.4 - 5.6 | 0.00% | 0.00% | 0.00% | 0.00% | 0.02% | 0.03% | 0.02% | 0.02% | 0.01% | 0.01% | 0.00% | 0.00% | 0.12% |
| 5.6 - 5.8 | 0.00% | 0.00% | 0.00% | 0.00% | 0.02% | 0.02% | 0.03% | 0.02% | 0.01% | 0.00% | 0.00% | 0.00% | 0.11% |
| > 5.8 | 0.00% | 0.00% | 0.00% | 0.01% | 0.08% | 0.19% | 0.11% | 0.12% | 0.03% | 0.02% | 0.00% | 0.00% | 0.56% |
| Total ( % ) | 10.86% | 11.47% | 11.31% | 11.77% | 11.65% | 12.66% | 11.32% | 8.60% | 5.95% | 3.23% | 0.93% | 0.25% | 100.00% |

Jan 2021 Lidar flight snow depth per elevation bin (masl)

| Snow Depth (m) | 1390 – 1500 | 1500 – 1600 | 1600 – 1700 | 1700 – 1800 | 1800 – 1900 | 1900 – 2000 | 2000 – 2100 | 2100 – 2200 | 2200 – 2300 | 2300 – 2400 | 2400 – 2500 | 2500 – 2630 | Total ( % ) |
|---|---|---|---|---|---|---|---|---|---|---|---|---|---|
| 0.0 - 0.2 | 0.01% | 0.00% | 0.00% | 0.01% | 0.00% | 0.00% | 0.01% | 0.02% | 0.00% | 0.00% | 0.00% | 0.00% | 0.05% |
| 0.2 - 0.4 | 0.00% | 0.00% | 0.00% | 0.00% | 0.01% | 0.02% | 0.03% | 0.05% | 0.01% | 0.00% | 0.00% | 0.00% | 0.12% |
| 0.4 - 0.6 | 0.03% | 0.01% | 0.08% | 0.12% | 0.22% | 0.42% | 0.49% | 0.48% | 0.35% | 0.23% | 0.05% | 0.02% | 2.50% |
| 0.6 - 0.8 | 0.74% | 0.30% | 0.29% | 0.27% | 0.31% | 0.46% | 0.52% | 0.62% | 0.58% | 0.50% | 0.17% | 0.04% | 4.80% |
| 0.8 - 1.0 | 3.54% | 1.46% | 0.99% | 0.54% | 0.41% | 0.50% | 0.56% | 0.61% | 0.57% | 0.45% | 0.15% | 0.05% | 9.86% |
| 1.0 - 1.2 | 3.86% | 3.16% | 1.68% | 1.11% | 0.61% | 0.53% | 0.49% | 0.52% | 0.50% | 0.33% | 0.13% | 0.04% | 12.94% |
| 1.2 - 1.4 | 1.98% | 3.91% | 2.54% | 1.16% | 0.86% | 0.61% | 0.48% | 0.47% | 0.42% | 0.24% | 0.06% | 0.02% | 12.75% |
| 1.4 - 1.6 | 0.60% | 1.68% | 3.10% | 2.07% | 0.91% | 0.86% | 0.51% | 0.48% | 0.35% | 0.17% | 0.05% | 0.01% | 10.78% |
| 1.6 - 1.8 | 0.08% | 0.71% | 1.24% | 2.49% | 1.51% | 1.39% | 0.83% | 0.59% | 0.38% | 0.14% | 0.03% | 0.01% | 9.41% |
| 1.8 - 2.0 | 0.01% | 0.16% | 0.70% | 1.46% | 1.65% | 1.54% | 1.10% | 0.68% | 0.40% | 0.12% | 0.04% | 0.01% | 7.88% |
| 2.0 - 2.2 | 0.00% | 0.05% | 0.38% | 1.02% | 1.41% | 1.50% | 1.02% | 0.68% | 0.41% | 0.16% | 0.04% | 0.01% | 6.68% |
| 2.2 - 2.4 | 0.00% | 0.02% | 0.15% | 0.61% | 1.00% | 1.20% | 1.14% | 0.68% | 0.38% | 0.19% | 0.03% | 0.01% | 5.41% |
| 2.4 - 2.6 | 0.00% | 0.00% | 0.06% | 0.35% | 0.78% | 0.91% | 0.99% | 0.55% | 0.36% | 0.18% | 0.03% | 0.01% | 4.23% |
| 2.6 - 2.8 | 0.00% | 0.00% | 0.04% | 0.19% | 0.55% | 0.70% | 0.81% | 0.47% | 0.29% | 0.10% | 0.03% | 0.01% | 3.18% |
| 2.8 - 3.0 | 0.00% | 0.00% | 0.01% | 0.12% | 0.39% | 0.53% | 0.64% | 0.41% | 0.26% | 0.06% | 0.02% | 0.01% | 2.46% |
| 3.0 - 3.2 | 0.00% | 0.00% | 0.01% | 0.07% | 0.30% | 0.39% | 0.47% | 0.35% | 0.16% | 0.05% | 0.01% | 0.00% | 1.80% |
| 3.2 - 3.4 | 0.00% | 0.00% | 0.00% | 0.06% | 0.19% | 0.28% | 0.34% | 0.25% | 0.13% | 0.05% | 0.01% | 0.00% | 1.33% |
| 3.4 - 3.6 | 0.00% | 0.00% | 0.01% | 0.03% | 0.14% | 0.19% | 0.25% | 0.17% | 0.08% | 0.05% | 0.01% | 0.00% | 0.92% |
| 3.6 - 3.8 | 0.00% | 0.00% | 0.01% | 0.03% | 0.11% | 0.14% | 0.17% | 0.11% | 0.06% | 0.03% | 0.01% | 0.00% | 0.67% |
| 3.8 - 4.0 | 0.00% | 0.00% | 0.00% | 0.02% | 0.07% | 0.11% | 0.11% | 0.08% | 0.04% | 0.03% | 0.01% | 0.00% | 0.47% |
| 4.0 - 4.2 | 0.00% | 0.00% | 0.00% | 0.02% | 0.06% | 0.08% | 0.08% | 0.06% | 0.04% | 0.03% | 0.01% | 0.00% | 0.38% |
| 4.2 - 4.4 | 0.00% | 0.00% | 0.00% | 0.01% | 0.04% | 0.06% | 0.05% | 0.05% | 0.03% | 0.03% | 0.01% | 0.00% | 0.27% |
| 4.4 - 4.6 | 0.00% | 0.00% | 0.00% | 0.01% | 0.02% | 0.06% | 0.05% | 0.03% | 0.03% | 0.02% | 0.00% | 0.00% | 0.21% |
| 4.6 - 4.8 | 0.00% | 0.00% | 0.00% | 0.01% | 0.03% | 0.04% | 0.04% | 0.03% | 0.02% | 0.02% | 0.01% | 0.00% | 0.20% |
| 4.8 - 5.0 | 0.00% | 0.00% | 0.00% | 0.01% | 0.02% | 0.03% | 0.03% | 0.03% | 0.02% | 0.01% | 0.00% | 0.00% | 0.15% |
| 5.0 - 5.2 | 0.00% | 0.00% | 0.00% | 0.00% | 0.02% | 0.02% | 0.03% | 0.04% | 0.01% | 0.01% | 0.00% | 0.00% | 0.13% |
| 5.2 - 5.4 | 0.00% | 0.00% | 0.00% | 0.00% | 0.01% | 0.02% | 0.02% | 0.02% | 0.01% | 0.00% | 0.00% | 0.00% | 0.08% |
| 5.4 - 5.6 | 0.00% | 0.00% | 0.00% | 0.00% | 0.01% | 0.03% | 0.01% | 0.02% | 0.01% | 0.01% | 0.00% | 0.00% | 0.08% |
| 5.6 - 5.8 | 0.00% | 0.00% | 0.00% | 0.00% | 0.01% | 0.01% | 0.01% | 0.01% | 0.00% | 0.00% | 0.00% | 0.00% | 0.05% |
| > 5.8 | 0.00% | 0.00% | 0.00% | 0.00% | 0.01% | 0.06% | 0.04% | 0.02% | 0.03% | 0.01% | 0.00% | 0.00% | 0.18% |
| Total ( % ) | 10.86% | 11.47% | 11.31% | 11.77% | 11.64% | 12.67% | 11.33% | 8.60% | 5.95% | 3.23% | 0.93% | 0.25% | 100.00% |

Mar 2021 Lidar flight snow depth per elevation bin (masl)

| Snow Depth (m) | 1390 – 1500 | 1500 – 1600 | 1600 – 1700 | 1700 – 1800 | 1800 – 1900 | 1900 – 2000 | 2000 – 2100 | 2100 – 2200 | 2200 – 2300 | 2300 – 2400 | 2400 – 2500 | 2500 – 2630 | Total ( % ) |
|---|---|---|---|---|---|---|---|---|---|---|---|---|---|
| 0.0 - 0.2 | 0.58% | 0.07% | 0.13% | 0.22% | 0.41% | 0.78% | 0.97% | 1.15% | 1.25% | 1.15% | 0.38% | 0.11% | 7.22% |
| 0.2 - 0.4 | 3.28% | 0.57% | 0.21% | 0.21% | 0.31% | 0.53% | 0.64% | 0.78% | 0.62% | 0.38% | 0.15% | 0.04% | 7.72% |
| 0.4 - 0.6 | 3.58% | 2.11% | 0.98% | 0.35% | 0.32% | 0.45% | 0.47% | 0.54% | 0.44% | 0.25% | 0.06% | 0.03% | 9.56% |
| 0.6 - 0.8 | 2.37% | 4.45% | 2.04% | 0.94% | 0.42% | 0.44% | 0.45% | 0.45% | 0.37% | 0.18% | 0.05% | 0.01% | 12.16% |
| 0.8 - 1.0 | 0.92% | 2.78% | 3.26% | 1.63% | 0.66% | 0.44% | 0.39% | 0.41% | 0.32% | 0.13% | 0.04% | 0.01% | 10.97% |
| 1.0 - 1.2 | 0.11% | 1.05% | 2.59% | 2.48% | 1.42% | 0.78% | 0.46% | 0.41% | 0.29% | 0.10% | 0.03% | 0.01% | 9.73% |
| 1.2 - 1.4 | 0.02% | 0.29% | 1.10% | 2.39% | 1.88% | 1.51% | 0.59% | 0.39% | 0.28% | 0.10% | 0.03% | 0.00% | 8.58% |
| 1.4 - 1.6 | 0.00% | 0.09% | 0.52% | 1.38% | 1.66% | 1.68% | 0.98% | 0.46% | 0.27% | 0.09% | 0.03% | 0.01% | 7.16% |
| 1.6 - 1.8 | 0.00% | 0.03% | 0.23% | 0.83% | 1.14% | 1.36% | 1.23% | 0.73% | 0.32% | 0.09% | 0.02% | 0.01% | 5.98% |
| 1.8 - 2.0 | 0.00% | 0.02% | 0.10% | 0.43% | 0.82% | 1.12% | 1.10% | 0.71% | 0.39% | 0.14% | 0.01% | 0.00% | 4.85% |
| 2.0 - 2.2 | 0.00% | 0.00% | 0.06% | 0.28% | 0.61% | 0.80% | 0.89% | 0.58% | 0.35% | 0.15% | 0.02% | 0.00% | 3.73% |
| 2.2 - 2.4 | 0.00% | 0.00% | 0.04% | 0.17% | 0.44% | 0.63% | 0.71% | 0.43% | 0.24% | 0.11% | 0.02% | 0.00% | 2.78% |
| 2.4 - 2.6 | 0.00% | 0.00% | 0.02% | 0.15% | 0.38% | 0.49% | 0.63% | 0.36% | 0.20% | 0.05% | 0.01% | 0.01% | 2.30% |
| 2.6 - 2.8 | 0.00% | 0.00% | 0.01% | 0.07% | 0.29% | 0.35% | 0.43% | 0.27% | 0.14% | 0.05% | 0.01% | 0.00% | 1.63% |
| 2.8 - 3.0 | 0.00% | 0.00% | 0.00% | 0.06% | 0.20% | 0.28% | 0.33% | 0.20% | 0.10% | 0.03% | 0.02% | 0.00% | 1.22% |
| 3.0 - 3.2 | 0.00% | 0.00% | 0.01% | 0.04% | 0.15% | 0.19% | 0.27% | 0.16% | 0.06% | 0.02% | 0.01% | 0.00% | 0.91% |
| 3.2 - 3.4 | 0.00% | 0.00% | 0.00% | 0.04% | 0.11% | 0.16% | 0.18% | 0.11% | 0.05% | 0.03% | 0.01% | 0.00% | 0.70% |
| 3.4 - 3.6 | 0.00% | 0.00% | 0.00% | 0.03% | 0.09% | 0.12% | 0.15% | 0.08% | 0.05% | 0.02% | 0.01% | 0.00% | 0.54% |
| 3.6 - 3.8 | 0.00% | 0.00% | 0.00% | 0.01% | 0.08% | 0.09% | 0.10% | 0.06% | 0.04% | 0.02% | 0.01% | 0.00% | 0.41% |
| 3.8 - 4.0 | 0.00% | 0.00% | 0.00% | 0.01% | 0.05% | 0.08% | 0.08% | 0.06% | 0.04% | 0.02% | 0.01% | 0.00% | 0.34% |
| 4.0 - 4.2 | 0.00% | 0.00% | 0.00% | 0.01% | 0.04% | 0.06% | 0.05% | 0.03% | 0.02% | 0.02% | 0.01% | 0.00% | 0.25% |
| 4.2 - 4.4 | 0.00% | 0.00% | 0.00% | 0.01% | 0.04% | 0.05% | 0.04% | 0.03% | 0.02% | 0.02% | 0.01% | 0.00% | 0.22% |
| 4.4 - 4.6 | 0.00% | 0.00% | 0.00% | 0.00% | 0.03% | 0.04% | 0.04% | 0.03% | 0.02% | 0.02% | 0.00% | 0.00% | 0.19% |
| 4.6 - 4.8 | 0.00% | 0.00% | 0.00% | 0.01% | 0.01% | 0.03% | 0.03% | 0.03% | 0.01% | 0.01% | 0.00% | 0.00% | 0.12% |
| 4.8 - 5.0 | 0.00% | 0.00% | 0.00% | 0.00% | 0.02% | 0.03% | 0.02% | 0.02% | 0.02% | 0.01% | 0.00% | 0.00% | 0.12% |
| 5.0 - 5.2 | 0.00% | 0.00% | 0.00% | 0.00% | 0.01% | 0.02% | 0.03% | 0.01% | 0.01% | 0.01% | 0.00% | 0.00% | 0.10% |
| 5.2 - 5.4 | 0.00% | 0.00% | 0.00% | 0.00% | 0.01% | 0.03% | 0.02% | 0.03% | 0.01% | 0.01% | 0.00% | 0.00% | 0.10% |
| 5.4 - 5.6 | 0.00% | 0.00% | 0.00% | 0.00% | 0.01% | 0.02% | 0.02% | 0.02% | 0.01% | 0.00% | 0.00% | 0.00% | 0.08% |
| 5.6 - 5.8 | 0.00% | 0.00% | 0.00% | 0.00% | 0.01% | 0.02% | 0.02% | 0.02% | 0.00% | 0.00% | 0.00% | 0.00% | 0.07% |
| > 5.8 | 0.00% | 0.00% | 0.00% | 0.00% | 0.02% | 0.10% | 0.06% | 0.05% | 0.03% | 0.01% | 0.00% | 0.00% | 0.27% |
| Total ( % ) | 10.86% | 11.47% | 11.31% | 11.77% | 11.64% | 12.67% | 11.33% | 8.60% | 5.95% | 3.23% | 0.93% | 0.25% | 100.00% |

Apr 2021 Lidar flight snow depth per elevation bin (masl)

| Snow Depth (m) | 1390 – 1500 | 1500 – 1600 | 1600 – 1700 | 1700 – 1800 | 1800 – 1900 | 1900 – 2000 | 2000 – 2100 | 2100 – 2200 | 2200 – 2300 | 2300 – 2400 | 2400 – 2500 | 2500 – 2630 | Total ( % ) |
|---|---|---|---|---|---|---|---|---|---|---|---|---|---|
| 0.0 - 0.2 | 4.52% | 1.20% | 0.66% | 0.45% | 0.56% | 0.89% | 0.96% | 0.97% | 1.00% | 1.00% | 0.34% | 0.09% | 12.64% |
| 0.2 - 0.4 | 3.26% | 2.27% | 1.15% | 0.50% | 0.41% | 0.54% | 0.69% | 0.89% | 0.76% | 0.44% | 0.17% | 0.06% | 11.12% |
| 0.4 - 0.6 | 2.24% | 3.60% | 1.79% | 0.90% | 0.50% | 0.52% | 0.46% | 0.56% | 0.47% | 0.29% | 0.07% | 0.02% | 11.42% |
| 0.6 - 0.8 | 0.73% | 3.02% | 2.93% | 1.40% | 0.58% | 0.50% | 0.49% | 0.46% | 0.38% | 0.16% | 0.05% | 0.01% | 10.70% |
| 0.8 - 1.0 | 0.08% | 0.97% | 2.41% | 2.01% | 1.00% | 0.54% | 0.46% | 0.45% | 0.33% | 0.15% | 0.04% | 0.01% | 8.45% |
| 1.0 - 1.2 | 0.01% | 0.26% | 1.25% | 2.19% | 1.53% | 0.94% | 0.48% | 0.43% | 0.28% | 0.10% | 0.03% | 0.01% | 7.51% |
| 1.2 - 1.4 | 0.00% | 0.09% | 0.51% | 1.58% | 1.72% | 1.70% | 0.74% | 0.41% | 0.29% | 0.11% | 0.03% | 0.01% | 7.19% |
| 1.4 - 1.6 | 0.00% | 0.03% | 0.30% | 0.97% | 1.21% | 1.58% | 1.03% | 0.58% | 0.30% | 0.09% | 0.03% | 0.00% | 6.15% |
| 1.6 - 1.8 | 0.00% | 0.01% | 0.12% | 0.60% | 0.89% | 1.22% | 1.12% | 0.75% | 0.38% | 0.09% | 0.02% | 0.01% | 5.23% |
| 1.8 - 2.0 | 0.00% | 0.00% | 0.06% | 0.33% | 0.68% | 0.79% | 0.98% | 0.58% | 0.37% | 0.11% | 0.02% | 0.00% | 3.93% |
| 2.0 - 2.2 | 0.00% | 0.00% | 0.05% | 0.23% | 0.58% | 0.65% | 0.74% | 0.50% | 0.28% | 0.13% | 0.02% | 0.00% | 3.19% |
| 2.2 - 2.4 | 0.00% | 0.00% | 0.03% | 0.15% | 0.42% | 0.57% | 0.65% | 0.38% | 0.23% | 0.14% | 0.02% | 0.00% | 2.60% |
| 2.4 - 2.6 | 0.00% | 0.00% | 0.02% | 0.12% | 0.36% | 0.48% | 0.58% | 0.34% | 0.17% | 0.07% | 0.01% | 0.00% | 2.15% |
| 2.6 - 2.8 | 0.00% | 0.00% | 0.01% | 0.10% | 0.29% | 0.34% | 0.41% | 0.26% | 0.18% | 0.05% | 0.01% | 0.00% | 1.66% |
| 2.8 - 3.0 | 0.00% | 0.00% | 0.00% | 0.05% | 0.20% | 0.27% | 0.33% | 0.22% | 0.10% | 0.05% | 0.01% | 0.00% | 1.26% |
| 3.0 - 3.2 | 0.00% | 0.00% | 0.01% | 0.05% | 0.15% | 0.22% | 0.27% | 0.15% | 0.08% | 0.04% | 0.01% | 0.00% | 0.97% |
| 3.2 - 3.4 | 0.00% | 0.00% | 0.00% | 0.03% | 0.11% | 0.17% | 0.20% | 0.13% | 0.05% | 0.02% | 0.01% | 0.00% | 0.73% |
| 3.4 - 3.6 | 0.00% | 0.00% | 0.00% | 0.03% | 0.08% | 0.14% | 0.14% | 0.10% | 0.05% | 0.02% | 0.01% | 0.00% | 0.56% |
| 3.6 - 3.8 | 0.00% | 0.00% | 0.00% | 0.01% | 0.08% | 0.09% | 0.11% | 0.06% | 0.04% | 0.02% | 0.01% | 0.00% | 0.43% |
| 3.8 - 4.0 | 0.00% | 0.00% | 0.00% | 0.02% | 0.07% | 0.10% | 0.09% | 0.07% | 0.04% | 0.02% | 0.01% | 0.00% | 0.41% |
| 4.0 - 4.2 | 0.00% | 0.00% | 0.00% | 0.01% | 0.04% | 0.05% | 0.07% | 0.04% | 0.03% | 0.02% | 0.00% | 0.00% | 0.25% |
| 4.2 - 4.4 | 0.00% | 0.00% | 0.00% | 0.00% | 0.03% | 0.05% | 0.06% | 0.03% | 0.02% | 0.02% | 0.01% | 0.00% | 0.23% |
| 4.4 - 4.6 | 0.00% | 0.00% | 0.00% | 0.01% | 0.03% | 0.03% | 0.03% | 0.04% | 0.02% | 0.02% | 0.01% | 0.00% | 0.19% |
| 4.6 - 4.8 | 0.00% | 0.00% | 0.00% | 0.00% | 0.02% | 0.06% | 0.04% | 0.03% | 0.02% | 0.02% | 0.00% | 0.00% | 0.19% |
| 4.8 - 5.0 | 0.00% | 0.00% | 0.00% | 0.00% | 0.02% | 0.03% | 0.03% | 0.02% | 0.01% | 0.01% | 0.00% | 0.00% | 0.13% |
| 5.0 - 5.2 | 0.00% | 0.00% | 0.00% | 0.00% | 0.02% | 0.03% | 0.02% | 0.02% | 0.01% | 0.01% | 0.00% | 0.00% | 0.11% |
| 5.2 - 5.4 | 0.00% | 0.00% | 0.00% | 0.00% | 0.02% | 0.03% | 0.02% | 0.02% | 0.01% | 0.01% | 0.00% | 0.00% | 0.10% |
| 5.4 - 5.6 | 0.00% | 0.00% | 0.00% | 0.00% | 0.01% | 0.01% | 0.03% | 0.02% | 0.01% | 0.00% | 0.00% | 0.00% | 0.09% |
| 5.6 - 5.8 | 0.00% | 0.00% | 0.00% | 0.00% | 0.01% | 0.02% | 0.02% | 0.02% | 0.01% | 0.01% | 0.00% | 0.00% | 0.07% |
| > 5.8 | 0.00% | 0.00% | 0.00% | 0.00% | 0.03% | 0.12% | 0.07% | 0.08% | 0.02% | 0.01% | 0.00% | 0.00% | 0.35% |
| Total ( % ) | 10.86% | 11.47% | 11.31% | 11.77% | 11.64% | 12.67% | 11.33% | 8.60% | 5.95% | 3.23% | 0.93% | 0.25% | 100.00% |